Yield stress fluid flows in uneven geometries: applications to the oil & gas industry

by

Ali Roustaei

BSc Mechanical Engineering, Sharif University of Technology, 2007

MSc Mechanical Engineering, Sharif University of Technology, 2010

A THESIS SUBMITTED IN PARTIAL FULFILLMENT OF THE REQUIREMENTS FOR THE DEGREE OF

Doctor of Philosophy

in

THE FACULTY OF GRADUATE AND POSTDOCTORAL STUDIES

(Mechanical Engineering)

The University of British Columbia

(Vancouver)

May 2016

Abstract

We study a set of yield stress fluid flows in channels with geometric non-uniformities, motivated by theoretical aspects and industrial applications. Methodology is primarily computational and we try to analytically investigate as much as possible. Theoretical interest arises from the self-selection phenomenon, meaning that the original flow geometry is modified by the fluid itself. This occurs due to yield stress and is accomplished via stagnant zones of the fluid attached to the boundary of original geometry. Industrial motivations stem from oil/gas well construction operations: primary and squeeze cementing and hydraulic fracturing. In all we have drilling mud, cement or a gelled fluid which exhibit yield stress. Specifically, we model a washout along the well as a non-uniform channel and extensively study flows through it. This is an enlarged segment of the well where the wellbore is washed out or collapsed. The main industrial concern is the residual mud left in the washout after primary cementing which weakens the hydraulic sealing function of the cement.

Self-selection has been analytically studied for duct flows [168, 169], and not much in 2D flows. Chapter 2 is a study of self-selection in wavy walled channels as a model for smooth non-uniform channels. We find similar results to [168, 169], however a complete understanding eludes us. Chapter 3 looks at the flow of Bingham fluid in fractures. We study the limits of validity of Darcy approach first and then focus at the minimal pressure drop required to mobilize the fluid in fracture. We demonstrate knowing self-selection properties can greatly improve approximations here. Chapters 4-6 are step by step investigation of the flows in washout, from Stokes to

inertial and finally displacement flow. In Chapter 4 we show self-selection in Stokes flow of washout and use it to estimate the residual fluid in the washout. We study the effects of inertia on it in Chapter 5, illustrating only finite amount of inertia would help in better displacement of the mud which is counter intuitive. Chapter 6 is a preliminary study of the displacement flow and we report some interesting observations.

Preface

The contents of this thesis are the results of the research of the author, Ali Roustaei during the course of his PhD studies at UBC, under the supervision of professor Ian Frigaard. The following papers have been published and/or are in progress

- Roustaei, A., and I.A. Frigaard. "The occurrence of fouling layers in the flow of a yield stress fluid along a wavy-walled channel." Journal of Non-Newtonian Fluid Mechanics 198 (2013):109-124.

  This paper was co-authored with I.A. Frigaard and I did the implementation of the code, running, data compilation and contributed to analysis of the results. I. A. Frigaard supervised the research.

- Roustaei, A., A. Gosselin, and I.A. Frigaard. "Residual drilling mud during conditioning of uneven boreholes in primary cementing. Part 1: Rheology and geometry effects in non-inertial flows." Journal of Non-Newtonian Fluid Mechanics 220 (2015): 87-98.

  This paper was co-authored with I.A. Frigaard and I did the implementation of the code, running, data compilation and contributed to analysis of the results. A. Gosselin–intern student–implemented the koch semi-fractal shape and assisted with running some of the computations. I.A. Frigaard supervised the research.

- Roustaei, A., and I.A. Frigaard. "Residual drilling mud during conditioning of uneven boreholes in primary cementing. Part 2: Steady

laminar inertial flows." Journal of Non-Newtonian Fluid Mechanics 226 (2015): 1-15.

This paper was co-authored with I.A. Frigaard and I did the implementation of the code, running, data compilation and contributed to analysis of the results. I.A. Frigaard supervised the research.

- Roustaei, A., T. Chevalier, L. Talon and I.A. Frigaard "Non-Darcy effects in fracture flows of a yield stress fluid" under review.

  This paper was co-authored primarily with I.A. Frigaard and L. Talon. I and I.A. Frigaard ran the main computations and analysis for the paper and T. Chevalier and L. Talon contributed to the affine fracture computations and collaborated on some aspects of the analysis.

- A. Maleki, S. Hormozi, A. Roustaei, and I. A. Frigaard. "Macro-size drop encapsulation." Journal of Fluid Mechanics 769 (2015): 482-521.

  This paper was the outcome of A. Maleki's masters thesis research. I helped in the implementation of his code, initial computations of the encapsulation flows and to validation/verification studies. The paper was authored primarily by the rest of authors. I read the draft and provided comments and participated in some of the analysis. I. A. Frigaard supervised the research.

Table of Contents

List of Figures

Acknowledgments

This research has been carried out at the University of British Columbia, supported financially by NSERC and Schlumberger through CRD project 444985-12 and I appreciate this support. I also thank the department of mechanical engineering of the University of British Columbia for giving me the excellence award.

I am deeply grateful to my PhD supervisor, Professor Ian Frigaard. Preparation and submission of this thesis would not have been possible without Ian's guidance, support and patience. The best I canb briefly describe Ian is a sharp scientifically disciplined supervisor with a great sense of humor who tries to pay attention to every aspect of his students, not only the academic one. I really enjoyed being your student and I wish you all the bests. It would be my privilege to continue working with you.

I would also like to thank my supervisory committee members, Anthony Wachs, Neil Balmforth and Carl Olivier-Gooch. Neil, I enjoyed your asymptotic analysis course. Carl, your computational transport phenomenon courses was a complete journey from introductory to advanced topics of finite volume method, which I liked much. Thank you Anthony for your *right to the point* advices which come from years of experience. Sometimes just one sentence from you was the key to the solution of a problem. It was always a joy to talk with you.

I thank all of our lab members, interns and everyone who I have worked with during these years. Forgive me if I am not mentioning the names as there would be too many people and I do not want to miss any, thank you all.

Mother and father, you are at my heart and I have no meaning without you. I do not know how to thank you for everything you gave me, your endless love, kindness, support and whatever I can think of. I hope this thesis can bring a small smile and feeling of satisfaction to you. Ali is still your small son and will remain so for ever.

Last but not least, I want to thank my wife, my close companion in experiencing every moment of this journey, especially the hard moments which were definitely much harder without you. We had some adversities in the early years of coming to Canada, however never forgot to love each other and the time taught us how we can overcome anything together. Now we are looking at the horizon together, ready for the future with more love and energy.

Ali Roustaei
Vancouver, BC
January 2016

To my big brother Mahdi,

I wish you were here ...

Chapter 1

Introduction

Much of the work presented in this thesis is motivated by flows that are found in oil & gas well construction and later in well stimulation (although also occurring in other industrial and natural settings). The fluids are viscoplastic, meaning that they are viscous fluids with a yield stress. The geometries that result in these industrial flows have certain non-uniform features that result in interesting static regions and also in limiting parameters that demarcate *flow* from *no-flow*, i.e. yielding.

In this chapter we first explain industrial origins of the flows that we study (§1.1) and hence part of the motivation for this thesis. Secondly, we review general features of yield stress fluids (§1.2). In §1.3 we give an overview of the variational principles that underly viscoplastic fluid flows. Computational methods are discussed in §1.4. Section 1.5 reviews specific yield stress fluid flows that show similar geometric effects to those studied here, e.g. static regions and self-selection of the flowing domain. Finally, we close the chapter with an overview of the research objectives and thesis outline (§1.6).

1.1 Industrial motivations

Since the production of oil from Edwin Drake's 1859 well near Titusville, Pennsylvania, the petroleum industry has grown tremendously. Drake's well

can be considered a founder of modern commercial oil production practice: (a) it was drilled, not dug; (b) it used a steam engine [251] to power the drilling; (c) there was a company associated with the drilling. Today oil represents the blood of the modern economy and many other industries like commercial aviation, automotive, electronics, chemical and pharmaceutical, materials and others heavily depend on the availability of oil.

This thesis considers single- and two-phase flows of viscoplastic fluids flows in a variety of nonuniform geometries. The main characteristic of these fluids is that they deform only when the applied stress exceeds a limit $\hat{\tau}_y$ called yield stress. Below $\hat{\tau}_y$ they show rigid solid-like behaviour. This rheological behaviour can have an impact on many upstream oil & gas processes, which we now review.

1.1.1 Primary cementing

Well construction is the most critical and technical part of oil & gas extraction engineering. Without a long life and trustworthy well, reservoir production is unlikely to reach its full potential. The key to such a well is effective zonal isolation of different layers of the reservoir at the well. An innovation of Drake's well was in drilling through a metal pipe (casing) to prevent collapse of the well and as a later pathway for producing oil. This idea is still employed and further improved by the process of primary cementing.

Primary Cementing is a technique in well construction for placing cement slurry in the annular space between the metal casing and the borehole. A typical primary cementing operation proceeds as follows. After the drilling is done, the casing is lowered into the well which is full of drilling mud. Then cement is pumped into the casing at the well head, cement goes all the way down inside the pipe (casing), exits at the bottom, and displaces drilling mud as it moves back up the annulus. The cement has several roles [176]:

1. The cement provides a hydraulic seal in the wellbore, preventing the migration of formation fluids in the annulus.

2. The cement anchors and supports the casing.

3. The cement protects the casing against corrosion, due to hot formation brines and/or hydrogen sulfide (H_2S)

As well as cement, a number of other specially designed fluids (e.g. washes and spacers) are pumped ahead of the cement slurry to aid displacement/removal of the drilling mud, reduce cement contamination and to improve the eventual bonding to the outside of the casing and to the formation.

Today's oil wells can be over 10km long, with long horizontal sections. For these wells, having good hydraulic sealing provided by the cement throughout the well is critical to both safety and efficiency. A poor seal results in production loss and environmental effects. In extreme situations it may lead to loss of well control and to a blow out. A notorious example is the Deepwater Horizon blow out in the Gulf of Mexico at April 2010, which caused eleven deaths, sinking and explosion of the rig and massive oil spill in the Gulf. It was the largest environmental disaster in U.S. history [250]. Later, investigations mentioned that not enough centralizers were used for the cementing job [142], resulting in poor mud removal and leaving well in an unstable state.

From a fluid mechanics perspective, primary cementing is a displacement flow. This is a term generally used for a two phase flow in which one phase (displacing fluid) is forcing another phase (displaced fluid) to move out from its current location. Initially the displaced fluid is at rest, the displacing fluid is injected with pressure at inlet(s) and the displaced fluid starts to exit from drain(s). Displacement flows are important in a wide variety of applications, including secondary and tertiary oil recovery, fixed bed regeneration in chemical processing, hydrology, and filtration [122]. Also in bio-medical applications (mucus [128] and biofilms [191]) and in food processing for cleaning of pipes and machinery [108]. An important parameter of these flows is the displacement efficiency, which is defined as the fraction of displaced fluid that is washed by the displacing fluid. A displacement efficiency of 1 is always desired as the goal is to completely evacuate the displaced fluid.

Displacement flows like primary cementing are very rich in terms of phys-

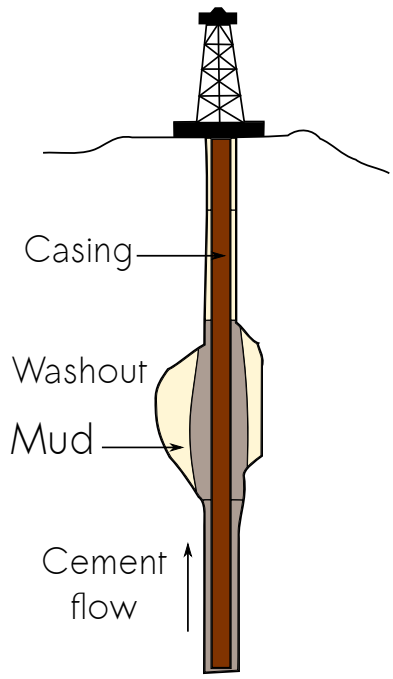

Figure 1.1: Primary cementing and static mud in washout region

ical phenomena. This is due to having (at least) two fluids with different density, viscosity, yield stress and other properties, all of can be differ. Buoyancy effects may be important and density and viscosity differences can cause complex interfacial dynamics, e.g. Kelvin-Helmholtz and Rayleigh-Taylor instabilities. In the case of primary cementing, drilling mud, spacer fluid and cement slurries are often miscible with a weak molecular diffusion that leads to high Péclet number in cementing flows. This means that over process timescales a relatively sharp interface exists between fluids, provided that no instability occurs.

Another interesting issue with primary cementing flow which makes the process more complicated is that it consists of two different stages: (a) flow inside the casing (pipe geometry) when cement has not yet exited at the bottom and moves downward; (b) flow inside the annular gap, in which the fluids move upward. Having both downward and upward flow inevitably causes density unstable flow in one direction which is not desired, due to

unstable mixing of the fluids. Usually for the downward displacement plastic plugs are used to separate the fluid stages. However, sometimes this is not possible due to the operating conditions. The geometries are also very different: the downward displacement geometry is a pipe of 3cm–50cm diameter; the upwards annular displacement can have an annular gap that varies between 2mm–5cm.

In this thesis we study features of the narrow annular flows, both single phase and displacement flow, and the focus is on the study of flow within **washouts**. As mentioned, the annular gap is usually narrow with some statistical variations in aperture due to drilling variability. However sometimes, there are large variations in the gap width due to partial collapse of wellbore during drilling. These regions are called washouts (Figure 1.1) and may exist due to several reasons [176]:

1. Soft and unconsolidated formations
2. In-situ rock stresses
3. Excessive jet velocity of fluids passing through the drillbit
4. Chemical reactions
5. Mechanical damage by the rotating drill string

Single phase flow occurs just prior to cementing, when the drilling mud is circulated around well to condition the mud. Displacement flows occur during mud removal/cement placement. Except for very shallow washouts, a washout always lowers the quality of primary cementing. This is because the cement fails to displace drilling mud in the depths of a washout section and mud stays attached to the wall after cementing. If static regions are connected longitudinally they can allow a path through which formation fluids and gas can migrate to surface. Geometry is a key factor in the appearance of static regions and washout geometries are unpredictable. Hence we need to systematically address the geometric diversity of washouts and the effects this has on the flow. This issue is examined in Chapter 4.

Figure 1.2: DeepWater Horizon explosion at Gulf of Mexico, April 2010. One of the main causes was poor primary cementing

1.1.2 Plug cementing for abandonment

Cement plugs are set in wells sometimes during construction, e.g. to initiate directional drilling by providing a firm base for drill bit to turn (sidetracking), and always at the end of a well's life in the abandonment process; see [176]. It is common to set a number of plugs to isolate producing zones of the reservoir. Different regulations and methods exist worldwide. The placement process typically involes pumping cement down a narrow tube, displacing upwards the wellbore fluids. The geometry in the upwards flowing stage is thus again annular, similar to the primary cementing operation, although the annulus is no longer narrow.

A recent trend in the North Sea has been to mill out the wellbore, through the casings and cement, so that the set plug fully isolates and seals across the steel and cement layers. These milled out sections are $\sim$ 100m in length. The annular geometry of the milled out "window" is thus somewhat similar to that of a deep and long washout in primary cementing. The

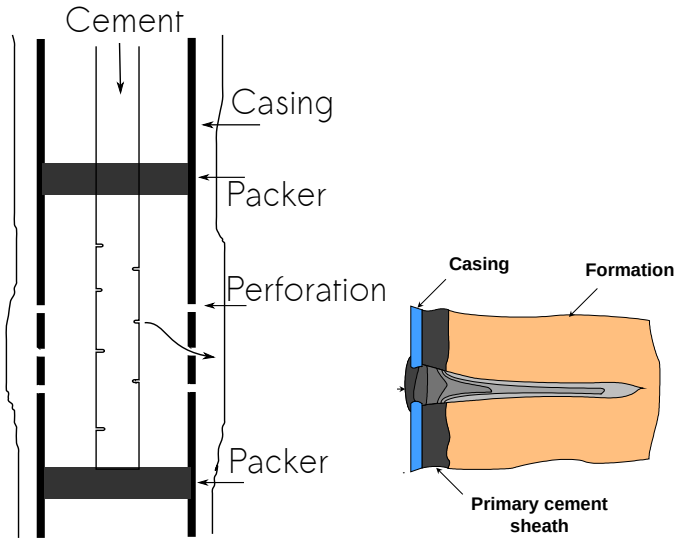

Figure 1.3: Squeeze cementing, used for correction of primary cement. Right: showing the schematic of equipment for squeeze. Left: a closer view to fracture flow, courtesy of GKE engineering

concern again is that the pumped slurry manages to effectively displace the wellbore fluids and bonds well to the rock formation.

1.1.3 Squeeze cementing and other remedial tasks

After primary cementing is performed, the hope is that a continuous seal has been obtained along the whole length of the well. However, this does not happen always. Equally, sometimes later in the producing life of a well the cement seal may deteriorate (e.g. due to thermal or geophysical stress cycling), and perhaps crack. These defects are repaired by the squeeze cementing process. In this operation the casing is typically perforated and isolated (Figure 1.3) with packers at the location of interest, before cement is forced into specific locations under an applied pressure.

Although squeeze cementing usually refers to the phase after well completion, i.e. to repair cracks/fissures or fill severe washouts, all in order to improve productivity, other similar scenarios arise. During construction, cement could be pumped into the rock formation to cure lost-circulation (also

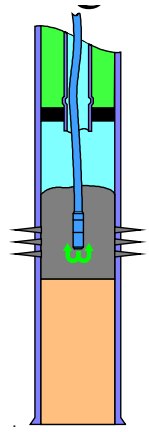

Figure 1.4: Plug cements are used to persistently isolate necessary zones for abandonment, Figure courtesy of GKE engineering

potentially linked to cement plugging). At the abandonment stage, some squeezing is done in sections of the wellbore that have been perforated/fractured for production, i.e. to fill the fissures before the well itself is plugged (Figure 1.4).

1.1.4 Hydraulic fracturing

Hydraulic fracturing is a well-stimulation technique used to boost oil and gas wells production. It is done by injecting a mixture of fluid and grains (called *proppant*) down the well at very high pressures (Figure 1.5). This mixture enters into well perforations (small explosively initiated fractures) and fracture the rocks, resulting in an increased effective permeability which allows hydrocarbon to flow easier. Common proppants are sand, ceramics or aluminum oxide. After the rock is fractured to the designed level, pressure is removed and the fracture closes on the proppant, squeezing the frac fluid away. During this *flowback* stage the returning fluid is a mix of injection fluid, formation brines, hydrocarbons and other well contaminants, all of which are collected at the well head.

Hydraulic fracturing is not a new technology, it has been used since at least 1950. However, there has been an increasing interest in recent

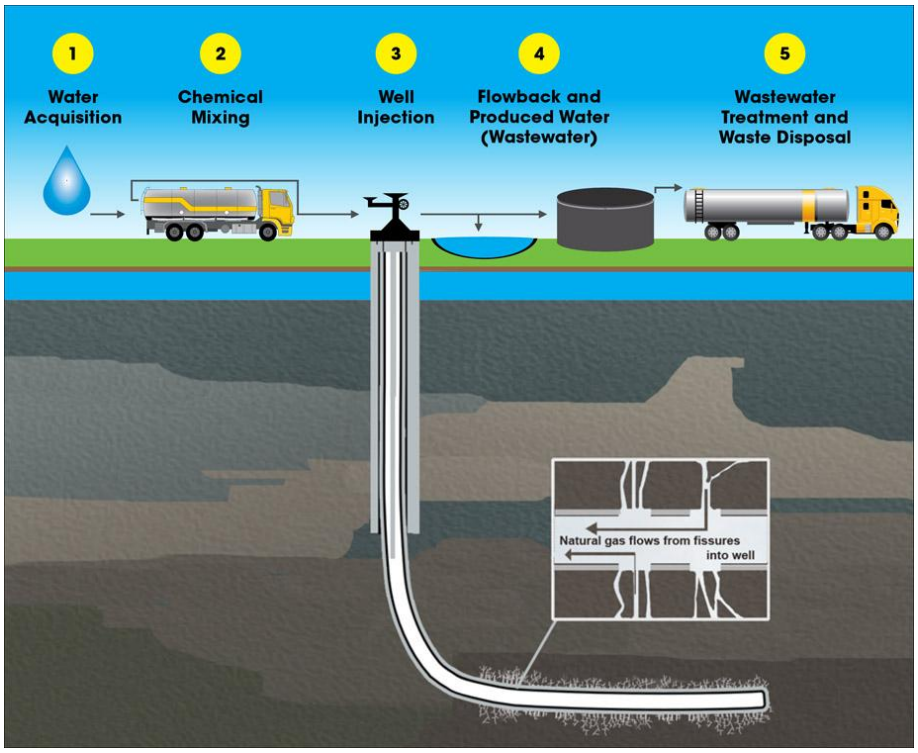

Figure 1.5: Depiction of fracturing, photo from US Environmental Protection Agency [3]

years, as conventional hydrocarbon resources are dwindling and production from unconventional reserves such as shale gas and sandstone oil/gas has become economically competitive with the aid of fracturing and extended reach horizontal drilling. These resources are present in Canada, where a large percentage of the reserves are held in sandstones. In British Columbia current reserves are mainly natural gas in held in tight shales. The fracturing process is essential for developing these resources. There are also environmental concerns associated with fracturing. First, large amounts of water are needed for fracturing, which is obtained from a mix of land and underground water. Usually the returned fluid (waste water) is treated and used again. However, during the process, frac fluid leaks off into the surrounding rocks. If not controlled properly, leak off can even be as large as %70 of

the initial volume [252]. This means that considerable fresh water will be needed for each new well. Second, the leak-off fluid can contaminate underground water reservoirs used for drinking and agriculture, causing public health problems. Third, large fracturing jobs change the stress distribution in rock layers and hence seismic activity of the location. There has been recent concern that fracking may potentially trigger earthquakes.

Many fracking operations simply use water with drag reducing agents, suspending the proppant (sand) in turbulent eddies. Viscous fluids are also used for fracking and these are basically water with the addition of different chemicals and gelling agent which creates a yield stress in the fluid. The yield stress helps to prevent proppant settling and gives better transport properties. Although the yield stress is useful in this role, it also results in higher frictional losses. Also during the flowback stage the gelled frac fluid might get stuck in the fracture, reducing the permeability of fracture. Therefore the design of fluid properties must be carefully considered.

In this thesis we consider the flow rate–pressure drop relation of a yield stress fluid flowing along simple fractures. We specifically consider the problem of the critical pressure drop necessary to start the flow in fracture, which is also related to the invasion type flows discussed in squeeze cementing (see chapter 3).

1.1.5 Other fracture-like geometries

As well as artificially occurring fractures, the flow of yield stress fluid in natural fractures is also important. Examples include drilling mud loss into formations during drilling and various methods advocated for sealing CO_2 sequestration reservoirs by injecting cement. In both scenarios we have the flow of a yield stress fluid into a porous media and due to yield stress the fluid invades only into a finite volume of the media for a given pressure. The question here is that how far does the fluid invades? This also relates closely to the problem of the critical pressure drop required to initiate flow along a fracture (see chapter 3).

1.2 Yield stress fluids

As mentioned yield stress or viscoplastic fluids deform only after a certain stress limit $\hat{\tau}_y$ is overcome. There are many examples of these fluids:

1. Health/Cosmetics: gels, creams, toothpaste
2. Foods: chocolate, yogurt, soft butter, cake batter, whipping cream, wet pasta ...
3. Natural and biological: Lava, mucus, some suspensions
4. Industrial: Cement slurries, drilling mud, mine tailing, ...

The simplest and most commonly used rheology model was first suggested by Bingham [32], which corresponds (in 1D) to adding a yield stress to the Newtonian viscosity:

$$\hat{\tau} = \hat{\tau}_y + \hat{\mu}\frac{d\hat{u}}{d\hat{y}}, \quad \Leftrightarrow \hat{\tau}_y < |\hat{\tau}| \tag{1.1}$$

$$\frac{d\hat{u}}{d\hat{y}} = 0, \quad \Leftrightarrow \hat{\tau}_y \geq |\hat{\tau}| \tag{1.2}$$

Here $\hat{\tau}$ is the shear stress in a 2D parallel flow with velocity field $\hat{u}(\hat{y})$ in the $\hat{x}$ direction, $\hat{\mu}$ is the plastic viscosity. The extension of this model to 3D tensorial formulation was introduced by Prager [120, 195]:

$$\hat{\tau}_{ij} = \left(\hat{\mu} + \frac{\hat{\tau}_y}{\hat{\dot{\gamma}}(\hat{\mathbf{u}})}\right)\hat{\dot{\gamma}}(\hat{\mathbf{u}}), \quad \Leftrightarrow \hat{\tau}_y < \hat{\tau} \tag{1.3}$$

$$\hat{\dot{\gamma}}(\hat{\mathbf{u}}) = 0, \quad \Leftrightarrow \hat{\tau}_y \geq \hat{\tau} \tag{1.4}$$

Where $\hat{\mathbf{u}}$ is velocity vector, $\hat{\tau}_{ij}$ is the deviatoric stress tensor,

$$\hat{\dot{\boldsymbol{\gamma}}}(\hat{\mathbf{u}}) = (\nabla\hat{\mathbf{u}} + \nabla\hat{\mathbf{u}}^T),$$

is the strain rate tensor and the norms of strain rate and stress are defined as:

$$\hat{\dot{\gamma}}(\hat{\mathbf{u}}) = \sqrt{\frac{1}{2}\hat{\dot{\gamma}}_{ij}\hat{\dot{\gamma}}_{ij}}, \qquad \hat{\tau} = \sqrt{\frac{1}{2}\hat{\tau}_{ij}\hat{\tau}_{ij}} \tag{1.5}$$

The locus of points with $\hat{\tau} = \hat{\tau}_y$ represents the boundary of yielded and unyielded regions and is called the *yield surface*. Prager also contributed to the variational theory of viscoplastic fluid, especially minimization-maximization principles for stokes flow which will be presented later. The Bingham model in dimensionless[1] form becomes:

$$\tau_{ij} = \left(1 + \frac{B}{\dot{\gamma}(\mathbf{u})}\right)\dot{\gamma}_{ij}, \quad \Leftrightarrow B < \tau, \tag{1.6}$$

$$\dot{\gamma}_{ij} = 0, \quad \Leftrightarrow B \geq \tau. \tag{1.7}$$

The dimensionless Bingham number $B = \hat{\tau}_y \hat{l}/\hat{\mu}\hat{U}$ is the ratio of the yield stress to a typical viscous stress; $\hat{l}$, $\hat{U}$ are length and velocity scales respectively.

In practice almost no fluid has the idealised behaviour of the Bingham model. A more realistic model is the Herschel-Bulkley fluid which considers a power-law type of viscosity in the Bingham model. In dimensionless form:

$$\tau_{ij} = \left(\dot{\gamma}^{n-1} + \frac{B}{\dot{\gamma}(\mathbf{u})}\right)\dot{\gamma}_{ij}, \quad \Leftrightarrow B < \tau, \tag{1.8}$$

$$\dot{\gamma}_{ij} = 0, \quad \Leftrightarrow B \geq \tau B. \tag{1.9}$$

For $n < 1$ the fluid is shear thinning, meaning that the viscosity decreases with increasing shear rate. For $n > 1$ the fluid is shear thickening and the viscosity grows with shear rate. For $n = 1$ the model reduces to Bingham fluid.

The Casson model is a more complicated and less common model that is based on a structural model for the dynamic behavior of a solid suspension. It also includes a shear thinning effect.

$$\hat{\tau}_{ij} = \left(\sqrt{\hat{\mu}} + \sqrt{\frac{\hat{\tau}_y}{\hat{\dot{\gamma}}(\hat{\mathbf{u}})}}\right)^2 \hat{\dot{\gamma}}_{ij}, \quad \Leftrightarrow \hat{\tau}_y < \hat{\tau}, \tag{1.10}$$

$$\hat{\dot{\gamma}}_{ij} = 0, \quad \Leftrightarrow \hat{\tau}_y \geq \hat{\tau}. \tag{1.11}$$

[1] In the thesis all physical quantities with dimension are shown with hat, vector and tensor entities with bold and scalar values using normal font

This model by also be generalised, replacing the square root with a power-law, i.e.

$$\hat{\tau}_{ij} = \left(\hat{\mu}^n + \left(\frac{\hat{\tau}_y}{\hat{\dot{\gamma}}(\hat{\mathbf{u}})}\right)^n\right)^{1/n} \hat{\dot{\gamma}}_{ij}.$$

Note that the Bingham, Herschel-Bulkley and Casson models are different only in the effective viscosity term. Hence, we expect the yielding behavior of the the models to be very similar.

1.2.1 Thixotropy

The origin of the yield stress is related to the structure of the material. This means that the value of the yield stress may change with the state of material structure. When the rheology is time dependent in this way, we say the the fluid shows *thixotropic* behaviour. In fact many viscoplastic fluids such as muds, paints and food products show this behavior; see [65].

Thixotropy generally widens the single yield stress value to a range between a dynamic yield stress ($\hat{\tau}_{yd}$) and a static yield stress ($\hat{\tau}_{ys}$). After a fluid stops deforming, at the dynamic yield stress, the thixotropic structure of the material starts to form and the yield stress increases to its static limit, which might be significantly higher than the dynamic limit. If the material is sheared again the structures is destroyed and the yield stress returns to the dynamic value. Usually the time scale for reaching $\hat{\tau}_{ys}$ is much longer than the reverse process, i.e. the structures are easily destroyed, but it takes long time to heal back.

Thixotropic yield stress fluid models usually make the yield stress (and other rheological parameters) dependent on a (scalar) structural variable λ. An evolution equation is introduced for this variable that contains both construction and destruction terms. One simple and illustrative model is

from Houska [151], which takes the form (fixing $n = 1$):

$$\hat{\tau}_y = \hat{\tau}_0 + \lambda\hat{\tau}_1 \tag{1.12}$$

$$\hat{\mu} = \hat{\mu}_0 + \lambda\hat{\mu}_1 \tag{1.13}$$

$$\frac{\partial\lambda}{\partial t} + \hat{\mathbf{u}}.\nabla\lambda = \hat{a}(1-\lambda) - \hat{b}\hat{\dot{\gamma}}^m \tag{1.14}$$

Here $\lambda \in [0\ 1]$ is the structure parameter, $\hat{\tau}_0, \hat{\mu}_0$ are the dynamic yield stress and viscosity, $\hat{\tau}_1, \hat{\mu}_1$ are the thixotropic yield stress and viscosity, $\hat{a}$ is the buildup parameter, $\hat{b}$ is the breakdown parameter and m an adjustable parameter. As you can see the yield stress and viscosity vary linearly with λ. Also we observe that when the fluid is at rest ($\hat{\mathbf{u}} = 0, \hat{\dot{\gamma}} = 0$) the structure builds up in an exponential way towards $\lambda = 1$, which is the static structure.

There are many different thixotropic models. In some of these destruction of the structure is shear stress dependent, rather than $\hat{\dot{\gamma}}$-dependent; see e.g. [77, 78]. In other models the yield stress results wholly from thixotropy; see e.g. [68, 69, 202].

1.2.2 The yield stress debate

No matter whether analytical or computational methods are used for the solution of viscoplastic flow, a key problem is to correctly identify unyielded regions in the flow. The reason is that classical viscoplastic models give constitutive relations only for the yielded part of the flow. Inside unyielded regions the only thing known is that the stress is below the yield stress and satisfies the momentum equations. So it is not possible to solve the system until we know the position of the yield surfaces, which themselves depend on the stress field and are not known initially. The singular behaviour at the yield surface has motivated a lot of efforts in the viscoplastic community to resolve the (yield surface) free boundary problem, in both analytical and computational directions. The naïve consideration of unyielded regions resulted in the so called *lubrication paradox* [146], where it was claimed that it would be impossible to have true unyielded regions within flows with complex geometries, e.g. a varying width channel. This paradox will be

discussed in more detail later.

The singularity of the effective viscosity has been a motivating force to question the actual existence of a *real* yield stress. This was first raised by Barnes and Walters [24] who argued that the unyielded fluid is actually a very high viscous state at low shear rates and the known yield stress is a threshold at which abrupt change of viscosity occurs. In a later paper [23] Barnes gives evidence to support his viewpoint and asserts that the so called "yield stress" fluids are merely shear thinning with a very high viscosity at low shear. Based on this idea, different rheological models have been proposed, e.g. [158], although such models were also proposed for computational ease much earlier. However, justification of Barnes' claim needs strong experimental evidence which is hard to obtain, as low shear rate experiments are very delicate to do even with todays high precision rheometers. One important discovery with the help of modern equipment, is that the flows at low stresses are not always steady; see [72]. Other complications such as wall slip and transient shear banding make low shear experiments hard to interpret [70, 87]. There is much recent and ongoing work around this issue [50, 55, 71, 167, 184]. However it is not yet fully agreed how to define and measure a true yield stress.

In practice even if a viscoplastic fluid is only highly viscous (and not really unyielded), the timescale of the low shear flow is often so long that we may consider the fluid as an ideal yield stress fluid. This is true for many problems in industry, such as those considered in this thesis. Thus, models like Bingham are still useful and effective. We will use this model for all the work presented in this thesis, as it simplifies but still keeps the main physical effects that we are interested in studying.

1.2.3 Governing equations

The Navier-Stokes equations govern the flow of a yield stress fluid. For an incompressible fluid with constant density the dimensionless equations are:

$$Re\left(\frac{\partial \mathbf{u}}{\partial t} + \mathbf{u}.\nabla\mathbf{u}\right) = -\nabla p + \nabla.\tau + f \tag{1.15}$$

$$\nabla.\mathbf{u} = 0 \tag{1.16}$$

where the second equation is the conservation of mass, which has been reduced to the divergence free condition for incompressible flows. Here the stresses are scaled with the viscous stress scale: $(\hat{\mu}\hat{U}_0/\hat{L})$ and the Reynolds number is $(\hat{\rho}\hat{U}_0\hat{L}/\hat{\mu})$, representing the ratio of inertial to viscous stresses. The dimensional values $\hat{\mu}, \hat{U}_0, \hat{L}, \hat{\rho}$ are the plastic viscosity, velocity scale, length scale and fluid density, respectively. The source term f represents any external body force, e.g. typically gravity.

Having the above equations and a rheological model e.g. Bingham, the system is closed and we should be able to solve the equations. Analytical solutions can be found for a number of situations like plane channel flow, or the lubrication approximation used for asymptotic solutions. For more complicated flows computation is used.

Poiseuille flow of Bingham fluid

To introduce the problem of finding free boundaries in yield stress fluid flows we consider the plane Poiseuille flow of a Bingham fluid. The solution of this flow of can be derived analytically. We consider the 2D infinite channel with $y = -1,\ 1$ as the dimensionless locations of bottom and top walls, respectively; see Figure 1.6. No-slip boundary conditions are is applied on these walls and we consider a steady fully developed flow. With these considerations the flow field and pressure gradient would be $\mathbf{u} = (u(y), 0),\ \nabla p = (-f, 0)$ respectively, i.e. the flow is driven by the applied pressure gradient f. The strain rate tensor and its norm becomes:

$$\dot{\gamma}_{xx} = \dot{\gamma}_{yy} = 0,\ \dot{\gamma}_{xy} = \dot{\gamma}_{yx} = \frac{du}{dy},\ \dot{\gamma} = |\frac{du}{dy}|. \tag{1.17}$$

It follows that the only non-zero component of stress is τ_{xy} and the Bingham model reduces to:

$$\tau_{xy} = \left(1 + \frac{B}{\left|\frac{du}{dy}\right|}\right)\frac{du}{dy}, \quad \Leftrightarrow |\tau_{xy}| \geq B; \qquad \frac{du}{dy} = 0, \quad \Leftrightarrow |\tau_{xy}| < B. \tag{1.18}$$

The momentum equations simplify to:

$$0 = \frac{\partial \tau_{xy}}{\partial y} + f. \tag{1.19}$$

By integrating the above equation and knowing that $\tau_{xy}(0) = 0$ (from symmetry) the stress distribution is found:

$$\tau_{xy} = -fy. \tag{1.20}$$

From this solution we can instantly identify $|y| \leq y_s = B/|f|$ as the unyielded region of the flow. This part would be moving with a constant velocity and is called a *plug* region as shown in Figure 1.6. Also we see that a minimum pressure gradient $|f| = B$ should be applied to start the flow in the channel. For $|f| \leq B$ the plug fills the entire channel and there would be no flow. Using (1.18) and knowing that $du/dy \leq 0$ for the upper half of channel we get:

$$\frac{du}{dy} - B = -fy \;\text{ for } y \in [y_s\ 1], \quad u(1) = 0, u(|y| < y_s) = u_p. \tag{1.21}$$

Integrating the above gives the velocity profile as:

$$u(y) = \begin{cases} \frac{f}{2}(1 - y_s)^2 = u_p, & \Leftrightarrow |y| \leq y_s, \\ \frac{f}{2}[(1 - y_s)^2 - (|y| - y_s)^2], & \Leftrightarrow |y| > y_s. \end{cases} \tag{1.22}$$

Here u_p is the velocity of central plug which is the maximum velocity.

Another formulation of the channel flow problem assumes a fixed flowrate (in place of fixing f). Here we would scale velocity with the mean velocity

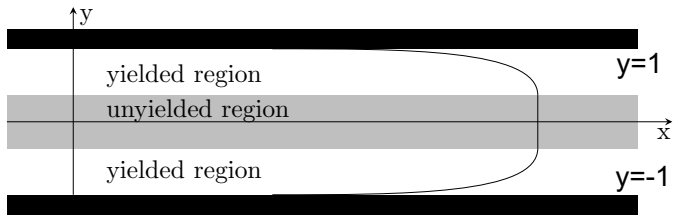

Figure 1.6: The velocity profile and yielded/unyielded fluid in channel flow of a yield stress fluid

and then can then find y_s by satisfying the flowrate constraint: $\int_0^1 u dy = 1$. This leads to the Buckingham equation [42]:

$$y_s^3 - 3(1 + \frac{2}{B})y_s + 2 = 0, \tag{1.23}$$

which has a single root $y_s \in [0, 1]$. Having found y_s, we can find $f = B/y_s$ and the rest is as before. This formulation is useful e.g. for flow in a nonuniform channel.

If we look back to the solution procedure, it was possible to solve this problem analytically because we could obtain the stress distribution first and then could use that to identify the unyielded region of the flow. Finally with knowing y_s we were able to integrate (1.22) over the appropriate range $[y_s\ 1]$ to obtain the velocity profile. In most of the problems it is not possible to find the stress distribution first, hence we cannot find the yield surfaces and this is the main challenge.

Other analytical solutions of yield stress fluid

Other than Poiseiulle flow there are a few other simple cases like Couette flow and flow between two concentric cylinders that can be solved with the same procedure. The review paper of Bird et al. [201] gives analytical solutions for a variety of standard geometries. One of the rare 2D analytical solutions is the shear flow in antiplane geometry which is derived by Burgos et al. [44], using a hodograph transformation. In addition to these, it is also possible to find asymptotic solutions if careful considerations are taken. Examples here

are [17, 102, 246], all of which were able to construct physically consistent velocity fields. Nevertheless in all of the mentioned work it is necessary to have some knowledge of (or make assumptions about) the location of yield surfaces, so that the velocity field can be solved. This might be possible for simple geometries, but becomes very hard as soon as it gets a bit more complicated.

A completely different direction for analytical investigation of yield stress flows is variational formulations, which turn to be very powerful. Here an integral (or weak) formulation is used which is valid throughout the whole domain of the flow. Hence, it can be used without knowing the position of yield surfaces, contrary to the differential formulation. These formulations usually do not give detailed information like the velocity profile, except in special cases. Instead through the use of functional analysis techniques, useful qualitative information can be obtained.

The first step was made by Prager [196] who introduced two variational formulations for Bingham fluid flow: velocity minimization and stress maximization principles. Further development was made by Duvaut and Lions [92] who generalized the previous work and introduced variational inequalities for yield stress fluids. Glowinski and co-workers expanded this direction and used variational formulations for the development of robust numerical methods based on convex optimization theory [99, 110, 111, 113]. These methods are able to exactly handle the singularity of yield stress rheological models.

The seminal work of Mosolov and Miasnikov [168, 169] are elegant examples of the use of variational formulation. They studied the flow of yield stress fluid inside ducts of arbitrary cross section shape. They gave qualitative predictions for the shape and location of yield surfaces and showed that the problem of finding the critical pressure drop necessary for the onset of the flow reduces to a geometric optimization problem. They derived exact values of critical pressure drop for several geometries like square, rectangle and others. This is explained more in Section 1.5.1.

Another very useful equality for yield stress fluids is the classical mechanical energy balance of the flow, relating viscous and plastic dissipation

of energy to the work done by external forces on the flow. Using it, an integral expression of the minimum critical yield stress for flow stoppage can be found. Also Glowinski [113] used it to show that certain transient flows of yield stress comes to rest in a finite time, in contrast to Newtonian fluids that need infinite time for the kinetic energy to decay.

1.2.4 Lubrication paradox

In 1984 Lipscomb and Denn published a paper [146] which puzzled the viscoplastic community for a decade or so. Basically they argued that it is not possible to have true unyielded regions for confined flows of yield stress fluids in any geometry which is more complicated than uniform channel. They were drawn to this conclusion by the study of lubrication type flows of the Bingham fluid in long-thin geometries, e.g. in molding. Lubrication/thin film scaling is a classical method of analysis for long-thin geometries and has been successfully applied to many types of fluids, so there was no reason not to apply it for yield stress fluids. However it was giving contradictory results when (naïvely) used for Bingham fluid.

To better understand this paradox let's reconsider the flow of Bingham fluid in the channel of Section 1.2.3 but with a varying width of $[-h(x)\ h(x)]$ where $h(x) \approx 1$. Because the width is slowly varying we can assume the flow is mainly parallel (lubrication scaling). Then at each cross section of the channel the zeroth order flow equations would be exactly the same as the plane Poiseuille flow. We can basically use (1.22) to obtain velocity profile. As the flow rate is constant through the channel we should use (1.23) with varying Bingham number $B(x) = \tau_y h(x)/\mu U_0(x)$. Note that (1.22) predicts a plug at the centre of channel with velocity u_p. Apparently u_p is varying along the channel as $B(x)$ is changing which means it is not possible to have a true unyielded central plug moving with a constant speed. This is basically the lubrication paradox argument by Lipscomb and Denn. The term pseudo-plug was coined for this region to make it distinct it from true plug and a decade of ambiguity started. The Bingham model was quickly charged with this problem and led many workers to consider regularized

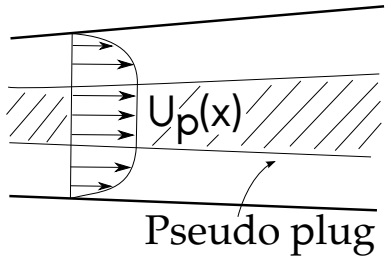

Figure 1.7: Lubrication paradox example: flow of yield stress fluid in a slowly varying channel with pseudo plug region

viscoplastic constitutive models as the correct one.

On the other hand the existence of true plugs at the points of symmetry of the flow geometry seems obvious, as the strain rate vanishes at these points. Following this idea, Walton and Bittleston [246] built asymptotic solutions with true plugs inside the pseudo plug region of axial flow between two eccentric cylinders. The main point was to go to higher terms of asymptotic expansion to get consistent stress fields which produce true plugs. One difficulty of resolving the paradox was that numerical verification of these results was very challenging. At the time most of the numerical solutions were computed using regularization, which could not account for the exact Bingham model. There was less awareness about the numerical methods developed by Glowinski and coworkers [99, 110, 111, 113], that were relatively new at the time. This, combined with lack of easily accessible hardware and software led to a longer survival of the lubrication paradox. Szabo and Hassager [225] were the first to compute the exact Bingham flow in the eccentric geometry of Walton and Bittleston and showed true plugs exist. Interestingly, they didn't use the augmented Lagrangian methods of Glowinski, instead they started with a good guess of yield surfaces and then found the exact locations of them iteratively.

Additional progress was made by Balmforth and Craster [17] who constructed consistent higher order expansions for thin film flows of Bingham fluid. They used it for many geophysical related problems such as lava flow down an inclined plane [20], iso-thermal lava domes [18] and non-isothermal

lava flows [19]. Frigaard and Ryan [102] considered a small amplitude wavy walled channel and again using higher order expansions they showed that a true intact plug exists in the centre of channel for small enough amplitudes. Putz et al. [199] used the augmented Lagrangian method and numerically verified results in [102]. They also showed that for larger amplitudes of wall the central plug breaks into two parts, each around a symmetry point of the wall variation and constructed the associated asymptotic solution, with numerical verification.

In summary, with the help of all these works, the lubrication paradox has been successfully resolved. Once again the Bingham model has secured its position as the simplest physically sensible model of yield stress fluids and we will be continuing to enjoy this simple but tricky model.

1.3 Variational principles for yield stress fluids

As mentioned in Section 1.2.3 weak formulations of yield stress fluid flows are very useful. Prager [196] stated two variational principles for the Stokes flow of Bingham fluid: *velocity minimization* and *stress maximization*. These principles can be generalized to the Herschel-Bulkley and many other rheological models of generic type [133]:

$$\tau_{ij} = (\phi(\dot{\gamma}) + \frac{\tau_y}{\dot{\gamma}})\dot{\gamma}_{ij}, \tag{1.24}$$

provided the function $\phi(t)$ has specific properties.

Let's consider a sufficiently regular domain Ω in 2D or 3D. The boundary is divided into two parts $\partial\Omega_t, \partial\Omega_v$ where the stress and velocity are given respectively and also $\partial\Omega_t \cap \partial\Omega_v = \varnothing$. The Stokes flow is governed by the

momentum equations, the continuity equation and the boundary conditions:

$$\nabla.\boldsymbol{\sigma} + \mathbf{f} = 0 \qquad \text{in } V \tag{1.25}$$

$$\nabla.\mathbf{u} = 0 \qquad \text{in } V \tag{1.26}$$

$$\boldsymbol{\sigma}.\mathbf{n} = \mathbf{T_n} \qquad \text{on } \partial\Omega_t \tag{1.27}$$

$$\mathbf{u} = \mathbf{U}_v \qquad \text{on } \partial\Omega_v \tag{1.28}$$

$$\tau_{ij} = (1 + \frac{B}{\dot{\gamma}})\dot{\gamma}_{ij}(\mathbf{u}) \qquad \text{if } B < \tau \tag{1.29}$$

$$\dot{\gamma}_{ij} = 0 \qquad \text{if } B \geq \tau \tag{1.30}$$

where $\boldsymbol{\sigma} = -p\mathbf{I} + \boldsymbol{\tau}$ is the total stress tensor, $\mathbf{n}$ is the unit normal vector pointing to the outside of the flow domain, $\mathbf{T_n}$ is an imposed traction vector and $\mathbf{U}_v$ an imposed Dirichlet velocity. A kinematically admissible velocity field is defined as one which satisfies the continuity equation (1.26) and the boundary condition (1.28) for the velocity. A statically admissible stress field is defined as one which satisfies stress equilibrium equation (1.25) and the boundary condition (1.27) for the traction. Note that the stress field corresponding to a kinematically admissible velocity field may not satisfy stress equilibrium (1.25). Accordingly the strain rate field corresponding to a statically admissible stress field does not necessarily satisfy continuity equation 1.26. Having these preliminaries we are ready.

Velocity Minimization principle

Let $\mathbf{v}^*$ be a kinematically admissible velocity field for the problem (1.25)–(1.30). Excluding the case $\partial\Omega_v = \varnothing$ then the unique solution $\mathbf{u}$ minimizes the following functional:

$$H(\mathbf{v}^*) = \frac{1}{2}\int \dot{\gamma}(\mathbf{v}^*)^2\, dV + B\int \dot{\gamma}(\mathbf{v}^*)\, dV - \int \mathbf{f}.\mathbf{v}^*\, dV - \int_{\partial\Omega_t} \mathbf{T_n}.\mathbf{v}^*\, dS \tag{1.31}$$

Note that the terms in this functional are not exactly those of the mechanical energy balance of the flow. It is half of viscous dissipation plus the

plastic dissipation, minus the power from the bodyforce and traction over the boundary.

Stress Maximization principle

Let $\mathbf{T}^*$ be a statically admissible stress field and $\mathbf{u}$ the unique velocity field solution for the problem 1.25–1.30. Excluding the case $\partial\Omega_t = \varnothing$, then the stress solution maximizes the following functional:

$$K(\mathbf{T}^*) = \int_{\partial\Omega_v} \mathbf{T}^*_{\mathbf{n}}.\mathbf{u}\, dS - \frac{1}{8}\int \left(|\tau^* - B| + (\tau^* - B)\right)^2 dV, \tag{1.32}$$

$$\tau^* = \sqrt{\frac{1}{2}\tau^*_{ij}\tau^*_{ij}}. \tag{1.33}$$

Here $\boldsymbol{\tau}^*$ is the deviatoric part of total stress $\mathbf{T}^*$ and τ^* is its norm as defined. Note that the stress solution is unique only in the yielded regions of the flow and the second integral is actually zero over any unyielded regions where $\tau^* \leq B$.

As mentioned in Section 1.2.3, these variational principles are the foundation for a family of numerical algorithms that consider the exact Bingham model without any modification. The augmented Lagrangian methods of Glowinski et al. [99, 110, 111, 113] all use the strain minimization. Very recently Treskatis et al. [232] introduced another method using the stress maximization formulation which shows promising results for a faster rate of convergence.

Equivalence of the variational principles for the solution

As noted in the previous sections the function $H(\mathbf{v})$ is minimized by the actual velocity field solution and the function $K(\mathbf{T})$ is maximized by the actual stress field solution. It can be proven [196] that these two functions are equal for the solution field. In other words

$$K(\mathbf{T}^*) \leq K(\mathbf{T}) = H(\mathbf{u}) \leq H(\mathbf{v}^*) \tag{1.34}$$

Where $\mathbf{u}, \mathbf{T}$ are solution velocity and stress fields and $\mathbf{v}^*, \mathbf{T}^*$ are admissible velocity and stress fields respectively.

Variational inequality

Duvaut & Lions [92] introduced variational inequalities for yield stress fluid flows. These include unsteady and inertial terms and are more general than the previous formulations for Stokes flow, (as considered above). Following Duvaut & Lions [92] we introduce the notation below for simplification:

$$a(\mathbf{u}, \mathbf{v}) := \frac{1}{2} \int \dot{\gamma}_{ij}(\mathbf{u}) \dot{\gamma}_{ij}(\mathbf{v})\, dV \qquad j(\mathbf{v}) := \int \dot{\gamma}(\mathbf{v})\, dV \tag{1.35}$$

$$b(\mathbf{u}, \mathbf{v}, \mathbf{w}) := \int \mathbf{u}.\nabla \mathbf{v}.\mathbf{w}\, dV \qquad L(\mathbf{v}) := \int \mathbf{f}.\mathbf{v}\, dV \langle \mathbf{u}, \mathbf{v} \rangle := \int \mathbf{u}.\mathbf{v}\, dV \tag{1.36}$$

The first 4 terms above represent the viscous dissipation, plastic dissipation (divided by B), inertial power and body force power, respectively. Consider $\mathbf{u}$ as the solution of the Bingham flow from differential formulation and $\mathbf{v}$ as a kinematically admissible velocity field, both divergence free. Then the theorem finally shows (Duvaut and Lions [92]):

$$Re[\langle \mathbf{u}_t, \mathbf{v} - \mathbf{u} \rangle + b(\mathbf{u}, \mathbf{u}, \mathbf{v} - \mathbf{u})] + a(\mathbf{u}, \mathbf{v} - \mathbf{u}) + B[j(\mathbf{v}) - j(\mathbf{u})] \geq L(\mathbf{v} - \mathbf{u}) + \int_{\partial \Omega_t} (\mathbf{v} - \mathbf{u}).\mathbf{T_n}\, dS \tag{1.37}$$

Here $\partial \Omega_t$ is part of boundary which stress is given and $\mathbf{T_n}$ is traction vector. This theorem has served for many numerical and analytical studies of Bingham fluid flow.

Variational equality (Mechanical Energy balance)

Another useful integral relationship for yield stress fluid flows is simply the mechanical energy balance of the flow. This is obtained by multiplying the momentum equation by the velocity and integrating. Using the notation

introduce in the above section:

$$Re[\langle \mathbf{u}_t, \mathbf{u}\rangle + b(\mathbf{u}, \mathbf{u}, \mathbf{u})] + a(\mathbf{u}, \mathbf{u}) + Bj(\mathbf{u}) = L(\mathbf{u}) + \int_\Omega \mathbf{T_n}.\mathbf{u}\, dS \tag{1.38}$$

This equation has been used by Glowinski [113] to show that yield stress fluid takes finite time to rest when the left had side of (1.38) vanishes i.e. when the driving force stops injecting energy to sustain the flow. Huilgol [133] gives more results of this type.

From this energy balance equation we can derive an expression for the critical $B = B_c$ at which the yield stress is large enough to stop the flow. For this purpose we can neglect the unsteady and inertial terms and the (1.38) simplifies as:

$$a(\mathbf{u}, \mathbf{u}) = L(\mathbf{u}) + \int_\Omega \mathbf{T_n}.\mathbf{u}\, dS - Bj(\mathbf{u}) \tag{1.39}$$

Let $\mathcal{L}(\mathbf{u}) = L(\mathbf{u}) + \int_\Omega \mathbf{T_n}.\mathbf{u}\, dS$. Thus we can write:

$$0 \leq a(\mathbf{u}, \mathbf{u}) = j(\mathbf{u}) \left\{ \frac{\mathcal{L}(\mathbf{u})}{j(\mathbf{u})} - B \right\} \leq j(\mathbf{u}) \left\{ \operatorname*{Sup}_{\mathbf{v}\in V, \mathbf{v}\neq 0} \frac{\mathcal{L}(\mathbf{v})}{j(\mathbf{v})} - B \right\} \tag{1.40}$$

Here the space V is the space of all admissible velocity fields. Note that $a(\mathbf{u}, \mathbf{u})$ and $j(\mathbf{u})$ are always positive. So the expression within the brackets should inevitably be positive, which means:

$$B \leq \operatorname*{Sup}_{\mathbf{v}\in V,\, \mathbf{v}\neq 0} \frac{\mathcal{L}(\mathbf{v})}{j(\mathbf{v})} = B_c \tag{1.41}$$

This expression gives the critical B that would stop the flow. In practice the problem is that we do not know how to evaluate B_c. However, we can use other velocity fields (e.g. Newtonian flow with the same boundary conditions) to obtain bounds for B_c or to give conditions for which there should be flow. An example is the paper by Dubash and Frigaard [91] who studied conditions for moving and trapped bubbles in a viscoplastic medium.

It is possible to get much better estimates of the B_c if we know the

approximate velocity field close to the stopping point. Numerical simulation can help here and by replacing the velocity field in (1.41) by an approximate velocity field, a good estimate of B_c can be found. Karimfazli et al. [141] have recently used this method for natural convection problems with yield stress fluids. We will also use this method later to estimate the critical pressure drop for the onset of flow in fractures.

Critical yield stress for Poiseuille flow using variational method

As an example we may apply (1.41) for the Poiseuille flow in Section 1.2.3. Let us first consider that we do not know anything about the velocity profile close to stopping. We insert the Newtonian solution into (1.41) and this gives us a **lower bound** on the value of B_c. For the Newtonian solution:

$$u(y) = \frac{f}{2}(1 - y^2), \tag{1.42}$$

$$\mathcal{L}(u) = \int_0^1 f u(y)\, dy = \frac{f^2}{3}, \tag{1.43}$$

$$j(u) = \int_0^1 |\frac{du}{dy}|\, dy = u(0) - u(1) = \frac{f}{2}, \tag{1.44}$$

which gives us $B_{Newtonian} = \frac{2f}{3}$ as a lower bound for $B_c > B_{Newtonian}$. To improve we need more information about velocity profile. Let us suppose that we suspect that close to the onset there would be a large plug in the centre or the channel, moving with speed U_p, separated from the walls by thin shear layers. Now we can approximate:

$$\mathcal{L}(u) = \int_0^1 f u\, dy \approx f U_p, \tag{1.45}$$

$$j(u) = \int_0^1 |\frac{du}{dy}|\, dy = U_p, \tag{1.46}$$

and hence $B_c \approx \frac{fU_p}{U_p} = f$, as the critical yield stress to stop the flow. We also know that this is actually the exact value, i.e. from the analytical solution. Note that we didn't know the actual value U_p, but the final result for B_c didn't depend on it. This means (1.41) is scale independent. The

same procedure can be applied to more complicated scenarios. We will use this idea for the critical pressure drop in fractures, considered in chapter Chapter 3.

1.4 Numerical methods

As mentioned before in Section 1.2.2 the singularity of yield stress models is the main problem for both numerical and analytical investigation. For simplicity we use the Bingham model, but without the loss of generality. In numerical simulation the different approaches that have been used can be grouped into 2 main categories:

- Methods considering the exact Bingham model
- Methods that modify the model to remove the singularity in the effective viscosity

We review each of the groups.

1.4.1 Methods that use the exact Bingham model

Szabo and Hassager [225] used a creative approach to compute the steady flow of Bingham fluid between two eccentric cylinders. Basically they guessed a reasonable initial shape for the yield surfaces and solved the flow problem only in the unyielded regions. The location of the yield surfaces was then corrected based on the obtained solution. This was repeated iteratively until convergence. This approach has the following advantages:

- It considers the exact Bingham model.
- The shape of the unyielded regions can be obtained with very high precision. They were able to resolve very sharp corners of the yield surface in [225], and showed that the stresses can be discontinuous on these corners

Some disadvantages of this approach include:

- It relies on knowing a good initial guess for the location of unyielded regions. Commonly we cannot guess these for non-trivial geometries.
- There is no general equation for the evolution of the yield surface, so that the method used to update the yield surface position at each iterate must be specially tailored to the problem.
- Computational cost is high, even for steady flows several iterations of solving a full problem is needed.

The first and second points above are quite restrictive. Although the results in [225] are impressive, there is also no theoretical basis to generalize the method to more complex flows in a way that would guarantee convergence of the iteration. In fact [225] is the only published paper using this kind of idea, which was not apparently extended by the community.

We should note here that Szabo and Hassager idea probably stems from the earlier work by Beris et al. [31] who studied the Bingham flow around a sphere. They used regularization, however a nice way of detecting and adjusting yield surface was used.

Augmented Lagrangian approaches

On the other hand, the methods developed by Glowinski and coworkers [99, 110, 111, 113] can handle the Bingham model exactly and can be used for any kind of geometry. The basic idea of these methods is to use the variational formulations of the problem as discussed in Section 1.3, (mainly the velocity minimization principle). We outline this here for convenience:

$$H(\mathbf{u}) = \frac{1}{2}a(\mathbf{u},\mathbf{u}) + Bj(\mathbf{u}) - L(\mathbf{u}) - \int_{\Omega_t} \mathbf{T_n}.\mathbf{u}\, dS \tag{1.47}$$

Where the functionals $a(\mathbf{u},\mathbf{u}),\ j(\mathbf{u}),\ L(\mathbf{u})$ are defined in (1.35)-(1.36). We see the term $j(\mathbf{u})$ which contains the plastic contribution is not differentiable at $\dot{\gamma}(\mathbf{u}) = 0$, which are the unyielded regions. The singularity of the Bingham model has thus shown itself here as well. This prevents the use of gradient-type methods for solution of the minimization problem. However thanks

to convex optimization theory we can still handle this situation if $H(\mathbf{u})$ is sufficiently regular and convex, which is true here. In fact, Glowinski formulates this optimization problem as the following more general type:

$$\min_x f(Ax) + g(x) \tag{1.48}$$

Here A is a linear operator and f, g are convex functions. This is a generic form for a large range of problems in solid/fluid mechanics, statistics and signal/image processing. Note that it is not required that f, g be differentiable.

The idea used by Glowinski et al is to introduce $y = Ax$ as a new variable into the problem and then enforce the equality condition of y and Ax with a Lagrange multiplier. So the problem becomes:

$$\min_{x,y} f(y) + g(x) \textbf{ subject to } y = Ax \tag{1.49}$$

This becomes a saddle-point problem of Lagrange multiplier type, for the principal variables (x, y). Fortin and Glowinski [99] proposed a set of augmented Lagrangian methods for the solution of (1.49) that have become well known as ALG1-ALG4. The algorithms are quite similar, with ALG2 perhaps the most popular method implemented for applications in engineering, finance and other fields. It is also a popular algorithm for numerical simulation of yield stress fluids, as we consider here.

To explain ALG2 for Bingham fluid we consider the velocity minimization principle (1.47) which is stated in terms of velocity $\mathbf{u}$. We set $x = \mathbf{u}$ as the principal variable in (1.49). The operator A in (1.49) is taken to be $\nabla + \nabla^T$, which means the relaxed variable $y = Ax$ would be the strain rate tensor of the associated velocity field and we use notation $\boldsymbol{\gamma}$ for this. The

minimization functional for the Bingham fluid becomes:

$$V(\mathbf{u},\boldsymbol{\gamma},\mathbf{T}) = \overbrace{\frac{1}{2}\int \boldsymbol{\gamma}^2\,dV + B\int \boldsymbol{\gamma}\,dV}^{f(Ax)} \overbrace{- \int \mathbf{f}.\mathbf{u}\,dV - \int_{\partial\Omega_t} \mathbf{T_n}.\mathbf{u}\,dV}^{g(x)}$$
$$+ \int (\boldsymbol{\gamma} - \dot{\gamma}(\mathbf{u})) : \mathbf{T}\,dV + \frac{a}{2}\int (\dot{\gamma}(\mathbf{u}) - \boldsymbol{\gamma})^2\,dV \quad (1.50)$$

The terms in the first row are just $H(\mathbf{u})$ as (1.47), but with $\dot{\boldsymbol{\gamma}}(\mathbf{u})$ replaced by relaxed variable $\boldsymbol{\gamma}$. With this selection the functions $f(Ax), g(x)$ in (1.49) of the Bingham flow are shown. Note that this is not the only way of splitting f, g. The second row is the Lagrange multiplier term and (with $a > 0$) the augmentation term, hence the name augmented Lagrangian. It is proven that the optimal point of functional $V(\mathbf{u},\boldsymbol{\gamma},\mathbf{T})$ is the same as the original $H(\mathbf{u})$. However, it depends on three variables instead of one. To handle this, the minimization is performed separately on each variable, in fixed point format and then iterated. The final form of the popular algorithm ALG2 of Glowinski is as follows. Start with initial value $\boldsymbol{\gamma} = \boldsymbol{T} = \mathbf{0}$ (or a better guess).

Step 1: Minimization with respect to u reduces to a Stokes flow like system with addition of a right hand side term:

$$-a\nabla.\dot{\boldsymbol{\gamma}} = -\nabla p + \nabla.(\mathbf{T} - a\boldsymbol{\gamma}), \qquad \text{With given BC} \quad (1.51)$$
$$\nabla.\mathbf{u} = 0 \quad (1.52)$$

Step 2: Minimization with respect to $\boldsymbol{\gamma}$

$$\boldsymbol{\gamma} = \begin{cases} 0, & \Leftrightarrow |\mathbf{T} + a\dot{\boldsymbol{\gamma}}(\mathbf{u})| \leq B \\ (1 - \frac{B}{|\mathbf{T}+a\dot{\boldsymbol{\gamma}}|})\frac{\mathbf{T}+a\dot{\boldsymbol{\gamma}}}{1+a}, & \text{otherwise} \end{cases} \quad (1.53)$$

Step 3: Update of $\mathbf{T}$, assuming that at each step, $0 < \rho < \frac{1+\sqrt{5}}{2}a$ is satisfied

$$\mathbf{T} = \mathbf{T} + \rho(\dot{\boldsymbol{\gamma}} - \boldsymbol{\gamma}) \quad (1.54)$$

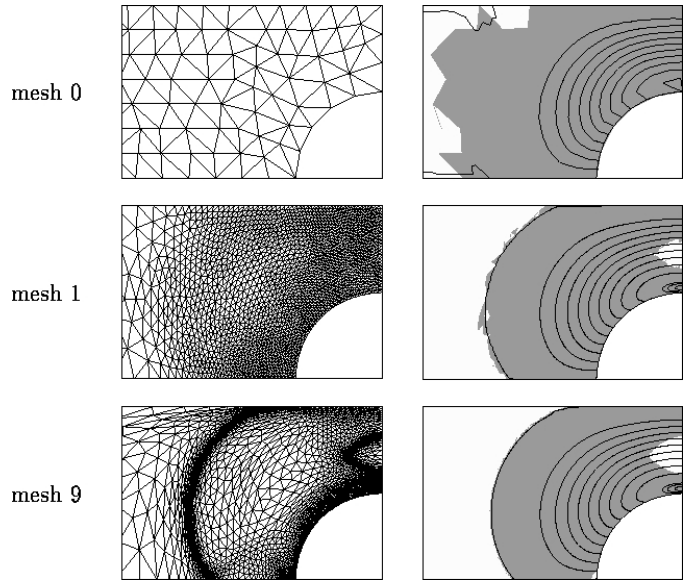

Figure 1.8: An example of mesh adaptation strategy suggested by Saramito and Roquet to improve accuracy of capturing yield surfaces. Very fine, highly anisotropic mesh can be observed around yield surfaces. Figure from the Gallery of Rheolef library [213]

These 3 steps are continued until convergence is achieved. In many cases it seems that the choice $\rho = a$ provides good convergence [109] and often we follow it. The choice of optimal a is however problem dependent and there is no easy way to find it in practice. We usually use $1 \leq a \leq 50$.

With this algorithm we can consider the exact Bingham model. However, due to meshing we may not be able to get nice sharp yield surface, e.g. as in Szabo and Hassager [225]. One remedy was suggested by Saramito and Rouqet [206, 214]. They used anisotropic mesh adaptation and showed yield surfaces can be very accurately tracked with this strategy. An example for the flow around a cylinder is shown in Figure 1.8. Our implementation of ALG2 very closely follows the works by Saramito and Rouquet [206, 214].

In addition to ALG1-ALG4, there are other variations e.g. combining regularization with multiplier for higher convergence rates or a multiplier like algorithm which is based on the introduction of viscoplastic extra ten-

sor λ and using projection. Further details can be found in the review article by Dean and Glowinski [80] and book chapter [112] by Glowinski and Wachs. We have used ALG2 for all of our computations combined with the anisotropic adaptation strategy by Roquet and Saramito [206].

All of the multiplier based methods discussed were developed about 3 decades ago. In practice these methods work effectively, however the main practical issue is the slow convergence rate which is $\mathcal{O}(1/\sqrt{k})$, where k is the iteration number. The reason for the slow convergence is that algorithms like ALG2 are quite general in terms of the requirements imposed on the functionals (convexity only). From the existing theory we cannot get a better convergence rate for such general problems.

A very recent work from Treskatis et al. [232] has revisited the problem of Bingham fluid flow and proposed a method with $\mathcal{O}(1/k)$ convergence. They note that the velocity minimization (1.50) is convex while the stress maximization (1.32) is strictly convex: this property can be used to obtain higher order of convergence. Strong convexity of a function f means that there exists $\sigma > 0$ such that for (x_1, x_2) in the domain of f and $t \in [0, 1]$

$$f(tx_1 + (1-t)x_2) \leq tf(x_1) + (1-t)f(x_2) - \frac{\sigma}{2}t(1-t)|x_1 - x_2|^2 \quad (1.55)$$

Instead of using velocity minimization Treskatis et al. use stress maximization and develop a variant of the FISTA method [27] for the solution of Bingham fluid flows. Their methodology has the following interesting properties:

- Considers the exact Bingham model.
- There is no heuristic parameter like a in ALG2, which must be selected and can significantly affect the convergence rate.
- Gives convergence rates of $\mathcal{O}(1/k)$.

All of these properties makes this algorithm very exciting for use. However we didn't have time to implement it as it was only very recently developed.

As a final remark we say that algorithm ALG2 is one of the well known set of algorithms under the name of *Alternating Direction Method of Multi-*

plier (ADMM), which have become extremely popular, due to applications in todays "hot topics", such as: machine learning, data mining, statistics and image processing [109].

1.4.2 Regularization methods

The methods described in the above section were efforts to keep the exact Bingham model. These algorithms rely on fairly complex theories and are usually slow in practice. As we know, the main problem is the singularity of the effective viscosity in the Bingham model (1.6) at $\dot{\gamma}(\mathbf{u}) = 0$. By looking at the model (1.6) we can think of eliminating this singularity by adding a small value ϵ, e.g.

$$\tau_{ij} = \left(1 + \frac{B}{\epsilon + \dot{\gamma}(\mathbf{u})}\right) \dot{\gamma}_{ij}(\mathbf{u}) \tag{1.56}$$

We can see that the modified rheological model becomes differentiable. In other words, the singularity has been *regularized*. We can now use the regularized model just like any generalized non-Newtonian fluid and solve the flow with available standard solvers. Several regularization models have been proposed.

Bercovier and Engleman model from (1980); see [28]:

$$\tau_{ij} = \left(1 + \frac{B}{\sqrt{\dot{\gamma}(\mathbf{u})^2 + \epsilon^2}}\right) \dot{\gamma}_{ij}(\mathbf{u}). \tag{1.57}$$

Bi-viscosity models, such as that from O'Donovan and Tanner [181] (1984):

$$\tau_{ij} = \begin{cases} (1 + \frac{B}{\dot{\gamma}_c})\dot{\gamma}_{ij}(\mathbf{u}), & \Leftrightarrow \dot{\gamma}(\mathbf{u}) \leq \dot{\gamma}_c, \\ (1 + \frac{B}{\dot{\gamma}(\mathbf{u})})\dot{\gamma}_{ij}(\mathbf{u}), & \Leftrightarrow \dot{\gamma}(\mathbf{u}) > \dot{\gamma}_c. \end{cases} \tag{1.58}$$

Papanastasiou model from (1987); see [186]:

$$\tau_{ij} = \left(1 + \frac{B}{\dot{\gamma}(\mathbf{u})}[1 - e^{-m\dot{\gamma}(\mathbf{u})}]\right) \dot{\gamma}_{ij}(\mathbf{u}) \tag{1.59}$$

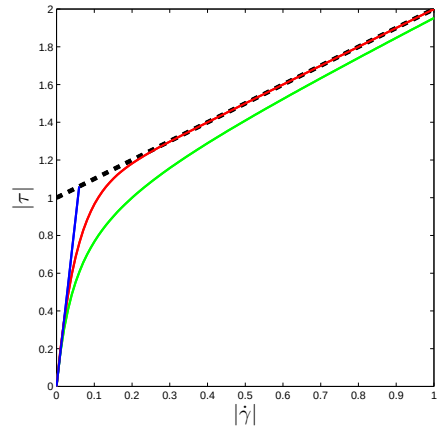

Figure 1.9: The Bingham model (dashed black line) and the typical curves for Papanastasiou (red), Bercovier (green) and bi-viscosity regularizations

Figure 1.9 shows a sketch of how each of these models modify the Bingham model.

Physically, regularization replaces the unyielded fluid with a very high viscosity fluid, which means that there wouldn't be any true unyielded regions with zero strain rate in the flow. This also makes the definition of unyielded regions ambiguous in such computations. Of course one can take $\tau \leq B$ as a definition of unyielded regions. However, the yield surfaces would depend on the value of regularization parameter ϵ (or $m = 1/\epsilon$). This is the main disadvantage of regularization.

One might intuitively expect from general continuity results that by letting $\epsilon \to 0$, the solution of the regularized model should converge to the exact Bingham model. Consideration of this limit by Frigaard and Nouar [101] shows that this intuition is only guaranteed for the velocity field and not necessarily for the stress field. This means that the yield surfaces predicted by a regularized method may not converge to the exact Bingham model.

This has been shown in a very nice paper by Burgos et al. [44]. They derive analytical solution for the anti-plane flow of a Herschel-Bulkley fluid and compare the analytic yield surface with those predicted by regularization models such as Papanastasiou, Bercovier and bi-viscosity. They show that

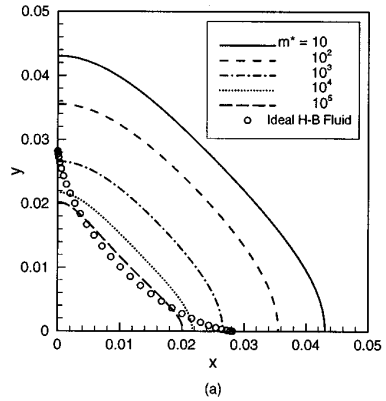

Figure 1.10: The original Fig 5a in paper by Burgos et al. [44]. Circles show the analytic yield surface and other lines are yield surfaces from Papanastasiou regularization with increasing value of m. The main difference is that the convexity of regularized yield surface is reversed compared to analytical.

some regularization methods (and parameters) predict a yield surface which is convex toward the corner, in disagreement with the analytic result which is concave. Figure 1.10 shows one example of the comparison in the original paper. With this shortcoming, one might think regularization methods are not useful at all, however we can mention these positive points:

- Easy to implement in standard Navier-Stokes solvers such as commercial software.
- The convergence is faster, hence less computing time is needed.
- If only the velocity field is of concern, it is guaranteed to converge to the exact Bingham model.

For many flows of industrial relevance e.g. in pipes, pumps, etc.. . . regularization methods are perfectly adequate and there is no real benefit to performing a more expensive computation for the same result.

However, if accurate resolution of the stress field (i.e. yield surfaces) is important for the problem at hand, then multiplier based methods are a better choice. One very important class of such problems is finding the

onset point of flow, as noted by Moyers-Gonzalez and Frigaard [171]. For example the minimum pressure drop to start the flow or the minimum yield stress required to stop a particle from sedimenting. Another class, are those dealing with computing finite time to rest of yield stress fluid flows, as noted by Glowinski and Wachs [112]. Superiority of multiplier methods is obvious in these cases. Industrial problems where multiplier based methods are advantageous include those considered in this thesis, where we are directly concerned with finding unyielded zones and yield limits of flows.

1.4.3 Selected applications of computational methods

We give a brief chronological review of some of the computational studies performed using both regularization and multiplier methods. Definitely this is not inclusive and the intention is to give a historical perspective of the of adoption and evolution of the methods for different applications.

Bercovier and Engleman (1.57)

This model was first used in analysis by Glowinski and co-workers, but the earliest computational application was for an inertial cavity flow; see [28]. A well known application of the regularization (1.57) is in the study of Bingham flow around a sphere by Beris et al. [31]. Indeed it is one of the nicest works with a regularization method. In this flow two plug zones appear at poles of the sphere and there is an envelope of unyielded fluid surrounding the sphere. They used a transformed mesh and carefully considered the yield surfaces via an iteration method. The result was very accurate shapes for the yielded regions and the critical yield stress needed to keep the sphere static in the fluid. They confirmed the quality of their results for the drag force by examining the equality of the functionals H & K, introduced for velocity minimization and stress maximization principles (Equation 1.34). Later Bercovier and Engleman used (1.57) for simulation of forming process [29]. Scott et al. [217] used (1.57) in the study of a 2:1 expansion, a stenosis and a bifurcation flow. Walton and Bittleston [246] solved the flow between two eccentric cylinders using (1.57). Other examples of duct flows include

Taylor and Wilson [230] and Wang [247]. Nouar et al. [180] numerically and experimentally considered the forced convection flows of Herschel-Bulkley fluid between concentric ducts using (1.57).

Bi-viscosity model (1.58)

O'Donovan and Tanner [181] introduced the bi-viscosity regularization (1.58) in 1984 and used it for study of squeeze flow. This model has been implemented in commercial CFD solvers, but has been used more often as an analytical tool, e.g. Wilson [253] used (1.58) in an asymptotic study of the squeeze flow.

Papanastasiou model (1.59)

The most popular regularization model was introduced by Papanastasiou [186] in 1987. He used (1.59) to compute the flow in a diverging channel and also the extrusion flow of Bingham fluid. Ellwood et al. studied jet flows using (1.59); see [93]. A set of high quality computational studies of the flows involving interface dynamics have been conducted using (1.59), by Tsamopoulos and co-workers. Direct tracking of the interface using mesh mapping methods gave them accurate resolution of the flow. Examples are: spin coating flow [234], squeeze flow of a Bingham fluid [140, 221], transient displacement of visco-plastic fluids in expansion-contraction geometries with air [86] and a nice study of bubble rise in viscoplastic fluids [136].

Fan, Phan-Tien and Tanner [95] used both (1.58) and (1.59) for the study of advective mixing of Bingham flow between eccentric cylinders, with the inner one rotating. Alexandrou, Georgiou and coworkers have also used (1.59) for analyzing several industrial flows such as injection molding [6], and squeeze flow [7, 97].

Mitsoulis and co-workers have extensively studied a wide range of industrially related flows, all using (1.59). Examples are the Stokes flow of a sphere in a tube [34], extrusion die flows [1, 143, 163, 190], duct flows [237], Bingham fluid flow around a cylinder [259], entry flow of a Bingham fluid in an expansion [164], squeeze flow [156, 165], fountain flow [161, 162],

toothpaste flow in extrusion dies with thixotropy [13] and dip coating flow [96]. The popularity of this regularization is due to it being very easy to implement and due to the usage of the exponential term for regularization, giving a very sharp yet infinitely continuous approximation of the Bingham model.

Augmented Lagrangian (AL) approaches

On the other side, there is much less works using augmented Lagrangian (AL) methods. First published in 1976 in French editions, widespread understanding waited until [99]. Various advanced texts have appeared from Glowinski and co-authors (e.g. [98, 99] and others), most of which contain benchmark computations. Hurez et al. [134] analyzed die swell flow. Huigol and Pinazzi [132] considered the eccentric cylinders of Walton and Bittleston [246] and tried to verify their results using ALG2. This work had the potential to support the idea that proper asymptotic solutions can resolve the lubrication paradox. Unfortunately they didn't make a comprehensive comparison for the shape of the plug zones (i.e. the controversial issue) and just showed a few velocity contour plots. This task was postponed to Putz and Frigaard [199], who compared AL and asymptotic solutions for lubrication flow in a long thin wavy channel. Roquet and Saramito [206, 214] introduced anisotropic mesh adaptation for computation of Bingham fluids and thus achieved higher rates of convergence. Vola et al. [240] computed gravity currents of Bingham fluids. Weakly compressible yield stress flows are studied by Vinay et al. [238, 239]. They modeled waxy crude oil as a compressible Bingham fluid and studied the pipeline restart process using AL. Wachs [245] and Yu and Wachs [256], introduced a combined fictitious domain + AL algorithm for particulate flows of yield stress fluids. Finally some recent papers show the increasing popularity of AL: Muravleva et al. [173] studied the time to rest of Bingham flows, Dimakopoulos et al. computed bubble rise flows in Bingham fluids [82].

There are two studies that directly compare numerical results of augmented Lagrangian with regularization for the same flow. Putz and Frigaard

[199] consider lubrication flow in a long thin wavy channel. For this case an intact plug exists at the center of channel. They showed regularization methods can produce reasonable yield surfaces, but only if a proper yield criterion is used and the numerical errors should be carefully controlled with respect to the regularization parameter, while augmented Lagrangian always converges to correct result. The other paper by Dimakopoulos et al. [82] compares Papanastasiou regularization and augmented Lagrangian for the steady bubble rise in yield stress fluid. They conclude that close to the yielding, augmented Lagrangian correctly captures asymptotic behavior of the drag coefficient while regularization fails.

To wrap up, regarding the main two methods (regularization and augmented Lagrangian) we should say that both are useful and applicable in the proper contexts. Regularization has been well established for the study of many kinds of application flows for > 30 years. Augmented Lagrangian methods have reached a mature state, however there is still room for application of AL to many flows of interest.

1.5 Related work on self-selection

This thesis largely deals with flows of yield stress fluids along channels with non-uniform geometries. This is one type of flows that is directly connected with the various oil & gas related flows introduced in §1.1. Flows of viscoplastic fluids have a unique feature which is the (possibility of) existence of regions with static fluid attached to the walls of a flow region. For such flows we can consider another geometry which is the same as initial one, but now the yield surfaces of static regions in the original flow are replaced by solid walls. Essentially the flow should be the same in these two geometries. The interesting mathematical interpretation is that the flow has *self-selected* its flowing geometry and is neutral (to some extent) to changes we make in parts of the domain that are static. This is a specific aspect of the free-boundary problem. We will repeatedly come back to self-selection in this thesis. Each chapter of this thesis has its own detailed related literature. However, here we try to give a centralized overview of works that are related

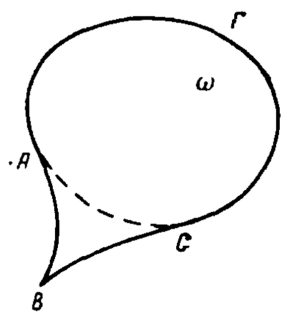

FIG. 3.

Figure 1.11: Original Fig 3 in paper [168], showing the stagnant zone ABC which exists in the corner point B and the convexity of the boundary

to flow in non-uniform geometries, stationary geometries and self-selection.

1.5.1 Self-selection of flow geometry in duct flows

The two seminal papers by Mosolov and Miasnikov [168, 169] study pressure driven flow of a Bingham fluid in ducts of an arbitrary cross-sectional shape. These papers explain probably the class of non-trivial yield stress fluid flows which we understand analytically the best. Mosolov and Miasnikov pioneered the use of variational principles. Also these papers give the best understood results about the self-selection mechanisms of yield stress fluids, which gives insights into more complicated flows.

Consider a fully developed flow of Bingham fluid in an arbitrary duct Ω in the (x, y)-plane. The boundary $\partial\Omega$ is assumed to be smooth, except at finite number of points. We consider no-slip conditions to be satisfied on

$\partial\Omega$, and the only non-zero velocity component is $u_z = u(x, y)$. Thus:

$$\dot{\gamma}_{xx} = \dot{\gamma}_{yy} = \dot{\gamma}_{zz} = \dot{\gamma}_{xy} = \dot{\gamma}_{yx} = 0 \tag{1.60}$$

$$\dot{\gamma}_{xz} = \dot{\gamma}_{zx} = \frac{du}{dx}, \qquad \dot{\gamma}_{yz} = \dot{\gamma}_{zy} = \frac{du}{dy} \tag{1.61}$$

$$\dot{\gamma} = \sqrt{(\frac{du}{dx})^2 + (\frac{du}{dy})^2} = |\nabla u| \tag{1.62}$$

With these assumptions, only τ_{xz} & τ_{yz} are non-zero stress components and the z-momentum equation is:

$$\frac{\partial \tau_{xz}}{\partial x} + \frac{\partial \tau_{yz}}{\partial y} = -f, \tag{1.63}$$

where f is the constant pressure gradient in the z-direction. Mosolov and Miasnikov [168, 169] consider the velocity minimization principle for this problem:

$$H(u) = \frac{1}{2}\int \nabla u^2 + B\int |\nabla u| - \int fu \tag{1.64}$$

Similar to Section 1.3 they show that flow exists if and only if:

$$f\int u \leq B\int |\nabla u|, \qquad u(\partial\Omega) = 0 \tag{1.65}$$

Which is written in the following form:

$$\int u \leq K\int |\nabla u|, \qquad u(\partial\Omega) = 0, \quad K = \frac{B}{f} \tag{1.66}$$

The above inequality is a pure functional analysis problem. The question is what are properties of the functions $u(x, y)$ that satisfy the inequality? and what is the constant K?

Through a detailed analysis of the above inequality Mosolov and Miasnikov [168] give a number of interesting answers. We summarize the main results from their paper as follows.

#1 If $u(x, y)$ is a smooth function with $u(\partial\Omega) = 0$, then we have:

$$\int u \leq K \int |\nabla u|, \quad K = \sup_{\omega \subseteq \Omega} \frac{\text{Area}\,\omega}{\text{Perimeter}\,\omega} \tag{1.67}$$

Where ω is an arbitrary sub-domain of Ω. This gives a critical pressure drop $B/K = f_c$. The necessary and sufficient value for having flow in the duct is for f to exceed f_c.

#2 There exist a sub-domain ω^* such that it gives the supremum value of K in the above. The parts of $\partial\omega^*$ which are not on $\partial\Omega$, should be arcs of circles that touch $\partial\Omega$. In addition the convexity of the arc should be towards the inside of the domain as shown in Figure 1.11

#3 If the domain Ω is p-connected, and d is the inner diameter of the domain, then the constant K satisfies:

$$\frac{d}{2} \leq K \leq 8pd \tag{1.68}$$

Where the lower bound is exact in the inequality. The inner diameter of the domain is defined as $max\,\rho(P, \Omega)$, where $P \in \Omega$ is any point in the domain and $\rho(P, \Omega)$ is the distance between P and boundary. This part gives lower and upper bounds for the critical pressure drop. Consider the biggest circle that fits in Ω completely. The lower bound states that if the pressure drop is higher than what is needed to move this circle ($2B/d < f$), then flow definitely exists. The upper bound states if $f \leq B/8pd$, then definitely there is no flow.

#4 The velocity distribution that minimizes (1.64) satisfies:

$$\int_\Omega u \leq 2K(fK - B)\text{Area}(\Omega), \tag{1.69}$$

which is a bound on the flow rate.

#5 Any local maximum of the solution $u(x, y)$ is achieved in a domain which contains a circle of diameter $B/8pf$ and does not contain a

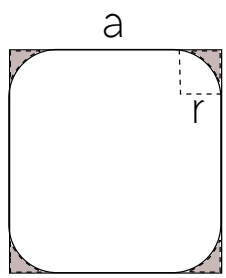

Figure 1.12: Flow of viscoplastic fluid in a square pipe. As shown in [168] the yield surface of static regions has the shape of arc of a circle

circle larger than $2B/f$ in diameter. Also

$$max\, u \leq \left(\frac{8pf}{B}\right)^2 \frac{2K\text{Area}(\Omega)}{\pi}(fK - B) \tag{1.70}$$

The subdomain which contains the local maximum of u is called a nucleus of the flow.

#6 For any pressure gradient that results in a positive flow, there exists at least one nucleus moving with constant speed, (i.e. such nuclei are simply unyielded interior plug regions).

All of the above results are very interesting. Using these we can compute the analytical critical pressure in many shapes. For example consider a square pipe with sides of length a. If there are static zones, we know they will be in the corners and will have the shape of an arc, say with radius r, as illustrated in Figure 1.12. According to result #2 we should find the r which maximizes the area to perimeter ratio:

$$\frac{B}{f_c} = K = Max\, \frac{a^2 - (4r^2 - \pi r^2)}{2\pi r + 4(a - 2r)} \tag{1.71}$$

$$\Rightarrow r = K = \frac{a}{2 + \sqrt{\pi}} \tag{1.72}$$

Similarly the critical pressure drop can be computed for several other shapes.

These results provide valuable insights about self-selection:

1. The self-selection mechanism that yield stress fluid adopts is to maximize the ratio of flow area to its perimeter. So self-selection can be formulated as a purely geometric problem.

2. As a result of the above strategy, there will often be stagnant zones at convex corners of the duct geometry. These are those corners for which a tangent arc will be inside the domain.

In the second paper titled as "*On stagnant flow regions of a visco-plastic medium in pipes*" Mosolov and Miasnikov [169] focus on properties of static zones and give more details and proofs:

#7 The boundary of stagnant zones are curved toward the unyielded domain and the radius of any arc is not less than B/f. Boundaries of nuclei are curved opposite (convex) to the unyielded domain with radius of curvature less than B/f at each point. Thus, for example there is a limiting f above which no fluid is trapped in corners.

#8 The yield surface of stagnant zones can approach the boundary at non-zero angle only at non smooth points of the boundary.

#9 Consider stagnant domain OAB in Figure 1.13 (original figure of the paper), where γ is the inner boundary of stagnant zone toward the flow. Assume arbitrary line L which divides OAB into two parts, then the solution of the flow will be the same if AOB is replaced by L. This is true also if the boundary of stagnant zone grows (shown at the right) within some limits. Particularly if the growth is so big that a circle of diameter B/f fits into the expanded region then stagnant zone would be flowing.

#10 Consider a sub-domain ω which completely lies in the main domain as shown in Figure 1.14. Then we will have $u_\omega \leq u_\Omega$, where u_ω is velocity solution for sub-domain with the same conditions and u_Ω is the velocity of main domain. The contour OR_1R_2 shows the stagnant zone in the main domain. The interesting result is that for the flow in ω we will have stagnant zone at least in the area shown by hatching.

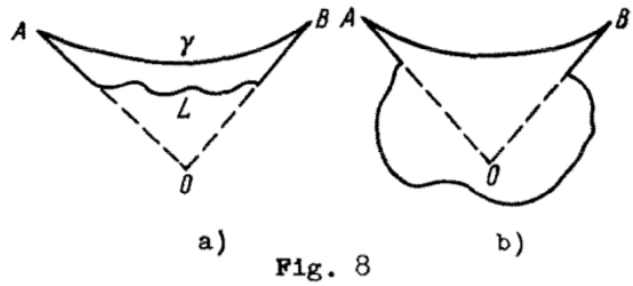

Figure 1.13: Original Fig. 8 in paper [169], showing how the boundary of duct can be arbitrarily changed without changing the solution.

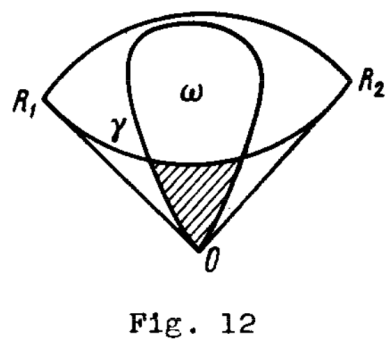

Figure 1.14: Original Fig. 12 of paper [169]. Showing arbitrary subdomain ω inside the main duct domain. The flow in main domain has stagnant zone OR_1R_2. This is sufficient condition for hatched area of subdomain ω to be stagnant

The theorems of these two papers represent the body of available analytical knowledge about self-selection. Unfortunately the results are limited to duct flows and do not necessarily extend to more general 2D flows such as flow in non-uniform channels that we are interested in. There are some 2D analytical works for very special cases, e.g. [14] that study local isolated flow in a corner. Otherwise, we will have to use computations for 2D flows. However, at least they provide some intuitions to interpret the features of self-selection for 2D flows. For example we will see later that static zones show up at the corners of an expansion-contraction channel, analogous to

duct flows. They also appear where the curvature of the channel wall is high and the yield surface of static region effectively reduces the curvature of the wall, again exactly the same mechanism shown by Mosolov and Miasnikov in ducts.

Another interesting connection concerns how the outer boundary of stagnant zones in 2D can be changed without affecting the flow? We saw that for ducts we can reduce the wall to any other line which is completely inside the static zone. Perhaps a similar result should be true for 2D flows, as we can pose the same stress and velocity field on the new boundary. But this is especially important for the case of growth of the wall, i.e. as in expanding a washout. In channels, what are the restrictions on expanding the boundary? These are the questions that we try to investigate in considering washout flows in primary cementing as the underlying industrial application.

1.5.2 Non-uniform channels and self-selection

There are a number of previous works in the literature that consider non-uniform channel flows and are related to self-selection phenomena. The works include both numerical and experimental studies. Also there are a few industrial papers (SPE) that study the flow in model washout geometries and are related to the basic motivation of this part of the thesis. We review here specific studies in which the appearance of stagnant zones and consequent self-selection are observed.

The oldest study reporting static zones of the flow of a yield stress fluid in a fully 2D setting is by Abdali and Mitsoulis [1], who studied both 2D and axisymmetric Stokes flows in a 4:1 contraction geometry. They were interested in this geometry due to extrusion die applications. Thus, most of the paper discusses issues like entrance and exit correction, swell ratio and pressure drop.... However, they also mention that the "well-known Newtonian vortex" in the corners becomes a "dead zone" even for small yield stress values, and that its size grows by increasing the yield stress. In a later work Mitsoulis and Huigol study the same flow in a wider range of parameters, confirm the previous results and extend to the new range, [164].

Vradis and coworkers published two papers related to flow in a 1:2 axisymmetric expansion. In the first work [243] numerical simulation using the bi-viscosity model is performed for a variety of Reynolds and Bingham numbers. They try to address the existence of stagnant zones at corners using this method, but finally state that no definite conclusion can be drawn. In their second work [115] higher quality simulations are performed and they conduct experiments using a PIV method. They show that both numerical and experimental results show the existence of stagnant zones in the corner. As we have seen in 1D (duct flow), in 2D and in axisymmetric geometries, static zones show up in the corner regions. This has also been observed in 3D by Burgos and Alexandrou [8, 43] who investigated Herschel-Bulkley flow in 1:2 and 1:4 three dimensional expansions.

Jay et al. [138] study structure of the flow in 1:4 axisymmetric expansion of Herschel-Bulkley fluid, experimentally and computationally, for a range of Reynolds, yield stress and shear thinning index. Again stagnant zone exists at corners for all range of parameters studied. However, depending on the Reynolds and Bingham number there might be a vortex as well at the corner region, which turns into a stagnant fluid zone by increasing the yield stress. They also nicely compared the shape of stagnant zone and vortex with experiments for a few cases. In a following study Jay et al. [139] consider axisymmetric contractions where, instead of an abrupt change, the contraction takes place through an angled section. They show by decreasing the angle for fixed contraction ratio the stagnant zone becomes smaller and eventually disappears, i.e. this means that the contracting section is becoming longer. More recently, de Souza Mendes et al. [79] conducted an experimental and numerical study of the slow flow of Carbopol through an axisymmetric expansion-contraction geometry. The static zones were nicely visualized by tracer particles and by taking long exposure time photos of the flow. With this technique the particles in stagnant zones are visible as shiny dots while the flowing particles show a faint light path. They observe static zones at corners in all range of parameters. When the length of expansion-contraction region is short these static zones are connected as one large piece which completely hides the walls of the test section from the flow. However

for longer lengths the flow touches the wall after a development region like expansion flows explained before.

To recap, most of the computational and experimental studies use a singular geometry, either sudden change in width or having corner points. We will try to study self-selection in a smooth sinusoidal channel in Chapter 2.

1.6 Thesis outline

The general class of petroleum industry problems that are closely related to this thesis were presented in above (e.g. §1.1). Broadly speaking, these flows all involve of a yield stress fluid through a duct/channel with non-uniform cross section. In fact, applications of these flows are not at all limited to well drilling/construction and hydraulic fracturing. Very similar flows are important and found in the food, pharmaceutical, health, cosmetics and mining and industries, as well as in natural settings, e.g. mammalian digestion and earthworms. Nevertheless, the need to understand these oil and gas industry flows remains the main motivation.

Three themes run through the thesis: (i) Physical phenomena for which there is novelty in our analysis and/or understanding. (ii) Development of numerical and analytical methodologies for understanding these phenomena. (iii) Building our knowledge progressively of specific flows.

Regarding (i) a pervading theme in each chapter is that of self-selection of the flowing region. In mathematical terms, yield stress fluid flows are free boundary problems, with the free boundary being the yield surface. Those parts of the flow for which the stress lies below the yield stress are not deformed and (when attached to a wall) they may remain static. These static *fouling* regions change the geometry of the fluid flow, which may in turn affect physical features such as the pressure drop. The fouled material may also itself have an adverse effect on a process flow. Thus, better understanding of self-selection is key to understanding our target oil and gas industry flows.

Regarding (ii) the methodological framework developed and used consists of: (a) Numerical computation of the flows, using the augmented La-

grangian method and mesh adaptivity (to define the yield surfaces), all within a finite element framework. (b) Dimensional analysis in order to reduce the problem parameter space and to help with analysis of the results. (c) Some asymptotic analysis, for exploring yield limits. Important in (a) is to understand that while each numerical computation is relatively quick to compute in 2D, we perform large-scale computations by investigating wide ranges of parameters for each problem.

Regarding (iii) we study two flows specifically. Chapters 2 & 3 study flows along varying channels, extending existing knowledge to include deep variations in width, the onset of fouling and eventually the limit of zero flow. Chapters 4-6 comprise a progressively complex study of flow past washouts. Starting with Stokes flow we then include inertia and finally a second displacing fluid. In more details, these chapters are as follows.

Chapter 2 considers the Stokes flow of Bingham fluid in a sinusoidal 2D channel. Here we focus on understanding the conditions when stagnant zones appear (i.e. the start of fouling and self-selection) in the channel. This is the first study that considers the self-selection mechanism in a 2D smooth channel. All previous works have studied singular geometries such as expansions and contractions. Furthermore, this chapter is the extension of the previous works of Frigaard and Ryan [102] and Putz and Frigaard [199] to larger wall amplitude and shorter channel length which are non asymptotic ranges. Adding this last piece, a full picture of the Bingham fluid flow in sinusoidal walls emerges.

Chapter 3 studies the slow flow of a Bingham fluid along fractures. We investigate the limits of applicability of the lubrication approximation and show that if self-selection is well understood then the valid range of lubrication can be extended to much wider limits of the geometrical parameters. For most of the study a simple wavy profile is used for fracture walls, thus extending Chapter 2. Also a few cases with more realistic *affine* fracture geometries are considered. We are interested in the pressure vs flow-rate relationship (effectively Darcy's law) and how non-linear effects for Bingham fluids affect Darcy's law, i.e. via

nonlinearity of the constitutive equations **and** via changing the flow domain through self-selection. Another important question examined here is the minimum required pressure to start flow.

Chapter 4 turns to the study of self-selection in geometries relevant to washed out sections of an oil/gas well, during cementing operations. These channels consist of one straight wall and one non-uniform wall. The former represents the casing and the latter is the rock formation/reservoir, which is irregular due to the washout. In reality the cementing geometry is a 3D annulus, but for simplicity we consider a 2D longitudinal section along the axis. Naturally, the geometry of washout is very complicated and unpredictable. We therefore consider four different classes of geometry for the washout. We observe that eventually self-selection gives very similar flow geometries, i.e. for sufficiently deep washouts and/or large yield stresses. Industrially this is very useful to give a big picture of the worst mud-conditioning scenario in the washout.

Chapter 5 extends the previous chapter by including inertia in the flow and looking how self-selection changes compared to the inertia-less case. This makes the study more relevant to the industrial application, but also makes the flows more complex. Thus we try to process the results mostly to give practical insights. As inertial effects are the focus of this chapter we use only the wavy wall shape for the washout geometry in this chapter.

An interesting result is the existence of a critical Reynolds number Re_c at which the minimum amount of static mud in the washout is reached. Beyond Re_c the amount of static mud actually increases. This is quite counter-intuitive to the common industrial perception that the higher the Reynolds number, the better mud conditioning will be. Also we observe that yield stress increases the stability limit of the flow, however we do not quantify this effect.

Chapter 6 starts to address the final problem relevant to washout in pri-

mary cementing, i.e. mud removal from the washout. This is a displacement flow and is very interesting theoretically as well as practically. Since the number of dimensionless parameters increases dramatically with two fluids, we study only the displacement flow of a yield stress fluid by a Newtonian fluid of the same density. This is the simplest displacement flow with the possibility of static layers (representing drilling mud that is not removed) on the walls. This serves as model for real cementing flows, giving insights into what new phenomena might need to be considered once a second fluid is introduced, and they might impact cementing. A sudden one-sided expansion-contraction channel is used for modeling the washout geometry, as suggested by the insights gained from the previous chapters.

Chapter 7 Wraps up the thesis, summarizing the main contributions, industrially and scientifically. Limitations of the work are discussed and a number of suggestions are made for future directions of the research.

Chapter 2

Flow of a Bingham fluid in wavy walled channels

Slow flows of Bingham fluids through sinusoidal wavy-walled channels are defined dimensionally by 3 dimensionless groups: (h, δ, B). These are the amplitude of the wall perturbation (h), the aspect ratio δ (half-width to length), and the Bingham number, B, denoting the ratio of yield stress to typical viscous stress. These flows are found to have stationary fouling layers at the wall in the deepest part of the channel, whenever the amplitude h exceeds some critical value h_f. We have characterised the occurrence of fouling and the main characteristics of fouling layers, by using Stokes flow computations extensively over the parameter space (h, δ, B).

Fouling can occur over a range of channel aspect ratios δ and progressively at larger h. Fouling begins at a value of $h\delta$ that varies primarily with B: both necessary and sufficient conditions for fouling are given. The limit of large B appears to plateau to constant values of $h\delta$, with the interpretation that for sufficiently shallow fixed geometries, as $B \to \infty$ (large yield stress) some channels will never foul. At moderate B, for $h > h_f$ the fluid appears to self-select the flowing region, i.e. the shape of the fouling layer. This phenomenon is partly understood in our analysis via selection of a new length-scale for the flow in the widest part of the channel. Fouling at small B (generally in deeply wavy channels) coincides with the onset of

recirculation in Newtonian fluid flows.[1]

2.1 Introduction

Shear flow of Newtonian fluids along wavy walled ducts and over wavy topography has received significant attention over the years, e.g. [116, 178]. Insofar as duct flows are concerned, at least initially much of the engineering motivation came from an interest in enhancing heat transfer, e.g. [185]. Other interest in such geometries comes from e.g. peristaltic pumping [45, 194] and pore scale modelling of porous media [258]. For non-Newtonian fluid flows in these geometries a different set of applications are important.

Here specifically we are interested in yield stress fluids and in the phenomenon of *fouling*, by which we mean that the fluid becomes stationary in layers attached to the wall of a duct. Fouling occurs in a variety of industrial flows (see [25, 51, 60, 129, 177, 219]) but is often associated with physicochemical changes in the fluid in the flowing fluid, e.g. dried deposits of milk solids [61, 64], precipitation of asphaltene deposits [10, 94]. An alternative terminology sometimes used in specific cases is *channeling*. Here we consider only the combination of rheological and geometric causes of fouling. Neither effect alone is able to cause fouling. Flow of a yield stress fluid along a uniform plane channel or circular pipe exhibits maximal shear stress at the wall and unyielded fluid is found only in the centre of the duct. Equally, Newtonian fluids flowing in wavy walled channels do not form stationary layers, although recirculatory regions may develop. Our use of the term *fouling* for our flows is perhaps a little unconventional, as often fouling refers to the build up of layers from the wall over time. However, one the layers have formed their continued status at the wall is determined mostly by mechanical considerations. Here we are concerned with the steady mechanical problem of whether layers may remain static at the wall under given flow and geometric conditions, rather than the actual formation process.

In order for fouling to occur in a wavy-walled duct flow of a yield stress

[1] A version of this chapter has appeared as: A. Roustaei & I. Frigaard. "The occurrence of fouling layers in the flow of a yield stress fluid along a wavy-walled channel." *J. Non-Newt. Fluid Mech.*, **198**:109–124, (2013).

fluid it is intuitive that a sufficiently large amplitude of perturbation from a uniform geometry is needed. Two important situations where such variations are likely are: (i) in the processing of food pastes through machinery; (ii) in the construction of oil and gas wells. In the first case, where geometric non-uniformities exist there is the risk of dead-zones appearing in the flow. As these represent sites for bacterial growth and a potential health hazard it is important to identify such zones, [236]. In oil and gas well drilling (see e.g. [41]) the well is drilled through a range of different geological strata. In soft or unconsolidated rock formations it is fairly common for the drilled wellbore to become uneven. This can depend on aspects of the drilling process (drill bit geometry and jetting), as well as on in-situ rock stresses, and on longer term effects due to prolonged contact of the rock with wellbore fluids (e.g. chemical effects, swelling, etc). Drilling muds that are used in well construction have a yield stress and are likely to become stationary in deep washouts. The consequences of this during drilling are not necessarily problematic but during the subsequent operation of primary cementing it is unlikely that the drilling mud will be displaced effectively from these regions; see e.g. [176].

Evidently, problems such as (i) and (ii) above are ill-defined in terms of the range of potential geometries and process conditions. The objective of our study is to begin to systematically understand geometric effects on fouling with yield stress fluid flows. We take the simplest non-trivial case, of a Bingham fluid in Stokes flow along a channel with a sinusoidal wavy-wall. The geometry is described by a wavelength and amplitude of the wall oscillation, and by the channel width, i.e. 3 parameters. Inertia is eliminated for ease, as in any case stationary flows are clearly non-inertial locally, and the Bingham rheology is certainly simplified compared to that of most yield stress fluids. Nevertheless, we can expect to gain insight into the main qualitative effects of fouling.

Wavy walled channel flows of Bingham fluids have been studied previously in [102, 199]. Although physically analogous to that studied here the focus was quite different. These studies looked at the asymptotic limit of small aspect ratio (long wavelength channels with small amplitudes), and in

particular sought to clarify the behaviour of the central plug region as the amplitude of the wall perturbation was increased from zero. In [102] it was shown that for sufficiently small perturbations of the wall, the flow retained its characteristic rigid central plug. In [199] the focus was on breaking of the central plug region as the wall perturbation amplitude was increased. This analysis was still focused at the long wavelength limit and showed that after the plug breaks the centre of the channel is occupied by a mix of rigid plugs and low shear extensional *pseudo-plug* regions. However, the amplitudes of wall perturbation were still modest in [199]. Here we continue these studies by looking firstly at a range of different wavelength wall perturbations and always at large amplitude wall perturbations, sufficient to allow the fluid to become stationary in the widest part of the channel.

The phenomenon of fouling of yield stress fluid flows due to geometric features has been identified before. Perhaps the oldest study is that of [168] who consider generically the conditions needed for stationary wall regions in one-dimensional duct flows. For example, in flow of a Bingham fluid along a duct of square cross-section, if the driving pressure gradient is too small then static regions form in the corners of the duct. Below a critical value of the pressure gradient (see [168]) the corner regions join with the central plug region and the entire flow becomes stationary. Computed examples of this type of phenomenon are given in [131, 171, 214].

Moving to multi-dimensional velocity fields, flow of yield stress fluids through an expansion-contraction has been studied experimentally and computationally in [79, 174, 175]. In [79] Carbopol solutions were pumped through a sudden expansion/contraction, i.e. narrow to wide to narrow pipe. A range of flow rates are studied and the yield surfaces are visualised nicely by a particle seeding arrangement. Although at fairly low Reynolds numbers, inertial effects are evident in the results via asymmetry of the flow (not present in the accompanying computations). There is a significant qualitative difference with the results from our study, presumably resulting from having the abrupt change in diameter. For all the experiments shown, stagnant regions first appear in the corners of the expansion (rather than at the centre of the widest part) and for all results shown there are stagnant

regions (whereas we shall see an onset value in terms of the amplitude). Comparisons are made between experimental and numerical results, which are at least qualitatively in agreement. The computations in [79, 174] use a finite volume method and a form of viscosity regularization to compute solutions. In [175] qualitatively similar computations are carried out, but using an elasto-viscoplastic model. We must also recognise that a similar phenomenon of fouling in sharp corners occurs in the flow of yield stress fluids through a sudden expansion (or contraction). For example, in [164] both planar and axisymmetric expansion flows are studied, over a wide range of Bingham and Reynolds numbers, showing significant regions of static fluid in the corner after the expansion. As already commented, the main geometric difference with the above studies is that the change in channel geometry that we consider is smooth, so that fouling occurs first in the widest part of the channel, driven by extensional stress gradients.

Other related flows include peristaltic pumping, which has been studied recently by [235] for Herschel-Bulkley fluids. It is worth noting that although geometrically similar, typically in models of peristaltic flow the wall itself is displaced in and out, shearing the fluid. Thus, it is not clear how yield stress effects manifest at all in such flows. Instead of fouling, there is the phenomenon of fluid trapping in which a region of recirculating fluid appears, translating with the wall wave speed. This is largely driven by kinematics and the results in [235] suggest that the effects of rheology on this phenomenon are rather minimal.

An outline of this chapter is as follows. Below in §2.2 we describe the physical problem and give a brief overview of the solution method and its implementation. Results are presented in §2.3, covering the main features of fouling layers as the three main dimensionless parameters are varied, with conclusions drawn from approximately 500 computations. The chapter closes with a brief summary of results and discussion.

2.2 The wavy-walled channel

The problem we consider is very much as described in [102, 199]: the two-dimensional (2D) Stokes flow of a Bingham fluid in a periodically wavy walled channel, periodic in x, as illustrated in Fig. 2.1. We adopt the convention of denoting dimensional variables with a *hat* symbol, e.g. $\hat{\cdot}$, and work primarily with dimensionless variables. The dimensionless Stokes equations are:

$$0 = -\frac{\partial p}{\partial x} + \frac{\partial}{\partial x}\tau_{xx} + \frac{\partial}{\partial y}\tau_{xy}, \tag{2.1a}$$

$$0 = -\frac{\partial p}{\partial y} + \frac{\partial}{\partial x}\tau_{xy} + \frac{\partial}{\partial y}\tau_{yy}, \tag{2.1b}$$

$$0 = \frac{\partial u}{\partial x} + \frac{\partial v}{\partial y}, \tag{2.1c}$$

where $\mathbf{u} = (u, v)$ is the velocity, p is the pressure and τ_{ij} is the deviatoric stress tensor. The constitutive laws are:

$$\tau_{ij} = \left(1 + \frac{B}{\dot{\gamma}(\mathbf{u})}\right)\dot{\gamma}_{ij} \iff \quad \tau > B \tag{2.2a}$$

$$\dot{\gamma}_{ij}(\mathbf{u}) = 0 \iff \quad \tau \leq B, \tag{2.2b}$$

where

$$\dot{\gamma}_{ij}(\mathbf{u}) = \frac{\partial u_i}{\partial x_j} + \frac{\partial u_j}{\partial x_i}, \qquad \mathbf{u} = (u, v) = (u_1, u_2),\ \mathbf{x} = (x, y) = (x_1, x_2).$$

and $\dot{\gamma}$, τ are the norms of $\dot{\gamma}_{ij}$, τ_{ij}, defined as

$$\dot{\gamma} = \sqrt{\frac{1}{2}\sum_{ij}\dot{\gamma}_{ij}^2} \qquad \text{and} \qquad \tau = \sqrt{\frac{1}{2}\sum_{ij}\tau_{ij}^2}. \tag{2.3}$$

The single dimensionless number appearing above is the Bingham number, B:

$$B \equiv \frac{\hat{\tau}_Y \hat{D}}{\hat{\mu}\hat{U}_0}, \tag{2.4}$$

where $\hat{\tau}_Y$ is the yield stress and $\hat{\mu}$ is the plastic viscosity of the fluid; see

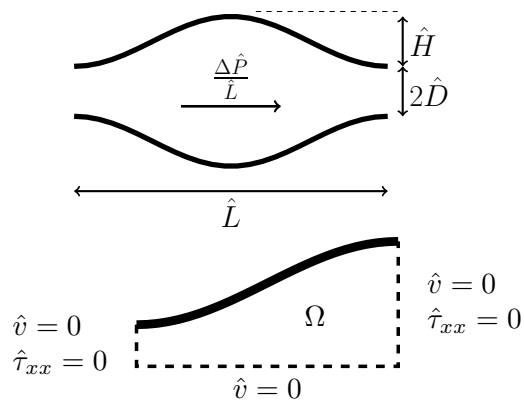

Figure 2.1: Schematic of the flow geometry and boundary conditions Ω.

[196]. The mean channel half-width is $\hat{D}$ and the mean flow velocity in the x-direction is $\hat{U}_0$. In (2.1) & (2.2), lengths have been scaled with $\hat{D}$, velocities with $\hat{U}_0$ and stresses with the viscous stress: $\hat{\mu}\hat{U}_0/\hat{D}$.

The channel geometry is as depicted in Fig. 2.1. The upper wall is at $y = y_w(x)$:

$$y_w(x) = 1 + \frac{h}{2}(1 - \cos 2\pi\delta x).$$

The parameter $\delta = \hat{D}/\hat{L}$ reflects the aspect ratio between the channel half-width and the dimensionless wavelength $\hat{L}$ of the wall variation. The parameter $h = \hat{H}/\hat{D}$ is the maximal depth of the wall perturbation.[2] More precisely, the unperturbed channel is considered to have uniform half-width 1 and the perturbed channel has half width varying from 1, at $x = 0$, to $(1 + h)$ at $x = 1/2\delta$, with periodicity δ^{-1}. We consider the flow as steady and periodic and consider only a single period of the channel. Further, as we consider a Stokes flow, in place of periodicity conditions we may infer symmetry about the channel centreline and maximal/minimal widths. Therefore, only one quarter of the channel is considered; see Fig. 2.1. At

[2]The definition of δ is identical with that in [102, 199]. The definition of h here differs from that in [102, 199], where h was defined so that the scaled channel half-width varied from $(1 - h)$ to $(1 + h)$.

the upper wall we impose no-slip conditions:

$$u(x, y_w(x)) = v(x, y_w(x)) = 0, \tag{2.5}$$

and at the channel centreline, symmetry conditions:

$$\tau_{xy}(x, 0) = v(x, 0) = 0. \tag{2.6}$$

Symmetry conditions are imposed at $x = 0$ and $x = 1/2\delta$:

$$\tau_{xx}(x, y) = v(x, y) = 0, \quad \text{at} \quad x = 0,\ 1/2\delta. \tag{2.7}$$

Finally, as we have scaled with the mean velocity, the mean pressure gradient in the x-direction must be adjusted to ensure that

$$\int_0^{y_w(x)} u(x, y)dy = 1. \tag{2.8}$$

2.2.1 Numerical solution method

The finite element method is used for discretizing the Stokes problem (2.1)-(2.8). Due to symmetry of the flow and to save computational time only a quarter of the channel is considered, as illustrated in Fig. 2.1. A limited number of computations were also carried out in the development stage, to verify the symmetry of the flow. The algorithmic approach we have used is the augmented Lagrangian (AL) method described by Glowinski and co-workers; see [99, 110, 111]. The chief advantage of AL over viscosity regularization is that the exact form of constitutive relation is used and the algorithm gives truly unyielded regions with exactly zero strain rate. As the ultimate goal of this chapter is to study the onset of fouling layers (which are stationary unyielded regions), it is important to distinguish true unyielded regions of the flow from those where the strain rate is merely small. This is the main motivation for using the AL method.

Very briefly, in AL the proper variational formulation of a Bingham fluid flow is used; see e.g. Duvaut & Lions [92]. This formulation contains

non-differentiable terms which hamper the use of conventional optimization methods for solving the variational form. To circumvent this problem two Lagrange multipliers (γ_{ij}, T_{ij}) are introduced into the variational formulation and the global optimization problem is split into three separate optimization problems, with respect to $\mathbf{u}, \gamma_{ij}$ and T_{ij}. These are solved sequentially until acceptable convergence is achieved. The minimization problem for $\mathbf{u}$ (step 1) reduces to a classical weak form of Stokes flow. The minimization problems for γ_{ij} & T_{ij} (steps 2 & 3) reduce to explicit algebraic updates on each discrete component (node or element, according to the implementation). The Lagrange multipliers (γ_{ij}, T_{ij}) have physical meanings: they represent the strain rate tensor and an admissible deviatoric stress tensor of the flow, when the algorithm has converged. Regions with $\gamma_{ij} = 0$ can be easily identified as unyielded regions of the flow. The details of the numerical method are explained in [199].

The AL was implemented within the excellent code *Rheolef* [213], a C++ FEM library by P. Saramito and colleagues in Grenoble. For a good explanation of the details of the algorithm we refer reader to the papers by Saramito & Roquet [206, 207, 214]. The special feature of this implementation is that the meshing is adaptive, according to the positions of the yield surfaces (identified via the Hessian of the strain rate). A typical computation is started with a nearly uniform triangular mesh in which the top wavy wall is divided to 100 ($.125 \leqslant \delta$) or 150 ($\delta < .125$) edges. For each step of the refinement cycle the computations are iterated up to the point that $max\left\{\left\|u^n - u^{n-1}\right\|, \left\|\gamma^n - \gamma^{n-1}\right\|\right\} \leqslant 10^{-6}$, or that a maximum number of iterations (4000) is reached. At the end of the computation a new mesh with denser cells around the yield surface is generated and the computation is repeated for the new mesh on the new cycle. An example of the meshes generated in a typical refinement cycle is shown in Fig. 2.2. Typically we use four mesh adaptation cycles. The yield surfaces are clearly identified in the last adaptation. BAMG performs the meshing [36, 37]. On any computation the maximum number of mesh points was limited to 40000, due to available hardware. The details of mesh adaptation strategy can be found at [206]. The code was validated with a uniform channel flow, for which

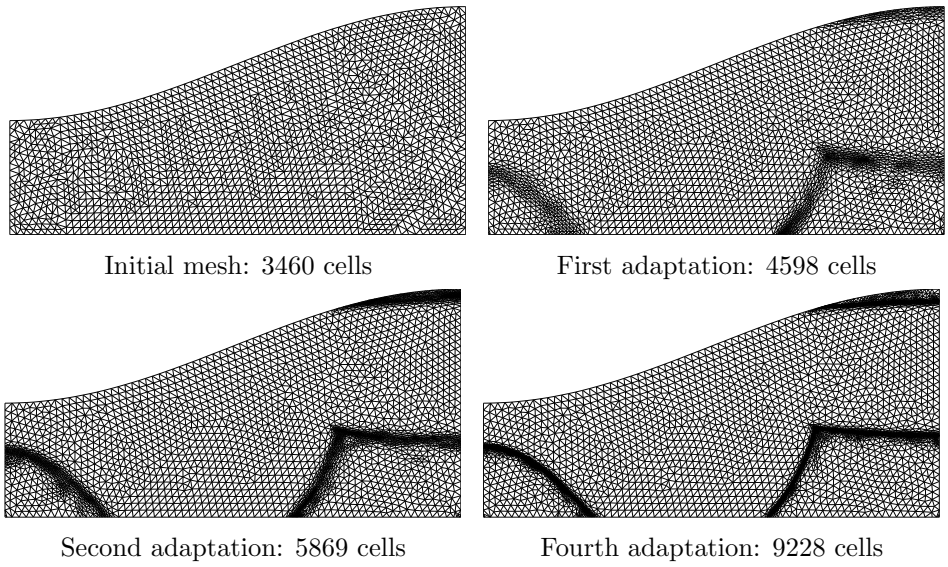

Figure 2.2: Showing a mesh adaptation cycle for the case of ($h = 1,\ \delta = .125,\ B = 10$)

the analytical solution is available. Other benchmark computations can be found in [199, 206].

2.3 Results

As discussed in §2.1 the aim of this chapter is to study the onset and characteristics of fouling layers in the widest part of the channel. For fixed (B, δ), these appear to arise as the depth h exceeds some critical value h_f. Here we start by presenting a range of typical flow results that illustrate the main features of this phenomenon. In §2.3.1 we examine numerical results computed for small δ, for which we find fouling layers. We examine the asymptotic solutions from [102, 199], to see if they are able to predict h_f. Section 2.3.2 considers channels of order 1 aspect ratio. We then give a broad overview of the types of flow observed, in terms of (B, δ, h); see §2.3.3. Characteristics of the shape of the yield surfaces when fouling occurs are explored in §2.3.4, for $B \sim O_S(1)$, focusing on self-selection of the flow regime. Interesting features of the Newtonian limit $B \to 0$ are considered in §2.3.5.

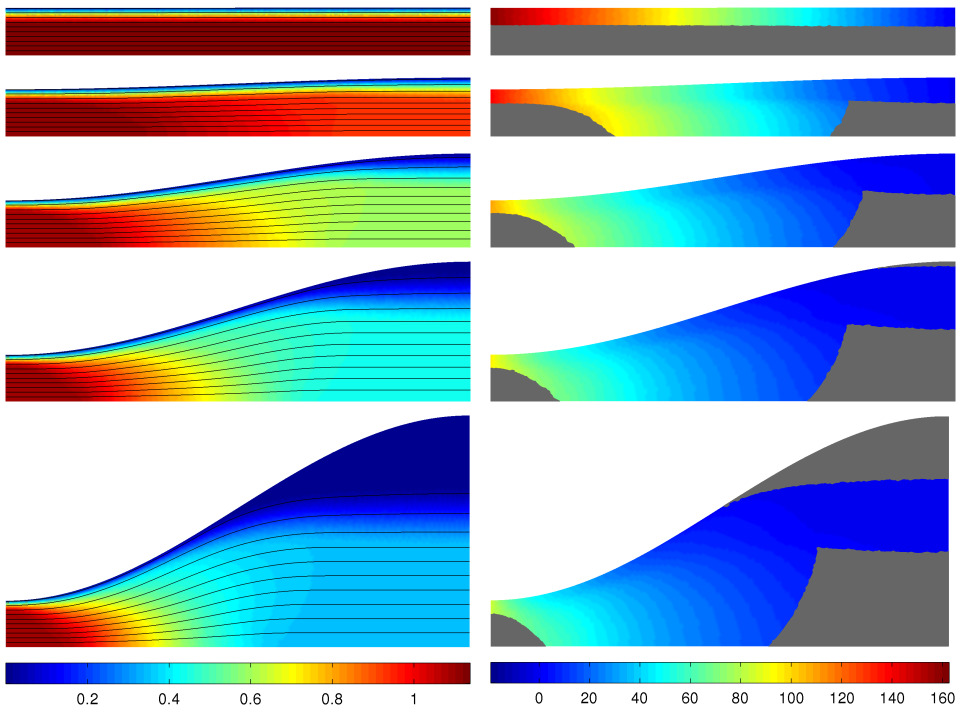

Figure 2.3: Effects of increasing amplitude h on speed (left panel) and pressure (right panel), for $\delta = .05$, $B = 10$. From top to bottom, $h = (.01, .25, 1, 2, 4)$. The same color scale is valid for each h. The dark lines in the left panel are the streamlines, gray regions in right are plugs.

2.3.1 Channels with small δ

Figure 2.3 shows a typical progression in the solution and plug regions as h is increased from zero in a channel of relatively small aspect ratio ($\delta = .05$). The small aspect ratio puts the computations in the range of the analysis of [102, 199] for small enough h. For $h = 0.01$ we can see that the unyielded plug remains intact, being slightly wider in the narrower part of the channel than in the wider part, as observed in [102]. The velocity field is only slightly perturbed from the uniform plane Poiseuille flow and the streamlines are pseudo-parallel.

At larger h the single central plug breaks, due to growth of extensional

stresses. The flow consists of two true plugs connected by an extensional pseudo-plug region. Outside the plug/pseudo-plug regions we find a sheared region extending to the wall for $h = 0.25,\ h = 1$. This breaking process and flow structure was studied in [199]. As h increases the speed in the wider part of the channel decreases. This induces extensional stress gradients and also lowers the pressure drop through the wider part of the channel. The combination of these allows the appearance of the fouling layer, at $h_f < 2$, as evidenced by the results for $h = 2$ (the exact value of h_f could be found iteratively). The fouling layer grows thicker as h increases. We also observe that as the single plug breaks in two, the plug region in the narrow part of the channel is initially wider than in the wide part. However as h increases, the plug in the widest part of the channel grows wider, mimicking the reduced pressure drop.

In Fig. 2.4 we examine the last case from Fig. 2.3 ($h = 4$) in more detail, showing the various stress fields and the strain rate. There are a number of interesting features. Firstly, the pressure is by far the largest component of the stress in the narrower part of the channel, up until approximately the position where the fouling layer appears at on the upper wall. From this point and into the widest part of the channel, the extensional stress has comparable size to the pressure. Indeed we observe that σ_{yy} is approximately zero between the larger plug and the fouling layer, suggesting that the pressure is balanced with $\tau_{yy}(= -\tau_{xx})$ in this region. We also observe that τ_{xy} appears to only just exceed the yield stress ($B = 10$) in this region. This is the key difference between this flow and the shear flow in a plane channel, where $|\tau_{xy}|$ increases linearly until the wall. Leaving the region between the plug and fouling layer, σ_{yy} remains approximately independent of y, suggesting that τ_{xy} is approximately independent of x (from the Stokes equations). Note however that near the upper wall, as we enter the expansion and the fluid is yielded, there is a thin layer of higher stress gradients.

For sufficiently small δ we may expect the asymptotic solutions of [102, 199] to be valid. A natural question is to ask if these solutions are able to predict the fouling layer? The general asymptotic structure of the solutions is to have two *outer* regions matched in an *inner* layer close to the

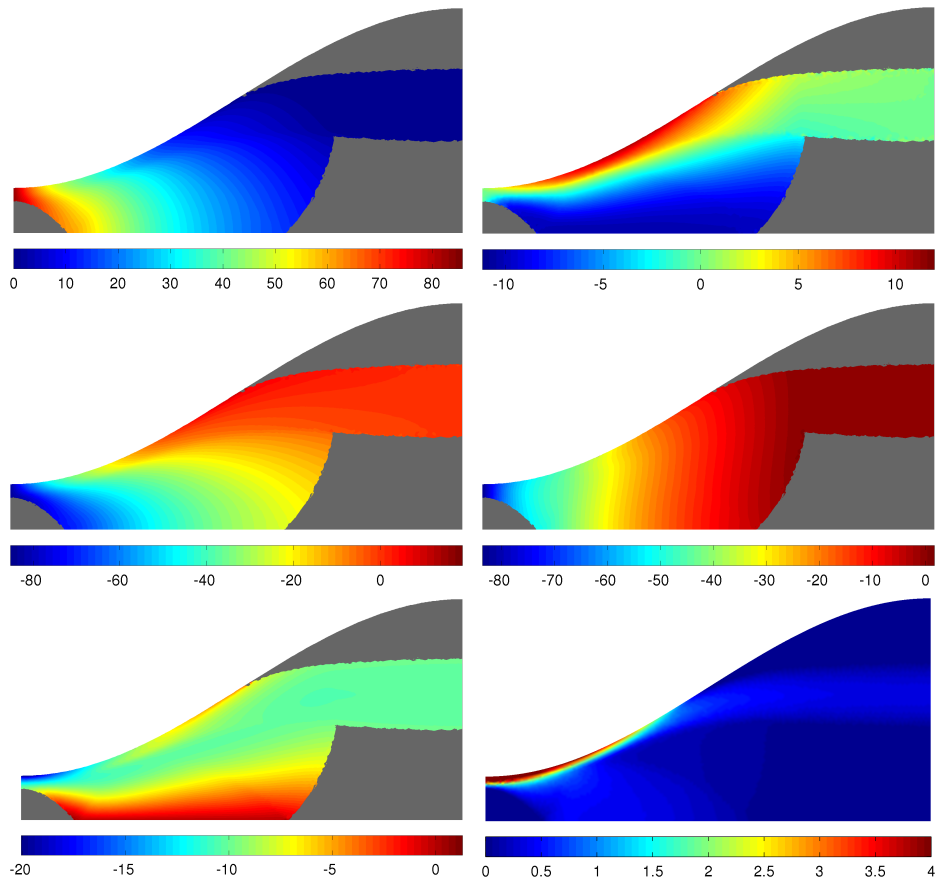

Figure 2.4: More detailed results from the case $\delta = .05$, $B = 10$, $h = 4$. Left panel, from top to bottom shows $(p, \sigma_{xx}, \tau_{xy})$. Right panel from top to bottom shows $(\tau_{xx}, \sigma_{yy}, \|\gamma\|)$ respectively.

pseudo-yield surface $y = y_y(x)$. The outer region that extends from the plug/pseudo-plug to the channel wall is of interest here, since this is where the fouling layer first appears as h increases. The lubrication approximation in [102, 199] considers an outer solution in the yielded region that is of form:

$$p \sim p_0(x) + \delta p_1(x)... \tag{2.9}$$

$$u \sim u_0(x, y) + \delta u_1(x) + ..., \tag{2.10}$$

The x-dependency in u_0 comes only via the channel width $y_w(x)$. The

leading order velocity is:

$$u_0(x,y) = \begin{cases} u_p(x), & y \in [0, y_y(x)] \\ u_p(x)\left[1 - \dfrac{(y - y_y(x))^2}{(y_w(x) - y_y(x))^2}\right] & y \in (y_y(x), y_w(x)] \end{cases} \tag{2.11}$$

where the pseudo-plug speed is:

$$u_p(x) = \frac{B}{2y_y(x)}(y_w(x) - y_y(x))^2. \tag{2.12}$$

The position of the pseudo-yield surface, $y_y(x) = y_w/\xi$, where $\xi = \xi(B^*)$, is the single root of the cubic Buckingham equation:

$$2\xi^3 - (3 + \frac{6}{B^*})\xi^2 + 1 = 0, \tag{2.13}$$

for which $\xi > 1$, and $B^* = By_w^2$. On finding the root, (see Fig. 2 in [102]), we can determine p_0 up to an additive constant from the pressure gradient:

$$y_y = \frac{B}{-p_{0,x}}. \tag{2.14}$$

The deviatoric stress components are:

$$\tau_{xy} \sim u_{0,y} + B\text{sgn}(u_{0,y}) + \delta u_{1,y} + O(\delta^2), \tag{2.15}$$

$$\tau_{xx} \sim 2\delta\left(1 + \frac{B}{|u_{0,y}|}\right)u_{0,x}, \tag{2.16}$$

The leading order shear stress term can also be represented as: $\tau_{xy} \sim -p_{0,x}y + O(\delta)$. The first order velocity is given in [102, 199] and gives the first order shear stress and pressure gradient.

We can see from the above that it is impossible for the leading order solution to exhibit fouling. The leading order pressure gradient is negative and the leading order shear stress satisfies $\tau_{xy} \sim yp_{0,x} + O(\delta)$. This is the usual Poiseuille flow solution resolved on a channel of width $2y_w(x)$. The only way in which the stress can fall below the yield stress at the outer wall is if the higher order terms become extremely large.

However, we can at least examine whether the trends towards fouling are present in the higher order terms. If we consider the widest part of the channel where $\tau_{xx} = 0$ then the occurrence of a fouling layer depends only on τ_{xy}. Instead of decreasing monotonically, it is necessary for τ_{xy} to increase near the wall. The axial momentum balance (2.1a) is valid at $x = 1/2\delta$, and we see that since p has no y-dependency up to second order in δ, an increase in τ_{xy} is only possible if $\frac{\partial}{\partial x}\tau_{xx} < 0$ in the yielded region.

The x-dependency of the leading order velocity u_0 enters only through the channel width, so that

$$\frac{\partial u_0}{\partial x} = \frac{\partial u_0}{\partial y_w}\frac{\mathrm{d}y_w}{\mathrm{d}x}.$$

We see that the x-derivative of τ_{xx} will contain terms with both 1st and second derivatives of $y_w(x)$. Since $x = 1/2\delta$ is a maximum of $y_w(x)$, only the second derivative terms are non-zero at $x = 1/2\delta$:

$$\left(\frac{\partial}{\partial x}\tau_{xx}\right)\bigg|_{x=1/2\delta} = 2\delta\left(\left[1 + \frac{B}{|u_{0,y}|}\right]\frac{\mathrm{d}^2 y_w}{\mathrm{d}x^2}\frac{\partial u_0}{\partial y_w}\right)\bigg|_{x=1/2\delta}. \tag{2.17}$$

The effective viscosity is positive and the second derivative of y_w is negative at the maximum, so that the sign of $\frac{\partial}{\partial x}\tau_{xx}$ depends on:

$$\frac{\partial u_0}{\partial y_w} = \frac{\partial u_p}{\partial y_w}\left[1 - \frac{(y-y_y)^2}{(y_w-y_y)^2}\right] + 2u_p\frac{(y-y_y)}{(y_w-y_y)^3}\left[(y_w-y)\frac{\partial y_y}{\partial y_w} + (y-y_y)\right] \tag{2.18}$$

The first term above is always negative as u_p decreases in a wider channel. In contrast, the second term is always positive as y_y increases with y_w. We also note that the first term, vanishes at the wall whereas the second term is positive at the wall, but vanishes near the pseudo-yield surface y_y. It follows that at the maximal channel width ($x = 1/2\delta$), $\frac{\partial}{\partial x}\tau_{xx} > 0$ close to the pseudo-yield surface y_y but changes sign so that $\frac{\partial}{\partial x}\tau_{xx} < 0$ close to the wall y_w. Therefore, the physical mechanism that would allow τ_{xy} to increase near the wall and a fouling layer to develop is present in the asymptotic solution.

The mechanism by which the fouling layer emerges is via a change in the streamwise gradient of the extensional stresses, as we approach in the upper wall. It is worth noting that the extensional stress effect represented in (2.17), although of the required sign, is also rather weak. The second derivative of y_w is of second order in δ. Therefore, it is unlikely to overcome bulk pressure gradient effects unless the pressure gradient is also significantly reduced in the wider part of the channel, as we have observed in Fig. 2.4, i.e. it seems that reduction in the pressure gradients is also necessary for a fouling layer to emerge. Finally, we need to note that the emergence of a fouling layer in the asymptotic solution would also mean the breakdown of the scaling assumptions that are behind the approximation.

2.3.2 Channels with $\delta \sim O_S(1)$

Fouling layers also occur in channels of larger aspect ratio δ, for which the asymptotic theories are not valid and which have not to our knowledge been systematically studied. An example of a shorter channel is shown in Fig. 2.5 for $(B, \delta) = (10, 0.25)$. Perhaps surprisingly, we observe that fouling occurs when the central plug region is still intact. Also we can see a large variation in the plug width, between the narrowest and widest part of the channel. At a larger depth ($h = 1$) the central plug breaks, but this is after the onset of fouling. An interesting feature of the pressure field is the region of negative pressure in Fig. 2.5 near the upper wall when fouling occurs. Essentially the fluid is being sucked away from the wall.

Related to the negative pressure, we observe that there are two competing influences that generate extensional strain rates (and stresses). Firstly, there is a bulk geometric effect in that the channel widens with x, so that we expect $\frac{\partial u}{\partial x} < 0$ as the flow rate is fixed. This in turn suggests $\tau_{xx} < 0$. On the other hand, the velocity at the upper wall is zero, whereas in the absence of fouling we expect a positive axial component of velocity away from the wall. Therefore, acceleration away from the wall within the undulation implies $\frac{\partial u}{\partial x} > 0$ and hence $\tau_{xx} > 0$. These effects are reversed as we move from the widest part of the channel to the narrowest. The distribution of

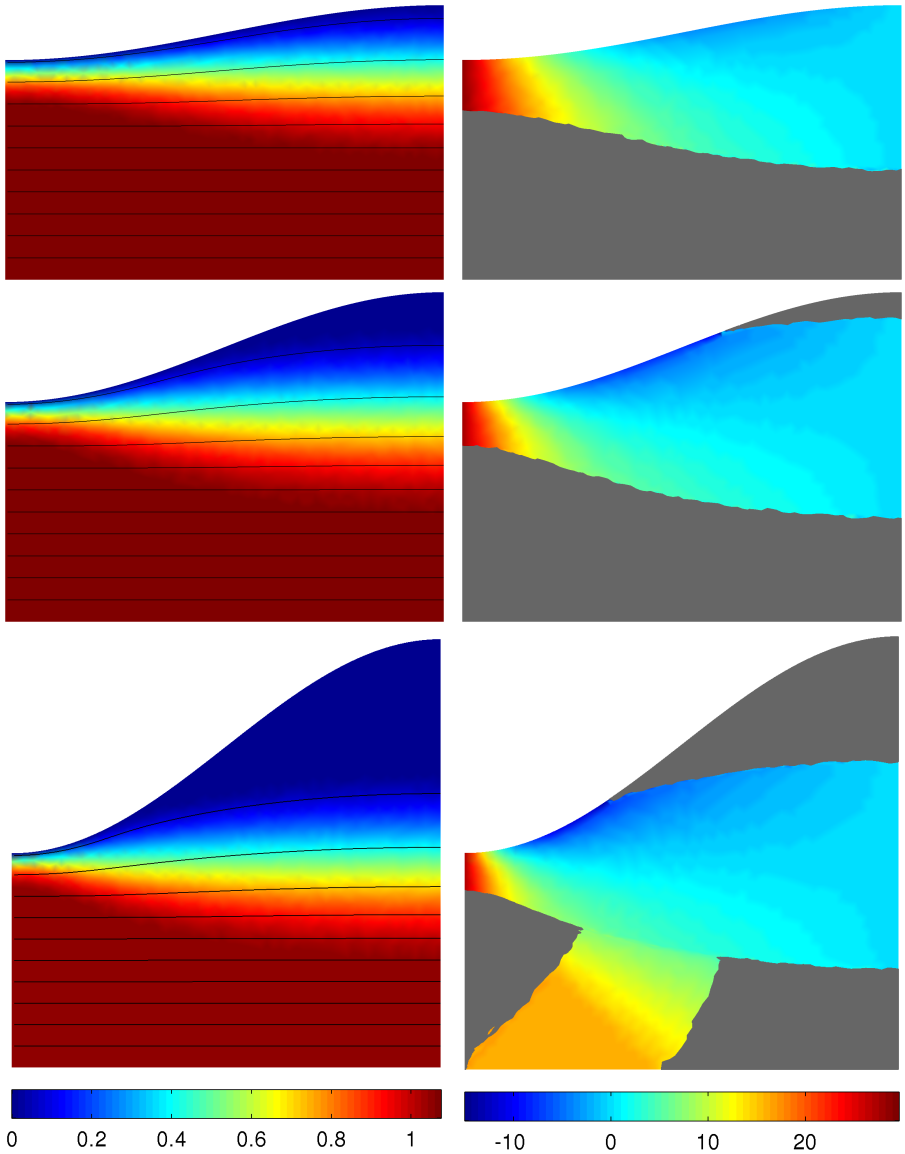

Figure 2.5: Effects of increasing amplitude h on speed (left panel) and pressure (right panel), for a bigger δ than Fig 2.3, $\delta = .25, B = 10$. From top to bottom, $h = (.25, .5, 1)$. The same color scale is valid for each h. The dark lines in the left panel are the streamlines, gray regions in right are plugs.

τ_{xx} inferred by the geometric/kinematic competition just discussed suggests that $\frac{\partial}{\partial x}\tau_{xx} < 0$ in the upper part of the channel, which is needed in (2.1a) in order for τ_{xy} to increase with y, which must occur at the onset of fouling.

2.3.3 Parameter regimes

Approximately 500 cases have been computed, covering a significant range of (B, h, δ). Here we present the main features of the results, in terms of a qualitative description of the flows. Figures 2.6 & 2.7 show the evolution of unyielded regions with changing (h, δ), each at fixed Bingham numbers: $B = (1, 2, 5, 10)$. Several interesting points can be observed. First, for the limit of short channels ($\delta \sim O_S(1)$) once h is large enough to have a significant fouling layer, the flowing region seems to become approximately invariant with h. It does not seem that sufficient extensional stresses are developed in order to break the central plug. The fouling layer appears to choose its own geometry of yielded fluid.

For longer channels (*e.g.* $\delta \leq .25$) increasing the unevenness h creates high extensional stresses close to the inflow which can break the central plug, as we see for $\delta = 0.05$ in Figs. 2.6 & 2.7. As h increases further we see an interesting phenomenon close to the entrance, where the plug effectively disappears. In fact, the plug is still there, but very reduced. Indeed, a symmetry and continuity argument establishes that there should always be a true plug at the centre of the narrowest part of the channel. At larger B we are able to follow the evolution of the narrow section plug for these intermediate δ. For example, for $(B, h, \delta) = (5, 1.5, 0.25)$ we see a triangular *mushroom shape* plug, connected to $(0, 0)$ by a thin strand of unyielded plug. Figure 2.8 explores this evolution in more detail. As h increases or B decreases the thickness of the *stalk* of the mushroom decreases to below the mesh resolution.

As the channel gets longer (smaller δ) extensional stresses grow and the central plug is broken even for large B, unless the case of $h \ll O(\delta)$ is considered; see [102]. On breaking, there appears to be a form of stress relaxation at the narrow part of the channel, as the plugs actually grow in

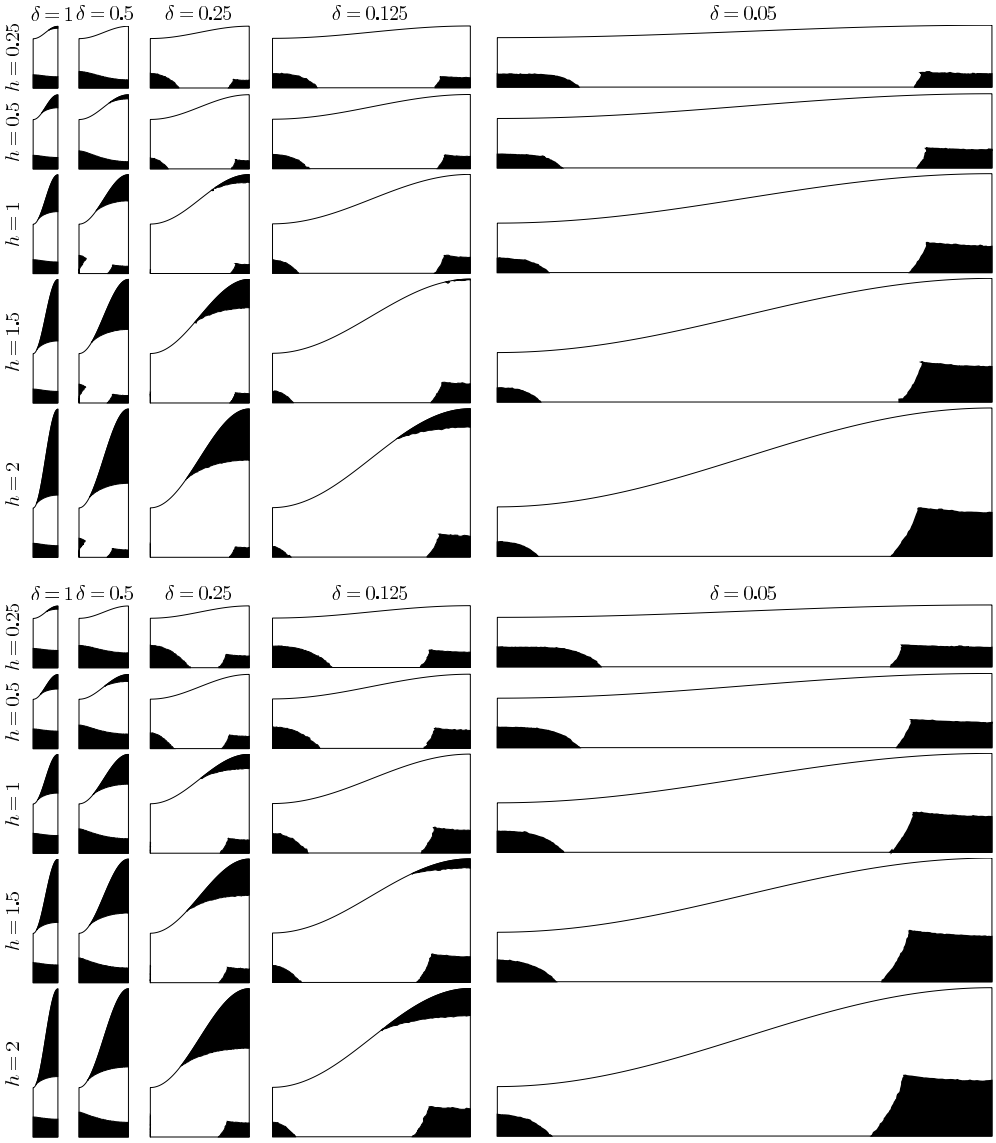

Figure 2.6: Panorama of plug shapes for $B = 1$ (top) and $B = 2$ (bottom)

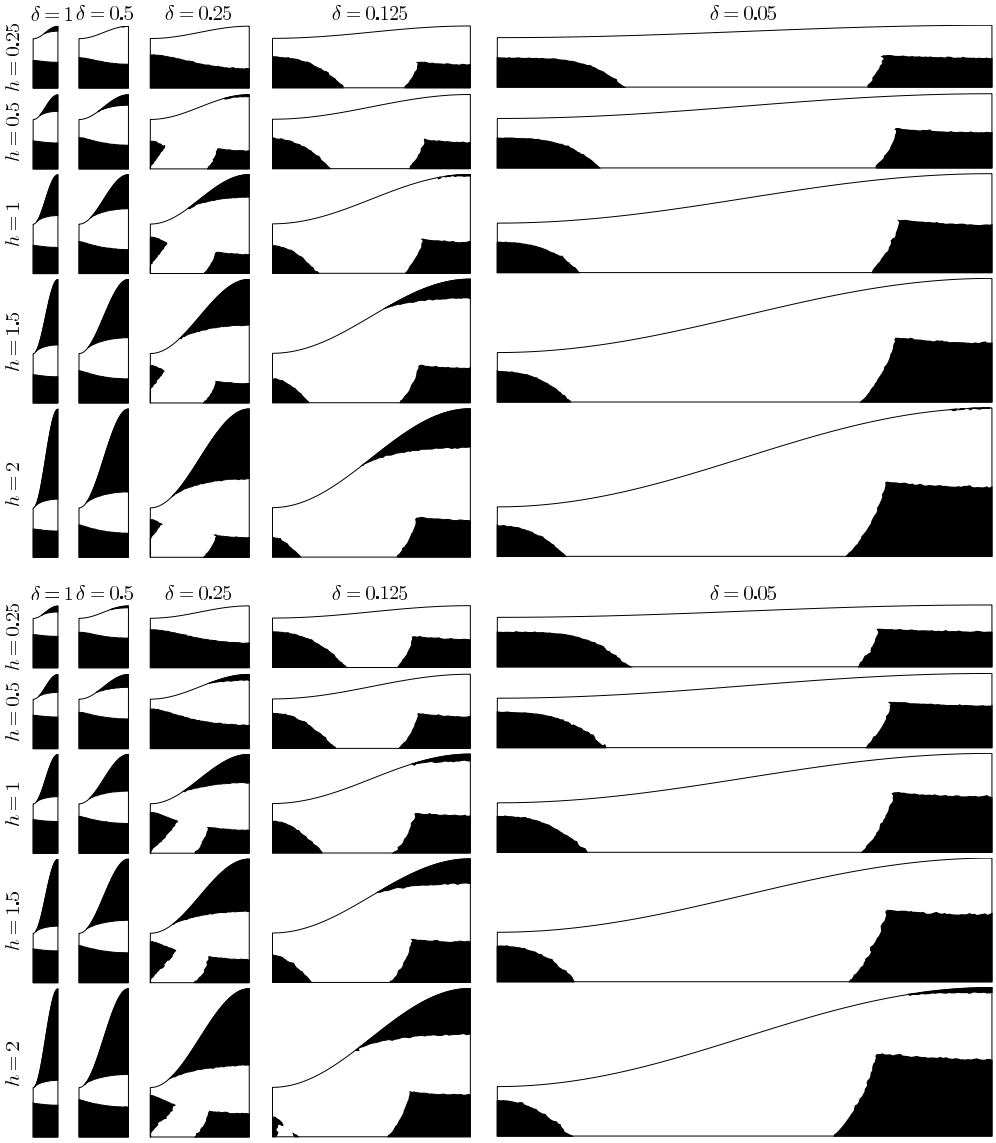

Figure 2.7: Panorama of plug shapes for $B = 5$ (top) and $B = 10$ (bottom)

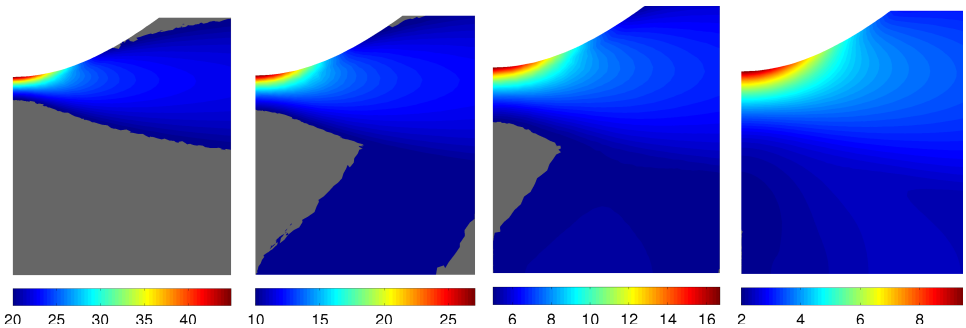

Figure 2.8: Appearance and evolution of mushroom shape plug and stress field ($\|\tau\|$) at the narrowest part of channel for ($h = 1, \delta = .25$) and $B = (20, 10, 5, 2)$ (from left to right); gray regions are plugs (figure zoomed on narrowest part of channel).

size and the mushroom shape is lost. However, small δ alone does not it seems prevent fouling, which still occurs for sufficiently large h and B.

Qualitatively, four different regimes have been observed: the central plug may be broken or unbroken, a fouling layer may be present or absent. From a practical perspective, we might be more concerned with the fouling layer than the central plug being broken. The results presented in Figs. 2.6 and 2.7 suggest that the product $h\delta$ as a relevant geometric criteria for detecting the onset of fouling layer (at fixed B). Dimensionally, note that $h\delta = \hat{H}/\hat{L}$, which is rather natural as an indicator of fouling (see the schematic in Fig. 2.1). Figure 2.9 plots the 4 different types of flow for $B = (.1, 1, 10, 100)$ and in each case attempts to delineate fouling regimes from non fouling regimes by a curve of constant $h\delta$. The value of $h\delta$ appears to decrease monotonically with B, i.e. at larger B and fixed aspect ratio δ we expect a lower value of h_f, as is intuitive. Equally, looking at Fig. 2.9 we see that our results confirm that if, for example, (B, h, δ) has a fouling layer then larger values of (B, h, δ) will also have fouling layers. We shall see later that there is some complexity as $B \to 0$, but for $B \sim O_S(1)$ this conclusion holds true.

Although a reasonable approximation is given by the curves of constant $h\delta$ in Fig. 2.9, this is not completely accurate as a prediction: there is also

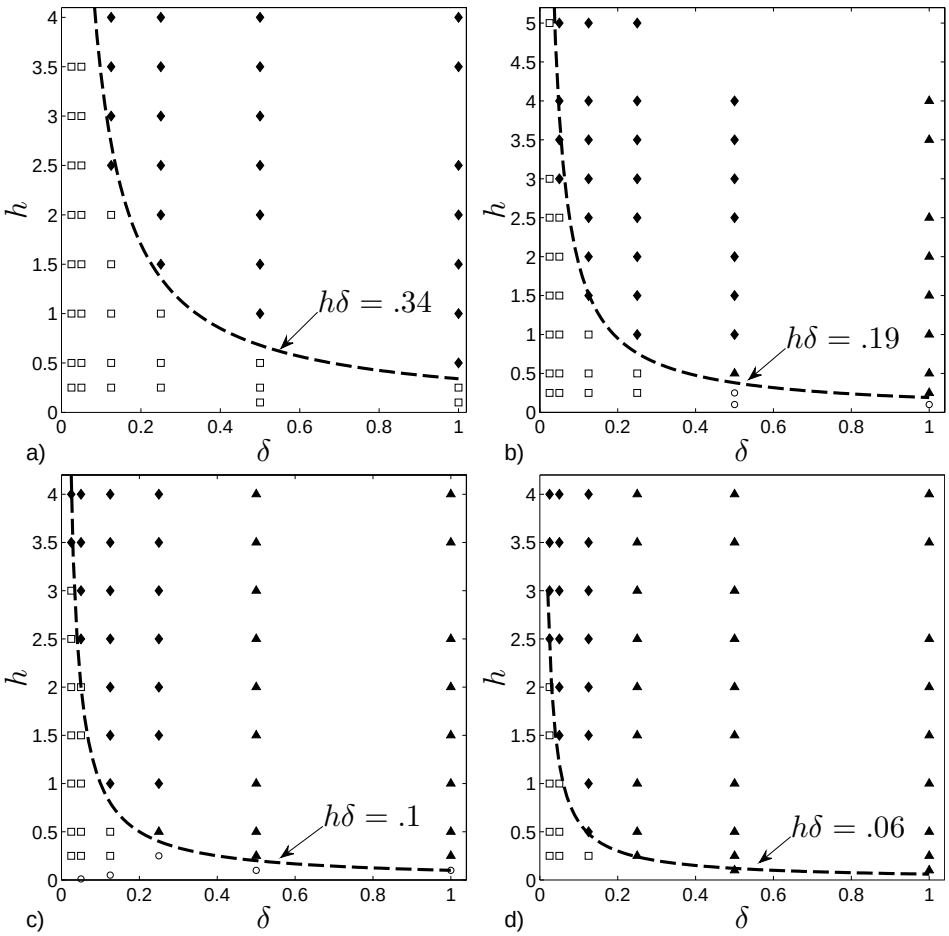

Figure 2.9: Plot of flow regimes in (h, δ) plane for different Bingham numbers, a) $B = .1$, b) $B = 1$, c) $B = 10$, d) $B = 100$. Markers of flow regimes: (▲) intact central plug+fouling, (♦) broken central plug+fouling, (□) broken central plug-no fouling, (○) intact central plug-no fouling.

some small independent variation with δ (or equivalently h). This is evident from Fig. 2.9 where in each case some points can be spotted in the wrong side of the constant $h\delta$ curves. Nevertheless, the characterization of the fouling transition as occurring for $h\delta = f(B)$ is very close. To explore this further Fig. 2.10 shows all of our computational results (≈500 different cases) plotted in the $(B, h\delta)$-plane. We see that there is not a single boundary separating fouling flows from non-fouling flows, but instead there is a narrow range of $h\delta$ at each B over which we transition. In other words, we can identify two critical curves in our results. The curve $h\delta_s = g(B)$ gives *sufficient* conditions for there to be a fouling layer. The curve $h\delta_n = f(B)$ gives *necessary* conditions for there to be a fouling layer. Between these two curves we find both fouling flows and non-fouling flows, with slight dependency on h and δ.

The sufficient and necessary curves have been fitted, as indicated in Fig. 2.10, by the following two functions:

$$g(B) = h\delta_s = \frac{0.054B^2 + 1.03B + 0.31}{B^2 + 5.67B + 0.66}, \tag{2.19}$$

$$f(B) = h\delta_n = \frac{0.039B^2 + 0.55B + 0.07}{B^2 + 3.21B + 0.15}; \tag{2.20}$$

evidently $f(B) \leq g(B)$. The above functions coincide approximately as $B \to 0$. This limit is closely related to the onset of recirculation for a Newtonian fluid, as we explore later in §2.3.5. Both expressions (2.19) & (2.20) approach constant plateaus (with constant offset) as $B \to \infty$. For any fixed h this confirms the insights from the asymptotic analysis that for sufficiently small δ there should be no fouling layer. However, although our numerical data supports the idea of a constant plateau, we have not explored the range of very high B.

2.3.4 Characteristic features of the fouling layer for $B \gtrsim O_S(1)$

We have seen that at fixed $B \sim O(1)$ a fouling layer appears at $h = h_f$ and remains for $h > h_f$. It was observed that the shape of the upper plug region

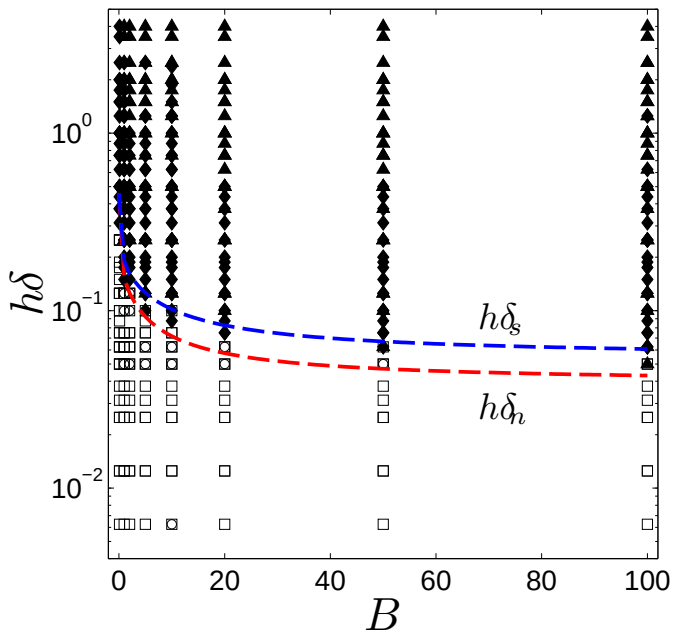

Figure 2.10: Phase plot of all computations (≈500 points), Markers of flow regimes: (▲) intact central plug+fouling, (♦) broken central plug+fouling, (□) broken central plug-no fouling, (○) intact central plug-no fouling, equations $h\delta_n = \frac{.039B^2+.55B+.07}{B^2+3.21B+.15}$, $h\delta_s = \frac{.054B^2+1.03B+.31}{B^2+5.67B+.66}$ represent fitted curves.

and central plug, although initially sensitive to $h > h_f$, becomes increasingly fixed. In particular, at the widest part of the channel ($x = 1/2\delta$) the width of yielded fluid between the two plugs appears to become constant as h increases. This is illustrated in Fig. 2.11 for a number of different values of (B, δ). Particularly for larger values of δ the positions of the yield surfaces become constant rapidly for $h > h_f$.

To some extent the above feature is expected. Once there is a significant fouling layer filling the undulation in the wall, changes in h have only a minor effect on the geometry of the yielded flow region. In other words the flow selects the shape of the yielded region close to the widest part of the channel, independent of the depth of the fouling region behind the

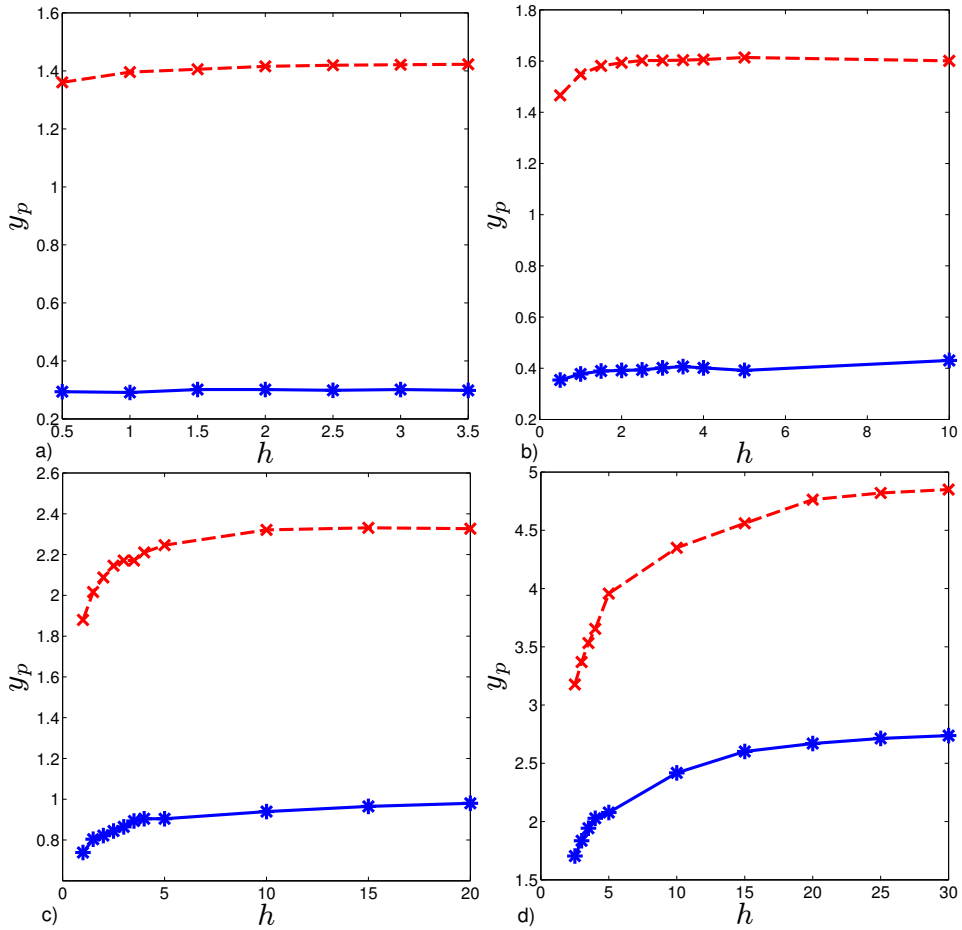

Figure 2.11: Positions $y = y_p$ of the two yield surfaces in the widest part of the channel: a) $\delta = .5, B = 2$; b) $\delta = .25, B = 10$; c) $\delta = .125, B = 10$; d) $\delta = .05, B = 10$.

yield surface.[3] This self-selection of the flow region is further illustrated in Fig. 2.12. Although the channel shape is significantly different the yielded flow region selected in each case is quite similar.

If the idea of self-selection of the (yielded) channel shape is correct, we might expect some kind of similarity scaling of the flow variables to be recovered in the widest part of the channel. Let us denote the width

[3]Strictly, this description applies only to $B \sim O_S(1)$ and we will explore $B \ll 1$ later.

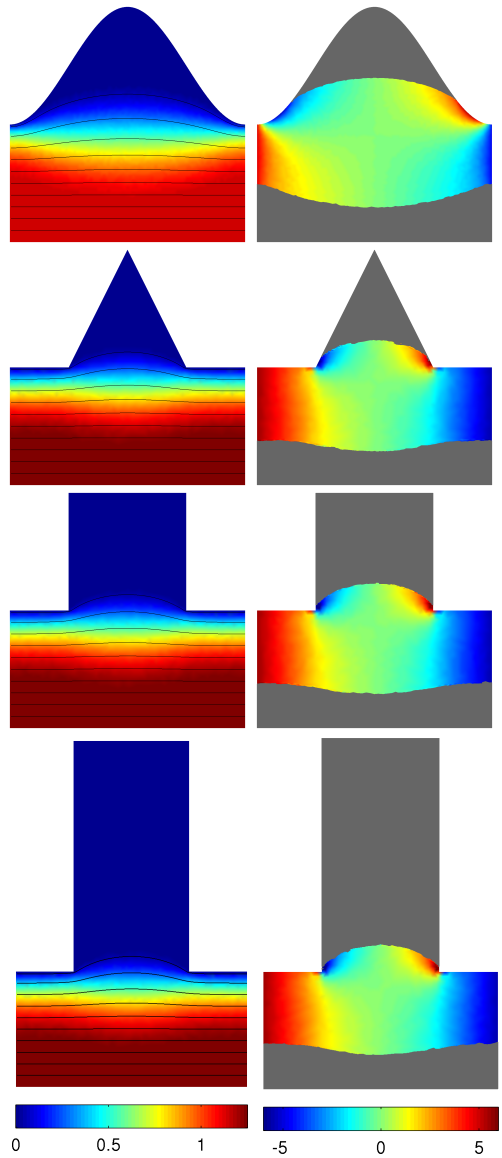

Figure 2.12: comparison of wavy wall flow ($\delta = .5, h = 1, B = 2$) with a triangular and rectangular walls, left panel: speed, right panel: pressure, The same color scale is valid for each column. The dark lines in the left panel are the streamlines, gray regions in right are plugs.

of the central plug by y_{pc} and the position of the second yield surface by $y = y_{pc}+2d_0$, i.e. the width of yielded layer at the widest part of the channel is $2d_0$. Once $h > h_f$ and the shape of the fouling layer becomes established, it follows that $\hat{D}$ is no longer the appropriate length-scale for the flow. Instead we may expect $\hat{D}(y_{pc} + 2d_0)$ to be the relevant length-scale. In Stokes flow the solution is generally dependent only on the Bingham number, so now we redefine

$$\tilde{B} = B(y_{pc} + 2d_0) = \frac{\hat{\tau}_Y \hat{D}(y_{pc} + 2d_0)}{\hat{\mu}\hat{U}_0}. \tag{2.21}$$

In terms of the new length-scale, the dimensionless ratio of yielded to unyielded fluid in the channel of maximum width $\hat{D}(y_{pc} + 2d_0)$ is ω:

$$\omega = \frac{2d_0}{y_{pc} + 2d_0}. \tag{2.22}$$

i.e. $(1 - \omega)$ is the scaled central plug width. Figure 2.13 plots ω against $\tilde{B}$ for each of our computations that have a fouling layer. As expected from the above discussion, at each δ the computed ω collapse onto a curve, dependent only on $\tilde{B}$. At $\tilde{B} = 0$ we have $\omega \to 1$ and $\omega(\tilde{B})$ asymptotes to a constant plateau at large $\tilde{B}$ (as far as our data suggest). The dependence on δ is rather weak and interestingly, the largest yielded ratios are observed at intermediate δ. We have no insights into why this might be.

We now focus on the yielded region between central plug and fouling layer, in an effort to gain insight into the flow structure. Figure 2.14 shows the same solution as in Fig. 2.4, (parameters: $\delta = .05$, $B = 10$, $h = 4$), but zoomed in close to the yielded part of the flow. Qualitatively similar solutions are obtained for other parameters. There is considerable symmetry in the flow, about the centreline of the yielded layer, evident in both velocity and stress fields.

Most interesting is the observation that $\sigma_{yy} \approx 0$ throughout this region. Note from Fig. 2.4 that the net pressure drop along the channel is approximately 80 for these parameters, yet this is largely focused in the narrow part of the channel. The consequence of $\sigma_{yy} \approx 0$ is that $p \approx \tau_{yy} = -\tau_{xx}$ at leading order. We also note that the main variation τ_{xy} appears to be with

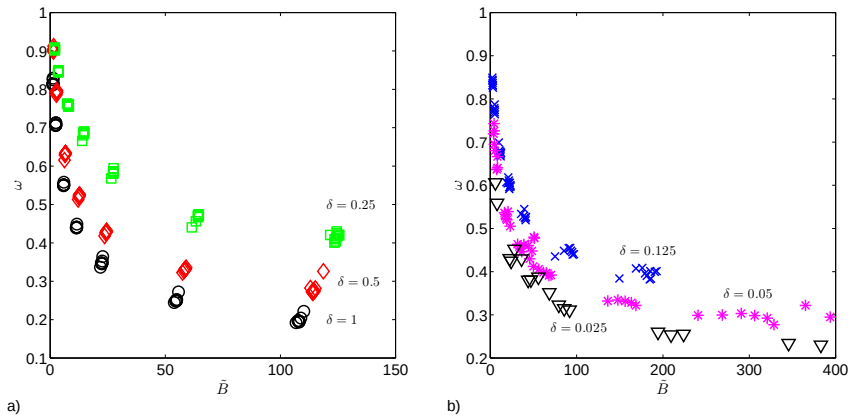

Figure 2.13: Ratio of yielded fluid, ω, plotted against $\tilde{B}$: a) $\delta = 1,\ 0.5,\ 0.25$; b) $\delta = 0.125,\ 0.05,\ 0.025$.

y, across the yielded region. We now consider the form of the solution based on these observations. First let us shift to a coordinate system based at the midpoint of the yielded region at the widest part of the channel and scaled with d_0:

$$\bar{x} = \frac{x - \frac{1}{2\delta}}{d_0}, \qquad \bar{y} = \frac{y - y_p c - d_0}{d_0}. \tag{2.23}$$

We rescale the stresses, pressure and Bingham number also with d_0: $\bar{\tau}_{ij} = d_0 \tau_{ij}$, $\bar{p} = d_0 p$, $\bar{B} = d_0 B$.

At $\bar{x} = 0$, the computational results suggest a shear stress distribution of form: $\bar{\tau}_{xy} = -\bar{B}[1 + a(1 - \bar{y}^2)]$, for some a. But there is also a weaker $\bar{x}$-dependency. Since the yielded region is observed to become narrower away from the widest part of the channel, and due to the expected symmetry at $\bar{x} = 0$, we assume the following form:

$$\bar{\tau}_{xy} = -\bar{B}[1 + a(1 - \bar{y}^2 - F(\bar{x}))] \tag{2.24}$$

where $F(\bar{x})$ is a positive even function of $\bar{x}$, vanishing at $\bar{x} = 0$. The pressure

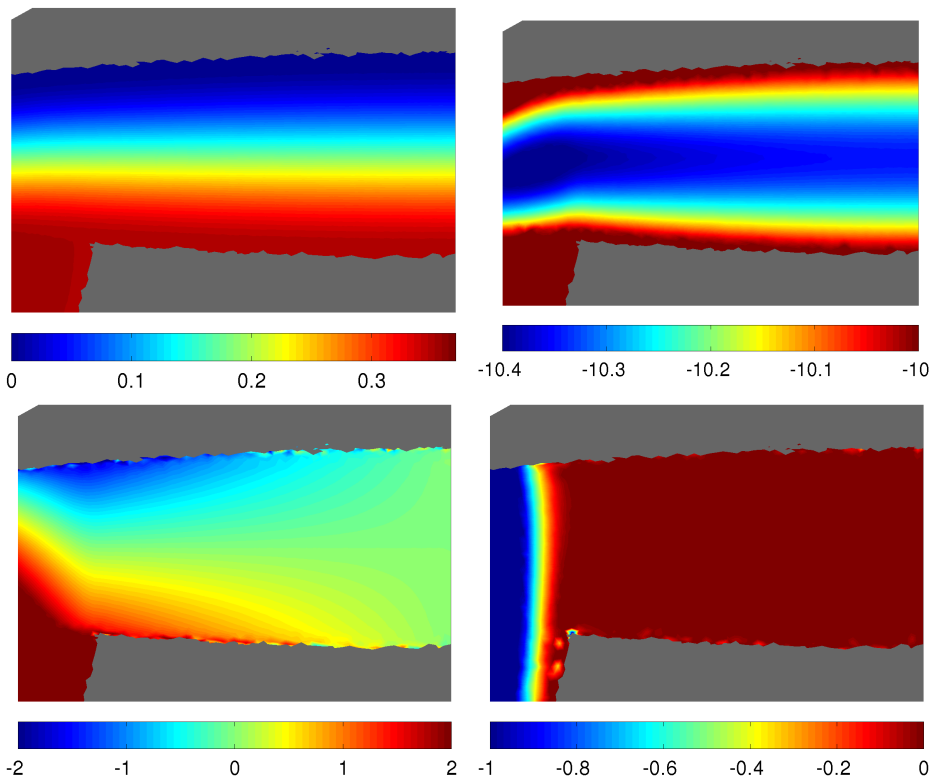

Figure 2.14: Detail of the yielded layer at the widest part of the channel for $(h = 4, \delta = .05, B = 10)$, (see also Fig 2.3). Left panel, from top to bottom shows (U_x, P). Right panel from top to bottom shows (τ_{xy}, σ_{yy}).

and extensional stress must adopt the forms:

$$\bar{p} = \bar{B}a\bar{y}\left[\bar{x} + \frac{1}{2}\frac{dF}{d\bar{x}}\right] \tag{2.25}$$

$$\bar{\tau}_{xx} = -\bar{B}a\bar{y}\left[\bar{x} - \frac{1}{2}\frac{dF}{d\bar{x}}\right]. \tag{2.26}$$

With this form of stress field, the yield surfaces are where: $\bar{\tau}_{xy}^2 + \bar{\tau}_{x2}^2 = \bar{B}^2$, i.e. where

$$[1 + a(1 - \bar{y}^2 - F(\bar{x}))]^2 + a^2\bar{y}^2\left[\bar{x} - \frac{1}{2}\frac{dF}{d\bar{x}}\right]^2 = 1.$$

We observe that firstly only $\bar{y}^2$ is determined by this equation and secondly that the yield surface positions are even functions of $\bar{x}$, as suggested by Fig. 2.4.

The constant parameter a we may determine via the solution at $\bar{x} = 0$. Since $\bar{\tau}_{xx} = 0$, we find that:

$$\frac{\partial u}{\partial \bar{y}} = -a\bar{B}(1 - \bar{y}^2), \qquad \Rightarrow \qquad u(0, \bar{y}) = a\bar{B}[1 - \bar{y} + \frac{\bar{y}^3 - 1}{3}].$$

The speed of the central plug is $u_{plug} = u(0, -1) = 4a\bar{B}/3$ and the parameter a is given by the condition that the mean flux through the half-channel is 1:

$$\frac{1}{d_0} = \bar{y}_{pc}u(-1) + \int_{-1}^{1} u(\bar{y})d\bar{y} = \frac{4a\bar{B}}{3}[\bar{y}_{pc} + 1], \tag{2.27}$$

where $\bar{y}_{pc} = y_{pc}/d_0$. Therefore,

$$a = \frac{0.75}{d_0\bar{B}(1 + \bar{y}_{pc})} \Rightarrow a(\tilde{B}, \omega) = \frac{0.75}{d_0\tilde{B}(1 - 0.5\omega)}. \tag{2.28}$$

Figure 2.15 plots the parameter $a(\tilde{B}, \omega)d_0$ for all our computed data with fouling layers. The data collapses in the form $a \approx f(\tilde{B})/d_0$.

Potentially now we might try to construct the function $F(\bar{x})$ and to find the yield surface positions $\bar{y} = \pm\bar{d}(\bar{x})$. The yield surface position is slaved to the form of $F(\bar{x})$ by the condition the yield stress is attained at the yield surface:

$$0 = [1 + a(1 - [\bar{d}(\bar{x})]^2 - F(\bar{x}))]^2 + a^2[\bar{d}(\bar{x})]^2 \left[\bar{x} - \frac{1}{2}\frac{dF}{d\bar{x}}\right]^2 - 1. \tag{2.29}$$

Two conditions are obvious for $F(\bar{x})$. Firstly, at any $\bar{x} \neq 0$, the velocity must attain the plug speed $u_{plug} = 4a\bar{B}/3$ at $\bar{y} = -\bar{d}(\bar{x})$. The velocity gradient is:

$$\frac{\partial u}{\partial \bar{y}} = \left(1 - \frac{\bar{B}}{\bar{\tau}}\right)\bar{\tau}_{xy}.$$

Since, $\bar{\tau} = [\bar{\tau}_{xy}^2 + \bar{\tau}_{xx}^2]^{1/2}$ and $\bar{\tau}_{xy}$ are even functions of $\bar{y}$, it follows that $[u(\bar{x}, \bar{y}) - u(\bar{x}, 0)]$ is an odd function of $\bar{y}$. Taking into account the symmetry

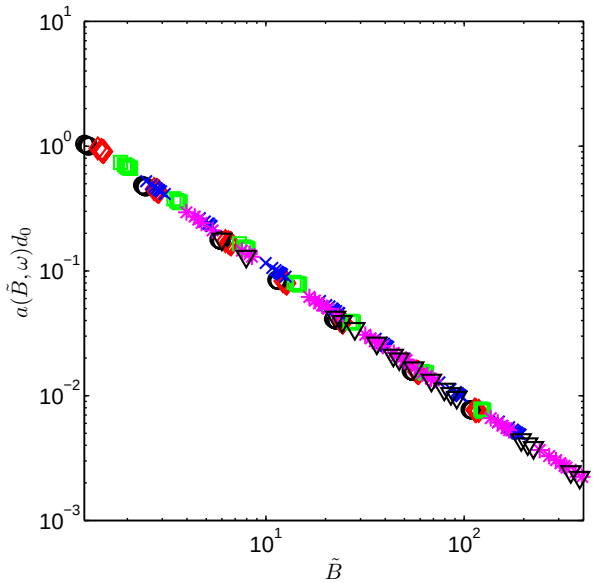

Figure 2.15: The parameter $a(\tilde{B},\omega)d_0$ from our computed data with fouling layers. The symbols are for different δ, following the key in Fig. 2.13.

of u, we can write the condition on the plug speed as:

$$\int_0^{\bar{d}(\bar{x})} \left(1 - \frac{\bar{B}}{\bar{\tau}}\right) \bar{\tau}_{xy} \; d\bar{y} = -\frac{2a\bar{B}}{3}. \tag{2.30}$$

We note that this is effectively a first order differential equation for $F(\bar{x})$ as the first derivative of $F(\bar{x})$ appears in $\bar{\tau}_{xx}$.

A second condition on $F(\bar{x})$ comes from mass conservation: all of the fluid must flow within the region bounded by the fouling yield surface at $\bar{y} = \bar{d}(\bar{x})$. Suppose that we have $F(\bar{x})$ and $\bar{d}(\bar{x})$ satisfying (2.29) and (2.30).

Then, in order to conserve the volume flux along the channel, we need:

$$\begin{aligned}
\frac{1}{d_0} &= \int_{-\bar{y}_{pc}-1}^{\bar{d}(\bar{x})} u(\bar{x},\bar{y})\ dy = u(\bar{x},-\bar{d}(\bar{x}))[\bar{y}_{pc}+1-\bar{d}(\bar{x})] + \int_{-\bar{d}(\bar{x})}^{\bar{d}(\bar{x})} u(\bar{x},\bar{y})\ d\bar{y} \\
&= \frac{4a\bar{B}}{3}[\bar{y}_{pc}+1-\bar{d}(\bar{x})] + 2\bar{d}(\bar{x})u(\bar{x},0) + \int_{-\bar{d}(\bar{x})}^{\bar{d}(\bar{x})} [u(\bar{x},\bar{y})-u(\bar{x},0)]\ d\bar{y} \\
&= \frac{4a\bar{B}}{3}[\bar{y}_{pc}+1-\bar{d}(\bar{x})] + 2\bar{d}(\bar{x})\frac{2a\bar{B}}{3} + 0 = \frac{4a\bar{B}}{3}[\bar{y}_{pc}+1] \qquad (2.31)
\end{aligned}$$

Remarkably, this condition is already satisfied. Therefore, it suffices to attain the true plug speed at $\bar{y} = -\bar{d}(\bar{x})$ in order to satisfy the flow constraint. This is essentially due to the symmetry properties of the assumed solution.

We have not proceeded further than this. Although in principle one could substitute from (2.29) for $\bar{d}(\bar{x})$ and then unravel (2.30) to produce the first order differential equation for $F(\bar{x})$, it does not appear straightforward to solve. Both $F(\bar{x})$ and the first derivative vanish at $\bar{x} = 0$, suggesting some indeterminacy. Note also that the equations are still effectively parameterised by $\bar{y}_{pc}$ and $\bar{B}$, which are not determined. Although results such as Fig. 2.15 suggest strong similarity properties these are derived *empirically* from the computation, rather than determined *a priori*. It is still unclear how $\bar{y}_{pc}$ and $\bar{B}$ are determined. Possibly, having determined the solution and shape of the central plug region, one could formulate a momentum balance on the plug (one condition) and impose continuity of velocity with the pseudo-plug region immediately preceding (second condition).

2.3.5 Complexity of the Newtonian limit

The results shown so far have not considered the Newtonian limit, $B \to 0$. The precise Newtonian flow has not to our knowledge been studied for $h \sim O_S(1)$. However, Pozikridis [193] studies a similar flow with one wavy wall and one plane wall, using a boundary element method. We can infer that our results, when both walls have symmetric undulations, should be at least qualitatively similar to those of [193]. Pozikridis finds instead of stationary regions that recirculatory vortices appear for sufficiently large

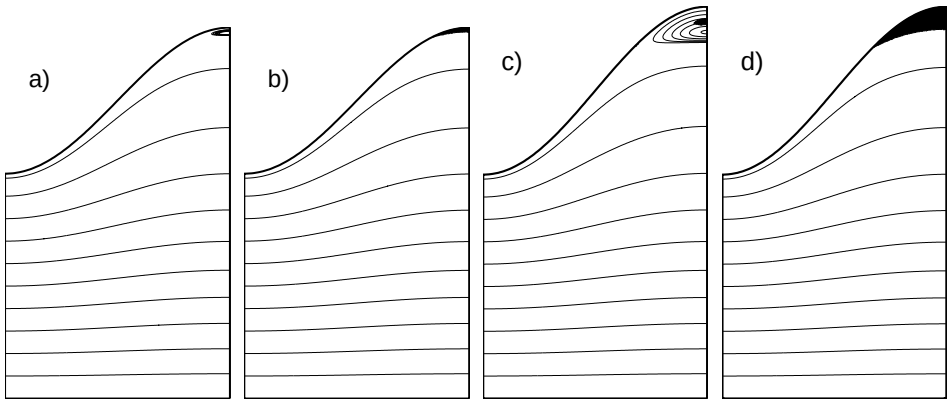

Figure 2.16: Streamlines and unyielded regions for a) Newtonian flow ($h = .65,\ \delta = .5$) where recirculation has just begun; b) same channel but now with $B = .01$; c) same B as b) but now h is increased to $h = 0.75$; d) same channel as c) but B is increased to $B = .04$.

$h\delta$. The critical values, say $(h\delta)_N$, now depend on δ. The limit $\delta \to 0$ finds $(h\delta)_N \approx 0.56$ and this decreases, asymptoting to a constant lower limit at large δ; e.g. for $\delta \approx 1$, $(h\delta)_N \approx 0.28$. Pozikridis [193] also compares his computed results against a first and second order perturbation theory prediction, neither of which produce quantitatively good predictions. For $h\delta > (h\delta)_N$, when the undulation is sufficiently deep, the Newtonian flow can have secondary vortices forming. An analogy can be formed between these flows and the classical corner vortex flows studied earlier by Moffatt [166]. As with Moffatt's vortices the length-scale and intensity of the eddies decay significantly with each successive vortex.

From the perspective of fouling and trapping fluid, we can consider recirculation as analogous to the onset of fouling, although the trapped Newtonian fluid is not static. At the onset of recirculation we do have $\tau_{xy} = \tau_{xx} = 0$ at the wall in the widest part of channel, suggesting that in the same geometry a Bingham fluid $B \approx 0$ would have a fouling layer appearing. Indeed, we can consider the Newtonian solution as the zero-th order term in a small B perturbation expansion for the Bingham fluid solution. Figure 2.16 explores some of the features of small B flows at $\delta = 0.5$. First of all, Fig. 2.16a

shows the Newtonian onset of recirculation, for $h \approx 0.65$, where we observe a very small vortex close to the upper wall. It is worth commenting that (at least for $\delta = 0.5$) the critical value of $(h\delta)_N$ appears close to that in [193]. This suggests that for Stokes flow the effects of the shape of the opposite wall are not critical in determining onset of recirculation.

As expected, the deviatoric stresses are close to zero at onset and we see that for a small $B = 0.01$ there is a small static layer in the same geometry (Fig. 2.16b). On increasing h to $h = 0.75$ we get the flow of Fig. 2.16c, in which the fouling layer has not survived! Instead we observe a vortex with a plug close to the centre. Initially this may look strange, but note that a zero strain rate is associated with the centre of the vortex, not with the point on the wall. As we increase h past its critical value for recirculation τ_{xy} becomes positive at the wall in the Newtonian solution. Although $|\tau_{xy}|$ is still much less than the bulk flow stresses $(\frac{\hat{\mu}\hat{U}_0}{\hat{D}})$, it can be sufficient to break the yield stress $\hat{\tau}_Y$, i.e. provided $B \ll 1$. On increasing the yield stress sufficiently ($B = 0.04$), we get Fig. 2.16d where the fouling layer is present again.

As in [193], as we increase h a second vortex appears in our computed Newtonian flow, as illustrated in Fig. 2.17a. Presumably these are also similar to Moffatt's vortices, [166]. Figures 2.17b-f show the same flow geometry but for an increasing sequence of B. Even for $B = .001$ the second vortex is replaced by a fouling layer (Fig. 2.17b). It is worth recalling that although both length and intensity of the Moffatt vortices decreases exponentially with successive generations, the intensity decrease is significantly larger (typically by a factor $\sim 10^3$). The deviatoric stress would follow a similar scaling and thus, it is hardly surprising that even for $B = .001$ there is no motion.

The transition in the primary vortex in Figs. 2.17b-f is also interesting. The small plug region at the vortex centre grows progressively with B (Figs. 2.17b-d). A small plug grows out from the stagnation point at the wall as both vortex plug and fouling layer approach each other (Fig. 2.17e). Finally, the yield stress is sufficient ($B = 0.13$) to extinguish flow even in the primary vortex (Fig. 2.17f).

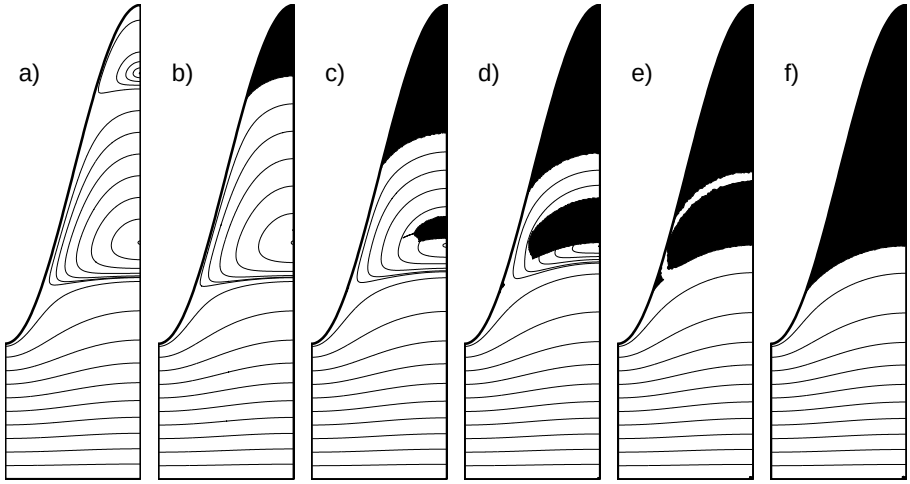

Figure 2.17: Streamlines and unyielded regions for $(h = 2.5, \delta = .5)$ and a) Newtonian flow b) $B = .001$ c) $B = .05$ d) $B = .09$ e) $B = .12$ f) $B = .13$

In conclusion, the Newtonian limit of this problem is rather interesting. Theoretically in a sharp-cornered wedge, we would expect to find an infinite number of vortices and hence an infinite number of small centre-vortex plugs should be possible as $B \to 0$. However, as the vortex intensity decays exponentially these will be difficult to capture computationally. Although we were only able to compute 2 generations of vortices, with a better resolution and a sharper/deeper wall undulation, we can expect to find further generations. With care, it is likely that the small B solutions could be computed with a second vortex (or perhaps approximated by a perturbation method). Finally, it is emphasized again that these flow regimes only happen for small B. When $B = \frac{\hat{\tau}_y}{\hat{\mu}\hat{U}_0/\hat{D}} \sim O_S(1)$ the yield stress is of the order of the bulk flow viscous stresses. The viscous stresses in the secondary flow zone are an order of magnitude smaller than the bulk flow viscous stresses, meaning for $B \sim O_S(1)$ insufficient stress is generated by the secondary flow and the recirculation zones become static.

2.4 Discussion and summary

In this initial chapter of the thesis, we have shown that slow flows of Bingham fluids through wavy-walled channels develop fouling layers if the amplitude of the wall perturbation h exceeds some critical value h_f. The fouling layer appears first at the widest part of the channel and is apparently unrelated to whether or not the central plug region is broken or intact. The main mechanism responsible for the onset of fouling is the influence of the geometry on the extensional stresses. At the widest part of the channel we find that τ_{xx} increases with x when close to the central plug, but τ_{xx} decreases with x close to the wall upper wall. This effect allows τ_{xy} to increase with y close to the upper wall, which is necessary for the fouling layer to form.

We have systematically studied the results of approximately 500 computations, largely covering the parameter space of (B, h, δ). Qualitatively, 4 types of flow can be distinguished (fouling or no fouling; broken plug or intact plug) and we have presented a new understanding of where these different regimes can be found. Perhaps surprisingly, for $\delta \sim O_S(1)$ intact central plugs are more prevalent that in the limit $\delta \to 0$. In the latter case, extensional stresses break the central plug before fouling occurs. Provided $B \sim O_S(1)$, if fouling occurs at (B, h, δ), then larger values of the 3 parameters also have fouling layers.

Regarding onset of fouling, our data suggests that this occurs at a value of $h\delta$ that varies mainly with B, but there is also some weak variation with h and δ. We have been able to characterise our results by two curves: $h\delta_s = g(B)$ and $h\delta_n = f(B)$, describing sufficient and necessary conditions for fouling, respectively. The fitted expressions are given in equations (2.19) & (2.20), valid within the range of our data $B \lesssim 10^2$. These fitted expressions suggest that at large B, there are constant values of $h\delta$ (independent of B) describing sufficient and necessary conditions for fouling. This has the interesting consequence that certain geometries will not have fouling layers in the widest part of the channel, even as $B \to \infty$. This interesting limit is studied more explicitly in Chapter 3, as it corresponds to the limit of zero flow along the channel: a fact hidden by the scaling adopted here.

At moderate B, as h is increased beyond h_f, further changes to the shape of the fouling layer are minimal. The fluid effectively selects the shape of the flowing region. Computations with different shapes of wall perturbation can tend to give very similar fouling layer shapes, at least in the widest part of the channel. The flow here is characterised by $\sigma_{yy} \approx 0$. We have attempted to understand the solution structure and selection mechanism, but a complete understanding eludes us. Re-scaling the flow variables with the width of the flowing fluid in the widest part of the channel shows a high degree of self-similarity in determining the yielded flowing region and the plug speed, (Figs. 2.13 & 2.15), but still leave undetermined parameters.

The limiting case of $B \to 0$ has also been examined. The flow analogy for this limiting case is with the onset of recirculation for a Newtonian fluid. For small enough B, as h increases beyond h_f, we can find cases of recirculation of the Bingham fluid. On increasing h still further a series of decaying vortices can be found for $B = 0$. The intensity of the Newtonian vortices decays rapidly with each successive vortex. Thus, for $B > 0$ we have found that secondary vortices tend to become stagnant even for very small B.

Qualitatively, we might expect very similar results for other common yield stress fluid models (Casson, Herschel-Bulkley, etc). The geometry considered here has a high degree of symmetry and there are many other wavy-walled variants that merit attention. For example, for well cementing applications, one wall planar and one wall uneven would correspond to a washout geometry (see Chapter 4). In porous media/fractures & cracks, it might be interesting to offset the sinusoidal variations to produce tortuous channels and/or to consider more complex geometries, avenues pursued to some extent in Chapter 3. On top of these interesting avenues, the effects of including inertia in computations of flows along such geometries may be significant (see Chapter 5) and eventually many industrial applications in the oil & gas industry involve displacement by another fluid (studied in Chapter 6).

Chapter 3

Flow of yield stress fluids along fracture: pressure drop prediction and flow onset

There are many situations where non-Newtonian fluids flow through porous media, narrow fractures or cracks. A common way of approximating this type of flow is to build a closure law based on geometrically simpler structures. Thus, fibre bundle and similar lubrication/Hele-Shaw approximations are frequently used to derive laws that are extensions of the classical Darcy law. In considering only Newtonian fluids, non-Darcy effects can arise from geometrical complexity and are often corrected via a variety of methods. In non-Newtonian fluids, these same complexities still remain, but one encounters additional non-Darcy effects. Firstly, the nonlinear nature of the constitutive law naturally results in flow laws that mimic nonlinear filtration. The coupling of geometry to flow is generally more complex in these nonlinear relationships than for Newtonian flows. A second important effect in considering yield stress fluids occurs in fouling of the pore-space/fracture, i.e. in regions of the domain in which the fluid remains stationary, attached to the walls, as explored in Chapter 2. This can be viewed as a novel type of non-Darcy effect, the study of which is the focus of this chapter.

We explore firstly the limits of validity of standard lubrication/Hele-

Shaw approximations to the flow laws, showing that the range of geometries for which the approximation is effective is indeed limited to small aspect ratios H/L. Included in this part of the study is the effect of the onset of fouling, at intermediate yield stresses (captured in the Bingham number B). Fouling leads to $O(1)$ errors in predicting the flow-rate vs pressure drop relationship, due to self-selection of the flowing domain. We then show how this can be corrected for if the fouled geometry is known. Next we focus on the critical limit of zero flow as the yield stress is increased (equivalently the pressure drop decreased). We derive a theoretical characterization of this limit, explore limiting asymptotic behaviours in short and long fractures, and derive a simplistic toy model that is able to approximate the computed critical limit remarkably effectively over a wide range of fracture aspect ratios. For more complex fractures we make less progress, but may infer that the limiting process could be approximated effectively provided the fouling phenomenon is better understood.[1]

3.1 Introduction

Many complex fluids used in industrial applications exhibit yield stress behaviour, e.g. polymers, colloidal suspensions, foams, cement slurries, paints, muds, heavy oil [66], and flows are actively studied from theoretical, rheological and experimental perspectives; [21, 67]. Here we are concerned with the flow of such fluids in natural rocks, both in porous media and along fractures. Interest in the flow characteristics of non-Newtonian fluids in these settings dates back at least 50 years, e.g. [187, 215]. Much of the early work is summarised in the text by [22], and particularly the large body of Soviet-era research.

Yield stress fluid interest initially stemmed from the production of heavy oils that exhibit a limiting pressure gradient (nonlinear filtration) and more recently from enhanced oil recovery operations, e.g. [188]. Sealants are routinely injected into brickwork to block the spread of moisture in old buildings

[1] A version of this chapter has been submitted for publication to *J. Fluid Mech.* in December 2015 and is under review: A. Roustaei, T. Chevalier, L. Talon & I. Frigaard. "Non-Darcy effects in fracture flows of a yield stress fluid.".

(a damp-proof course). Cement injection into porous media is advocated as a means of sealing CO_2 storage reservoirs. Cement slurries and drilling fluids flow along uneven narrow eccentric annuli in the primary cementing process. In the squeeze cementing process oil & gas wells are repaired by injecting cements and other thin slurries into thin cracks; see [176]. Injection of yield stress fluids has also been proposed as a potential method for porosimetry by [11]. In hydraulic fracturing operations, some frac fluids used have a yield stress (designed in order to enhance proppant transport). At the end of hydraulic fracturing, the flowback phase attempts to clean the gelled fluids from the proppant laden fracture. Thus, we see that many different industrial processes are concerned with these flows.

Consequently, the determination of a constitutive law to relate the flow rate to the applied pressure in porous or fractured materials has been the subject of many investigations in the past, e.g. [4, 15, 16, 52, 56, 57, 62, 187, 215, 223, 227]. However, this remains a challenging and sometimes controversial issue; see [35]. Based on experimental observations [4, 53, 57, 187], the common constitutive law proposed in the literature between the flow rate and the applied pressure has the following form:

$$\hat{Q} \propto (\Delta\hat{P} - \Delta\hat{P}_c)^n,$$

where $\hat{Q}$ is the mean flow rate, n is the Herschel-Bulkley power law index and $\Delta\hat{P}_c$ is a minimal limiting pressure drop, below which there is no flow.

However, theoretical models and direct simulations [56, 59, 210, 212, 228, 229] have revealed that the presence of heterogeneities in the porous medium can induce a complex dependence of the flow rate with the pressure. Since each flow path experiences different heterogeneous pore throats, their critical opening pressures are different. As a result, the disorder of the porous media induces a hierarchy in the flow paths that open, leading to a non-trivial relationship between the flow rate and the applied pressure drop; see [59, 228].

A rather simple approach to model the flow in porous media is the so-called "fibre bundle model" [56, 75], where the material is considered as a

succession of parallel tubes, each with a uniform throat (i.e. cross-sectional area). This model has the advantage of being easily solved because the constitutive equation and the critical pressure is known in each throat. The major drawback is of course that it neglects the influence of heterogeneity along each flow path, which can be non-trivial. It is therefore crucial to better investigate flows along a single channel with spatially varying width (or equivalently a tube of varying cross-section for 3D porous media), in order to better understand the flow in both porous media and in rough 2D fractures.

As with the Newtonian case, the most classical approach is to assume a lubrication or Hele-Shaw approximation [88, 106, 154, 205], i.e. the mean flow is driven by uniform pressure gradient along the varying gap. This approach has been long exploited in the modelling of laminar primary cementing flows, e.g. [33, 189]. After some algebra involving the solution of the Buckingham-Reiner equation, the flow rate can the be related to the local width of the gap. In a single rough channel [227] show that the critical pressure is proportional to the harmonic mean of the gap width and the flow-pressure relationship is related to a series of power-means. In non-uniform Hele-Shaw geometries the critical pressure is local and the fluid flows preferentially, e.g. in the eccentric annular cementing flows of [33, 189] the widest part of the annulus can flow while the narrowest part is stationary.

While the Hele-Shaw/lubrication approach can be straightforwardly applied to randomized varying gap widths, it has been long recognised that to do so may result in significant error where yield stress fluids are concerned. First of all, one faces the usual geometric restrictions of slow geometric variation that are likely to be invalid for many fractures. Secondly, as demonstrated by [146], straightforward application of Hele-Shaw/lubrication scaling arguments leads to an apparent contradiction in the leading order flow solutions. Although this inconsistency has long since been resolved in different geometries [17, 199, 246], the leading order stress fields exhibit an $O(1)$ deviation from those of the naïve Hele-Shaw/lubrication approach. This discrepancy is due to extensional stresses that develop within the (initially unyielded) central plug eventually causing it to break; see [102, 199].

While plug-breaking occurs for relatively modest heterogeneities that would normally allow for lubrication approaches to retain validity, larger amplitude heterogeneity leads to the emergence of so-called "fouling layers" at the walls of the duct, in which residual fluid is held stationary by the yield stress. This geometric effect has been observed scientifically in various experimental and computational/analytical studies [35, 58, 79, 208, 209], as well as being an everyday observation for those who spread butter/margarine on Ryvita or adhesive on the back of ceramic bathroom tiles. [208] demonstrate that as the heterogeneity amplitude increases at fixed yield stress, fouling occurs beyond a critical amplitude and give an empirical prediction for the onset of fouling; (see Chapter 2). Such predictions are however strongly dependent on the specific geometry, e.g. in the abrupt expansion of [79] fouling occurs first in the corners, whereas for the smooth geometries of [208], fouling is first found in the deepest part of the channel.

The most important result, from the perspective of predicting flow rate-pressure drop relationships, is that fouling results in self-selection of an $O(1)$ variation of the flowing geometry [209], which should therefore have an $O(1)$ effect on such relationships. However, such phenomena have not been systematically studied from the perspective of flow rate-pressure drop. This is one of the objectives of this chapter. In particular, we have the objective of understanding and quantifying the flow onset problem, i.e. in a given section of an uneven fracture what is the critical pressure drop at which the fluid begins to flow? Other objectives are to examine the ranges of fracture amplitude to fracture length for which lubrication/Hele-Shaw type scaling remains valid and to begin to explore how to apply these results to fracture geometries of high complexity.

A plan of the chapter is as follows. In §3.2 following we present the model problem and fracture geometries that we consider in this chapter, scale the corresponding equations, give an overview of the computational method and present example results. This is followed in §3.3 by a systematic comparison of the flow rate-pressure drop relationships from the computations, with those from a naïve lubrication approximation, including some methods to improve the approximations in the situation where fouling occurs. Section

3.4 focuses on analysis of the critical limit of zero flow, both from mathematical and computational perspectives. This is largely focused at characterizing the limiting flows in simple fracture geometries, although insights are also gained from these results for more complicated and realistic fractures. The chapter closes with a discussion of the main results and future directions.

3.2 Model setup

Figure 3.1 shows the flow geometry and notation used in the current study. We assume a fracture of nominal minimal width $2\hat{D}$, with walls located at $\hat{y} = \pm[\hat{D} + \hat{Y}_{\pm}(\hat{x})]$, where $0 \leq \hat{Y}_{\pm}(\hat{x}) \leq \hat{H}$. Both walls and the flow are assumed to be periodic in $\hat{x}$ with period $\hat{L}$. The periodic fracture cell is assumed to be filled with a yield stress fluid (assumed a Bingham fluid for simplicity), that is flowing slowly in Stokes flow. The Stokes equations are made dimensionless using $\hat{D}$ as length-scale. As we wish to understand how Darcy law type behaviour is modified geometrically and rheologically, we are interested in the mapping from flow rate (mean velocity) to pressure drop (and vice versa).

In a fracture of varying width the flow rate $\hat{Q}$ is constant and the pressure gradient varies along the flow direction. An imposed flow formulation will be adopted. Let $\hat{U}_0$ denote the mean velocity along the fracture, defined at the minimum fracture width, i.e. $\hat{U}_0 = \hat{Q}/2\hat{D}$, which is used to scale the velocity. The shear stresses are scaled with $\hat{\mu}\hat{U}_0/\hat{D}$, where $\hat{\mu}$ is the plastic viscosity of the Bingham fluid. Any static pressure component is subtracted from the pressure, before also scaling with $\hat{\mu}\hat{U}_0/\hat{D}$. The resulting equations are:

$$0 = -\frac{\partial p}{\partial x} + \frac{\partial}{\partial x}\tau_{xx} + \frac{\partial}{\partial y}\tau_{xy}, \tag{3.1}$$

$$0 = -\frac{\partial p}{\partial y} + \frac{\partial}{\partial x}\tau_{xy} + \frac{\partial}{\partial y}\tau_{yy}, \tag{3.2}$$

$$0 = \frac{\partial u}{\partial x} + \frac{\partial v}{\partial y}, \tag{3.3}$$

where $\mathbf{u} = (u, v)$ is the velocity, p is the modified pressure and τ_{ij} is the

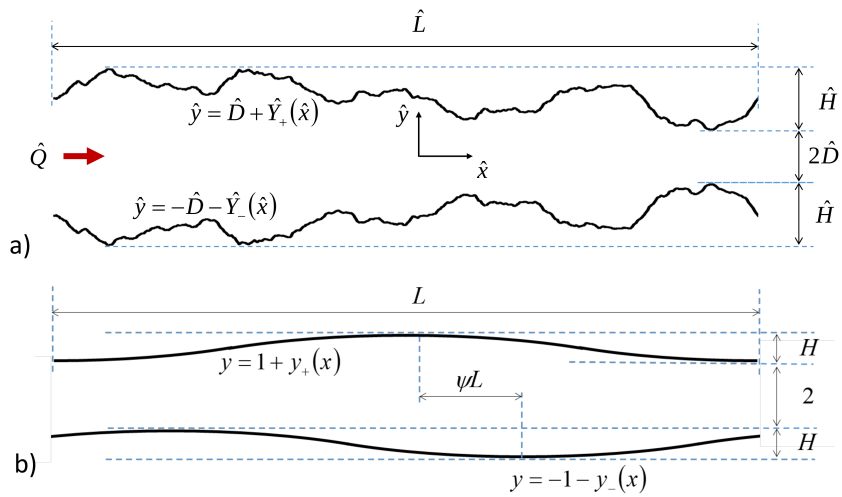

Figure 3.1: a) Schematic of the fracture geometry showing dimensional parameters; b) schematic of the wavy-walled dimensionless geometry, with lower wall shifted to the right by ψL.

deviatoric stress tensor. The scaled constitutive laws are:

$$\tau_{ij} = \left(1 + \frac{B}{\dot{\gamma}(\mathbf{u})}\right)\dot{\gamma}_{ij} \iff \quad \tau > B \tag{3.4a}$$

$$\dot{\gamma}_{ij}(\mathbf{u}) = 0 \iff \quad \tau \leq B, \tag{3.4b}$$

where

$$\dot{\gamma}_{ij}(\mathbf{u}) = \frac{\partial u_i}{\partial x_j} + \frac{\partial u_j}{\partial x_i}, \qquad \mathbf{u} = (u, v) = (u_1, u_2),\ \mathbf{x} = (x, y) = (x_1, x_2).$$

and $\dot{\gamma}$, τ are the norms of $\dot{\gamma}_{ij}$, τ_{ij}, defined as

$$\dot{\gamma} = \sqrt{\frac{1}{2}\sum_{ij}\dot{\gamma}_{ij}^2} \qquad \text{and} \qquad \tau = \sqrt{\frac{1}{2}\sum_{ij}\tau_{ij}^2}. \tag{3.5}$$

A single dimensionless number appears above, the Bingham number, B:

$$B \equiv \frac{\hat{\tau}_Y \hat{D}}{\hat{\mu}\hat{U}_0}, \tag{3.6}$$

represents the competition between the yield stress $\hat{\tau}_Y$ and the viscous stresses. Two other geometric groups characterize the fracture shape: the dimensionless length $L = \hat{L}/\hat{D}$, and the maximal out of gauge depth, $H = \hat{H}/\hat{D}$; see Fig. 3.1.

No-slip conditions are satisfied at the upper and lower walls

$$\mathbf{u} = 0, \quad \text{at} \quad y = 1 + y_+(x) \quad \text{and} \quad y = -1 - y_-(x), \tag{3.7}$$

where $y_\pm(x) = \hat{Y}_\pm(\hat{x})/\hat{D}$. At the ends of the fracture we impose periodicity:

$$\mathbf{u}(-L/2, y) = \mathbf{u}(L/2, y), \qquad \tau_{ij}(-L/2, y) \quad = \tau_{ij}(L/2, y), \qquad p(-L/2, y) = p(L/2, y) + \Delta p, \tag{3.8}$$

$$2 = \int_{-1-y_-(x)}^{1+y_+(x)} u_1(x, y)\ \mathrm{d}y. \tag{3.9}$$

Here Δp denotes the frictional pressure drop, which is part of the solution and is determined by satisfying the flow rate constraint (3.9).

3.2.1 Fracture geometries

The dimensionless fracture wall shape $y_\pm(x)$ satisfy the bounds: $0 \leq y_\pm(x) \leq H = \hat{H}/\hat{D}$. We consider 2 generic simplified fracture geometries (sinusoidal walls and triangular walls) and a more complex affine geometry. An example affine geometry is shown schematically in Fig. 3.1a and the sinusoidal wavy fracture in Fig. 3.1b. The sinusoidal fracture widths are given by:

$$y_+(x) = \frac{H}{2}[1 + \cos(2\pi x/L)], \qquad y_-(x) = \frac{H}{2}[1 + \cos(2\pi[x/L - \psi])], \tag{3.10}$$

with $\psi \in [0, 1]$ denoting a phase shift of the lower wall relative to the upper, i.e. the lower wall is translated ψL to the right. The triangular geometry is

defined analogously.

In many applications it has been observed that fracture roughness may display self-affine correlations, [38, 155, 216]. A surface $\hat{y}(\hat{x})$ is self-affine if the probability to find the increment $\Delta\hat{y}$ after a distance $\Delta\hat{x}$ displays the scaling invariance:

$$p(\Delta\hat{y}, \Delta\hat{x}) = \lambda^{\zeta} p(\lambda^{\zeta}\Delta\hat{y}, \lambda\Delta\hat{x}),$$

where λ is any scaling factor and ζ is called the Hurst exponent. An important property of self-affine surfaces is that all the moments scale with the length of measurement as:

$$M_n(\hat{x}) = (\langle|\hat{y}(\hat{x}+\hat{x}_0) - \hat{y}(\hat{x}_0)|^n\rangle)^{1/n} \propto |\hat{x} - \hat{x}_0|^{\zeta}$$

For the present chapter, we have generated three types of fracture. In the first type, the two walls $y_{\pm}$ are independently generated with a Hurst exponent $\zeta = 0.5$ using a Fourier transform method (see [212, 226]). Both surfaces are scaled to have $\min y_{\pm} = 0$ and $\max y_{\pm} = H$. In the second type, we used $y_+ = y_-$. In the third type, we used $y_+ = -y_-$.

3.2.2 Computational overview

Numerical solution of viscoplastic fluids poses a unique challenge which is the singularity of the effective viscosity in the constitutive equation (3.4), where $\dot{\boldsymbol{\gamma}} \to 0$, (unyielded regions). Aside from such points, the Bingham fluid is simply a generalized Non-Newtonian fluid with an effective viscosity $\mu = (1 + \frac{B}{\dot{\gamma}(\mathbf{u})})$. A common work around to the singular effective viscosity is to simply *regularize* the viscosity, introducing a small parameter $\epsilon \ll 1$, such that the effective viscosity scales like ϵ^{-1} as $\dot{\boldsymbol{\gamma}} \to 0$. Many such regularizations are possible. It can be shown that as $\epsilon \to 0$ the velocity solution will converge to that of the exact Bingham fluid, but the stress field may not; see [101]. Consequently we may not infer the correct shape of yield surface from $\tau = B$, e.g. [247].

Instead we use the augmented Lagrangian (AL) method [99, 110], which

uses the proper variational formulation of the problem as formulated for example by [92]. The AL method introduces two new fields: the strain rate $\boldsymbol{\gamma}$ and stress $\mathbf{T}$, in addition to the velocity and pressure $(\mathbf{u}, p)$ of the original problem. In this way it relaxes the convex but non-differentiable velocity minimization problem to an associated saddle point problem. The saddle point problem is solved iteratively. Each iteration consists of 3 Uzawa split steps, to update $(\mathbf{u}^n, p^n)$, γ^n and T^n respectively. These iterations are repeated until $max\{|\boldsymbol{\gamma}^n - \dot{\gamma}(\mathbf{u})^n|_{L2}, |\mathbf{u}^n - \mathbf{u}^{n-1}|\} \leq 10^{-6}$ is satisfied, or a maximum number of iterations (here 10000) is reached. The $\boldsymbol{\gamma}, \mathbf{T}$ fields of the AL method converge respectively to the strain rate and deviatoric stress tensors of the exact Bingham flow.

We have implemented the AL method using the freely available FreeFEM++ finite element environment [118]. Our algorithm is based on that in [214] with the addition of a flowrate constraint. To satisfy the inf-sup condition, Taylor-Hood $(P2 - P1)$ elements are used for velocity and pressure. Linear discontinuous elements $P1_d$ are used for γ and $\mathbf{T}$ fields, to follow compatibility conditions between the velocity space and strain/stress spaces. Both velocity and pressure are implicitly solved and the system matrix is factorized once for all iterations. To improve the accuracy of the solution while keeping reasonable runtime, five cycles of the anisotropic mesh adaptation [36] is used. A typical computation starts with size of 8000-10000 mesh points. A new mesh is generated based on a metric computed from the current solution. We use the dissipation field as the metric which results in finer mesh around the yield surface. After the fifth cycle the mesh may contain up to 150,000 mesh points and the yield surfaces can be clearly identified by a much finer local mesh. More details of the numerical algorithm are presented in [208, 209] and skipped here for conciseness.

3.2.3 Example results

We have computed over 2000 flows, covering a wide range of H, L, B, for both triangular and wavy fracture profiles with different ψ. In addition we have computed a smaller number of flows in affine fracture geometries.

Before analyzing specific features of the flow, we present some examples to illustrate qualitative features of our results.

Figure 3.2 shows results from a relatively modest fracture geometry and yield stress rheology ($H = 1$, $L = 10$, $B = 2$). The top two rows show the triangular and wavy profiles for $\psi = 0$ (symmetric fracture). The flow is evidently symmetric about the centreline and widest part of the fracture. Unyielded plug regions are found at the symmetry points in x and close to the fracture centreline. There is very little difference, qualitatively or quantitatively, between triangular and wavy profiles. The bottom row shows the wavy profile at $\psi = 0.5$, where the lower wall is out of phase with the upper wall. Here the differences are quite significant. The velocity field appears to adapt smoothly to the wavy geometry, but no longer has the fastest fluid in the centre of each cross-section. Instead the fastest travelling fluid moves at larger radius of curvature, while the plug regions are displaced into each bend. Due to symmetry effects we observe a rather spectacular effect on the pressure field: the displaced central plug regions are joined by thin strands of unyielded fluid. It appears that the pressure is discontinuous across these strands, which is possible. Note however that the traction vector, defined by the normal to these strands, is continuous.

Figure 3.3 explores the effects of increasing the yield stress on the flow of Fig. 3.2 ($H = 1$, $L = 10$, $\psi = 0$). The flow of course remains symmetric and, since the flow rate is fixed, we only observe a relatively small change in the streamlines (left column) as B is increased. This however masks the changes that are occurring in the pressure and stress fields. Increasing B results in a widening of the plugs in both narrow and wide parts of the fracture (right column). The magnitude of the pressure field also increases with B: the flow rate is fixed and the pressure gradient therefore needs to overcome the yield stress everywhere along the fracture to ensure flow (hence p/B is shown to aid comparison). For $B \approx 10$ we observe that a region of stationary fluid emerges at the upper and lower walls, in the deepest part of the fracture. We refer to this as a fouling layer. The fouling layer grows in size as B increases. Growth of the fouling layer has effects on the pressure drop along the fracture and is an important part of the yield limit that is attained as

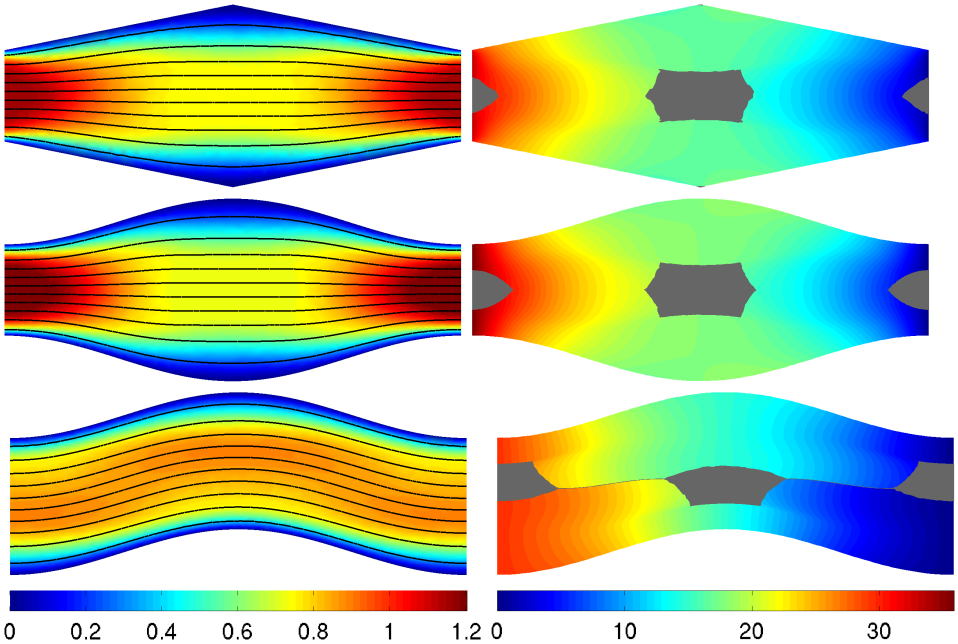

Figure 3.2: Computed examples of speed $|\mathbf{u}|$ & streamlines (left column), and pressure p with (gray) unyielded plugs (right column), at $H = 1$, $L = 10$, $B = 2$. Top row: triangular fracture profile, $\psi = 0$; middle row: wavy fracture profile, $\psi = 0$; bottom row: wavy fracture profile, $\psi = 0.5$.

$B \to \infty$, both of which are studied later; see §3.4.

Figure 3.4 explores the effects of increasing H on the flow illustrated in the last row of Fig. 3.2 ($B = 2$, $L = 10$, $\psi = 0.5$). The flow asymmetry is preserved as H is increased, together with the interesting unyielded fluid strands. The main observation is that, although the yield stress is maintained constant, the region of fouled fluid in the deepest parts of the fracture increases markedly with H. The increase in fouling has the interesting effect of reducing the tortuosity of the flowing region of fluid. This self-selection of the flowing area is a unique effect of the yield stress.

Finally we show an example from an affine fracture at $H = 2$, $L = 20$, for increasing B; see Fig. 3.5. We observe that even for $B = 1$ much of

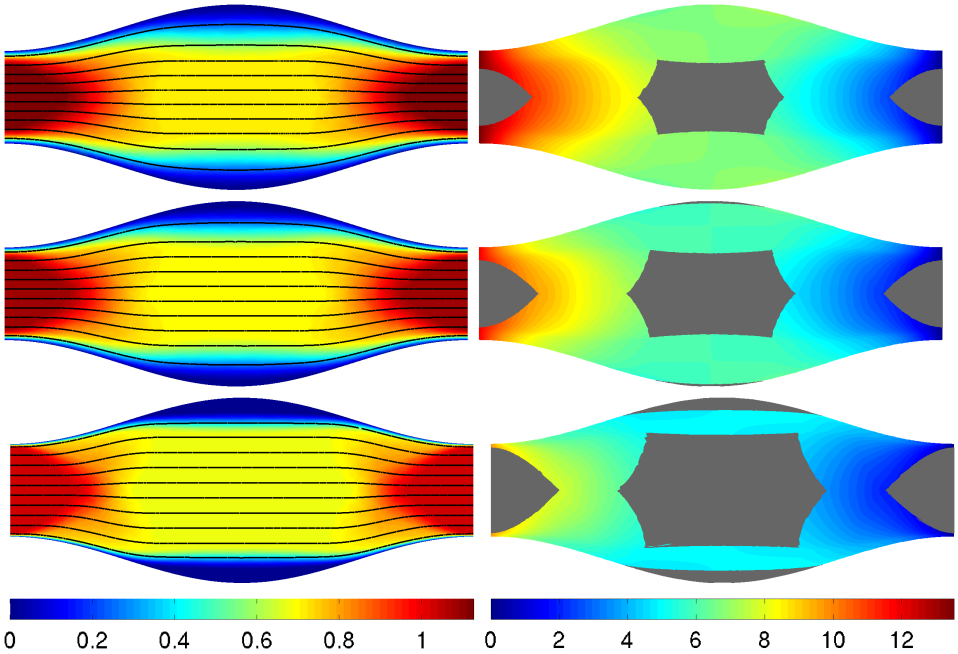

Figure 3.3: Computed examples of speed $|\mathbf{u}|$ & streamlines (left column), and scaled pressure p/B with (gray) unyielded plugs (right column), at $H = 1$, $L = 10$, $\psi = 0$, wavy fracture profile. Top row: $B = 5$; middle row: $B = 10$; bottom row: $B = 100$.

the small scale roughness of the fracture wall is smoothed out by fouled immobile fluid. This effect increases with B as also the size of plug regions within the flowing region increases. Unyielded flowing plugs are observed at the symmetry points of the flow. We can observe a slight asymmetry in the positions of the flowing plug regions, although for all practical purposes the velocity field is symmetrical about the x-axis. This asymmetry is due to the unstructured mesh, which is not constrained to be symmetric.

3.3 Darcy-law estimates

In a uniform channel of dimensionless width $2(1+h)$ the dimensionless pressure gradient is found from the constraint of fixed flow rate. This amounts

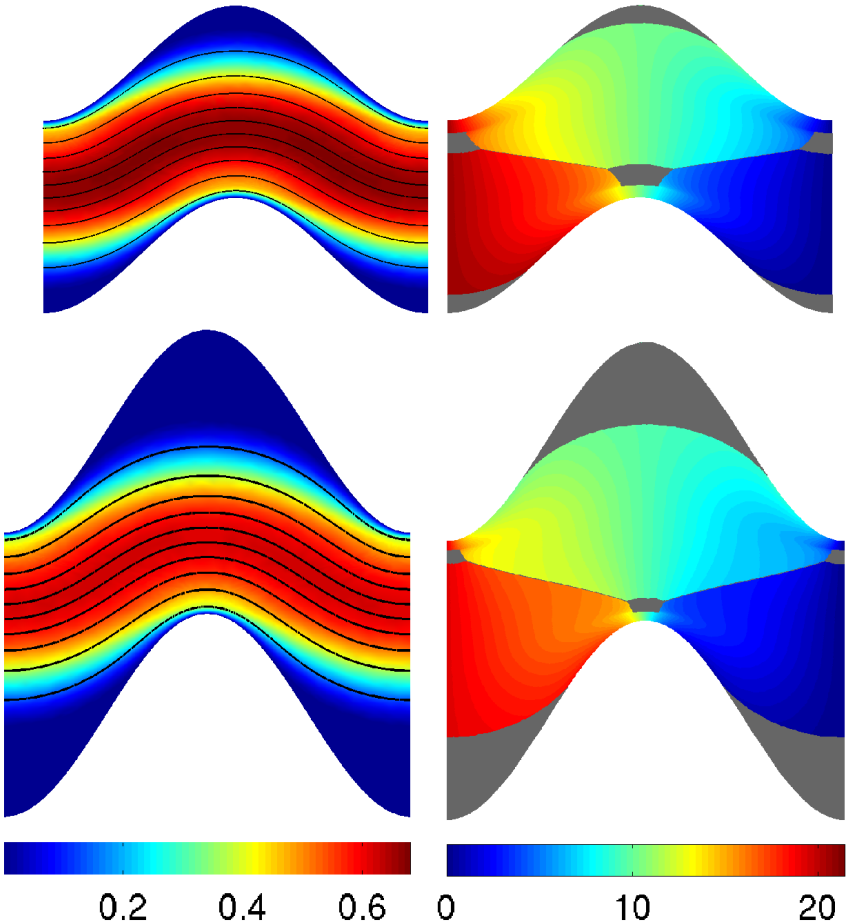

Figure 3.4: Computed examples of speed $|\mathbf{u}|$ & streamlines (left column), and pressure p with (gray) unyielded plugs (right column), at $B = 2$, $L = 10$, $\psi = 0.5$, wavy fracture profile. Top row: $H = 3$; bottom row: $H = 5$.

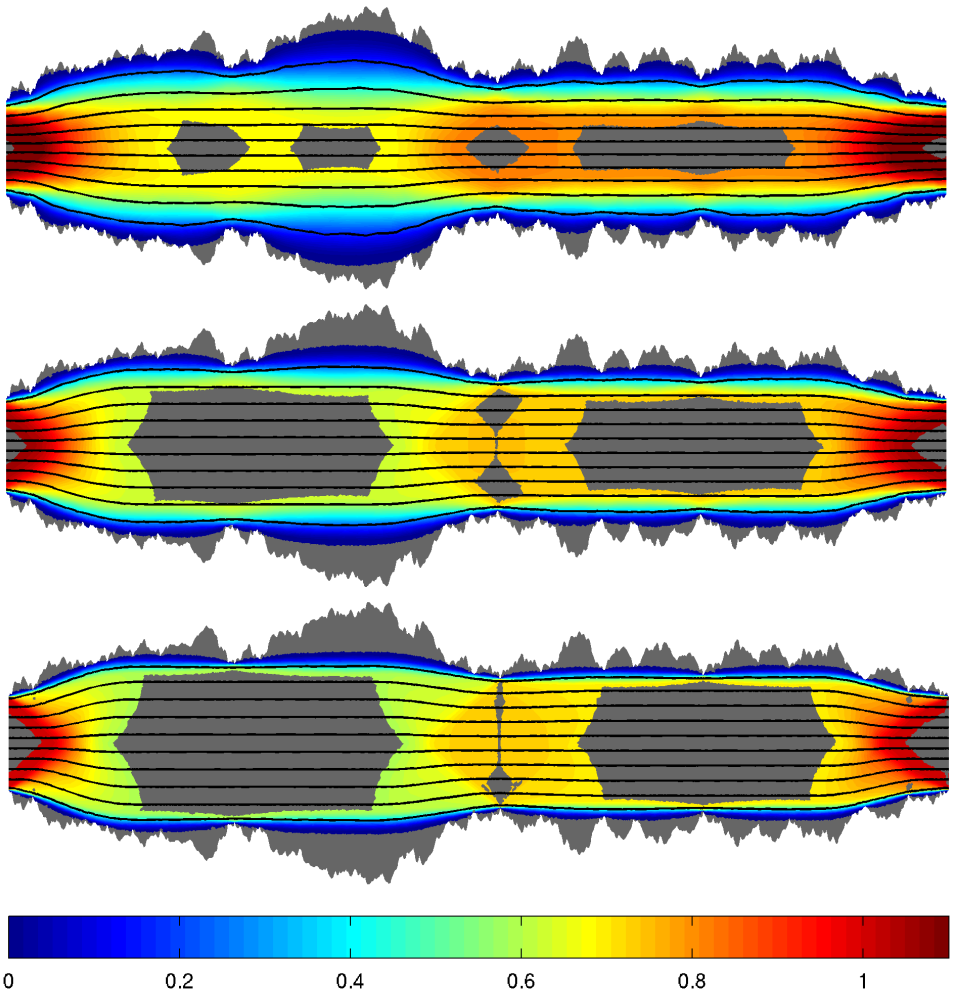

Figure 3.5: Computed examples of the speed $|\mathbf{u}|$ & streamlines with (gray) unyielded plugs, at $H = 2$, $L = 20$, for a symmetric affine fracture. Top row: $B = 1$; middle row: $B = 10$; bottom row: $B = 100$.

to solving the Buckingham-Reiner equation:

$$1 = \frac{B(1+h)^2}{3\phi}(1-\phi)^2(1+\phi/2) \tag{3.11}$$

for the dimensionless parameter $\phi \in [0,1]$, which denotes the ratio of yield stress to wall shear stress. We note that ϕ depends only on the parameter $B(1+h)^2$, which can be interpreted as an appropriately modified Bingham number, i.e. the mean velocity is reduced by $1/(1+h)$ due to mass conservation, and the minimal width is amplified by $(1+h)$. Having found ϕ by solving (3.11) numerically, the pressure gradient is computed from:

$$\left|\frac{\partial p}{\partial x}\right| = \frac{B}{(1+h)\phi}. \tag{3.12}$$

In the case that the fracture has slowly varying width in x, it is natural to expect that the uniform channel solution gives a leading order approximation. The flow rate is the same at each x along the fracture, so we simply compute $\phi(x)$ from (3.11) using the varying width:

$$2(1+h(x)) = 2 + y_+(x) + y_-(x), \qquad \Rightarrow \qquad h(x) = \frac{1}{2}[y_+(x) + y_-(x)]. \tag{3.13}$$

We then evaluate the pressure gradient from (3.12). For example, for the wavy channel we have:

$$h(x) = \frac{H}{4}[2 + \cos(2\pi x/L) + \cos(2\pi[x/L - \psi])].$$

Adopting this procedure, we compute the lubrication pressure drop along the fracture Δp_L, using (3.11) & (3.12). This may be compared directly with the numerical pressure drop Δp_N, from the finite element solution. We evaluate the accuracy of the lubrication approximation using the relative error in predicted pressure drops:

$$\text{Relative error } = \frac{2|\Delta p_N - \Delta p_L|}{\Delta p_N + \Delta p_L}.$$

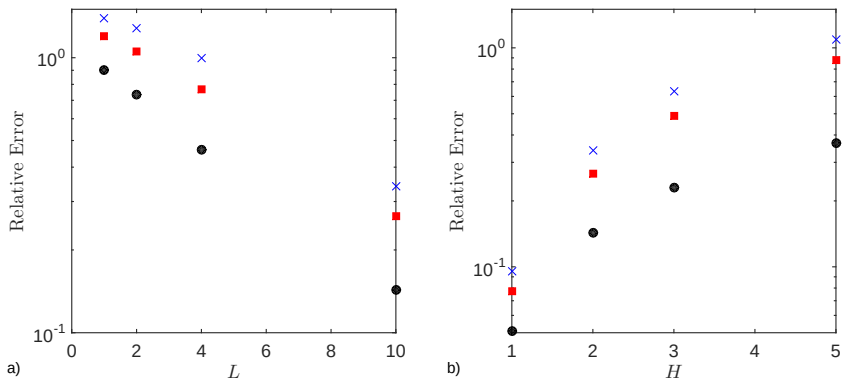

Figure 3.6: Relative error in predicted pressure drops between numerically computed and lubrication approximation (3.12), for $B = 0.1$ in wavy fracture: a) $H = 2$ and varying L; b) $L = 10$ and varying H. For both figures: black circle $\psi = 0$, red square $\psi = 0.25$, blue cross $\psi = 0.5$.

Figure 3.6 shows typical variations in relative error as both H and L are varied, for relatively small $B = 0.1$. For this small value of B the velocity field is very close to that of a Newtonian fluid as are the relative errors in pressure drop. We observe that the relative error decreases for fixed H as L increases and for fixed L as H decreases. The relative errors appear largest for $\psi = 0.5$, when the sinusoidal walls variations are out of phase. This particular effect is due to tortuosity.

For Newtonian fluids various authors have proposed corrections to Darcy's law, based on improved representations of the geometric effects. For example, [258] have used an effective fracture width, derived by calibrating with the analytical solution from a sinusoidal variation. They have then generalized this approach somewhat to more general planar fractures. A slightly different approach is followed by [106], who essentially use the fracture wall geometry to define a centreline of the fracture and consequently the local fracture width. This new fracture width is used in the classical lubrication approximation, integrated along the fracture length. This approach does

have the advantage of addressing tortuosity directly, i.e. the increase in flow path length, but is impractical in rough fractures as it relies on differentiating the fracture geometry. In general we can say that the main efforts to correct geometric effects on Darcy's law for Newtonian fluids do not involve fluid rheology. This is for the simple reason that the geometry and rheology decouple for a Newtonian fluid, due to the linearity of the Stokes equations. We may infer from general continuity results as $B \to 0$ that any of these correction methods could be extended perturbatively into the weakly nonlinear regime of $0 < B \ll 1$; indeed this is a relatively straightforward but laborious algebraic exercise to so.

We turn instead to moderate values of B. Figure 3.7a shows the ratio of pressure drops along the fracture: $\Delta p_N/\Delta p_L$, for $B = 1,\ 5,\ 10$ and at $\psi = 0$. Both wavy and triangular fracture shapes are plotted. We observe that the computed pressure drop exceeds the lubrication pressure drop. The ratio approaches 1 as $H/L \to 0$. Note that multiple computations in our data set have the same values of H/L. Taking now $B \geq 1$ and $L \geq 10$, we plot in Fig. 3.7b the relative error for the wavy fracture, grouped by phase shift ψ. We observe that the relative errors are numerically of size $\sim H/L$ over all parameters. Note that at the same ψ and H/L different data points correspond to different B. Interestingly, the smallest errors are found for $\psi = 0.5$, i.e. out of phase (reversing the trend at small B). Possibly this results from some form of cancellation of errors when averaged over a full wavelength (due to the phase shift). Analogous results are found for the triangular fracture profile. This leads us to suppose that for quite general geometries with $H/L \ll 1$, using (3.12) will give a reliable approximation to the pressure drop; roughly speaking, errors of 10% or less are found for $H/L < 0.05$.

We now explore a slightly different yield stress effect. We have seen in Fig. 3.3 that the flow domain may self-select. From our earlier work [208, 209] we expect to find this phenomena for sufficiently large H/L and B. The occurrence of a significant unyielded plug region in the deep parts of the fracture (called fouling layers) clearly changes the flow geometry, making this is a non-Darcy flow effect that is unique to yield stress fluids. In the

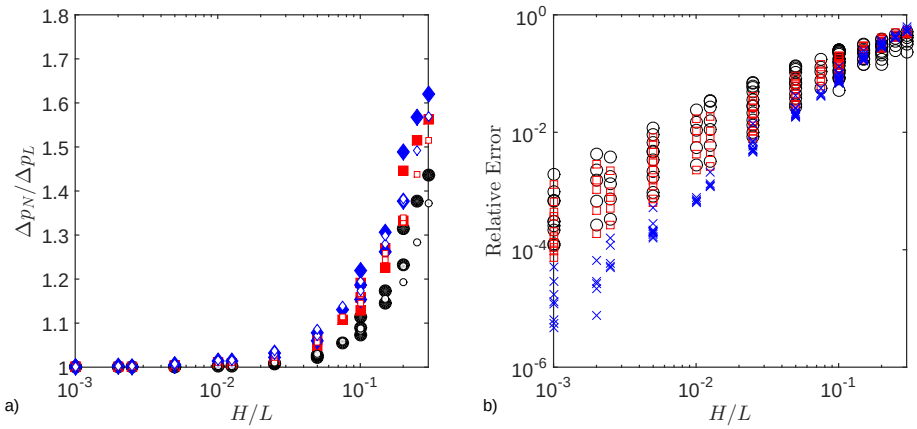

Figure 3.7: a) Ratio of pressure drops computed numerically (Δp_N) and from the lubrication approximation (Δp_L): $B = 1$ (circles), $B = 5$ (squares), $B = 10$ (diamonds); filled symbols from triangular fracture profile, hollow symbols from wavy profile; $\psi = 0$. b) Relative error in predicted pressure drops between numerically computed and lubrication approximation (3.12), for $L \geq 10$ and $B \geq 1$ in a wavy fracture: black circle $\psi = 0$, red square $\psi = 0.25$, blue cross $\psi = 0.5$.

case that we have fouling layers, the yield surface forms one boundary of the flow domain. This surface is defined as a contour of constant $\tau = B$, and is coincidentally a material surface when $\mathbf{u} = 0$ within the plug. Imposing the condition $\mathbf{u} = 0$ on the yield surface and solving only within the flowing region of the fracture gives the same velocity solution. This suggests that a reasonable way of approximating the pressure drop through such a fracture would be to replace $y_\pm(x)$ in (3.13) with the yield surface positions of the boundary of the fouling layer, denoted say $y = \pm y_{y,\pm}(x)$, i.e.

$$h(x) = \frac{1}{2}[\min\{y_+(x), y_{y,+}(x)\} + \min\{y_-(x), y_{y,-}(x)\}]. \tag{3.14}$$

To illustrate this approach, we take a fracture geometry $H = 2$ & $L = 2$, for which the lubrication approximation (3.12) should not provide a good

approximation. The 2D computed mean pressure gradients and those approximated from (3.12) are shown in Fig. 3.8a for both triangular and wavy profiles, over $\psi = 0,\ 0.125,\ 0.25,\ 0.5$, and for increasing values $B \geq 1$. Both mean pressure gradients increase with B, as might be expected, and we observe a consistent and significant error for all parameters. The relative error is shown in Fig. 3.8b for the same data (squares) and we see this is ~ 1 over all parameters. Also in Fig. 3.8b (diamonds) are the results of predicting the pressure drop using (3.12) but taking the modified fracture width from (3.14), i.e. where there is a fouling layer we take the yield surface position instead of the fracture wall position. Physically, as B increases the fouling layer progressively fills in and smoothes the fracture wall variations. Thus, as B increases the geometry of (3.14) resembles a geometry more suited to a lubrication approximation. On using (3.14) we see a significant decrease in the relative error, so that at large B equation (3.12) again leads to a reasonable approximation of the pressure drop, but with the inconvenient caveat that we must first know the extent of the fouling region in order to make this prediction! Nevertheless, this is an interesting and unusual flow in that increasing the non-Newtonian nature of the fluid leads to improved approximation.

Finally, we must note that the improvement in approximation is geometry dependent. For a fracture that is anyway relatively long and thin, as $B \to \infty$ we may either: (i) have no fouling at all, or (ii) have a fouling layer that does not fill the entire wall profile at large B. Characteristics of the limit of large B relate to the limit of no flow along the fracture, which we study below in §3.4. Fig. 3.8c illustrates the reduction in relative error, using (3.14) compared to (3.13), for two specific fracture geometries. We see that *short* wavelength fractures are most affected by using (3.14).

3.4 The limit of no flow

When yield stress fluids are pushed through a pipe or duct, it is well known that a certain critical pressure gradient must be exceeded in order for flow to occur. For example, in pipe of diameter $\hat{D}$ the pressure gradient must

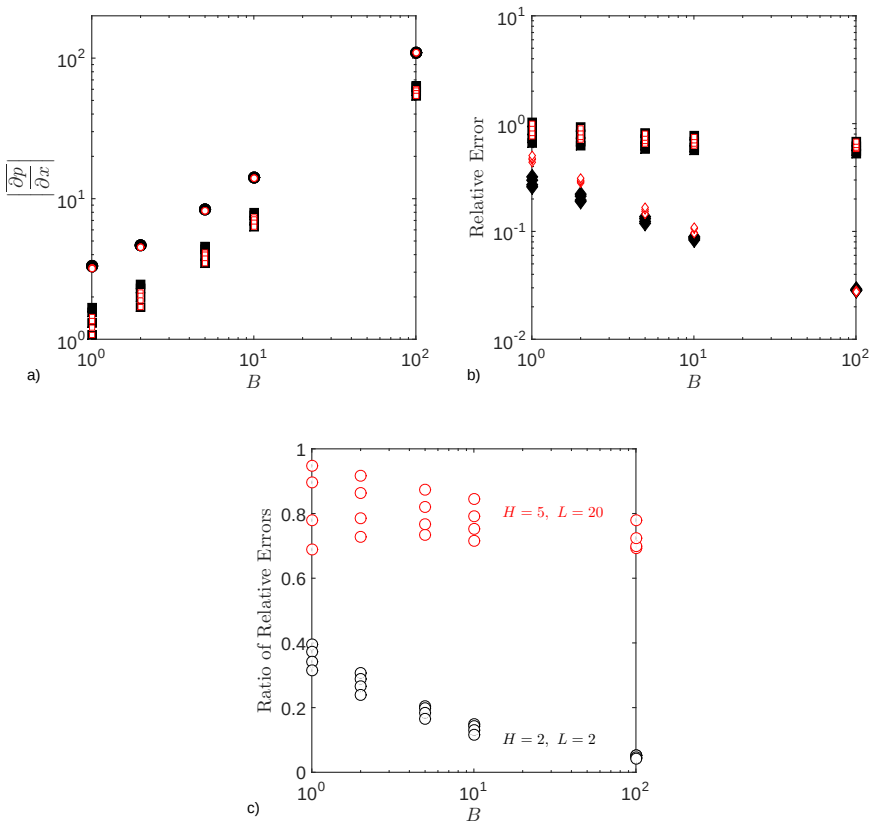

Figure 3.8: a) Consistent errors in average pressure gradient prediction using (3.12), for $H = 2$, $L = 2$: black = wavy, red/white = triangular; circles = numerical, squares = lubrication approximation. b) relative error for the data in a) (squares); relative error using the lubrication approximation (3.12) with the fracture width replaced by yield surface position (diamonds). c) Ratio of relative errors (lubrication approximation using yield stress position vs lubrication approximation using fracture width): $H = 2$, $L = 2$ in black; $H = 5$, $L = 20$ in red. Note that the multiple points displayed at the same B correspond to different values of ψ.

exceed $4\hat{\tau}_Y/\hat{D}$. Critical pressure gradients are known for many other duct cross-sections shapes, following the seminal work of [169, 170]. Here the fully two-dimensional nature of the flow along the fracture complicates things, but physical intuition still suggests that a critical pressure drop is required in order to initiate flow.

One approach to finding the critical pressure drop would be to compute flows at successively large pressure drops, until flow initiates. However, the dimensionless formulation we have adopted appears to prevent this, since we have scaled with a mean velocity so that (3.9) is always satisfied. Thus, an alternative scaling is needed to study this limiting flow directly. Suppose therefore that we impose a fixed pressure drop $\Delta\hat{P}$ along the fracture. We then define a velocity scale $\hat{U}^*$ to implicitly balance with the shear stress, i.e.

$$\frac{\Delta\hat{P}}{\hat{L}} = \frac{\hat{\mu}\hat{U}^*}{\hat{D}^2} \quad \Rightarrow \quad \hat{U}^* = \frac{\Delta\hat{P}\hat{D}^2}{\hat{L}\hat{\mu}}.$$

The viscous stresses and the modified pressure are scaled with $\hat{\mu}\hat{U}^*/\hat{D}$, the velocity is scaled with $\hat{U}^*$ and lengths again with $\hat{D}$. This results in the same system (3.1)-(3.4b), with all variables now designated with a $*$ to denote the different scaling. In place of B in the constitutive laws (3.4a) & (3.4b) we now have:

$$Od \equiv \frac{\hat{\tau}_Y\hat{D}}{\hat{\mu}\hat{U}_*} = \frac{\hat{L}}{\hat{D}}\frac{\hat{\tau}_Y}{\Delta\hat{P}}, \tag{3.15}$$

representing the balance between the yield stress and the imposed pressure drop. We refer to Od as the Oldroyd number. The boundary conditions are again:

$$\begin{aligned}
&\mathbf{u}^* = 0, \quad \text{at} \quad y = 1 + y_+(x) \quad \text{and} \quad y = -1 - y_-(x),\\
&\mathbf{u}^*(-L/2, y) = \mathbf{u}^*(L/2, y),\\
&\tau^*_{ij}(-L/2, y) = \tau^*_{ij}(L/2, y),\\
&p^*(-L/2, y) = p^*(L/2, y) + L,
\end{aligned}$$

i.e. now the pressure drop is known (with average gradient -1 along the fracture); the flow rate must be calculated. Our physical intuition about

requiring a finite pressure drop to initiate flow along the fracture translates into the belief that there will be a critical value, say $Od = Od_c$, that separates flowing and static fractures. This notion will be made more precise below in §3.4.2.

As in either formulation described, the flow is a Stokes flow with a unique velocity solution, we expect that the solutions may be mapped to one-another. Equivalence of the 2 formulations is established straightforwardly by re-scaling, from which we deduce:

$$Od = L\frac{B}{\Delta p} = Bq^*, \qquad 2q^* = \int_{-1-y_-(x)}^{1+y_+(x)} u_1^*(x,y)\ \mathrm{d}y, \tag{3.16}$$

i.e. $2q^*$ is the areal flow rate from the imposed pressure formulation, which is equivalent to the inverse of the mean pressure gradient, $L/\Delta p$, computed in the imposed velocity formulation.

Although it is quite possible to compute $\mathbf{u}^*$ from the imposed pressure formulation and then vary Od to study the limit of no flow, numerically this is less well-conditioned than using the fixed flow rate formulation. Since the computational method is iterative and has tolerances imposed for convergence, it proves easier to impose a tolerance on an iteration for which $\mathbf{u} \sim O(1)$, than where $\mathbf{u}^* \to 0$. The identity (3.16) shows that it is feasible to work in this way. Using the imposed flow formulation we find Δp as part of the solution and monitor convergence of $Od = LB/\Delta p \to Od_c$ as we increase B. We also see that if a critical stress balance is achieved, $\mathbf{u}^* \to 0$ (i.e. as $Od \to Od_c$), then implicitly $q^* \sim B^{-1}$ as $B \to \infty$.

3.4.1 Examples

We now examine 3 example sequences where we take increasingly large B at fixed geometry, to understand the limiting behaviour. For simplicity we fix $\psi = 0$. Figure 3.9 shows a relatively short fracture ($H = 1.5,\ L = 4$) at $B = 10,\ 100,\ 1000$. Even at $B = 10$ the majority of the flow is unyielded, with stationary fouling regions filling the deep parts of the fracture and an intact plug moving along the centre. These regions are separated by a

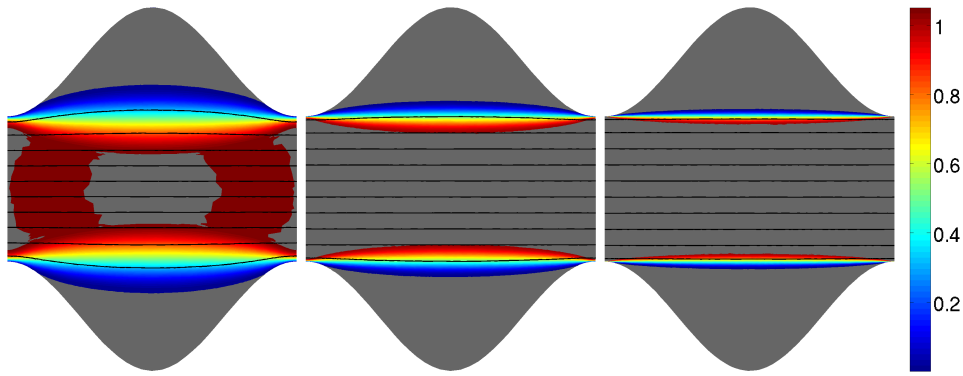

Figure 3.9: Colormap of the speed with superimposed streamlines in a relatively short fracture $H = 1.5,\ L = 4$: increasing $B = 10,\ 100,\ 1000$ (from left to right). Unyielded regions are shown in gray.

thin shear layer that extends between the narrowest parts of the fracture, widening slightly at the deepest parts. As B increases the width of this sheared layer is reduced, albeit slowly.

Next we consider a relatively long fracture with small H/L, ($H = 0.1,\ L = 20$); see Fig. 3.10. The flow has unyielded plug regions at the narrowest and widest parts of the fracture, but no static fouling layers in the deepest parts of the fracture. The plug in the widest part is moving slower than that in the narrowest part and these two plugs remain separated as B is increased.

Lastly, we consider a more intermediate geometry ($H = 2,\ L = 20$); see Fig. 3.11. As may be expected the limiting process at large B is qualitatively somewhere between the previous 2 examples. The narrowest and widest parts of the fracture have moving central plug regions, but there is also a static fouling layer in the deepest part of the fracture, extending between say $x \in (-x_f, x_f)$. The fouling layer and central plug are separated by a shear layer, that decreases slowly in width as B increases (similar to the short fracture). The length x_f appears to approach a constant value as B increases. Similar to the long fracture, the narrow and wide plugs remain separated at large B, moving at different speeds.

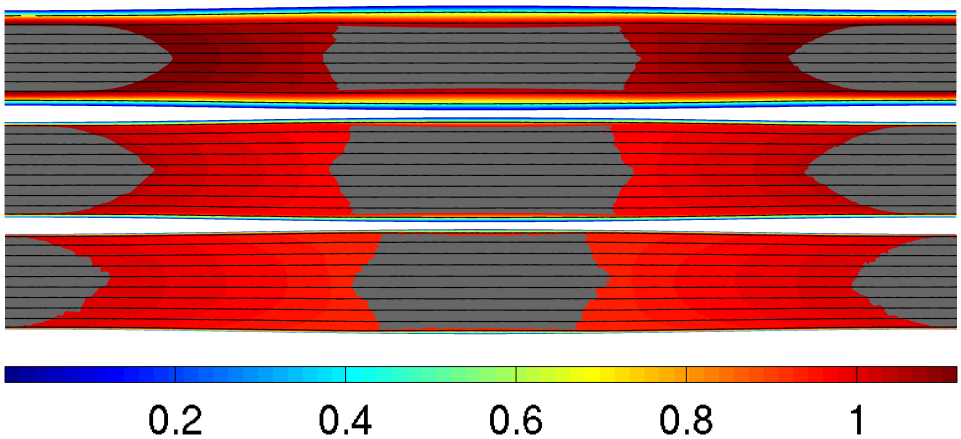

Figure 3.10: Colormap of the speed with superimposed streamlines in a relatively short fracture $H = 0.1$, $L = 20$: increasing $B = 10,\ 100,\ 1000$ (from top to bottom). Unyielded regions are shown in gray.

Figure 3.12 plots the variation of Od and $\Delta P/L$, with increasing B, for the 3 geometries illustrated in Figs. 3.9-3.11. We see that in all cases the computed Od appears to asymptote to a constant value at large B. This value denotes the critical limit Od_c. Interestingly, the short and long fractures appear to asymptote to $Od_c \approx 1$, whereas the intermediate geometry asymptotes to a value that is significantly larger. These examples are typical of the behaviour found over the whole range of our results.

3.4.2 The critical limit from a variational method

We now define the critical limit more precisely. Using the imposed pressure formulation has some advantages for this, as we may use standard variational techniques (as in e.g. [198]) to consider the zero flow limit. The solution $\mathbf{u}^*$

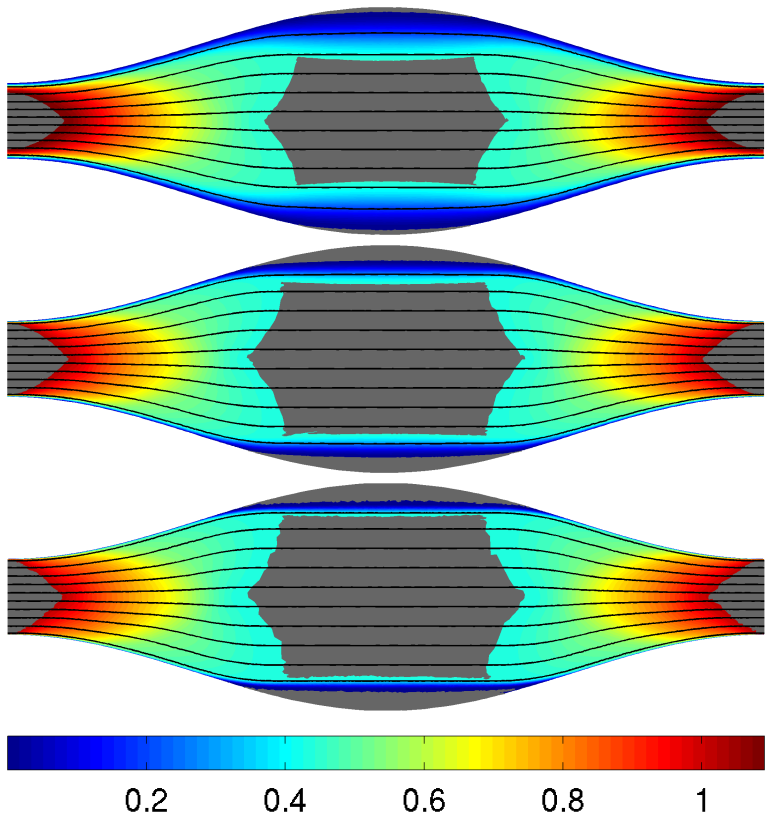

Figure 3.11: Colormap of the speed with superimposed streamlines in a relatively short fracture $H = 2,\ L = 20$: increasing $B = 10,\ 100,\ 1000$ (from top to bottom). Unyielded regions are shown in gray.

satisfies:

$$
\begin{aligned}
0 \le a(\mathbf{u}^*, \mathbf{u}^*) &= -Od\, j(\mathbf{u}^*) + L \int_{-1-y_-(x)}^{1+y_+(x)} u_1^*(x,y)\ \mathrm{d}y \\
&= -Od\, j(\mathbf{u}^*) + \int_{-L/2}^{L/2} \int_{-1-y_-(x)}^{1+y_+(x)} u_1^*(x,y)\ \mathrm{d}y\ \mathrm{d}x = Od\, j(\mathbf{u}^*) + Q(\mathbf{u}^*).
\end{aligned}
\tag{3.17}
$$

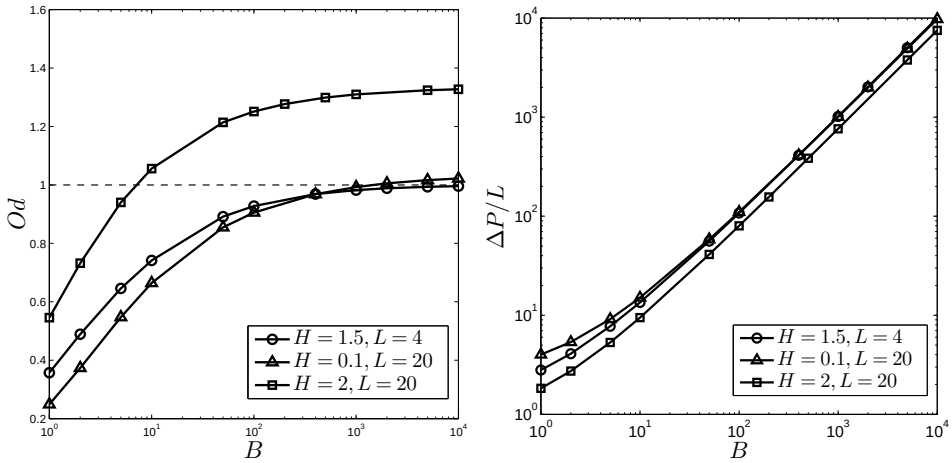

Figure 3.12: Limiting behaviour as $B \to \infty$ for the geometries of Figs. 3.9-3.11: a) Od plotted against B; b) $\Delta P/L$ plotted against B.

The functionals $a(\mathbf{u}^*, \mathbf{u}^*)$ and $j(\mathbf{u}^*)$ denote respectively the viscous and plastic dissipation rate functionals:

$$a(\mathbf{u}^*, \mathbf{v}^*) \equiv \int_{-L/2}^{L/2} \int_{-1-y_-(x)}^{1+y_+(x)} \frac{1}{2}\dot{\gamma}_{ij}(\mathbf{u}^*)\dot{\gamma}_{ij}(\mathbf{v}^*)\ \mathrm{d}y\ \mathrm{d}x, \qquad \mathbf{u}^*, \mathbf{v}^* \in \mathcal{V}$$
$$j(\mathbf{v}^*) \equiv \int_{-L/2}^{L/2} \int_{-1-y_-(x)}^{1+y_+(x)} \dot{\gamma}(\mathbf{v}^*)\ \mathrm{d}y\ \mathrm{d}x, \qquad \mathbf{v}^* \in \mathcal{V},$$

and note that we have extended the velocity integral at the inflow to the entire fracture:

$$Q(\mathbf{u}^*) \equiv \int_{-L/2}^{L/2} \int_{-1-y_-(x)}^{1+y_+(x)} u_1^*(x, y)\ \mathrm{d}y\ \mathrm{d}x,$$

as the flow rate is identical through each cross-section. Continuing this analysis:

$$0 \leq a(\mathbf{u}^*, \mathbf{u}^*) \leq -j(\mathbf{u}^*) \left[Od - \sup_{\mathbf{v}* \in \mathcal{V}, \mathbf{v}* \neq 0} \frac{Q(\mathbf{v}^*)}{j(\mathbf{v}^*)} \right] \equiv -j(\mathbf{u}^*) \left[Od - Od_c \right], \tag{3.18}$$

where $\mathcal{V}$ denotes the space of admissible velocity solutions. The critical value of Od is thus formally defined as:

$$Od_c = \sup_{\mathbf{v}*\in\mathcal{V},\mathbf{v}*\neq 0} \frac{Q(\mathbf{v}^*)}{j(\mathbf{v}^*)}. \tag{3.19}$$

Following a similar procedure to [198] we can show that

$$a(\mathbf{u}^*, \mathbf{u}^*) \sim O([Od_c - Od]^2) \qquad \text{as } Od \to Od_c^{*-}, \tag{3.20}$$

$$Odj(\mathbf{u}^*) \sim Q(\mathbf{u}^*) \sim O(Od_c - Od) \qquad \text{as } Od \to Od_c^{*-}, \tag{3.21}$$

$$j(\mathbf{u}^*) \gtrsim \frac{a(\mathbf{u}^*, \mathbf{u}^*)}{[Od_c - Od]} \geq 0 \qquad \text{as } Od \to Od_c^{*-}. \tag{3.22}$$

Figure 3.13 shows the computed values of $a(u^*, u^*)$, $j(u^*)$ and $Q(u^*)$ as B is increased, for the 3 geometries illustrated in Figs. 3.9-3.11. We see that $a(u^*, u^*)$ does indeed converge much faster than $j(u^*)$ and $Q(u^*)$, as is implicit in the above bounds. Note that the $O([Od_c - Od]^2)$ in (3.20) is a lower bound on the decay rate of the viscous dissipation and we can see that the decay rate is indeed faster than quadratic. Equation (3.22) ensures that the plastic dissipation decays to zero at least one order slower and (3.21) ensures that the limiting balance is between the plastic dissipation and flow rate. We again observe this in Fig. 3.13. This in turn can be used to argue that the supremum in (3.19) is in fact achieved by the solution. Indeed, if one knows the distribution of the limiting velocity solution, this can be used to estimate Od_c by inserting in (3.19). Note that the size of the limiting velocity is not important in this determination as (3.19) is scale invariant.

For computing the velocity, especially numerically, it can be more convenient to work with $O(1)$ quantities, e.g. in tracking convergence. In moving between formulations it is necessary to rescale velocities with q^*. Thus, to evaluate Od_c by inserting the limiting solution $\mathbf{u}^*$ into (3.19), we may instead work directly with $\mathbf{u}$ in the large B limit, i.e.

$$Od_c \sim \lim_{B\to\infty} \frac{Q(\mathbf{u})}{j(\mathbf{u})} = \lim_{B\to\infty} \frac{2L}{j(\mathbf{u})}, \tag{3.23}$$

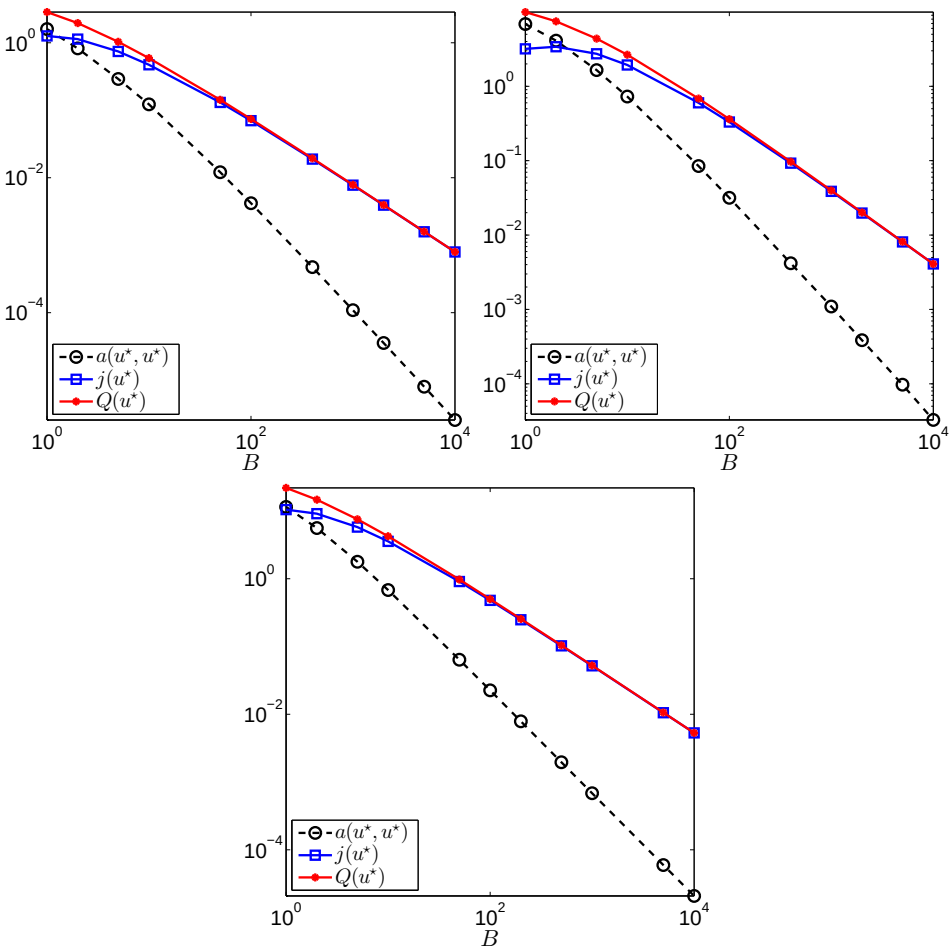

Figure 3.13: Viscous dissipation, plastic dissipation and flow rate, $a(u^*, u^*)$, $j(u^*)$ and $Q(u^*)$ for the 3 geometries illustrated in Figs. 3.9-3.11, from left to right.

on noting that $Q(\mathbf{u}) = 2L$ in the fixed flow rate formulation. In the next sections we will estimate $j(\mathbf{u})$ in order to derive approximations to Od_c.

3.4.3 Short fractures

In short fractures we have seen that increasingly narrow sheared layers separate fouling layers and the moving plug. As the plug remains intact as $B \to \infty$, from mass conservation we may assume that the plug velocity $u_p \sim 1$. There is an evident symmetry in the shape of the sheared regions, which we assume can be reasonably approximated by boundaries: $y = \pm[y_c \pm d_0(B, x)]$, in upper and lower sheared layers respectively. Here $y = \pm y_c$ denote the central positions of the sheared layers at $x = 0$. To leading order we may expect that within the sheared layers:

$$\dot{\gamma}(\mathbf{u}) \sim \left|\frac{\partial u}{\partial y}\right| \sim O\left(\frac{u_p}{d_0}\right).$$

On integrating first with respect to y and then along the sheared layer we find a leading order contribution to $j(\mathbf{u})$, of size $\sim u_p L$, from each sheared layer. Therefore, we find that $j(\mathbf{u}) \sim 2u_p L \sim 2L$, and hence that $Od_c \sim 1$, as observed.

We may extend this analysis to examine the convergence of $Od \to Od_c^-$. Let us suppose that $d_0(B, 0) \sim B^{-k}$ as $B \to \infty$. Examination of the velocity profile at $x = 0$ reveals that $u(0, y)$ shows a variation across the sheared layer that is approximately cubic in $y \mp y_c$. This leads to the approximation:

$$u(x, y) \approx \frac{u_p}{2} - \frac{3u_p}{2}\left[\left(\frac{y - y_c}{d_0(B, x)}\right) - \frac{1}{3}\left(\frac{y - y_c}{d_0(B, x)}\right)^3\right],$$

in the upper sheared layer. In fact as the ends $x = \pm L/2$ are approached the cubic approximation changes to quadratic, but at the same time $d_0(B, x)$ decreases, so that contributions from these regions are smaller. It can be observed that the above profile integrates in y to satisfy the flow rate constraint exactly with $u_p = 1$ (and analogously in the lower shear layer). The

leading order components of the shear rate are:

$$\dot{\gamma}_{xy} \sim \frac{\partial u}{\partial y} \approx -\frac{3}{2d_0}\left[1-\left(\frac{y-y_c}{d_0}\right)^2\right], \quad \dot{\gamma}_{xx} \sim 2\frac{\partial u}{\partial x} \approx 3\frac{d_0'}{d_0}\left[\left(\frac{y-y_c}{d_0}\right)-\left(\frac{y-y_c}{d_0}\right)^3\right].$$

As the sheared layers are relatively long and thin we may assume that $|d_0'(B,x)| \sim d_0'(B,0)/L \ll 1$, and therefore find in the upper layer:

$$\begin{aligned}\dot{\gamma}(\mathbf{u}) &\approx \frac{3}{2d_0}\left[1-\left(\frac{y-y_c}{d_0}\right)^2\right]\left[1+4[d_0']^2\frac{\left[\left(\frac{y-y_c}{d_0}\right)-\left(\frac{y-y_c}{d_0}\right)^3\right]^2}{\left[1-\left(\frac{y-y_c}{d_0}\right)^2\right]^2}\right]^{1/2} \\ &\sim \frac{3}{2d_0}\left[1-\left(\frac{y-y_c}{d_0}\right)^2\right]+\frac{3[d_0']^2}{d_0}\left[\left(\frac{y-y_c}{d_0}\right)^2-\left(\frac{y-y_c}{d_0}\right)^4\right]+O([d_0']^4)\end{aligned} \tag{3.24}$$

and a similar contribution from the lower layer. Integrating over the 2 sheared layers gives:

$$j(\mathbf{u}) \sim 2L + \frac{8}{5}\int_{-L/2}^{L/2}[d_0']^2\ dx,$$

and therefore as $B \to \infty$:

$$Od \sim \frac{Q(\mathbf{u}^*)}{j(\mathbf{u}^*)} = \frac{Q(\mathbf{u})}{j(\mathbf{u})} \sim 1 - \frac{4}{5L}\int_{-L/2}^{L/2}[d_0']^2\ dx \sim 1 - O\left(\frac{1}{L^2B^{2k}}\right). \tag{3.25}$$

Therefore, we have $Od_c - Od \sim L^{-2}B^{-2k}$ and since also $Od = Bq^*$, as $B \to \infty$ we have: $q^* \sim 1/B - O(L^{-2}B^{-2k-1})$. Returning now to (3.21):

$$Q(\mathbf{u}^*) = 2Lq^* \sim 2L/B - O(L^{-1}B^{-2k-1}) \sim O(Od_c - Od) \sim O(L^{-2}B^{-2k}).$$

This implies that $k \leq 1/2$ is the maximal convergence rate for the width of the sheared layer in short fractures, (recall $d_0(B,0) \sim B^{-k}$).

Following on similar lines, for short fractures, we may deduce that $a(\mathbf{u}^*, \mathbf{u}^*) \sim$

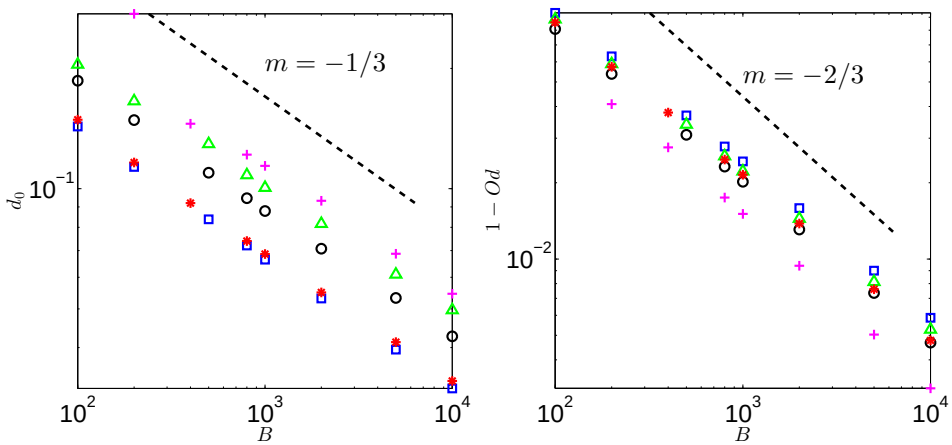

Figure 3.14: Limiting behaviour as $B \to \infty$ for 5 short fracture geometries: a) shear layer thickness d_0; b) $Od_c - Od$. Data is shown for: $\circ, H = 1, L = 3)$, $(\square, H = .5, L = 2)$, $(\triangle, H = .25, L = 4)$, $(*, H = 3, L = 2)$, $(+, H = 4, L = 4)$; recall that $Od_c = 1$ for short fractures.

$L(q^*)^2/d_0$, as $B \to \infty$. From the bound (3.20) we deduce that:

$$LB^{-2+k} \sim L(q^*)^2/d_0 \sim a(\mathbf{u}^*, \mathbf{u}^*) \sim O([Od_c - Od]^2) \sim O(L^{-4}B^{-4k}), \quad \Longrightarrow \quad 5k \leq 2, \tag{3.26}$$

i.e. $k \leq 0.4$. Finally, we examine (3.22):

$$LB^{-1} \sim Lq^* \sim j(\mathbf{u}^*) \gtrsim \frac{a(\mathbf{u}^*, \mathbf{u}^*)}{[Od_c - Od]} \sim \frac{L(q^*)^2}{d_0 L^{-2} B^{-2k}} \sim L^3 B^{3k-2} \quad \Longrightarrow \quad k \geq 1/3. \tag{3.27}$$

To summarise, as $B \to \infty$, theoretical arguments imply that $Od \to 1 - O(B^{-2k})$ and $d_0 \sim B^{-k}$ for some $k \in [1/3, 0.4]$. Figure 3.14 explores the same convergence from our numerical results, taken from 5 different *short* fracture geometries, each as B is increased. It appears that in fact $d_0 \sim B^{-1/3}$ with $Od \to 1 - O(B^{-2/3})$, in accordance with this analysis.

3.4.4 Long fractures with no fouling

In a long symmetric fracture we commonly observe true plug regions in the widest and narrowest parts of the fracture, separated by pseudo-plug regions. For $L \gg 1$ we can expect that the flow is pseudo 1D and that the lubrication approximation should give a reasonable estimate of the pressure gradients and flow velocity. Indeed this has been verified in §3.3. Therefore, we may use the lubrication pressure gradient to evaluate the limiting Od. At large B we may expand (3.11) in series form:

$$\phi \sim 1 - \frac{\sqrt{2}}{(1+h)B^{1/2}} + \frac{2}{3(1+h)^2 B} + \frac{\sqrt{2}}{9(1+h)^3 B^{3/2}} + ... \tag{3.28}$$

Thus, the total pressure drop is

$$\begin{aligned}
\Delta p &= \int_{-L/2}^{L/2} |\frac{\partial p}{\partial x}| \, dx = \int_{-L/2}^{L/2} \frac{B}{(1+h)\phi} \, dx, \\
&\sim B \int_{-L/2}^{L/2} \frac{1}{1+h} + \frac{\sqrt{2}}{(1+h)^2 B^{1/2}} + O(B^{-1}) \, dx, \\
Od = \frac{BL}{\Delta p} &\sim \frac{L}{\displaystyle\int_{-L/2}^{L/2} \frac{1}{1+h} \, dx + \frac{\sqrt{2}}{B^{1/2}} \int_{-L/2}^{L/2} \frac{1}{(1+h)^2} \, dx + O(LB^{-1})}, \\
&\sim \left(\frac{1}{L} \int_{-L/2}^{L/2} \frac{1}{1+h} \, dx \right)^{-1} \left[1 - \frac{\sqrt{2}}{B^{1/2}} \frac{\frac{1}{L}\int_{-L/2}^{L/2} \frac{1}{(1+h)^2} \, dx}{\frac{1}{L}\int_{-L/2}^{L/2} \frac{1}{1+h} \, dx} + O(B^{-1}) \right].
\end{aligned} \tag{3.29}$$

The first term above is clearly Od_c, and can be derived by effectively integrating the yield stress along the slowly varying wall. For example, for the wavy interface we find the expression:

$$Od_c = \sqrt{1 + H + \frac{1 - \cos(\pi\psi)}{8} H^2}.$$

Referring back to Fig. 3.10 and the limiting behaviour illustrated in Fig. 3.12, we note that typically $Od_c > 1$ for this flow regime. The condition for having

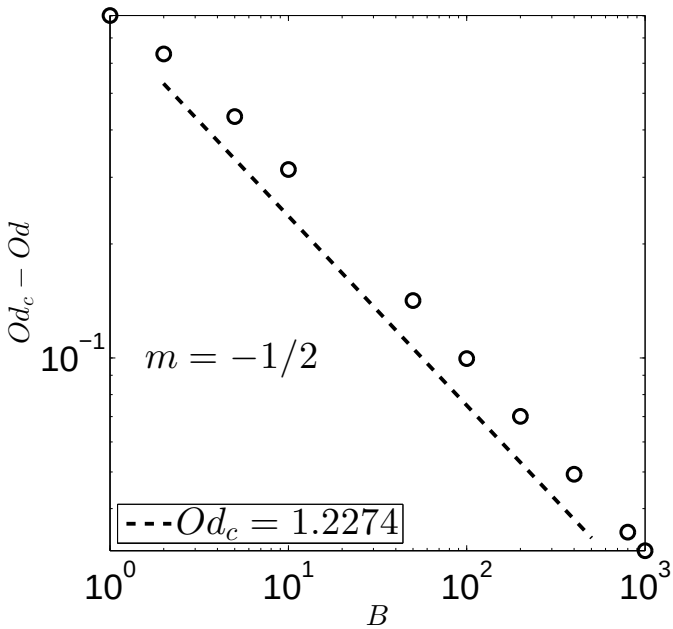

Figure 3.15: Convergence of $Od_c - Od$ as $B \to \infty$ for $H = 1$, $L = 20$.

no fouling layer seems to require a small ratio H/L. Provided this is satisfied, Od_c is in fact independent of L. In the example shown, since we have small H it appears that $Od_c \approx 1$, but this need not be the case.

From the analysis leading to (3.29) we see that $Od_c - Od \sim B^{-1/2}$ as $B \to \infty$, i.e. faster than convergence with B for the short fractures. Comparing with the bounds (3.20)-(3.22) we deduce that:

$$q^* \sim \left(\frac{B}{L} \int_{-L/2}^{L/2} \frac{1}{1+h} \, dx \right)^{-1} + O(B^{-3/2}), \quad j(\mathbf{u}^*) \sim \frac{2L}{B} + O(B^{-3/2}), \text{ as } B \to \infty,$$

and the following bound

$$a(\mathbf{u}^*, \mathbf{u}^*) \lesssim O(B^{-3/2}), \qquad \text{as } B \to \infty.$$

Figure 3.15 illustrates the convergence rate of $Od_c - Od$ as $B \to \infty$ for one of our computed "long" fractures. The $B^{-1/2}$ scaling is verified.

3.4.5 Intermediate fractures with partial fouling

In the previous 2 subsections we have seen that for both short and long fractures, it is possible to estimate the critical limit using (3.12). For sufficiently short periodic fractures the flow yields at the narrowest width, which means that (3.12) can be used, taking the modified fracture width from (3.14), which amounts to $h(x) \to 0$ as $B \to \infty$. For long enough fractures, no fouling occurs and (3.12) is applied directly. However, as we have seen in Fig. 3.11 for intermediate H/L the limit $B \to \infty$ results in only a limited portion of the fracture being fouled, say $x \in [-x_f, x_f]$ for a symmetric fracture ($\psi = 0$). So far it is unclear: (i) how to predict Od_c for such intermediate fractures; (ii) how is the fouling length x_f determined; (iii) what determines transitions from nominally *short* to *intermediate* to *long* fractures?

One feature observed in e.g. Fig. 3.11 is that for intermediate H/L a significant portion of the fracture length remains yielded in the limit $B \to \infty$. Indeed the limiting solutions appear to result in true unyielded regions only in the narrowest and widest parts of the fracture (approximately $x \in [-x_f, x_f]$), with a sheared pseudo-plug region in between. The pseudo-plug region is of course necessary, since the true plug speeds in wide and narrow parts of the fracture are different. This type of region arises in many visco-plastic flows.

The classical pseudo-plug procedure

Analysis of the pseudo-plug region stems from the studies of [246] and [17] that resolved the so-called lubrication paradox of [146]. We examine this approach as offering a potential description of the pseudo-plug observed here. In this approach, the plug velocity is derived from the Buckingham-Reiner equation (3.11), which is approximated at large B by (3.28). From ϕ we deduce the yield surface position at $y = \pm y_Y(x) = (1 + h(x))\phi$:

$$y_Y(x) \sim 1 + h(x) - \frac{\sqrt{2}}{B^{1/2}} + \frac{2}{3(1 + h(x))B} + \frac{\sqrt{2}}{9(1 + h(x))^2 B^{3/2}} + ... \quad (3.30)$$

Interestingly, the thickness of the high shear layer is independent of $h(x)$ to leading order at large B, simply following the wall profile. The pseudo-plug velocity to leading order is calculated as:

$$u_{p,0} \sim \frac{1}{1+h}\left[1 + \frac{\sqrt{2}}{3(1+h)B^{1/2}} - \frac{16}{9(1+h)^2 B} + O((1+h)^{-3}B^{-3/2})\right] \tag{3.31}$$

As for the thin shear layers observed in short fractures, we deduce that $\dot{\gamma}_{xy} \sim u_{p,0}B^{1/2}$ within the sheared layer. The size of $\dot{\gamma}_{xx}$ comes from differentiating $u_{p,0}$ with respect to x, i.e.

$$|\dot{\gamma}_{xx}| \sim \left|\frac{dh}{dx}\right| \sim \frac{1}{L},$$

since the x-dependency is through both $h(x)$ and $y_Y(x)$, both derivatives of which scale with $\frac{dh}{dx}$ at large B (we assume $H \sim O(1)$.

In the sheared layers, the leading order shear rate varies linearly with y:

$$\frac{\partial u}{\partial y} \sim \dot{\gamma}_{xy} = \dot{\tau}_{xy} + B \sim B\left(1 - \frac{y}{y_Y}\right),$$

so that the velocity profile is parabolic in y. It becomes apparent that the scaling arguments that have been made (i.e. assuming $|\dot{\gamma}_{xy}| \gg |\dot{\gamma}_{xx}|$), break down as $y \to y_Y^+$ and more specifically for:

$$y - y_Y \sim \frac{dh}{dx}B^{-1} \sim \frac{1}{BL}.$$

The above is the usual argument for emergence of a pseudo-plug region, within which the strain rates are of comparable size. Since, within any pseudo-plug the main cause of straining will come from the geometrical changes we may assume that $|\dot{\gamma}_{xy}| \sim |\dot{\gamma}_{xx}| \sim \left|\frac{dh}{dx}\right| \sim 1/L$. Therefore, within the pseudo-plug we expect that:

$$\tau_{ij} = \left[1 + \frac{B}{\dot{\gamma}}\right]\dot{\gamma}_{ij} \sim B\frac{\dot{\gamma}_{ij}}{\dot{\gamma}}\left[1 + O(\frac{1}{BL})\right].$$

At leading order therefore we have that $\tau = B$ in the pseudo-plug.

For large L, the x-momentum equation at leading order in the pseudo-plug still does not include τ_{xx}. It follows that:

$$\tau_{xy} \sim -B\frac{y}{1+h(x)}, \qquad \tau_{xx} \sim -\text{sign}(h'(x))B\sqrt{1-\frac{y^2}{(1+h(x))^2}}, \tag{3.32}$$

noting that $y_Y(x) \sim 1+h(x)$. Equally we may deduce that to leading order:

$$\dot{\gamma}_{xx} \sim -\frac{2h'(x)}{(1+h(x))^2}, \qquad \dot{\gamma}_{xy} \sim \frac{-y|\dot{\gamma}_{xx}|}{\sqrt{y^2+(1+h(x))^2}}, \tag{3.33}$$

which may be integrated to give the velocity distribution across the pseudo-plug:

$$u \sim u_{p,0} + |\dot{\gamma}_{xx}|\left[\sqrt{2}(1+h(x)) - \sqrt{y^2+(1+h(x))^2}\right].$$

Note that under the assumption of near-parallel flow, i.e. $L \to \infty$, both strain rates scale with $|\dot{\gamma}_{xx}| \sim H/L$ and consequently the correction to the leading order velocity from the variation across the plug is also $\sim H/L$.

In Fig. 3.16 we make a comparison between the predicted pseudo-plug x-velocity and that from the 2D computations. We can see that the prediction is not particularly good, in terms of the shape of the velocity profiles. Note that we have not carried out a matching procedure here [199], which would soften the corners of the pseudo-plug x-velocity. The shape of the corrected velocity, across the pseudo plug, does not capture the variations in the computed velocity field.

Pseudo-plug regions

One reason for the poor performance of the classical pseudo-plug procedure above is that the limit we consider at zero flow is the critical limit of zero flow as $B \to \infty$, for reasonably large L. However, it is not necessarily close to the asymptotic limit $L \to \infty$, which is required for the preceding analysis to be valid. The stress distribution found as $L \to \infty$ is shear-dominated, even within the pseudo-plug. Thus, for example $\tau_{xx} \to 0$ in (3.32) as the yield surface is approached, as the solution must match with that in the

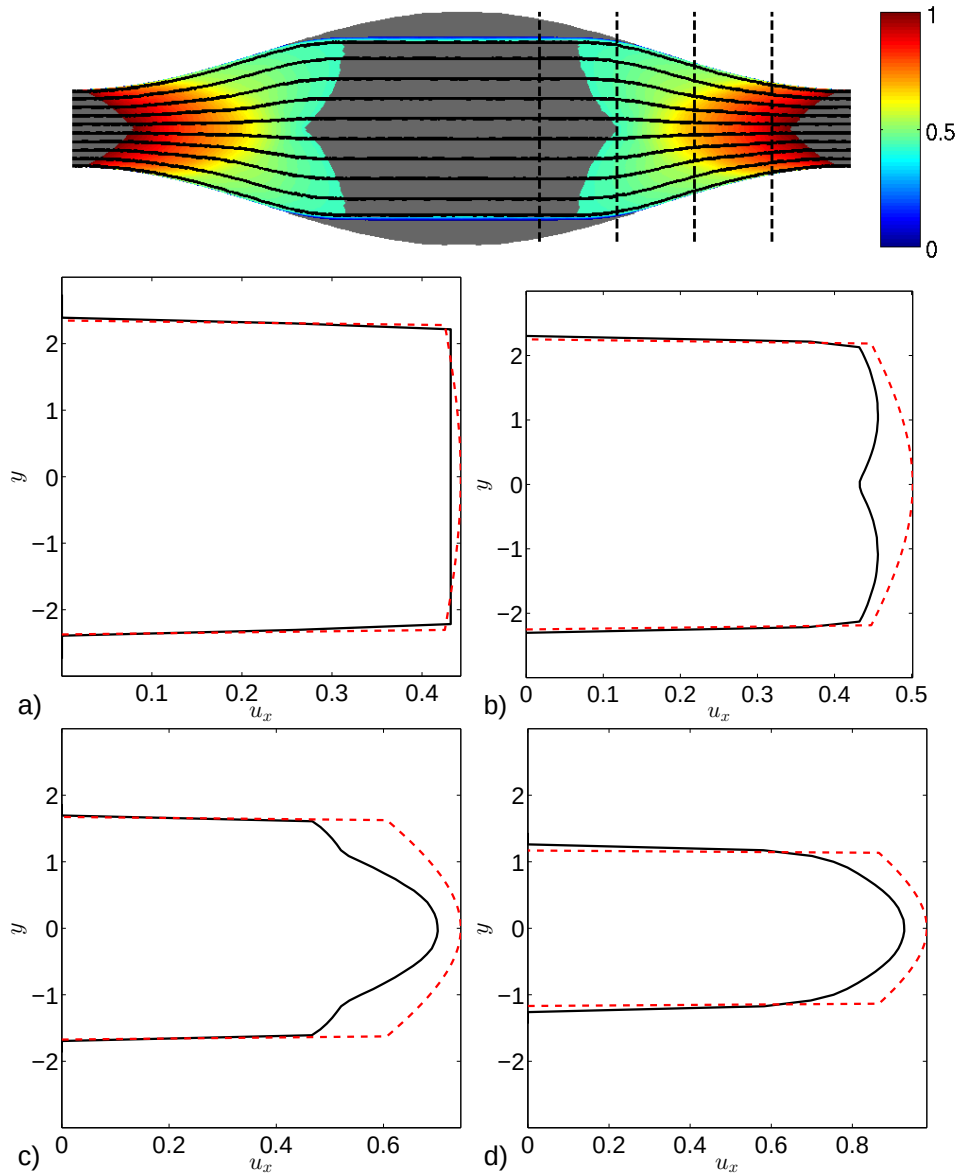

Figure 3.16: Comparison of computed velocity (solid line) with the asymptotic approximation at: a) $2x/L = 0.2$; b) $2x/L = 0.4$; c) $2x/L = 0.6$; d) $2x/L = 0.8$, (as marked by vertical broken lines in the colormap). Main figure shows the colormap of speed with streamlines and unyielded regions in gray; $H = 2,\ L = 20,\ B = 10000$.

thin shear-layer close to the wall. This is not found to be the case here at intermediate L.

On the other hand, parts of the scaling of the previous section are correct. Firstly, the velocity is observed to vanish in a relatively thin layer close to the wall. Secondly, since the strain rate is $\dot{\gamma} \ll B$ within the pseudo-plug, the approximation $\tau \sim B$ holds throughout the pseudo-plug. In place of (3.32), the following is found to give a reasonable representation of the shear stress field within the pseudo-plug:

$$\frac{\tau_{xy}}{B} \sim -\text{sign}(y)\sqrt{1-\left[f_0|h'(x)|\eta^2+\sqrt{1-\eta^2}\right]^2} \tag{3.34}$$

$$\frac{\tau_{xx}}{B} \sim -\text{sign}(h'(x))[f_0|h'(x)|\eta^2+\sqrt{1-\eta^2}] \tag{3.35}$$

where $\eta = y/(1+h(x))$. Note that $f_0 h'(x)$ approximates a normalized τ_{xx} as the walls are approached. Setting $f_0 = 0$, the distribution of (3.32) is recovered, but generally we find that $f_0 \approx 1$ within the pseudo-plug. Figure 3.17 compares (3.35) with the computed stress distributions across the pseudo-plug for 2 different intermediate geometries, in both cases illustrating the good agreement.

Toy model for estimating $j(\mathbf{u})$ as $B \to \infty$

We expect that the intermediate fractures have asymptotic behaviour as $B \to \infty$ that is intermediate between that of the short fractures and the long fractures with no fouling. Let us therefore consider fractures with relatively large L and $H \sim O(1)$ so that $h'(x)$ is relatively small. For simplicity we consider $\psi = 0$. The flow rate constraint determines $Q(\mathbf{u}) = 2L$ and therefore, to estimate Od in the limit $B \to \infty$ it suffices to estimate $j(\mathbf{u})$. We suppose that the limiting flows are divided into 2 distinct regions. Firstly, in the wider part of the fracture we assume that there are fouling layers that fill the deepest parts of the fracture for $x \in (-x_f, x_f)$. Secondly, for $x \notin (-x_f, x_f)$ we assume that there are no fouled regions at the walls of the fracture.

In the unfouled regions the mean velocity in the x-direction is simply

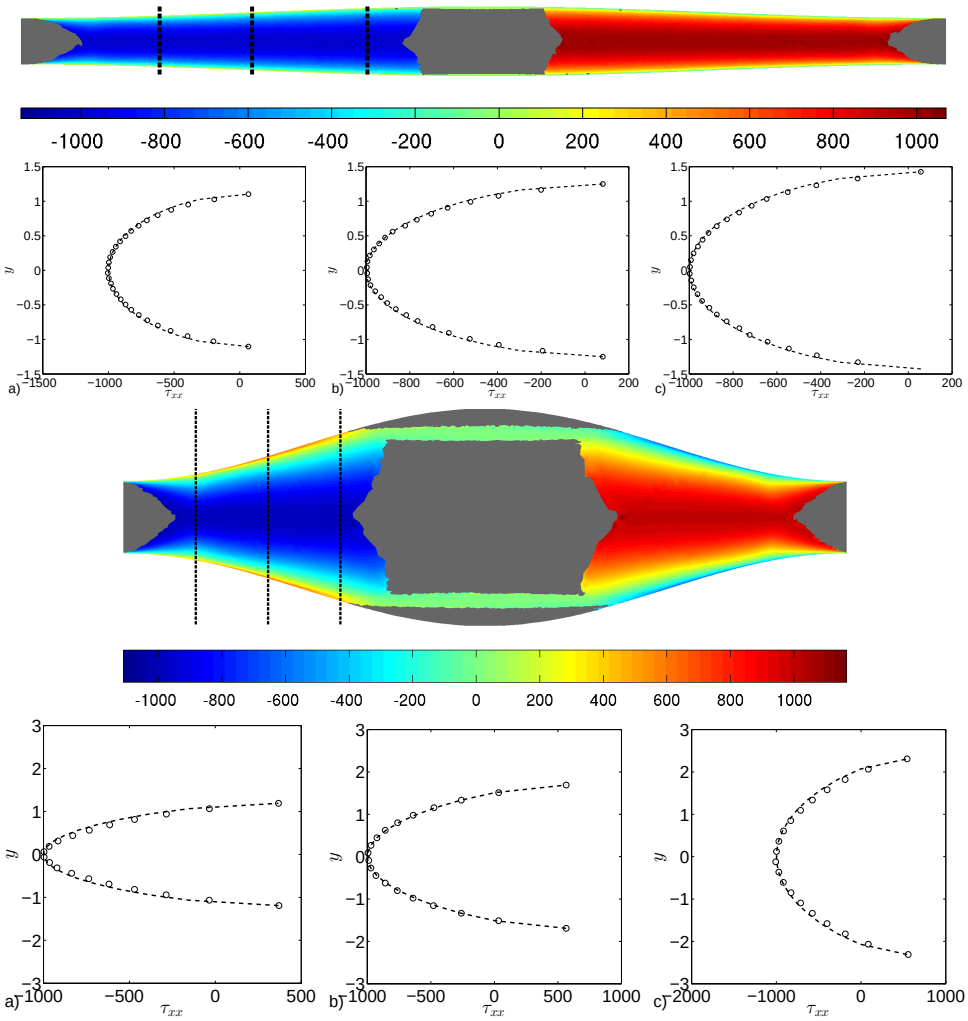

Figure 3.17: Colormaps of τ_{xx} (unyielded regions in gray) for $B = 1000$. Top panels: $H = 0.5$, $L = 40$, comparisons are shown with the predictions of (3.35) at values $2x/L = 0.25,\ 0.5,\ 0.7$, as marked with broken lines on the colormap. Lower panel: $H = 2$, $L = 20$, comparisons are shown with the predictions of (3.35) at values $2x/L = 0.45,\ 0.6,\ 0.8$

$\bar{u} = 1/(1 + h(x))$. In these regions, as we approach the walls, the velocity drops from $u \approx \bar{u}$ to zero over a thin layer of $O(B^{-1/2})$. This thin layer gives a contribution to $j(\mathbf{u})$ of approximate size

$$j_s(\mathbf{u}) \approx 4 \int_{x_f}^{L/2} \frac{1}{1 + h(x)} \, dx,$$

with the subscript denoting the shear layer. Further away from the wall, in the pseudo-plug, we assume that variations from the mean velocity are driven by axial variations in the fracture shape, and that $u \approx \bar{u}$. Assuming $u \approx \bar{u}$ suggests that:

$$\frac{\partial u}{\partial x} \approx -\frac{h'(x)}{(1 + h(x))^2} \quad \Rightarrow \quad v \approx O(h'(x)),$$

and hence we expect the next order of terms approximating u to also have size $O(h'(x))$. It follows that within the pseudo-plug:

$$\dot{\gamma}(\mathbf{u}) = |\dot{\gamma}_{xx}| \left[1 + \left(\frac{\dot{\gamma}_{xy}}{\dot{\gamma}_{xx}} \right)^2 \right]^{1/2} \sim \frac{2|h'(x)|}{(1 + h(x))^2} \left[1 + \left(\frac{\dot{\gamma}_{xy}}{\dot{\gamma}_{xx}} \right)^2 \right]^{1/2}. \tag{3.36}$$

The contributions to $j(\mathbf{u})$ for $x \notin (-x_f, x_f)$, within the pseudo-plug is therefore:

$$j_{pp}(\mathbf{u}) \approx 4 \int_{x_f}^{L/2} \frac{2|h'(x)|}{(1 + h(x))^2} \int_0^{1+h(x)} \left[1 + \left(\frac{\dot{\gamma}_{xy}}{\dot{\gamma}_{xx}} \right)^2 \right]^{1/2} dy \, dx$$

Note that since we have assumed $\psi = 0$ we have exploited symmetry in both x and y to simplify this expression. To calculate the strain rates we assume that (3.34) & (3.35) approximate the stresses in the pseudo-plug. The ratio

of the strain rates is then given by that of the stresses. Therefore, we find:

$$\int_0^{1+h}\left[1+\left(\frac{\dot{\gamma}_{xy}}{\dot{\gamma}_{xx}}\right)^2\right]^{1/2} dy = (1+h)\int_0^1 \frac{1}{f_0|h'|\eta^2+\sqrt{1-\eta^2}}\, d\eta$$
$$= \frac{\pi}{2}\frac{1+h}{1+\sqrt{f_0|h'|}} \approx (1+h)\frac{\pi}{2}[1+O(|h'|^{1/2})],$$
$$j_{pp}(\mathbf{u}) \approx 4\pi\int_{x_f}^{L/2}\frac{|h'|}{(1+h)}\frac{1}{1+\sqrt{f_0|h'|}}\, dx = 4\pi\ln(1+h(x_f))[1+O(|h'|^{1/2})].$$

Secondly, we consider $x \in (-x_f, x_f)$, where only a thin layer of fluid is sheared. The contribution $j_f(\mathbf{u})$ to $j(\mathbf{u})$ from the fouling region comes from the thin shear layers, at $y \approx \pm[1+h(x_f)]$. The plug velocity is approximately $u_p \approx [1+h(x_f)]^{-1}$ and it therefore follows that:

$$j_f(\mathbf{u}) \approx \frac{4x_f}{1+h(x_f)}[1+O((d_0')^2),$$

where again $d_0(x,B)$ is taken to represent the width of the sheared layer (see the analysis of the short fracture). To summarise, if x_f is known then $j(\mathbf{u})$ is approximately:

$$j(\mathbf{u}) \approx j_s(\mathbf{u}) + j_{pp}(\mathbf{u}) + j_f(\mathbf{u})$$
$$\approx 4\int_{x_f}^{L/2}\frac{1}{1+h(x)}\, dx + 4\pi\ln(1+h(x_f)) + \frac{4x_f}{1+h(x_f)} + ...$$

where the additional terms are of smaller order in either $1/L$ or $1/B$. Consequently, as $B \to \infty$ we approximate:

$$Od(x_f) \sim \frac{Q(\mathbf{u})}{j(\mathbf{u})} \approx$$
$$\frac{L/2}{\displaystyle\int_{x_f}^{L/2}\frac{1}{1+h(x)}\, dx + \frac{x_f}{1+h(x_f)} + \pi\ln(1+h(x_f))} \tag{3.37}$$

In general we expect that the strain rate is minimized, amongst all con-

straints. If we regard x_f as being selected in this way, the actual x_f is determined by maximizing $Od(x_f)$ with respect to x_f, thus giving Od_c. Note that the first 2 terms in the denominator of (3.37) effectively interpolate between the limiting Od_c derived for short channels ($x_f \to L/2$) and that for long channels with no fouling ($x_f \to 0$). The 3rd term in (3.37) also vanishes as $x_f \to L/2$, so that the expression for short channels is contained in (3.37).

Figure 3.18a shows examples of the variation of $Od(x_f)$ computed from (3.37) for $L = 20,\ H = 0,\ 1, ...8$ (black), and $L = 6,\ H = 0,\ 0.25,\ 0.5...2$ (red). The maximum of $Od(x_f)$ is attained either at an endpoint or at the zero of:

$$x_f = \pi(1 + h(x_f)), \tag{3.38}$$

which is straightforwardly computed. For the examples shown, for $L = 6$ the maximum is $Od_c = 1$, attained at $x_f = L/2$, for all H. As $(1 + h(x_f)) \in [1, 1 + H]$, we see that the above equation has a root only for $L > 2\pi$. Since when this is not satisfied we find $Od_c = 1$, which is the short fracture limit we adopt the condition

$$L < 2\pi, \tag{3.39}$$

as our definition of *short* fractures. At larger L we see that there is a maximum in $(0, L/2)$ and compute this numerically. As $L \to \infty$ we find that $2x_f/L \to 0$ since $x_f \to (1+H)\pi$. The 2nd and 3rd terms in the denominator of (3.37) then become $O(1/L)$ smaller than the first, which converges to Od_c for the long fracture limit without fouling. Figure 3.18b shows the variation of Od_c with L for 2 values of H, computed as the maximum of (3.37). For L satisfying (3.39) we see $Od_c = 1$, increasing smoothly to the asymptotic values for no fouling at large L, marked with the broken lines.

We have computed Od_c from this toy model, by maximizing (3.37) over x_f. Figure 3.19a & b plot respectively Od_c and x_f as functions of (H, L). We see that the limiting behaviour for both short and very long fractures is represented in Od_c. As (H, L) both increase the predicted Od_c also increases away from 1. The computed values of x_f are close to $L/2$ for short fractures and approach zero only for very long fractures (Fig. 3.19b). Figure 3.19c presents a contour plot of the largest values of Od attained in our compu-

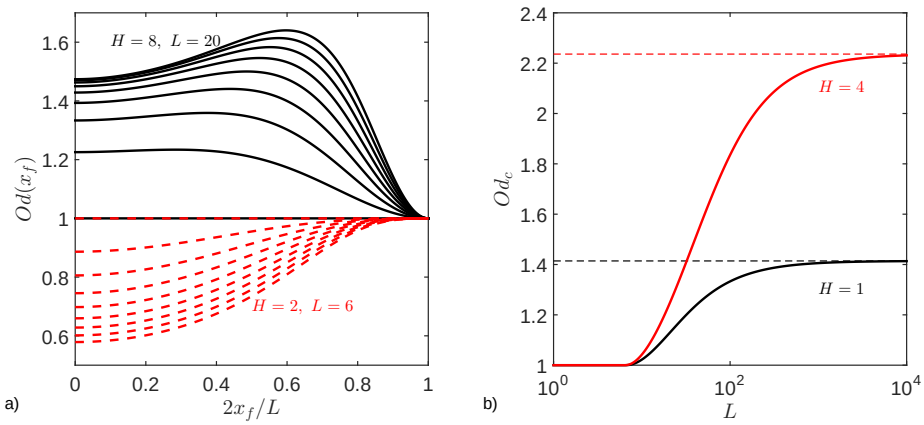

Figure 3.18: a) Variation of $Od(x_f)$ from (3.37) for: $L = 20$, $H = 0,\ 1, ...8$ (black); $L = 6$, $H = 0,\ 0.25,\ 0.5...2$ (red). b) Variation of Od_c (computed by maximizing $Od(x_f)$ in (3.37)) with L for $H = 1$ (black) and $H = 4$ (red). Broken lines indicate the limit of Od_c with no fouling.

tations at each (H, L), (typically computed for $B = 10^4$), which may be regarded as a computed estimate of Od_c. Comparing with Fig. 3.19a we see that the qualitative trends are extremely well represented by this approximation and the quantitative agreement is good for either smaller H or smaller L, but deteriorates as both parameters increase. This is of course not surprising as the approximation is based on the strain rates being driven mostly by variation in $\bar{u}$ with x, and we have neglected correction terms involving $f_0|h'|$ (valid for large L). Figure 3.19d plots the relative error between the computed Od_c from our 2D computed results and that approximated from maximizing (3.37). We see that the relative error is $< 10\%$, close to the axes and increases to approximately 15% over much of the (H, L) parameter space explored. Evidently, once both H and L are much larger than 1 the geometry represents a large vacuous space rather than a fracture.

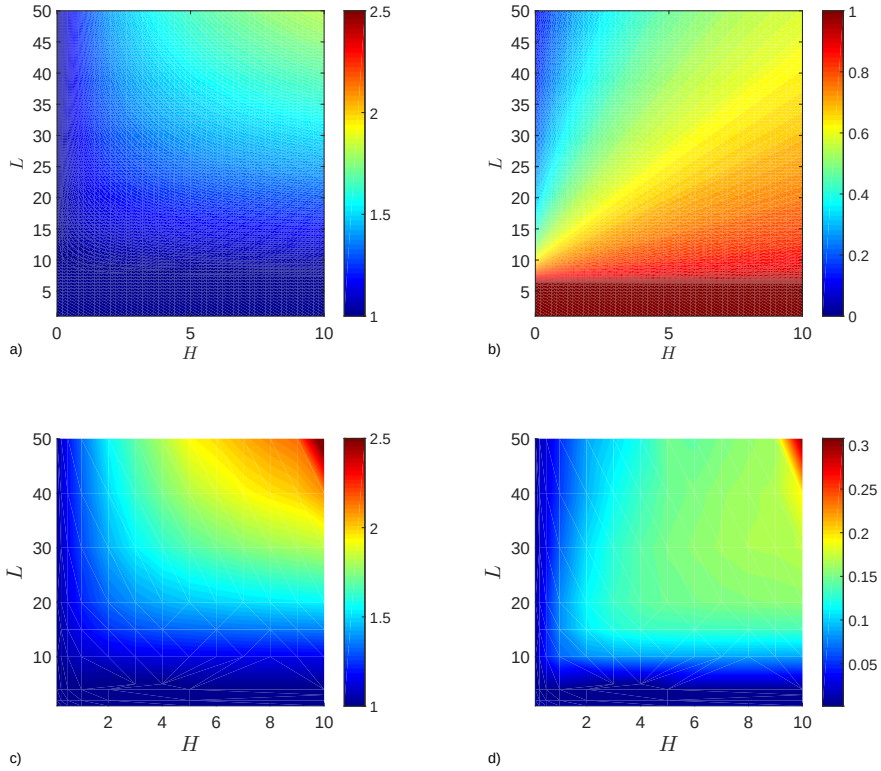

Figure 3.19: a) Variation of Od_c, computed by maximizing (3.37). b) Variation of the value of x_f, that maximizes (3.37), scaled with $L/2$. c) Variation of Od_c, approximated as the largest value of Od from our 2D computations, typically at $B = 10^4$. d) Absolute relative error between a & c.

An improved toy model

Although the relative errors in Fig. 3.19d are reasonable, it is possible to improve the estimate of $j(\mathbf{u})$. From consideration of Fig. 3.16 and similar, it is evident that the pseudo-plug behaviour is more complex than that given by the proposed $j_{pp}(\mathbf{u})$. The simplest improvement is to include the

neglected $f_0|h'|$ term, i.e.

$$j_{pp}(\mathbf{u}) \approx 4\pi \int_{x_f}^{L/2} \frac{|h'|}{(1+h)} \frac{1}{1+\sqrt{f_0|h'|}}\, dx. \tag{3.40}$$

The stress approximations (3.34) & (3.35) can be matched with the computed stresses at each x in the pseudo-plug, approximating $f_0(x)$ from the stress values close to the wall. Interestingly, this procedure suggests that $f_0(x) =$ constant throughout the pseudo-plug region. Inspection of many computations suggests that $f_0 \approx 1$.

We may now repeat the same procedure as for the toy model. We find x_f by maximizing Od_{x_f}, now given by:

$$Od(x_f) \sim \frac{Q(\mathbf{u})}{j(\mathbf{u})} \approx \frac{L/2}{\displaystyle\int_{x_f}^{L/2} \frac{1}{1+h(x)}\, dx + \frac{x_f}{1+h(x_f)} + \pi \int_{x_f}^{L/2} \frac{|h'|}{(1+h)} \frac{1}{1+\sqrt{f_0|h'|}}\, dx}. \tag{3.41}$$

This results in Od_c and x_f as illustrated in Fig. 3.20a & b, respectively. We observe a general increase in Od_c and a small shift in x_f. The relative error with the computed 2D results is however diminished; see Fig. 3.20c, now typically remaining below 10% for most of the parameter space.

3.4.6 Affine fractures

Finally we present some examples of the limiting process in affine fractures. Three different styles of affine fracture are generated for intermediate $H = 2$, $L = 20$. Figures 3.21-3.23 present the sequence $B = 100,\ 1000,\ 10000$ for each case, plotting the speed, streamlines and unyielded plug regions. In general we observe that the small scale fracture roughness is always fouled. As B increases a larger fraction of the fracture becomes immobilised. The boundaries of the flowing part of the fracture are formed by arc-like surfaces that span between locally narrow points of the fracture wall. The radius of curvature of these surfaces increases with B.

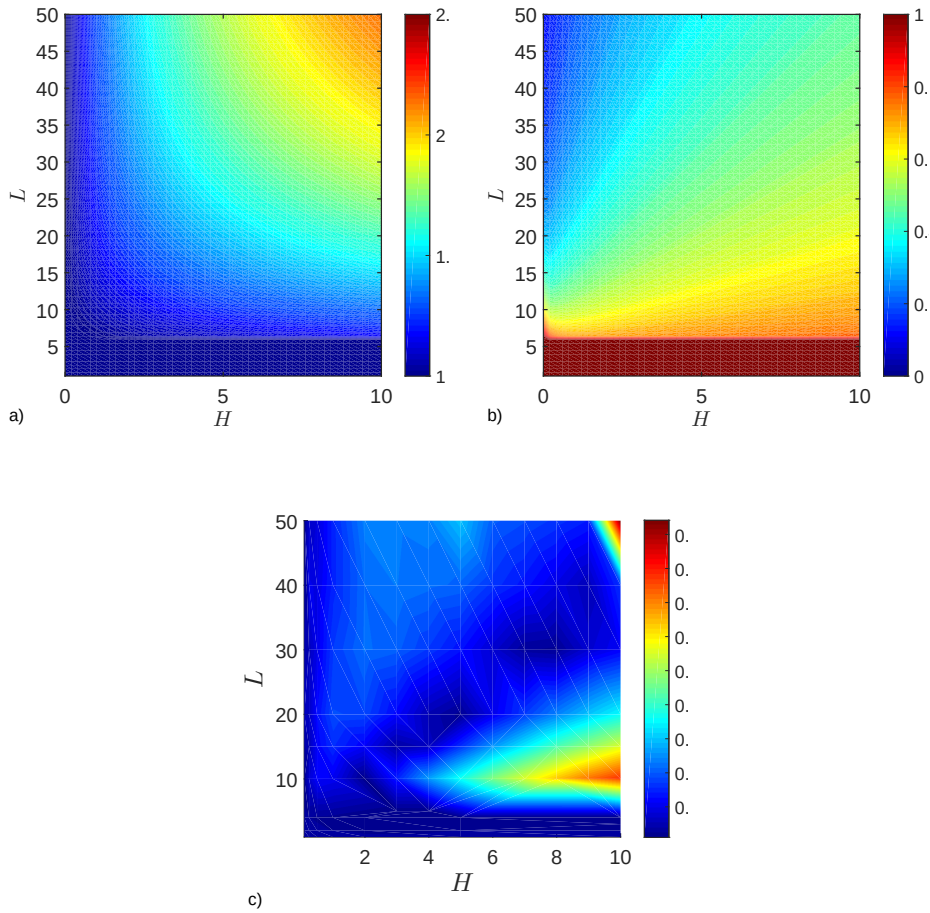

Figure 3.20: a) Variation of Od_c, computed by maximizing (3.41). b) Variation of the value of x_f, that maximizes (3.41), scaled with $L/2$. c) Absolute relative error between a & our Od_c calculated from the 2D computations.

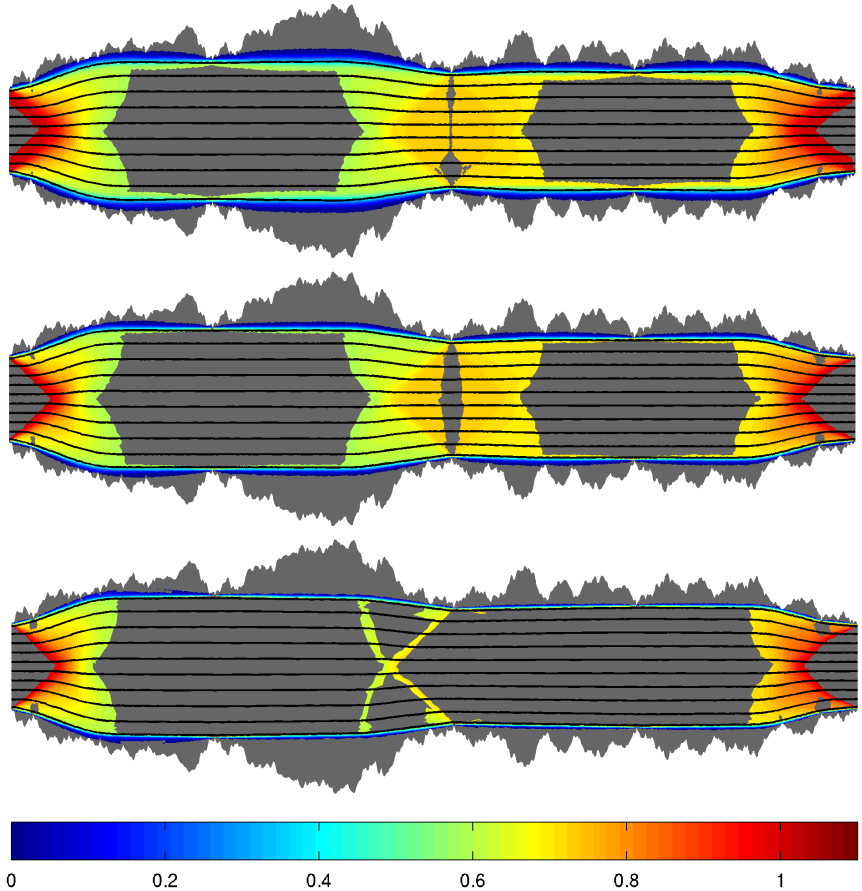

Figure 3.21: Computed examples of speed $|\mathbf{u}|$ & streamlines for a symmetric affine fracture. Parameters are: $H = 2$, $L = 20$, $B = 100,\ 1000,\ 10000$, from top to bottom, with (gray) unyielded plugs.

It is notable that as B increases, the self-selected flowing channel geometry consists of a series of joined segments along which the streamlines are approximately parallel. In such sections shear components evidently dominate. These parallel segments are connected by angular converging and diverging segments, in which extensional stresses and strain rates will be significant. The limiting process as $B \to \infty$ appears to result again in a combination of thin yielded shear-layers and non-vanishing $O(1)$ pseudo-plug

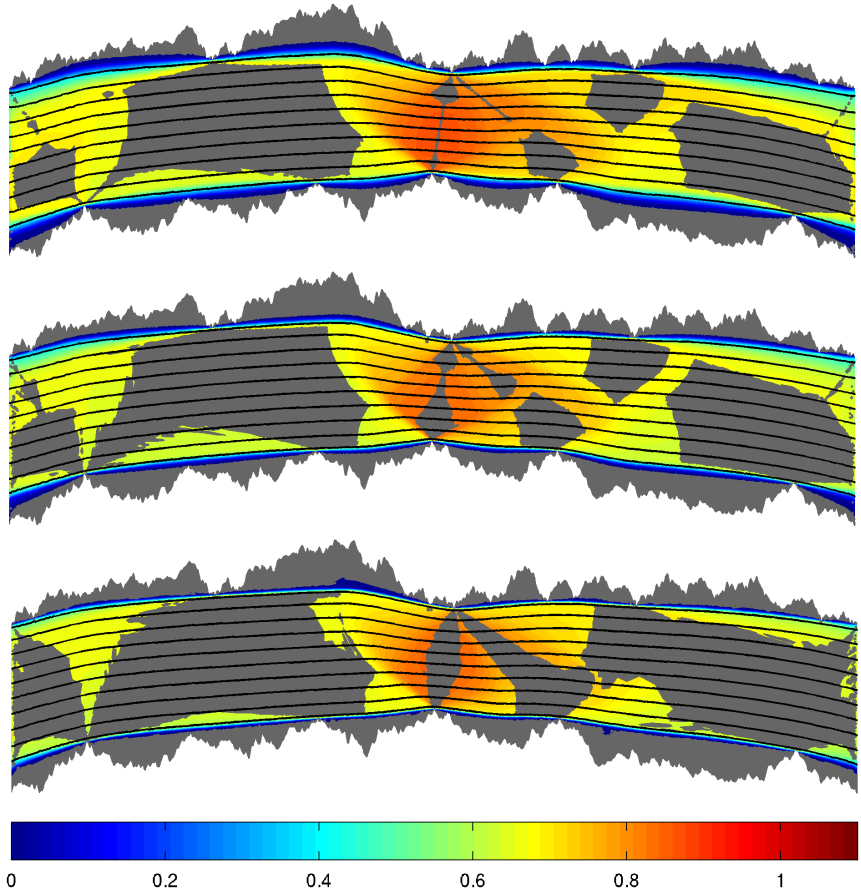

Figure 3.22: Computed examples of speed $|\mathbf{u}|$ & streamlines for a fracture formed from two different affine surfaces. Parameters are: $H = 2$, $L = 20$, $B = 100,\ 1000,\ 10000$, from top to bottom, with (gray) unyielded plugs.

regions. Although the evident complexity of the self-selection and limiting processes so far elude a simple explanation, there is some hope that these component structures can be understood. Thus, if one can first understand the geometric features of flow self-selection (meaning the fouling process and orientation of flowing part of the fracture, generating tortuosity) it should be possible to estimate the critical pressure drops (or yield stresses).

More quantitatively, we may evaluate Od_c for these geometries from the

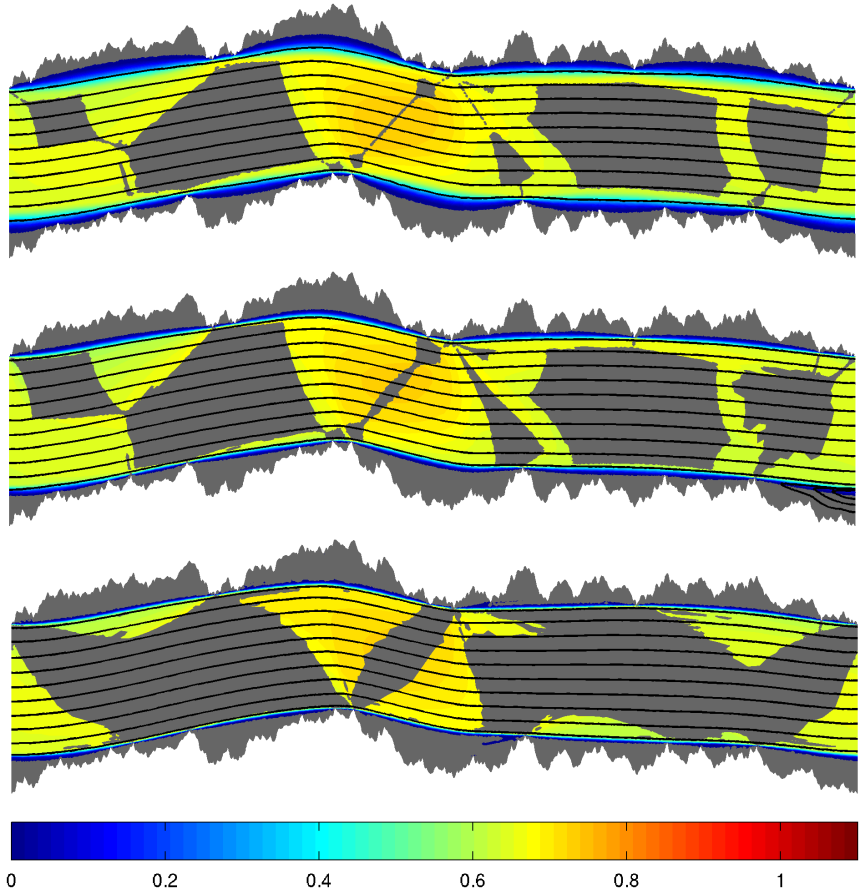

Figure 3.23: Computed examples of speed $|\mathbf{u}|$ & streamlines for a fracture formed from two identical affine surfaces, shifted. Parameters are: $H = 2$, $L = 20$, $B = 100,\ 1000,\ 10000$, from top to bottom, with (gray) unyielded plugs.

computed 2D solution. Figure 3.24 shows convergence of $Od \to Od_c$ as $B \to \infty$. The symmetric fracture has the smallest Od_c, and also appears to have the more constricted flow apertures. The other 2 geometries appear to compensate increasing tortuosity (smaller Od) with an larger effective channel width (larger Od).

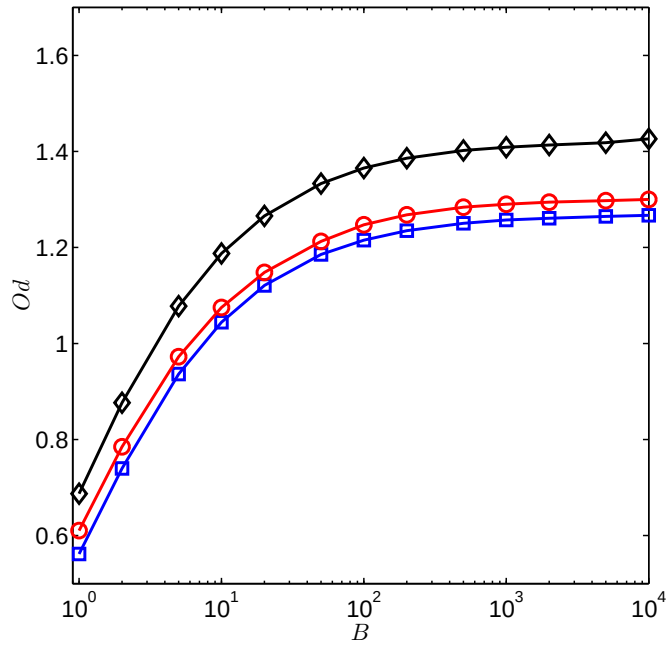

Figure 3.24: Computed Oldroyd number as function of the Bingham number for the three different affine fractures of Figs. 3.21-3.23. Blue squares: the two surface are symmetrical. Red circles: the two surfaces are uncorrelated. Black lozenges: the two surfaces are identical, shifted laterally with a constant gap.

3.5 Discussion and summary

In this chapter we have investigated the two-dimensional flow of a Bingham fluid along an uneven fracture. The work has 2 principal foci. Firstly, to determine numerically the flow rate-pressure drop relationship in such geometries (the appropriate Darcy law), to understand better the limits of simple approximations that are presently used in a somewhat *ad hoc* manner. Secondly, we explore the limiting values of pressure drop (equivalently yield stress) at which non-zero flows are first found. This question has critical consequences for the study of flow onset in pressure driven porous media

flows, i.e. selection of the critical initial path, as well as helping provide practical estimates for invasive sealing of porous media/channels, i.e. how far will a sealing fluid penetrate under a given driving pressure?

The initial part of the chapter has extensively studied geometric effects in idealised fractures (periodic with wavy or triangular profiles) of dimension (H, L). Strict application of lubrication/Hele-Shaw type approximations to the Darcy law has been shown to be limited to $H/L \ll 1$, as may be expected. As a rule of thumb, errors of 10% or less appear to require $H/L \lessapprox 1/20$. For geometries outside of these limits, flow approximations are vulnerable to similar effects to Newtonian fluids, e.g. developing tortuosity etc. One significant difference between Newtonian and Bingham (or other generalised Newtonian) fluids is in the coupling of geometrical and rheological parameters in the flow law. In the Newtonian fluid literature there are many efforts to improve and extend Darcy-law type estimates to these situations. Here we have resisted the temptation to develop analogous methods. It is clear that some of these methods would be effective, especially in the limit of low B and for H/L increasing away from the lubrication limit, but inflicting this algebraic misery on the reader is left to other researchers.

Moving to larger B or for $H/L \not\ll 1$ a more serious limitation of lubrication type approximations to the Darcy law emerges. Unyielded fluid appears at the wall in deeper parts of the fracture (fouling layers). Fouling layers provide an $O(1)$ adjustment of the flowing area and hence $O(1)$ errors in the predictions of lubrication type approximations. We have demonstrated that these errors can be reduced significantly, by adopting the yield surface of the fouling layers as the new fracture wall and applying the usual lubrication approximation. Therefore, approximating the flow-law presents no particular problem provided the fouling layers are known. Unfortunately, this is not the case as the fluid self-selects the flowing area.

Previous work has addressed the question of onset of fouling in idealized geometries with $O(1)$ variations [208, 209]; (see Chapter 2 & Chapter 4). Smaller scale roughness also seems to readily foul, although to our knowledge this has not been quantified. At intermediate B estimating the degree of fouling appears difficult, as a general problem for which one would like to

specify a simple predictive closure relationship. However, numerical solution as here is an effective tool even for the very complex affine geometries, and can be easily extended to more general yield stress fluid models. The other parameter range where fouling can be predicted is that in which $B \to \infty$ and the flow stops.

A significant part of the chapter has considered the limit of no flow $B \to \infty$, which via a rescaling can be characterized with the Oldroyd number:

$$Od \equiv \frac{\hat{L}}{\hat{D}} \frac{\hat{\tau}_Y}{\Delta \hat{P}}, \tag{3.42}$$

directly representing the balance between applied pressure and resisting yield stress. Above a critical value Od_c there is no flow. On the theoretical side, we have formally characterized Od_c as a limiting ratio of flow rate to plastic dissipation, shown that this limit is attained by the velocity solution, and provided general bounds on convergence of the viscous dissipation, plastic dissipation and flow rate, in the limit $Od \to Od_c^-$. We have then studied the approach to Od_c numerically and asymptotically for simpler symmetric fracture geometries, deriving the leading order behaviour in the cases of both short and long-thin fractures.

For short fractures we find that $Od_c = 1$: at large B the flow consists of an intact central plug region separated from the walls (and fouling layers) by a progressively thinning shear layer. This limit is analogous to the flow in a uniform channel, for which also $Od_c = 1$. Short fractures, for the purposes of this limiting process, are defined as $L < 2\pi$. For long-thin fractures no fouling occurs and the lubrication approximation is valid, leading to a readily calculable $Od_c > 1$.

Intermediate fractures are more interesting. The central plug region here is broken into 2 parts (in wide and narrow parts of the fracture) and remains so as $B \to \infty$. The plug in the widest part occupies a length approximately equal to that of the fouling layer (defined as $2x_f$), whereas the size of plugs in the narrowest part of the fracture remains of $O(1)$. Between the two plug regions we find a slightly sheared pseudo-plug region. The pseudo-plug joins to the wall in a narrow layer of high shear and a similar high shear layer

separates fouling layers and the central plug in the wide part of the fracture. Based on these observations, we have proposed a rather simple toy model to describe the limiting flows. In each of the above regions we are able to estimate the strain rate and hence construct an approximation to the plastic dissipation that depends only on the single parameter x_f, the half-length of the fouled layers. Via minimizing the plastic dissipation at fixed flow rate we are able to estimate both x_f and to calculate the limiting Od_c. The relative errors in this crude approximation are typically $\lessapprox 10 - 15\%$, allowing us to effectively predict critical pressure for the onset of flow.

We have also performed several simulations in self-affine fracture as shown in Figs. 3.21-3.23. Although these geometries deserve a far more complete study, we may infer some trends from our current results. Firstly, both pseudo-plugs and the fouling layers are present in the affine fractures. Secondly, the limiting zero flow behaviours again appears to be characterized by geometries that simplistically are componentwise constructed of shear layers, pseudo-plugs and fouled regions. This leads us to the conclusion that to understand the flow one needs to understand how the fouling layer is self-selected. It seems for instance obvious that it acts as a filter for the small scales - the roughness problem. It is however unclear how the larger-scale heterogeneities are filtered. Similarly to the wavy fractures, the final selected flowing channel seems to have a rather constant width, at least in sections.

Finally, we should observe that the critical Oldroyd number frequently is quite far from that obtain by the lubrication approximation, where it is derived from the harmonic mean of the fracture width. The result has a strong consequence if one want to investigate onset/channelization in porous media or in a rough Hele-Shaw cells (2D fractures). As seen, the range of wavelengths for which the naïve lubrication approximation is valid is limited and its usage will incur $O(1)$ errors.

Chapter 4

Stokes flow through washouts

In this chapter we begin to study the industrial flows that arise in the primary cementing of oil and gas wells, in cases where the well has a washed out section. This narrow annular geometry is idealized by studying flows in a longitudinal 2D section. We perform a detailed computational study of the flow of a Bingham fluid along a narrow channel, with one locally uneven wall (the washed out section of an oil well about to be cemented). By studying a wide range of different washout geometries, of differing shapes characterized by dimensionless height h and length L, we discover that the flows exhibit a type of self-similarity in the limit of large h and B. More specifically, in this limit we find that regardless of the washout geometry, the area of the channel that contains moving fluid is the same for each L. Essentially, uneven and distant parts of the washout become full of static fluid, below the yield stress, while the flow self-selects its own unique geometry. The washout geometry with the largest flowing region within the washout, appears to be the square wave. We show how a simple correction can be calculated that allows one to predict the flowing area for other washout geometries. Lastly, we examine the effect on the pressure drop of different washout geometries.

The flows considered in this chapter are Stokes flows, which might correspond to the breaking of circulation in the well, i.e. low initial flow rate. This restriction is to enable us to study a simplified initial problem with only 3 dimensionless groups, while addressing some of the complexity of the geom-

etry (which is typically unknown in a washout). Subsequently, in Chapter 5 we consider inertial flows and later in Chapter 6 we consider later in the cementing process when the drilling mud is displaced by another fluid.[1]

4.1 Introduction

A crucial part of the primary cementing operation [176] is the removal of drilling mud from the annular space between casing and formation. This occurs during the fluid displacement (or cement placement) phase of the process, which is itself a complex flow not fully understood; see e.g. [33, 49, 189]. Prior to the fluid displacement phase, most service companies and operators recommend to pre-circulate the well, by pumping the drilling mud from the bottom to the top of the well at least once ("circulating bottoms-up").

The circulation phase has two main purposes. Firstly, drilled cuttings and other solids still in the well, which may have settled as the casing is run in to the borehole, are cleared from the flowpath. Secondly, the circulation serves to shear the mud and hence condition it prior to displacement. Depending on the operational circumstances and the type of drilling mud, the mud may have been static in the borehole for a period of hours before circulation. Over this time significant gel strengths may develop due to thixotropic effects. Simplistically speaking this gel strength is destroyed by shear, returning the drilling mud to its dynamic yield stress (which may still be significant).

Unlike drilling geometries, the annuli in primary cementing are relatively narrow. If the borehole is reasonably uniform, the flow is primarily in the axial direction and on each azimuthal section the largest shear stresses are found at the walls of the annulus. The wall shear stresses are smaller on the narrow side of the eccentric annulus. This means that there is a critical minimal pressure gradient that must be exceeded in order to mobilize the

[1] A version of this chapter has appeared as: A. Roustaei, A. Gosselin & I. Frigaard. "Residual drilling mud during conditioning of uneven boreholes in primary cementing. part 1: Rheology and geometry effects in non-inertial flows." *J. Non-Newt. Fluid Mech.*, **220**:87–98, (2015).

drilling fluid on the narrow side of the annulus; see e.g. [157, 225, 246]. Thus, stationary residual drilling fluid is an inherent part of flowing through irregular geometries.

A different type of irregularity occurs in poorly consolidated formations that may partially collapse during the drilling process. The resulting "washouts" (see e.g. Fig. 4.1) are geometrically dependent on both the drilling hydraulics and the local geology, hence unpredictable, although sometimes measured using a caliper. The effect on mud circulation of such geometries can however be guessed: for sufficiently deep washouts we expect the drilling mud to remain static within parts of the washout during the circulation operation. The objective of this chapter is to begin to systematically study this phenomenon, with the aim of being able to offer quantitative predictions.

We have not found any work that directly studies this problem. Three difficulties present themselves. First, the washout geometries are unpredictable and three-dimensional (3D), making analytical study difficult and computational study slow. Second, the critical feature of the yield stress in the drilling mud must be accounted for physically and computationally in a way that distinguishes slowly flowing regions from stationary regions. For example, slow flows past cavities of Newtonian fluids can yield arbitrarily slowly moving fluid, see e.g. [166]. Thirdly, a range of flows are experienced in cementing and drilling operations (see [41, 176]), ranging from the breaking of circulation through to fully turbulent flows. Thus, at the outset it is necessary to focus in on specific flow types and make simplifications in order to make the problem tractable while still preserving some relevance. In this chapter we study non-inertial or Stokes flow solutions ($Re = 0$) past two-dimensional (2D) washout regions.

A number of authors have studied flow of yield stress fluids past cavities or expansions, either in 2D or axisymmetric geometries. Mitsoulis and coworkers (e.g. [164]) have studied both planar and axisymmetric expansion flows, over a wide range of Bingham and Reynolds numbers, showing significant regions of static fluid in the corner after the expansion. Flow of yield stress fluids through an expansion-contraction has been studied experimen-

tally and computationally in [79, 174, 175]. In [79] Carbopol solutions were pumped through a sudden expansion/contraction, i.e. narrow pipe – wide pipe – narrow pipe. A range of flow rates were studied and the yield surfaces were visualised nicely by a particle seeding arrangement. Inertial effects are evident in asymmetry of the flow. For all the experiments shown, stagnant regions first appear in the corners of the expansion and for all the results shown there are stagnant regions. Comparisons are made between experimental and numerical results, which are at least qualitatively in agreement, see [79, 174]. In [175] qualitatively similar computations are carried out, but using an elasto-viscoplastic model.

Previous work has studied flow along a symmetric 2D wavy channel. Small amplitude long wavelength perturbations from a uniform channel geometry have been studied in [102, 199]. The focus is on deformation and breaking of the central plug region. Secondly, in [208] (see Chapter 2) we have studied larger amplitude perturbations, using a numerical method similar to that here. We have derived predictions for the onset of stationary fluid regions (*fouling layers*), which occurred always initially at the walls in the widest part of the channel, quantified in terms of a critical *slope* of the wall. The main difference between the present chapter and [208] is that, having noticed qualitative difference between smooth wavy walls and abrupt expansion-contractions, we now begin to consider geometric variability in a more systematic way, i.e. we aim to derive results that may be applicable to generic washout shapes.

An outline of this chapter is as follows. In §4.2 we derive the general model and describe the four washout geometries that we study. We also present an overview of the computational method, targeted here at $Re = 0$. For the results we first present examples of typical variations in the velocity, unyielded plug boundaries and the stress components, for the four washout geometries as the depth is increased; see §4.3.1. This is followed by a more systematic study of geometry and yield stress effects in §4.3.2, focusing only on the plug regions. We show that the onset of stationary flow is more complex than suggested in [208], but in contrast for large enough amplitudes a type of similarity emerges between geometries as the flow self-selects the

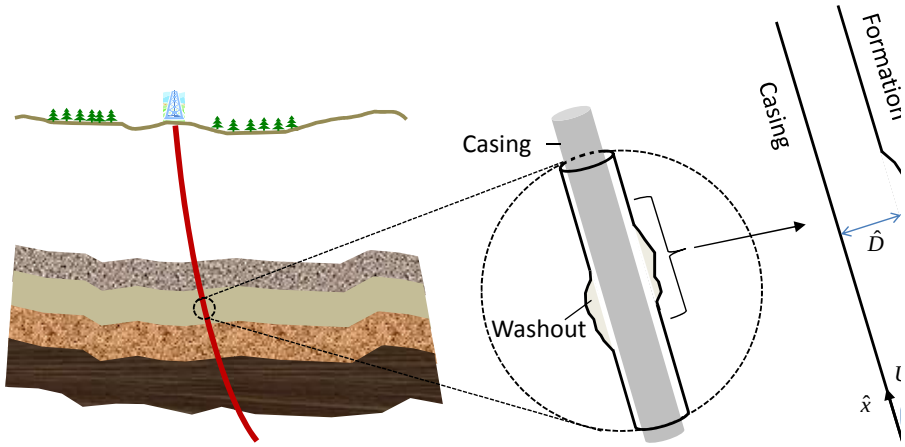

Figure 4.1: Geometry of the washout in a section along the annulus.

flowing area. Section 4.3.3 describes our analysis of this self-selection and how to predict the flowing area of the washout. In 4.3.4 we describe the effects of the washout on the pressure drop along the channel, in terms of a correction. The chapter closes with a summary in §4.4.

4.2 A simplified washout model

Primary cementing circulation occurs through a long narrow eccentric annulus. In many situations, restrictions on frictional pressures limit the flow rates to the laminar regime, in which case the main velocity components are along the borehole axis, with azimuthal flows driven by slow axial variations in eccentricity. Supposing in this situation that we have a washout section, a reasonable simplification of the flow might be to consider a two-dimensional (2D) azimuthal-axial slice through the annulus; see Fig. 4.1. Neglecting azimuthal flow, the channel formed has an in-gauge width $\hat{D}$ (dependent on the inner and outer diameters and the eccentricity), being bounded on the inside by the casing and on the outside by the formation.

The washout geometry is as yet unspecified, but in the 2D section described we will characterize the washout as having a length $\hat{L}$ and a maximum amplitude $\hat{H}$. Coordinates $(\hat{x}, \hat{y})$ are aligned along the channel and

across the annular gap, respectively; see Fig. 4.1. Fluid circulates axially along the 2D section and we might assume a mean velocity $\hat{U}_0$ in the $\hat{x}$-direction. As a typical width, $\hat{D}$ is in the range $3-80$ mm, the drilling mud may be considered as locally incompressible over the length of the washout, even for $\hat{L}$ of the order of a few meters. A suitable model therefore is given by the Navier-Stokes equations for an incompressible viscous fluid. Non-Newtonian effects are significant and principal amongst these is the yield stress effect (at least for the flows we consider). The simplest rheological model containing a yield stress is the Bingham fluid. This model is also one that is used in drilling applications, although more complex models (e.g. Herschel-Bulkley) are also used. We use the Bingham constitutive model here, characterizing the fluid via its density $\hat{\rho}$, yield stress $\hat{\tau}_Y$ and plastic viscosity $\hat{\mu}$. Although a gross simplification, the key feature of yielding/not-yielding is captured by this model.

The Navier-Stokes equations are made dimensionless using $\hat{D}$ and $\hat{U}_0$ as length and velocity scales, respectively. Time is scaled with $\hat{D}/\hat{U}_0$, the shear stresses are scaled with $\hat{\mu}\hat{U}_0/\hat{D}$ and the static pressure is subtracted from the pressure before also scaling with $\hat{\mu}\hat{U}_0/\hat{D}$. The resulting equations are:

$$Re\frac{Du}{Dt} = -\frac{\partial p}{\partial x} + \frac{\partial}{\partial x}\tau_{xx} + \frac{\partial}{\partial y}\tau_{xy}, \tag{4.1}$$

$$Re\frac{Dv}{Dt} = -\frac{\partial p}{\partial y} + \frac{\partial}{\partial x}\tau_{xy} + \frac{\partial}{\partial y}\tau_{yy}, \tag{4.2}$$

$$0 = \frac{\partial u}{\partial x} + \frac{\partial v}{\partial y}, \tag{4.3}$$

where $\mathbf{u} = (u, v)$ is the velocity, p is the modified pressure and τ_{ij} is the deviatoric stress tensor. The constitutive laws are:

$$\tau_{ij} = \left(1 + \frac{B}{\dot{\gamma}(\mathbf{u})}\right)\dot{\gamma}_{ij} \Longleftrightarrow \quad \tau > B \tag{4.4a}$$

$$\dot{\gamma}_{ij}(\mathbf{u}) = 0 \Longleftrightarrow \quad \tau \leq B, \tag{4.4b}$$

where

$$\dot{\gamma}_{ij}(\mathbf{u}) = \frac{\partial u_i}{\partial x_j} + \frac{\partial u_j}{\partial x_i}, \qquad \mathbf{u} = (u, v) = (u_1, u_2),\ \mathbf{x} = (x, y) = (x_1, x_2).$$

and $\dot{\gamma}$, τ are the norms of $\dot{\gamma}_{ij}$, τ_{ij}, defined as

$$\dot{\gamma} = \sqrt{\frac{1}{2}\sum_{ij} \dot{\gamma}_{ij}^2} \qquad \text{and} \qquad \tau = \sqrt{\frac{1}{2}\sum_{ij} \tau_{ij}^2}. \tag{4.5}$$

Two dimensionless numbers appear above. Firstly, the Reynolds number, Re:

$$Re \equiv \frac{\hat{\rho}\hat{U}_0\hat{D}}{\hat{\mu}}, \tag{4.6}$$

which represents the ratio of inertial to viscous effects. Secondly, the Bingham number, B:

$$B \equiv \frac{\hat{\tau}_Y\hat{D}}{\hat{\mu}\hat{U}_0}, \tag{4.7}$$

represents the competition between yield and viscous stresses. As well as these, two geometric dimensionless parameters result: $h = \hat{H}/\hat{D}$, representing the maximal depth of the washout, and $\delta = \hat{D}/\hat{L}$, characterizing the aspect ratio of the washout.

4.2.1 The model problem, $Re = 0$

For the remainder of this chapter we consider only steady non-inertial flows ($Re = 0$), which would characterize the flow directly after the breaking of circulation, i.e. as the pressure drop is increased sufficiently for drilling mud to begin to flow. The main reason however for the neglect of inertial effects is that our study is focused at the relative importance of viscous and yield stress effects, i.e. the potential for immobility of the mud in the washout, and is sufficiently complicated by geometric considerations. Some simplification is needed in order to be able to extract meaningful results. We might intuitively expect that more problematic cases industrially are likely to be in wells where Re is restricted and stationary regions consequently

large, i.e. does neglect of inertia reflect a worst case situation?

The equations we study therefore are:

$$0 = -\frac{\partial p}{\partial x} + \frac{\partial}{\partial x}\tau_{xx} + \frac{\partial}{\partial y}\tau_{xy}, \tag{4.8}$$

$$0 = -\frac{\partial p}{\partial y} + \frac{\partial}{\partial x}\tau_{xy} + \frac{\partial}{\partial y}\tau_{yy}, \tag{4.9}$$

$$0 = \frac{\partial u}{\partial x} + \frac{\partial v}{\partial y}, \tag{4.10}$$

For a computational domain we extend the channel uniformly both upstream and downstream of the washout section; see Fig. 4.2. The two extensions are determined empirically (see below in §4.2.3), to be sufficient to allow that imposition of a constant drop in pressure along the channel produces fully developed velocities at both $x = -1/2\delta - l_d$ (entry development length) and at the exit, $x = 1/2\delta + l_e$. If the washout geometry is symmetric, then due to symmetry properties of the Stokes equations, we would expect that $l_d = l_e$. Boundary conditions of

$$\mathbf{u} = 0, \tag{4.11}$$

are applied at the walls (no-slip). The flow is assumed fully developed at entry and exit:

$$\sigma_{xx} = -p + \tau_{xx} = -s, \quad v = 0, \quad \text{at } x = -1/2\delta - l_d, \tag{4.12}$$

$$\sigma_{xx} = -p + \tau_{xx} = 0, \quad v = 0, \quad \text{at } x = 1/2\delta + l_e. \tag{4.13}$$

Since we have scaled the velocity with the mean axial velocity along the channel, the pressure drop s must be found as part of the problem. Essentially, s is increased until the mean velocity at the entry is 1, i.e. s satisfies:

$$1 = \int_0^1 u(x, y)\ \mathrm{d}y, \quad \text{at } x = -l_d. \tag{4.14}$$

The computational domain and boundary conditions are illustrated schematically in Fig. 4.2.

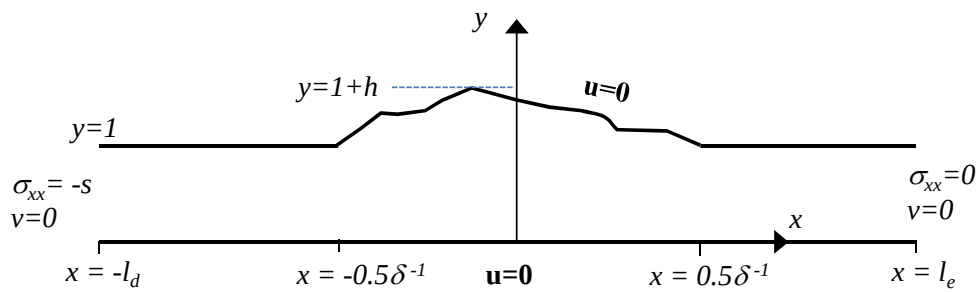

Figure 4.2: Dimensionless computational domain and boundary conditions for this study.

4.2.2 Washout geometries

We consider 4 families of washout geometry in this study. For all geometries the maximum depth of the washout is $h = \hat{H}/\hat{D}$ and the length is $\delta^{-1} = \hat{L}/\hat{D}$, i.e. the length of that part of the channel that does not have unit width. For each geometry we explore a range of h, δ. The geometries are describes as follows.

- Square wave: an abrupt change in channel width from 1 to $1 + h$.
- Triangular wave: a linear change in channel width from 1 to $1 + h$, over a distance $0.5/\delta$, i.e. the angle of the washout wall, relative to the uniform channel wall is α_0, where $\tan \alpha_0 = 2h\delta$.
- Sinusoidal wave: linear change in channel width from 1 to $1 + h$, over a distance $0.5/\delta$ following a sine wave. The upper wall of the washout is given by: $y_w = 1 + 0.5h[1 + \cos 4pi\delta x]$.
- Koch snowflake: the shape is based on the Koch snowflake curve; see [242]. The typical Koch snowflake construction involves repeated subdivision of each straight edge into 3, with the addition of a triangular shape on the central 1/3 of each edge. Normally, this is carried out on an equilateral triangle. Here the initial triangle is formed only on the washout length: $x \in [-0.5/\delta, 0.5/\delta]$, and has depth h, i.e. as for the triangular wave. Subsequent iterations form an isosceles triangle with

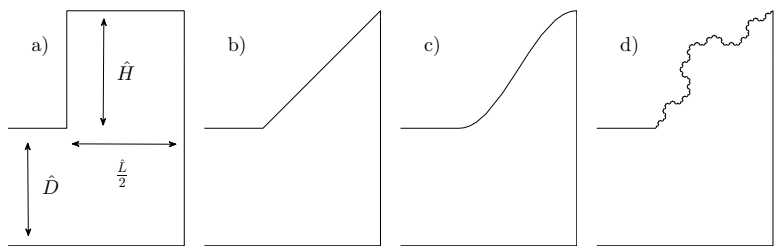

Figure 4.3: Four different categories of symmetric washout geometry, shown for $x < 0$: a) sudden expansion-contraction (square wave); b) triangular wave; c) sinusoidal wave; d) semi-fractal, based on the Koch snow flake. All washout shapes are fully determined by (h, δ).

equal angles α_0 on each central third of each straight edge. The number of iterations is stopped when the straight edges being subdivided are just greater than the initial mesh size used for the computation.

These 4 geometries are illustrated in Fig. 4.3 for clarity.

4.2.3 Computational overview

The main difficulty in finding solutions of Bingham fluid flows (and other yield stress models) is due to the singularity in the effective viscosity as $\dot{\gamma} \to 0^+$. This limit marks the boundary of unyielded (or plug) regions, which may be either attached to the walls of the flow domain or moving rigidly in the interior of the flow domain. The deviatoric stress is undetermined in these regions, satisfying the inequality $\|\tau\| \leq B$. Only in simple flows are the boundaries known and stresses calculable analytically, e.g. due to symmetry considerations. With some pre-knowledge of the plug topology, numerical solution can be attempted with an iteration loop for the shape of the unyielded regions, e.g. [225]. Although effective in some cases, extension of these methods to general flows with no initial guess for the plug shape is unclear.

A common way to compute general flows is to *regularize* the singularity by introducing a numerical perturbation into (4.4), to define the effective viscosity everywhere in the flow domain. Typically this perturbation is charac-

terized by a small parameter ϵ, that characterizes the transition to low shear-rates. Several types of regularization have been proposed, e.g. [9, 28, 186]. In these schemes the computational method is exactly as for a nonlinearly viscous (generalised Newtonian) fluid with *unyielded* regions characterised by very viscous fluid. The usual method to interpret *unyielded* fluid is by the criterion: $\|\tau\| \leq B$, but note that the shape of the unyielded regions then depends on the choice of regularization parameter and regularization method. In addition, on taking $\epsilon \to 0$ it is known that the velocity solution converges to that of the exact Bingham model, but the stress field will not necessarily converge; see the discussion in [101]. This method is clearly inappropriate for a study that seeks to distinguish static regions from non-static and to characterize the shapes of unyielded regions. Therefore, instead we have used the augmented Lagrangian (AL) method developed by Glowinski and co-workers; see [99, 110, 111]. The chief advantage of AL over viscosity regularization is that the exact form of constitutive relation is used and the algorithm gives truly unyielded regions with exactly zero strain rate.

Basically, the AL method finds the velocity field which minimizes a functional $J(u)$; see e.g. [92]. Because $J(u)$ contains a non-differentiable term, conventional optimization methods cannot be used for solving the minimization. In the AL method $J(u)$ is made differentiable by substituting a strain-rate variable γ into the plastic dissipation functional. Then the equality constraint of γ and $\dot{\gamma}$ is relaxed, to be enforced by introducing a Lagrange multiplier T. Interestingly, T will converge to the stress field in yielded regions and to an admissible stress field for unyielded regions. The unyielded regions are easily identified by the condition $\gamma = 0$ in the AL method. The rest of details are skipped here for conciseness, but for a good explanation we refer to papers by Saramito & Roquet [206, 207, 214]. The final AL algorithm consists of three steps. The first step is a standard Stokes flow problem with a right-hand side term. The second and third steps are simple point-wise updates of γ_{ij} and T_{ij} fields. These steps are shown in Algorithm 1, repeated until the acceptable convergence is achieved.

Algorithm 1 shows our solution procedure for the washout flow. Basically it is the same as Algorithm 1 of [199] with a modest improvement for

Algorithm 1 augmented Lagrangian algorithm (AL) for washout

repeat

Step 1: **u** minimization with unit flow constraint:

$$-a\nabla.\dot{\gamma}(u^\star) = -\nabla p^\star + \nabla.(T - a\gamma)^{n-1}$$

Applying pressure drop for unit flow constraint:

$$(u^n, p^n) = (u^\star, p^\star) + \frac{1 - Q^\star}{Q_{\Delta p=1}}(u_{\Delta p=1}, p_{\Delta p=1})$$

Step 2: γ minimization is explicit update at each node:

$$\gamma_{ij}^n = \begin{cases} 0, & \text{if} \quad \left\| T_{ij}^{n-1} + a\dot{\gamma}_{ij}(u^n) \right\| < B \\ \left(1 - \dfrac{B}{\left\| T_{ij}^{n-1} + a\dot{\gamma}_{ij}(u^n) \right\|}\right) \dfrac{T_{ij}^{n-1} + a\dot{\gamma}_{ij}(u^n)}{1 + a}, & \text{otherwise} \end{cases}$$

Step 3: T minimization is explicit update at each node:

$$T_{ij}^n = T_{ij}^{n-1} + a(\dot{\gamma}_{ij}(u^n) - \gamma_{ij}^n)$$

until $\left\| \gamma_{ij}^n - \dot{\gamma}_{ij}(u^n) \right\|_{L^2} \leq 10^{-6}$ or 1000≤iterations

applying unit flow constraint. The parameter $a > 0$ is a constant for the algorithm. In step 1 of the algorithm 1 of [199] the unit flow is obtained using a secant iteration for finding the proper overall pressure drop Δp that gives a unit flow rate across the channel. However we note that a secant iteration is not necessary as the equation is linear with respect to Δp. This means the flow rate $Q = \int_{inlet} u_x dy$ also depends linearly on Δp. Therefore, we simply find the solution of the system when the only right hand side comes from a unit pressure $\Delta p = 1$, and save this solution $(u_{\Delta p=1}, p_{\Delta p=1}, Q_{\Delta p=1})$ denoting velocity, pressure and flow rate, respectively. Then we can simply find the correct Δp needed to get unit flow based on the flow rate $Q^\star$ obtained from all other right hand side contributions except Δp. As shown in step 1 of algorithm 1, we find the solution without any overall pressure drop term as $(u^\star, p^\star, Q^\star)$ and then correct the solution to enforce the unit flow rate. Note

that the alternative to this procedure is to enforce the flow rate constraint separately, e.g. in an outer iterative loop, which is generally more costly. Basically, this can be done for free in step 1 due to the linearity.

The finite element method is used for discretizing the Stokes problem in step one of algorithm 1. Due to symmetry of the flow and to save computational time only half of the channel is considered, as illustrated in Fig. 4.3. A limited number of computations were also carried out in the code development stage with the full geometry channel, to verify the symmetry of the flow. For boundary conditions, no-slip is applied at the top and bottom walls and symmetry conditions are used for the left/right boundaries.

The AL algorithm was implemented using the *Rheolef* [213] C++ FEM library developed by P. Saramito and colleagues in Grenoble. The special feature of this implementation is an anisotropic mesh adaptation. First, the solution is obtained on an initial mesh that is unstructured but of approximately uniform size. Then a new mesh is generated that evenly distributes the interpolation error of the dissipation field, as discussed in [214]. The adapted mesh is refined and aligned along the boundary of unyielded regions. This greatly helps to improve convergence and accuracy of the steady state results, particularly for flow applications such as here. We perform 5 cycles of adaptation. The yield surfaces are clearly identified in the last adaptation. On any computation the maximum number of mesh points was limited to 100000, due to available hardware. BAMG performs the meshing [36, 37]. The details of mesh adaptation strategy can be found at [206]. A typical computation is started with a nearly uniform triangular mesh with 9000 elements and iterations are finished when $\|\gamma_{ij} - \dot{\gamma}_{ij}\|_{L^2} \leq 10^{-6}$ or after a maximum of 1000 iterations. The code was validated with a uniform channel flow, for which the analytical solution is available. Other benchmark computations can be found in [199, 206].

4.3 Results

In total we have run approximately 1000 computations for the 4 different generic geometries, with the numerical procedure described above. The

ranges of parameters covered for each washout geometry are the same: $1 \leq B \leq 100$; $0.5 \leq h \leq 10$; $0.05 \leq \delta \leq 1$. Examples of the computed results are presented first in §4.3.1. Section 4.3.2 gives a qualitative description of the parametric results for the 4 geometries, with the focus being on the occurrence of static zones of fluid within the washout zone. In §4.3.3 we uncover some of the universal aspects of stationary zones, showing that at large h these adopt a yield surface profile that is largely independent of washout shape. This enables us to define in a meaningful way parameters that are useful for design of flows through channel-like geometries with washouts.

4.3.1 Examples results

For very small h and $\delta < 1$ the flows are effectively perturbations from a plane Poiseuille flow. The central plug region initially remains intact, but eventually breaks as h is increased. The breaking process has been studied in [102, 199] for channel flows with walls that are symmetrically perturbed and similar methods might potentially be employed here. However, this is not the main focus of our study.

Figures 4.4 and 4.5 present examples of variations in fluid velocity (speed plus streamlines) for the 4 geometries at fixed $\delta = 0.25$ and for $h = 0.5,\ 1,\ 2,\ 4$, at $B = 5$ and $B = 100$, respectively. We show half of the domain, with the full development length extending upstream to $x = -5 - 0.5/\delta$. The flow in the development section is very close to a plane Poiseuille flow near the inflow, but as the washout approaches the streamlines spread and are diverted into the washout. This asymmetry couples with axial compression to create deviatoric stresses that yield the fluid in the entry region to the washout. Further along the washout (and in particular for smaller δ) the flow in the main part of the channel recovers into a Poiseuille-like flow with unyielded plug region. However, the shear layers above and below the plug are different and the plug is asymmetrically positioned in the moving part of the fluid.

The main interest of the flow is in the washout part of the channel, where

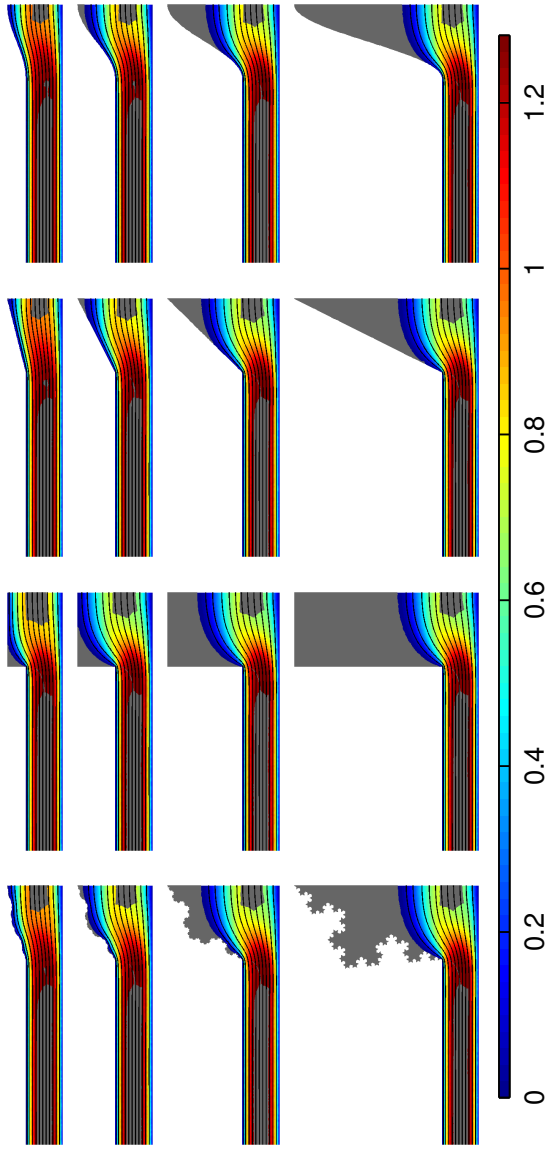

Figure 4.4: Streamlines superimposed on colourmaps of the fluid speed for different types of washout: $\delta = 0.25$, $B = 5$. Columns are $h = (0.5, 1, 2, 4)$ from left to right and unyielded regions are shown in gray.

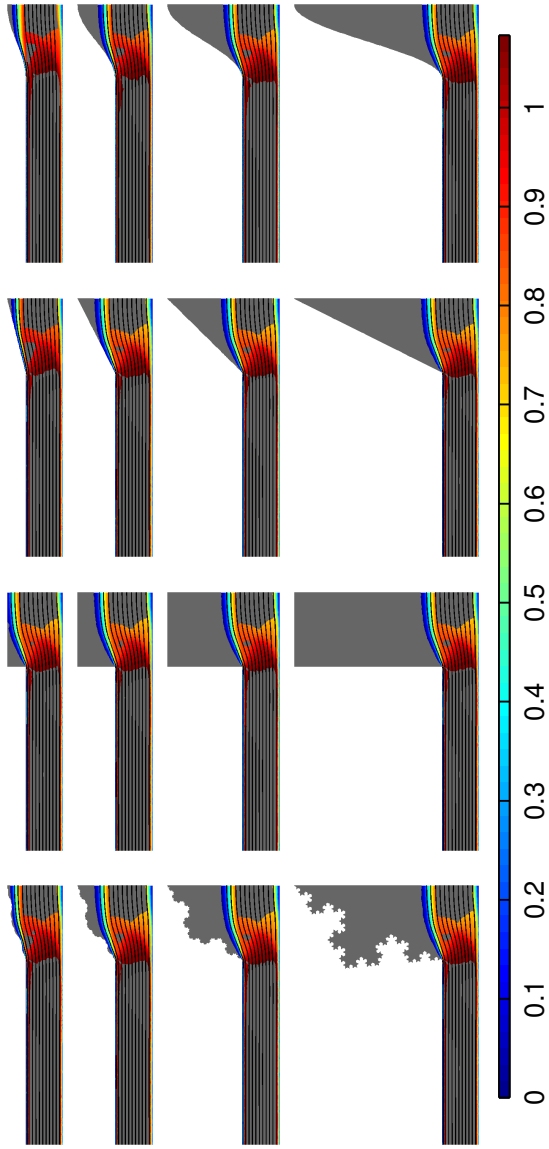

Figure 4.5: Streamlines superimposed on colourmaps of the fluid speed for different types of washout: $\delta = 0.25$, $B = 100$. Columns are $h = (0.5, 1, 2, 4)$ from left to right and unyielded regions are shown in gray.

we find areas of stationary fluid growing with h. The onset of the stationary areas is however qualitatively different, depending on geometry. First of all, for the Koch snowflake it is common to have stationary fluid trapped in the smallest scale structures, even for relatively small h and B. This effect is essentially a wall roughness effect, i.e. simulations with a repeating roughness pattern at the wall would likely also trap fluid on small scales. Secondly, we note that the abrupt step change in channel width exhibits the feature that stationary fluid is first found in the corner regions; see also [79, 164, 174]. The other geometries (discounting small scale roughness) each first encounter stationary fluid zones at the widest part of the channel as h increases through a critical value.

As h increases further, the stationary zone increases but the yield surface position in the upper part of the channel and the streamlines in the flowing region become increasingly insensitive to geometry of the washout. To the eye it appears that the shapes are broadly similar between washout geometries. Larger B results in more stationary fluid in the washout, as might be expected.

Typical stress distributions are explored for the 4 geometries for $B = 5$ and $B = 100$, in Figs. 4.6 and 4.7, respectively (at $\delta = 0.25$, $h = 4$). The columns (from left to right) show τ_{xx}, τ_{xy}, σ_{yy}, p for each of the washout geometries. We observe broadly similar features between the different geometries. The development region (just prior to entering the washout) is characterised by large negative τ_{xx}, except close to the beginning of the washout at the upper wall. There is a singularity in the stress gradients around the entry corner of the washout (square and triangle shapes), where we may expect relatively poor local convergence of our computations. We also observe an intriguing wispy strand of unyielded fluid that extends from the plug upwards towards the corner of the flow domain. Across this thin plug we appear to have a jump in tangential component of the deviatoric stress from positive to negative. Similar singular behaviours near the corner of a yield surface were found in [225, 246] in studying eccentric annular duct flows; see also [199]. The shear stresses are reduced in the washout part of the flowing fluid, suggesting a significantly reduced pressure drop. As in

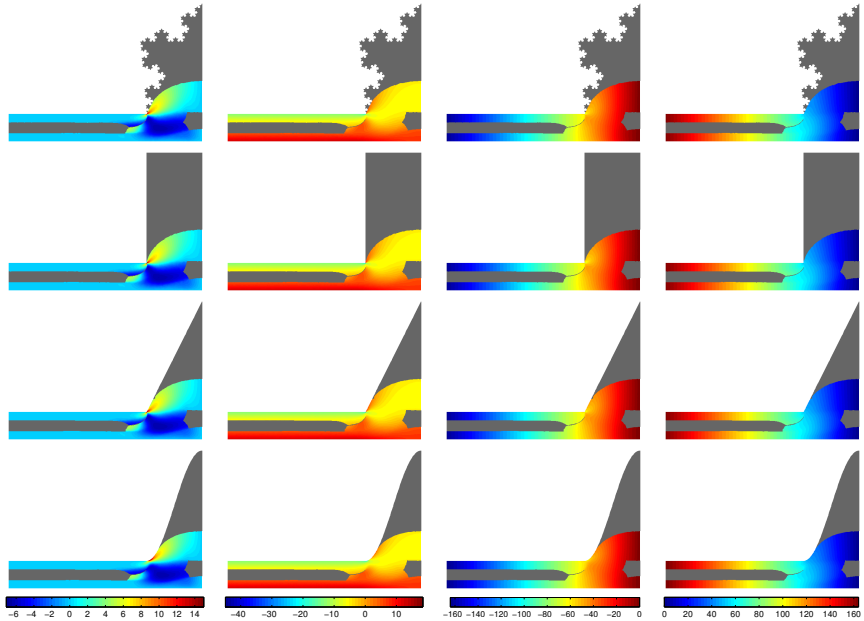

Figure 4.6: Components of the stress for different types of washout: $\delta = 0.25$, $B = 5$, $h = 4$. Columns show τ_{xx}, τ_{xy}, σ_{yy}, p respectively, from left to right. The color key for each column is same shown at the bottom. Unyielded regions colored with gray.

[208], we find that σ_{yy} becomes largely independent of y in the shear layers, in the region of the washout where there is a plug.

4.3.2 Parametric variations

Figs. 4.8 and 4.9 show a wide range of unyielded fluid regions for the 4 geometries, again at $B = 5$ and $B = 100$, respectively. The Koch snowflakes exhibit the "roughness" feature at larger δ, but for long washouts ($\delta = 0.05$) the snowflake construction does not result in sharp enough undulations to trap fluid. Instead the general effect is of an uneven/rough washout, gradually increasing in size. The uneven wall produces interesting stress variations in the bulk of the flowing region that result in plugs of different sizes and shapes. However, since all these regions are flowing, the practical implications are minimal. For larger h than is shown, even for long washouts

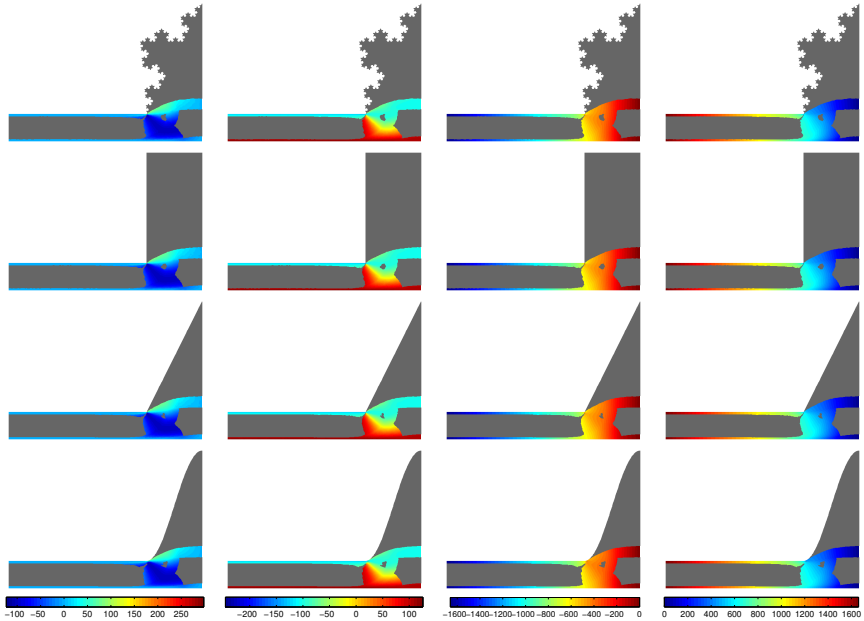

Figure 4.7: Components of the stress speed for different types of washout: $\delta = 0.25$, $B = 100$, $h = 4$. Columns show τ_{xx}, τ_{xy}, σ_{yy}, p respectively, from left to right. The color key for each column is same shown at the bottom. Unyielded regions colored with gray.

the stationary zones at the wall increase to form a single connected area. For shorter washouts the upper part of the washout has stationary fluid for relatively moderate h.

The step change in channel width is interesting in that we see a two stage transition for long washouts. Even for relatively small h we find stationary zones in the corners. The central part of the washout is then simply a uniform channel of width $1 + h$, within which the flow develops into a uniform Poiseuille flow again. As h increases, both the corner regions and yielded development zone at the entry to the washout appear to grow in length. Finally at a critical value of h the corner regions join and the washout has a simply connected region of stationary fluid. After this point, the upper boundary is a yield surface and the moving plug zone becomes asymmetrically located in the washout, i.e. closer to the lower wall.

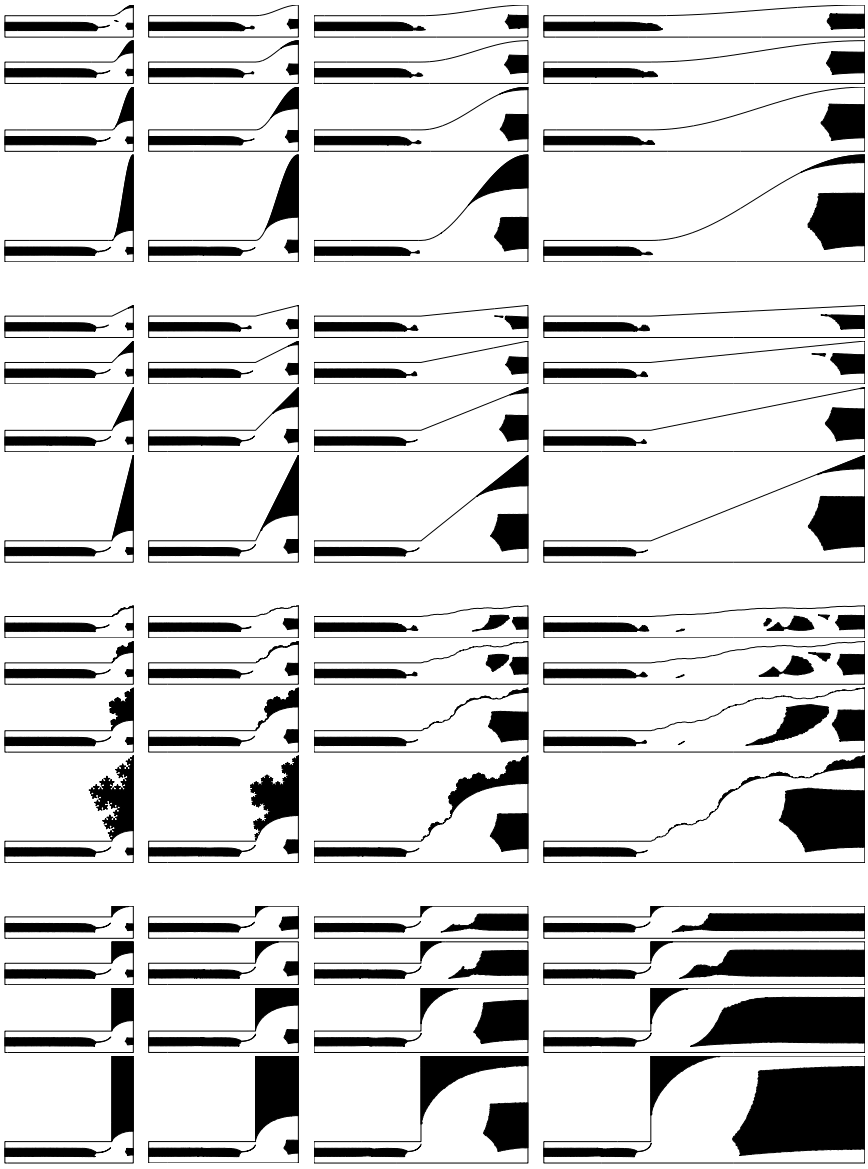

Figure 4.8: Unyielded regions of the flow (shown in black) for different types of washout at $B = 5$. For each type of washout columns show $\delta = (.5, .25, .1, .05)$ from left to right respectively and rows are $h = (.5, 1, 2, 4)$ from top to bottom respectively

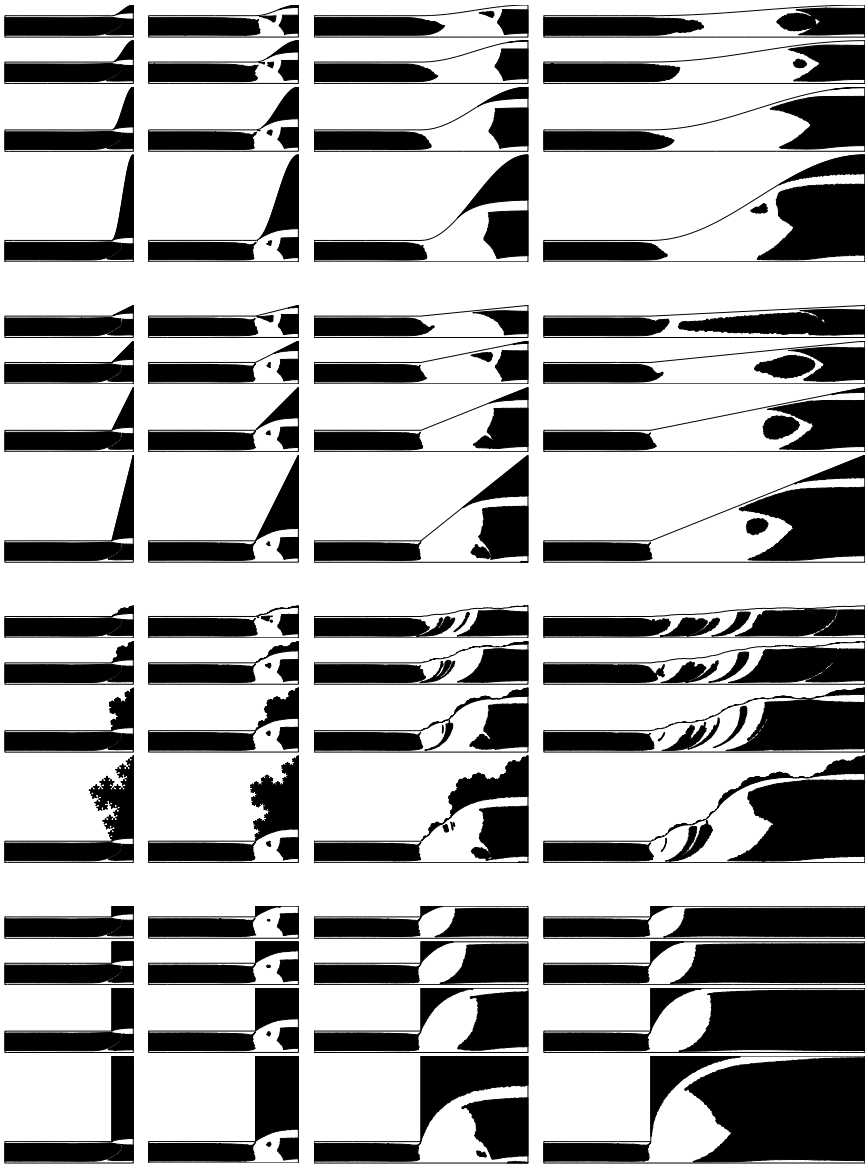

Figure 4.9: Unyielded regions of the flow (shown in black) for different types of washout at $B = 100$, for each type of washout columns show $\delta = (.5, .25, .1, .05)$ from left to right respectively and rows are $h = (.5, 1, 2, 4)$ from top to bottom respectively

The two most similar geometries are the triangular and sinusoidal washouts. Stationary regions appear at the centre of the washout at the upper wall, at approximately the same h, the plug regions in the flowing zone are qualitatively very similar. The differences with larger B are as expected: a general increase in all unyielded regions. However, we also observe an interesting feature for short washouts, in that the central plug region yields only in a narrow *fracture* at the start of the washout. This suggests that as we take the washout length to zero, there is likely to be a critical δ above which the central plug does not yield. This is perhaps analogous to a wall roughness effect.

The above figures and our earlier observations suggest that there is little universal about the onset of stationary fluid at the upper wall, i.e. the position of the initial fouling depends on wall roughness and the abruptness of the angle at the end of the washout. Nevertheless, for the triangular and sinusoidal washouts the onset of fouling (stationary fluid at the wall) appears unambiguously at the widest part of the washout. As in our previous work [208], it appears that the onset occurs at a combination of $(h\delta)$, which is effectively the slope of the washout wall. Figure 4.10 plots the results of all our computations for these 2 geometries, classified as either having stationary or mobile fluid in the washout. The critical values of $(h\delta)$ appear to be primarily a function of B; see also Fig. 10 in [208].

4.3.3 Flowing area

Since successive increases in washout size do not appear to have a large effect on the area of mobile fluid, it becomes of interest to characterize this effect. In all our computations stationary fluid has only been observed within the washout region. We therefore define A_F as the area of the washout that has non-zero velocity, i.e. meaning that part of the flow geometry above $y = 1$ and between $x = \mp 0.5\delta^{-1}$.

The initial increase in A_F scales for some washout geometries and parameter ranges like h/δ (i.e. increasing like the washout area) and for others like δ^{-2} (characterized approximately by the arc of a circle). However, none

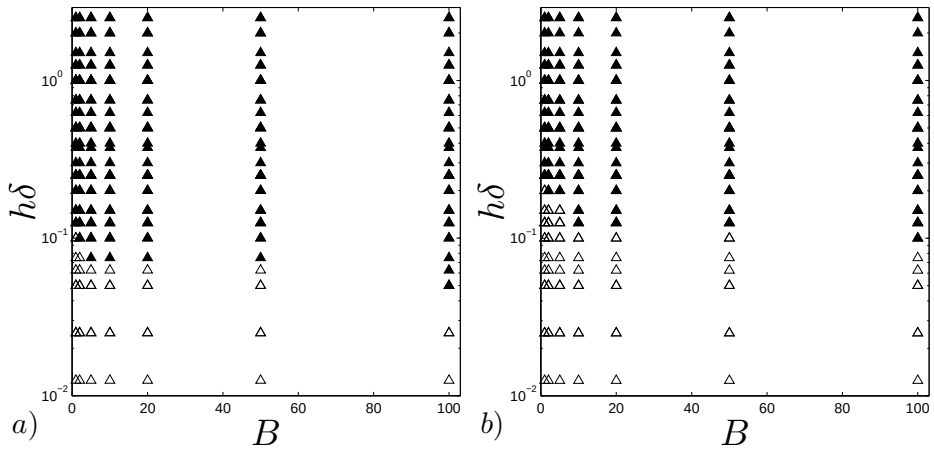

Figure 4.10: Onset of stationary fluid at the upper wall for: a) triangular wave; b) sinusoidal wave. Dark symbols indicate stationary fluid at the upper wall.

of these scalings was found to be uniformly valid. For any non-zero B we have observed that A_F increases and asymptotically approaches a constant value as $h \to \infty$. It was also noted in parametric studies such as those in Figs. 4.8 and 4.9, that the shape of the yield surface bordering the static fluid, in the widest part of the channel, appeared to be similar between geometries, as h increases. Figure 4.11 illustrates this effect for two sets of (B, δ) with both triangular and wavy washout geometries, compared against the square washout. The broken black line indicates the computed position of the yield surface in the square washout. The red line indicates the yield surface in the wavy (or triangular) washout. As h increases we see that the red and black profiles converge in the centre of the washout. Away from the centre of the washout the yield surfaces cannot coincide, since the wall of the washout (for triangular and wavy geometries) lies inside the yield surface of the square washout. Effectively, the convergence must wait until $h \to \infty$ and the washout wall progressively approaches the square washout shape. This convergence is consequently relatively slow and is slowest for the wavy washout, which is always smooth.

Although the convergence is slow the trend is clear, and a simple method

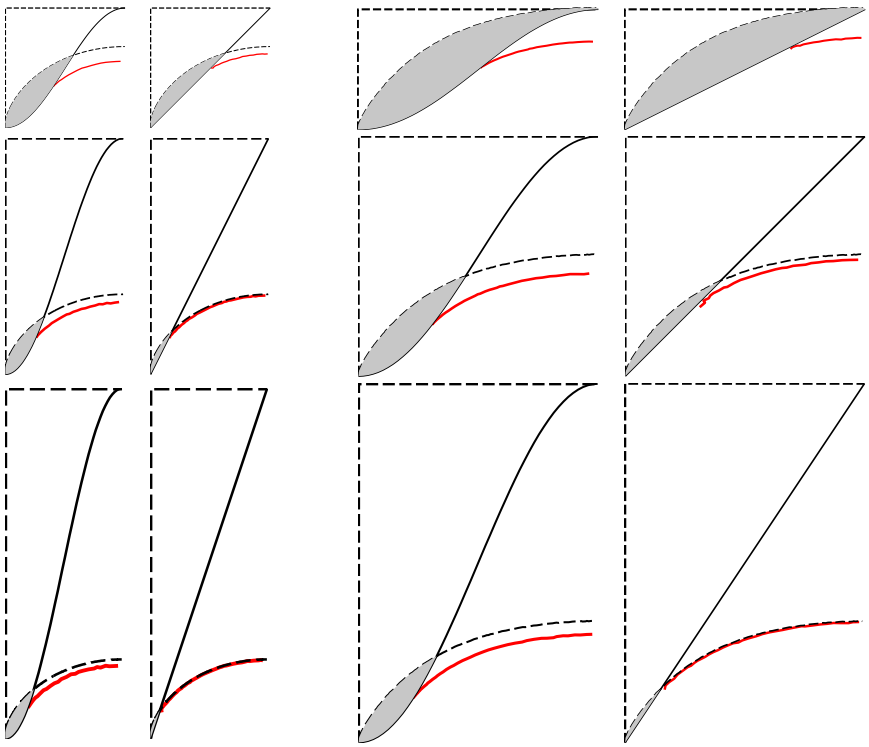

Figure 4.11: Comparison of static region for triangular and wavy washout (solid black/red) with the corresponding square washout (dashed). Only washout enlargement section is shown. Flowing are correction is shown in gray. Rows are $h = (1, 2, 3)$ from top to bottom, for the two left columns $(B, \delta) = (2, .5)$ and two right columns $(B, \delta) = (10, .25)$

of predicting A_F suggests itself. Suppose that we are able to characterize A_F for the square washout, as $h \to \infty$ and the yield surface approaches a constant shape. We call this (square washout) limiting flowing area $A_{F,\infty}(B, \delta)$ and note that in fact the convergence to $A_{F,\infty}$ with h appears to be relatively fast for the square wave. For any other shape of washout, we now define a correction by subtracting the areas of the washout from that of the square washout yield surface, say $A_{C,h}(B, \delta)$. These corrections correspond to the shaded gray areas in Fig. 4.11. Note that these corrections are computed from the known washout geometry and the square washout yield surface,

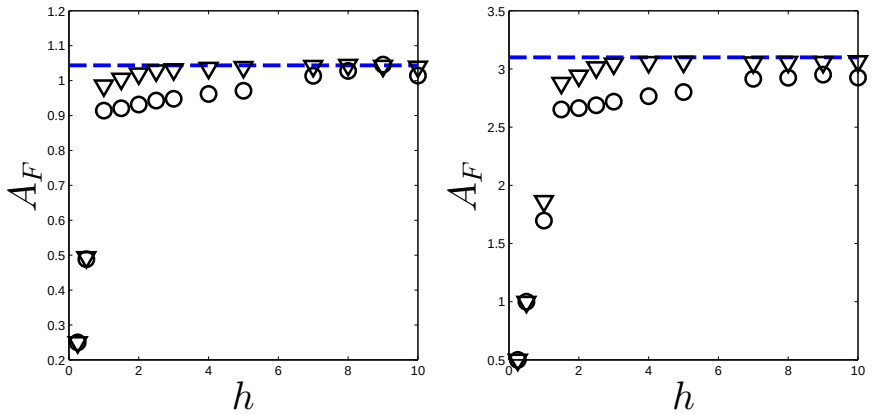

Figure 4.12: Corrected flowing area of wavy and triangular washouts against the square washout flowing area as the washout gets deeper (increasing h). Left plot $(B, \delta) = (2, .5)$ and right plot $(B, \delta) = (10, .25)$. Markers are $\circ$) Wavy washout and $\triangledown$) linear washout. The dashed blue line shows $A_{F,\infty}(B, \delta)$, the limiting flowing area of square washout

without any need to compute the actual flow. The flowing area is then approximated by:

$$A_F(h, B, \delta) \approx A_{F,\infty}(B, \delta) - A_{C,h}(B, \delta). \tag{4.15}$$

To test the validity of this approach, we calculate $A_{C,h}(B, \delta)$ for the triangular and wavy washouts and add the correction to the computed $A_F(h, B, \delta)$. Figure 4.12 plots $A_F(h, B, \delta) + A_{C,h}(B, \delta)$ for triangular and wavy washouts, comparing against $A_F(h, B, \delta)$ for the corresponding square washout. We can see that the corrected flowing areas converge to that of the square washout relatively well.

4.3.4 Pressure drop

Apart from flowing area a second parameter of interest to flow design is the effect that the washout has upon the pressure drop. Intuitively, since the washout section is wider we expect that the pressure drop is reduced in comparison to that experienced through a uniform channel of the same

length. We define ΔP as this reduction in pressure drop, i.e.

$$\Delta P = -(L/2+5)\frac{\partial p}{\partial x}|_{Poiseuille} - [\bar{p}(-L/2-5) - \bar{p}(0)]\,, \tag{4.16}$$

where $\frac{\partial p}{\partial x}|_{Poiseuille}$ is the pressure gradient of the plane channel Poiseuille flow and $\bar{p}(x)$ is the computed pressure, averaged with respect to y across the channel. Note that $\tau_{xx} = 0$ at the symmetry plane $x = 0$ and $\tau_{xx} \approx 0$ at $-(L/2+5)$, due to the entry length. Thus, the drop in $\bar{p}$ is essentially that in $-\sigma_{xx}$.

Figure 4.13 shows typical variations in ΔP with h at fixed B, for the square wave washout. In each case, as h increases ΔP approaches a constant value that depends on both B and L (or δ). This convergence to a constant value is of course mimicked by the yield surface approaching a constant shape, as we have seen in the previous sections. Comparing between Figs. 4.13a & b we see that there is an increase in ΔP with B and each figure illustrates the increase in ΔP with L. At significant B we have seen previously that the flowing areas for all geometries converge to that for the square wave as h increases. Fig. 4.13b plots (red broken line) the same data for the wavy washout for 2 values of δ. We can see that convergence of the pressure drops is evident but relatively slow, as we have seen for the flowing area.

Figure 4.14 shows typical variations in $\bar{p}(x)$, compared against the Poiseuille flow pressure distribution. As expected the pressure drop in the washout section is significantly smaller than the Poiseuille flow gradient would have been. The gradients converge as we approach the entrance to the channel. The square washout induces a sharp change in gradient at the start of the washout: other geometries are smoother.

To quantify the significance of the pressure drop we first note that ΔP arises mostly from the washout section (although there is some variation in the development length). To compensate (partly) for the evident increases in ΔP with L we consider instead $2\Delta P/L$ (note ΔP is for $L/2$ in equation (4.16)), which has an interpretation as the reduction in pressure gradient, (averaged over the washout length). We scale this quantity with $\frac{\partial p}{\partial x}|_{Poiseuille}$

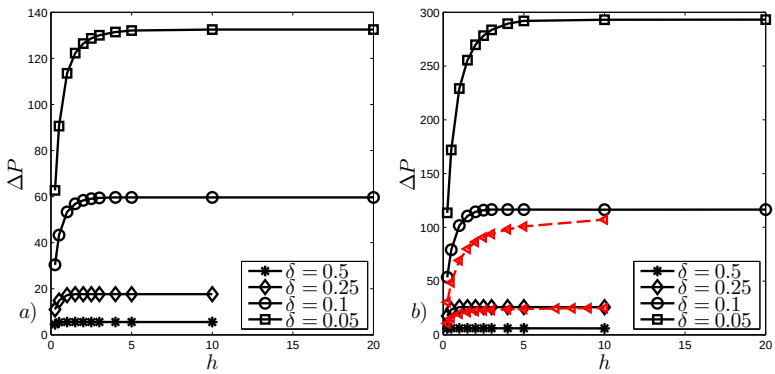

Figure 4.13: Pressure drop reduction (compared to uniform channel) for the square washout: a) $B = 1$; b) $B = 10$. In b the broken red line indicates the analogous results for the wavy washout.

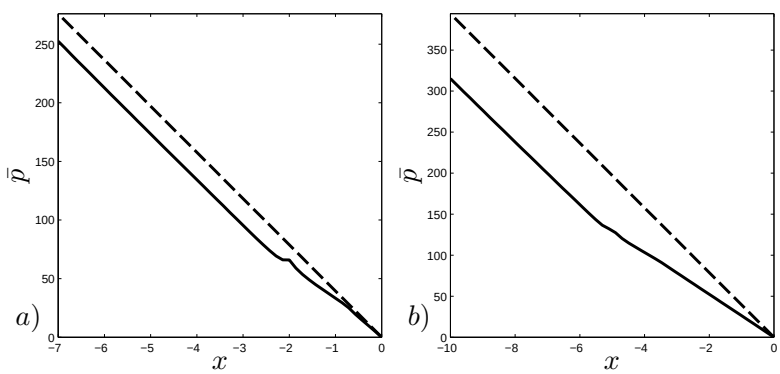

Figure 4.14: Averaged computed pressure $\bar{p}(x)$ (square washout) compared with the pressure in the uniform channel (broken line): a) $(h, \delta, B) = (.5, .25, 10)$; $(h, \delta, B) = (.5, .1, 10)$.

to give a dimensionless ratio, plotted in Fig. 4.15. We can see that typically for shorter washouts and larger B the pressure gradient reduction is significantly less that the frictional pressure gradient of the channel flow. It is only for long washouts and smaller B that the pressure gradients become comparable.

Although potentially from our results we could attempt to derive a pressure drop *correction* to apply to washout geometries, we have not done so. Firstly, in oil well cementing geometries the static pressure is usually dom-

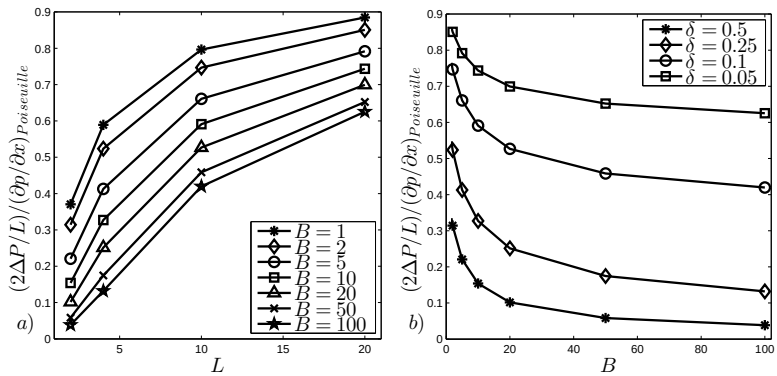

Figure 4.15: Computed pressure gradient reduction for large h, compared to Poiseuille flow uniform pressure gradient (for the square washout)

inant over the frictional pressure, so that the washout effect is minimal in terms of total pressure. Secondly, it is unclear how such a correction should be applied over a full annular geometry, where the washout geometry may change azimuthally but the axial pressure drop does not.

4.4 Discussion and summary

This chapter has considered slow flows of a yield stress fluid through a plane channel with a non-uniformity on one side. This provides a model for circulation of drilling fluid through a narrow annulus with washouts. Washout geometries are usually not measured and may vary considerably. Although at first it seems an impossible problem to study the mechanics in such an *unknown* geometry, this proves not to be the case. Our results have shown that in the case that the washout is relatively deep and the yield stress relatively large (high B), the fluid acts to self-select the flowing region in a way that is (practically speaking) independent of the washout geometry. Practical estimates may be gained by studying the square washout, which becomes the limiting case for all other geometries studied, as $h \to \infty$.

This chapter is of course acknowledged to be an idealisation of the industrial situation. Firstly, the rheological description is incomplete. Drilling

fluids are known to be shear-thinning. Although interesting to study, e.g. a Herschel-Bulkley fluid flowing in the same situations, we cannot expect to see qualitatively different results. Another rheological complication is that drilling fluids tend to thicken when left stationary in a wellbore for any appreciable time, i.e. they are thixotropic. Possibly, an estimate of this effect could be accounted for by assuming that B is based on the drilling mud gel strength, rather than dynamic yield stress. Secondly, we have simplified the study considerably by focusing on $Re = 0$. In Chapter 5 following directly, we look at inertial flows. Thirdly, there are other operational features to be studied, e.g. the 3D geometry, the later displacement flow of the drilling mud, etc. Chapter 6 presents our initial results on the displacement flow problem.

Chapter 5

Inertia effects in the flow of yield stress fluid in washout

In this chapter we extend the work of Chapter 4 into the inertial regime. That is, we study steady inertial flows of a Bingham fluid through 2D "washout" geometries, that represent longitudinal sections of an oil and gas well under construction. The washout geometry is again characterised by dimensionless depth h and length $L = \delta^{-1}$. The other dimensionless parameters of problem are the Reynolds number Re and the Bingham number B. The effects of increasing Re are studied both for fixed B and for fixed Hedström number, $He = ReB$. The former of these represents a straightforward increase in the parameter space of Chapter 4, by adding Re. However, varying Re at fixed B does not correspond to a flow rate increase, which would be a common parameter to vary in the cementing process. Instead, an increase in flow rate for fixed geometry and fluid properties is represented by fixing He and increasing Re.

In both cases we observed that the variation in flowing area of the washout (i.e. that area that is mobilised during pre-circulation) was non-monotone. Increasing Re resulted in a straightening of the streamlines passing through the washout region, in the main part of the channel. For fixed He, beyond a first critical value of Re the flowing area was observed to decrease, i.e. increasing the flow rate results in larger parts of the washout

being static, as is quite counter-intuitive and contrary to the industrial perception that pumping faster will circulate/condition the mud better. This trend persists for a significant range of Re. On passing a second critical value of Re, we observed the onset of zones of recirculation within the washout. The flowing area thus increases but the area of washout from which fluid is actually displaced during conditioning continues to decrease. Since the recirculating zones typically have a low velocity (and shear rate), it is unclear whether practically speaking this is sufficient to condition the mud. Finally, we consider self-selection of the flow geometry, as observed in Chapter 4 for $Re = 0$. We conclude that the same phenomenon arises in inertial flows for a given geometry, i.e. at large enough h the flowing areas of differently shaped washouts with static regions become similar in shape.[1]

5.1 Introduction

We continue our study of drilling mud conditioning during the pre-circulation phase of a primary cementing operation. This paper extends the study performed in [209] (see also Chapter 4) into inertial flow regimes. Primary cementing is a critical operation in the construction of every oil and gas well; see [176]. The fluid mechanical aspect of this process involves the removal of drilling mud from the annular space between casing and formation, to be replaced by a cement slurry. When the well is drilled in poorly consolidated formations that may partially collapse during the drilling process, a non-uniform annular space results with outer wall consisting of "washout" sections (see e.g. Fig. 5.1) that will be geometrically dependent on both the drilling operation and the local geology.

Prior to the fluid displacement phase, most service companies and operators recommend to pre-circulate the well, by pumping the drilling mud from the bottom to the top of the well at least once ("circulating bottoms-up") and this is the phase of the operation that we study. The circulation phase has two main purposes. Firstly, drilled cuttings and other solids still in the

[1] A version of this chapter has appeared as: A. Roustaei & I. Frigaard. "Residual drilling mud during conditioning of uneven boreholes in primary cementing. Part 2: Steady laminar inertial flows." *J. Non-Newt. Fluid Mech.*, **226**:1–15, (2015).

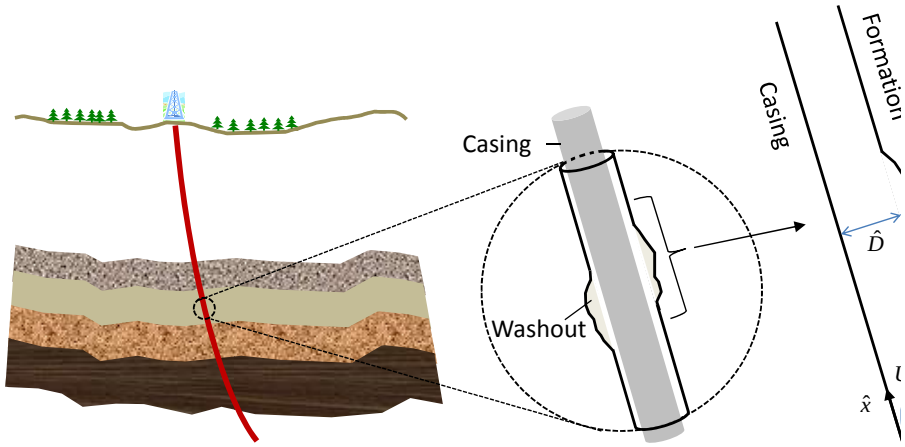

Figure 5.1: Geometry of the washout in a section along the annulus.

well, which may have settled as the casing is run in to the borehole, are cleared from the flowpath. Secondly, the circulation serves to shear the mud and hence condition it prior to displacement. Depending on the operational circumstances and the type of drilling mud, the mud may have been static in the borehole for a period of hours before circulation. Over this time, significant gel strengths may develop due to thixotropic effects. Simplistically speaking this gel strength is destroyed by shear, returning the drilling mud to its dynamic yield stress (which may still be significant).

In Chapter 4 (and [209]) we simplified the flows in a number of ways. First, we considered only a two-dimensional (2D) section of the wellbore as in Fig. 5.1. Second we modeled the drilling mud as a Bingham fluid. Third, we considered only Stokes flows, neglecting inertial effects. These simplifications allowed us to study a wide range of different washout geometries, in terms of both shape and scale (length and depth relative to the annular gap width). As might be expected, yield stress fluid became trapped in sharp corners and small scale features of the washout walls. Whereas initially the geometric uncertainty was a daunting obstacle to understanding, our results showed that for sufficiently large yield stress ($\hat{\tau}_Y$) and for sufficiently deep washouts ($\hat{H}$), the actual washout geometry had little effect on the amount of fluid that is mobilized. Essentially what was observed for a deep washout

of length $\hat{L}$ was that the flowing fluid "self-selects" its geometry. Having established a stationary region within the depths of the washout, further increasing $\hat{H}$ does not significantly effect the position of the yield surface.

This phenomenon of self-selection is not a new phenomenon, but is a significant feature of many interior laminar flows of yield stress fluids. As perhaps the simplest example of this consider a circular Couette flow, in which the single non-zero shear stress component $\hat{\tau}_{r\theta}$ decreases in magnitude with radial distance. Depending on the torque exerted at the inner cylinder and the yield stress of the fluid, there can be a stationary layer attached to the outer cylinder. As this stationary layer can be replaced with an outer cylinder of any radius larger than the radius of the yield surface without affecting the moving part of the fluid, we may consider that the fluid has selected its own flow geometry. Yield stress fluid flows are of course, mathematically speaking, free-boundary problems.

One of the few classes of flow for which this self-selection phenomena has been studied in some depth are uniaxial flows, i.e. $\hat{\mathbf{u}} = (0, 0, \hat{w}(\hat{x}, \hat{y})$; see [168, 169]. In [168] various results are proven concerning the critical pressure gradient required for flow, which is a limiting case of a flow with stationary regions at the walls. More generally it is shown that the flowing domain should have a convex boundary. Quantitative bounds on the radius of curvature of the flow boundary are proven in [169]. Stagnant regions clearly occur in sharp corners, but can also be found in smooth geometries such as an eccentric annulus, bridging between walls as in [246]. Burgos et al. [44] considered a two-dimensional anti-plane shear flow in a wedge between 2 plates, for which a mapping method gives the shape of the yield surface bounding the stationary fluid in the corner. Similar methods have been used by Craster [74].

For more general flows, analytical prediction of the flowing area has not been successful to our knowledge, although there exist limiting cases of zero flow where the flow domain is known. There are however many computational studies that show self-selection of the flow domain via stationary regions close to the wall. Mitsoulis and co-workers (e.g. [164]) have studied both planar and axisymmetric expansion flows, over a wide range of Bing-

ham and Reynolds numbers, showing significant regions of static fluid in the corner after the expansion. Flow of yield stress fluids through an expansion-contraction has been studied both experimentally and computationally in [79, 174, 175]. In [79] Carbopol solutions were pumped through a sudden expansion/contraction, i.e. narrow pipe – wide pipe – narrow pipe. A range of flow rates were studied and the yield surfaces were visualised nicely by a particle seeding arrangement. Inertial effects are evident in asymmetry of the flow. For all the experiments shown, stagnant regions first appear in the corners of the expansion and for all the results shown there are stagnant regions. Comparisons are made between experimental and numerical results, which are at least qualitatively in agreement; see [79, 174]. In [175] qualitatively similar computations are carried out, but using an elasto-viscoplastic model. In [208] (see Chapter 2) we have studied large amplitude wavy walled channel flows numerically. We have derived predictions for the onset of stationary fluid regions, which occur initially at the walls in the widest part of the channel, unlike the abrupt expansions discussed above.

Although here we focus on primary cementing as the application of interest, yield stress materials are common in the food and cosmetics industries. The above works may be considered as relevant to processing flow of such materials through machinery and/or during mixing. The occurrence of dead zones where fluid is not circulated/mobilized can seriously affect product homogeneity and have potential health consequences.

In this chapter we study the effects of inertia on the results of Chapter 4 (and [209]), while retaining the simplifications both of a 2D flow and a Bingham fluid. The importance of including inertia lies in that varying the flow rate is one of the few methods to influence mud conditioning and hence rheology, prior to the displacement stage of the process. At very high flow rates turbulent flows are likely to mobilize the fluid efficiently. However, fully turbulent flows are not always operationally possible (due to either pumping limitations or frictional pressure restrictions from the pore and frac envelope). Thus, many flows are at significant Re but are laminar. For these flows the effects of increasing flow rate in the laminar regime are less predictable. Hence the motivation for this work. The underlying motives are

that poorly conditioned mud will develop a higher yield stress and be harder to displace later on in the cementing process, even in uniform geometries e.g. [9].

A brief outline of this chapter is as follows. In §5.2 we present the general model and flow geometries. This is followed by §5.3 in which we outline the computational algorithm used, present benchmark results for validation and determine a suitable entry length for our flows. The main physical results are in §5.4, where we start with a general description of flow observations as the Reynolds number Re is increased from zero at fixed Bingham number B. We show that the flowing area is not monotonically increased, as would be intuitive. Similar effects are observed as Re is increased at fixed Hedström number He, simulating a flow rate increase; see §5.4.1. Finally in §5.4.3 we study the effects of varying washout geometry on flow domain self-selection and invariance, following [209]. The chapter closes with a summary in §5.5.

5.2 The simplified washout

The flow geometry considered is similar to that in our previous work, [209]. Primary cementing circulation occurs through a long narrow eccentric annulus for which we may assume that the main velocity components are along the borehole axis, with azimuthal flows driven by slow axial variations in aperture. A reasonable simplification of the flow through a washout section is therefore to consider a two-dimensional (2D) azimuthal-axial slice through the annulus; see Fig. 5.1. Neglecting azimuthal flow, the channel formed has an in-gauge width $\hat{D}$ (dependent on the inner and outer diameters and the eccentricity), being bounded on the inside by the casing and on the outside by the formation.

In the 2D section described we will characterize the washout as having a length $\hat{L}$ and a maximum amplitude $\hat{H}$, as illustrated. Coordinates $(\hat{x}, \hat{y})$ are aligned along the channel and across the annular gap, respectively; see Fig. 5.1. Fluid circulates axially along the 2D section with mean velocity $\hat{U}_0$ in the $\hat{x}$-direction. A typical width, $\hat{D}$ is in the range $3 - 80$ mm and a typical $\hat{U}_0$ might be in the range $0.01 - 1$ m/s. The drilling mud is considered

incompressible over the length of the washout, even for $\hat{L}$ of the order of a few meters. Non-Newtonian effects are significant and principal amongst these is the yield stress effect (at least for the flow effects that concern us). The simplest rheological model containing a yield stress is the Bingham fluid, as often used in drilling applications although more complex models (e.g. Herschel-Bulkley) are also used. Although a gross simplification, the key feature of yielding/not-yielding is captured by this model.

The Navier-Stokes equations are made dimensionless using $\hat{D}$ and $\hat{U}_0$ as length and velocity scales, respectively. Time is scaled with $\hat{D}/\hat{U}_0$, the shear stresses are scaled with $\hat{\mu}\hat{U}_0/\hat{D}$ and the static pressure is subtracted from the pressure before also scaling with $\hat{\mu}\hat{U}_0/\hat{D}$, where $\hat{\mu}$ is the plastic viscosity of the Bingham fluid. The resulting equations are:

$$Re\frac{Du}{Dt} = -\frac{\partial p}{\partial x} + \frac{\partial}{\partial x}\tau_{xx} + \frac{\partial}{\partial y}\tau_{xy}, \tag{5.1}$$

$$Re\frac{Dv}{Dt} = -\frac{\partial p}{\partial y} + \frac{\partial}{\partial x}\tau_{xy} + \frac{\partial}{\partial y}\tau_{yy}, \tag{5.2}$$

$$0 = \frac{\partial u}{\partial x} + \frac{\partial v}{\partial y}, \tag{5.3}$$

where $\mathbf{u} = (u, v)$ is the velocity, p is the modified pressure and τ_{ij} is the deviatoric stress tensor. The scaled constitutive laws are:

$$\tau_{ij} = \left(1 + \frac{B}{\dot{\gamma}(\mathbf{u})}\right)\dot{\gamma}_{ij} \iff \quad \tau > B \tag{5.4a}$$

$$\dot{\gamma}_{ij}(\mathbf{u}) = 0 \iff \quad \tau \leq B, \tag{5.4b}$$

where

$$\dot{\gamma}_{ij}(\mathbf{u}) = \frac{\partial u_i}{\partial x_j} + \frac{\partial u_j}{\partial x_i}, \qquad \mathbf{u} = (u, v) = (u_1, u_2),\ \mathbf{x} = (x, y) = (x_1, x_2).$$

and $\dot{\gamma}$, τ are the norms of $\dot{\gamma}_{ij}$, τ_{ij}, defined as

$$\dot{\gamma} = \sqrt{\frac{1}{2}\sum_{ij}\dot{\gamma}_{ij}^2} \qquad \text{and} \qquad \tau = \sqrt{\frac{1}{2}\sum_{ij}\tau_{ij}^2}. \tag{5.5}$$

Two dimensionless numbers appear above. Firstly, the Reynolds number, Re:

$$Re \equiv \frac{\hat{\rho}\hat{U}_0\hat{D}}{\hat{\mu}}, \tag{5.6}$$

which represents the ratio of inertial to viscous effects. Secondly, the Bingham number, B:

$$B \equiv \frac{\hat{\tau}_Y\hat{D}}{\hat{\mu}\hat{U}_0}, \tag{5.7}$$

which represents the competition between yield and viscous stresses. The fluid density is denoted $\hat{\rho}$, and the yield stress is denoted $\hat{\tau}_Y$. As well as these, two geometric dimensionless parameters result: $h = \hat{H}/\hat{D}$, representing the maximal depth of the washout, and $\delta = \hat{D}/\hat{L}$, characterizing the aspect ratio of the washout.

For the computational domain we extend the channel uniformly both upstream and downstream of the washout section; see Fig. 5.2. The two extensions are determined empirically (see below in §5.3), to be sufficient to allow fully developed velocities at both $x = -0.5\delta^{-1} - l_d$ (entry development length) and at the exit, $x = 0.5\delta^{-1} + l_e$. For simplicity we set $l_d = l_e$, although unlike [209] we no longer expect symmetry of the flow. No slip conditions, $\mathbf{u} = 0$, are applied at the walls. The flow is assumed fully developed at entry and exit, driven by a constant pressure drop:

$$\sigma_{xx} = -p + \tau_{xx} = -s, \quad v = 0, \quad \text{at } x = -0.5\delta^{-1} - l_d, \tag{5.8}$$

$$\sigma_{xx} = -p + \tau_{xx} = 0, \quad v = 0, \quad \text{at } x = 0.5\delta^{-1} + l_e. \tag{5.9}$$

The pressure drop s must be found as part of the problem: s is increased until the mean velocity at the entry is 1, i.e. s satisfies:

$$1 = \int_0^1 u(x, y)\ \mathrm{d}y, \quad \text{at } x = -l_d. \tag{5.10}$$

For all geometries the maximum depth of the washout is $h = \hat{H}/\hat{D}$ and the length is $\delta^{-1} = \hat{L}/\hat{D}$, i.e. the length of that part of the channel that does not have unit width. The main geometry considered is that of a

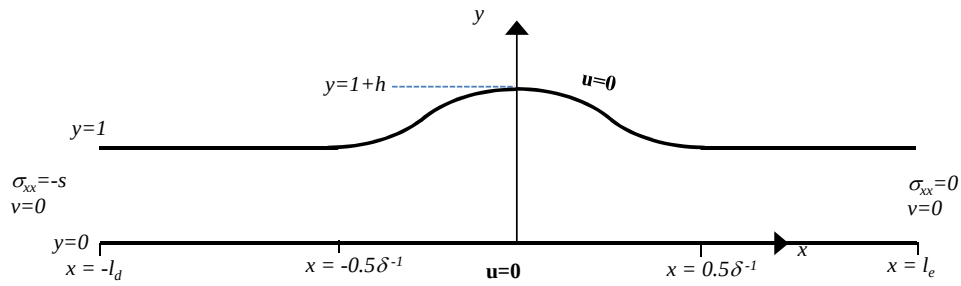

Figure 5.2: Dimensionless computational domain and boundary conditions for this chapter.

sinusoidally wavy washout: the channel width changes from 1 to $1+h$, over a distance $0.5/\delta$ following a sine wave. The upper wall of the washout is: $y_w = 1 + 0.5h[1 + \cos 2\pi\delta x]$. Other geometries will be introduced only to compare geometric effects.

5.3 Computational method

Our objective is to compute steady inertial flows in the washout geometries discussed. The usual difficulties of the yield stress are handled via an augmented Lagrangian method analogous to that used in [209]. The equations are however changed by the addition of the inertial terms which are approximated using a characteristics-based method. As in [209] the saddle point problem is solved iteratively for updated velocity vector, strain rate and stress tensors: denoted $\mathbf{u}^n$, γ^n and $\mathbf{T}^n$, respectively. The main modification comes in the generalized Stokes problem, which takes the form:

$$\frac{3Re}{2\Delta t}\mathbf{u}^{n+1} - \nabla\cdot[a\dot{\gamma}(\mathbf{u}^{n+1})] + \nabla p^{n+1} = \mathbf{g}, \tag{5.11}$$

$$\nabla\cdot\mathbf{u}^{n+1} = 0, \tag{5.12}$$

$$-p^{n+1} + a\dot{\gamma}_{xx}(\mathbf{u}^{n+1}) = 0, \quad v^{n+1} = 0, \quad \text{at } x = \pm 0.5\delta^{-1} \pm l_d, \tag{5.13}$$

$$\mathbf{u}^{n+1} = 0, \quad \text{at } y = 0, \quad y = y_w(x), \tag{5.14}$$

where $a > 0$ is the augmentation parameter, Δt is a pseudo-timestep and $\dot{\gamma}(\mathbf{u}^{n+1})$ is the strain rate tensor evaluated from $\mathbf{u}^{n+1}$. The method is outlined below as Algorithm 2.

We have implemented the above algorithm using the FreeFEM++ finite element environment [118], which is freely available. Following [40] we have used a backward second order (BDF2) discretization for the time derivative $\frac{D\mathbf{u}}{Dt}$, and to calculate characteristic points the velocity $\tilde{\mathbf{u}} = 2\mathbf{u}^n - \mathbf{u}^{n-1}$ is used. Note that $\tilde{\mathbf{u}}$ approximates $\mathbf{u}$ at $n+1$ and for given position $\mathbf{x}$ the positions $\mathbf{X}^n(\mathbf{x})$ and $\mathbf{X}^{n-1}(\mathbf{x})$ track backwards along the streamlines until times n and $n-1$, respectively. Thus, combining $\mathbf{g}$ in (5.15) with (5.11) uses a second order consistent approximation to the derivative of $\mathbf{u}$ along the streamline, i.e. $\frac{D\mathbf{u}}{Dt}$. The expression $\mathbf{u}^n(\mathbf{X}^n)$ is evaluated by interpolation from the mesh values of $\mathbf{u}^n$ at the position $\mathbf{X}^n$; similarly for $\mathbf{u}^{n-1}(\mathbf{X}^{n-1})$.

Both viscous and pressure terms are implicit. As shown in [40] this configuration leads to an unconditionally stable scheme which is a desired property. We use Taylor-Hood ($P^2 - P^1$) elements for velocity and pressure spaces, respectively. Having set the velocity space, it's discrete derivative space P^1_d, consisting of discontinuous elements, is used for both strain and stress spaces: $(\gamma, \mathbf{T})$. This constraint is necessary to get full convergence of strain and stress fields as explained in [214].

We also implemented a mesh adaptivity strategy similar to that in [209]. In each adaptation cycle, first the steady solution is computed and then a new mesh is generated based on a metric that depends on the velocity field. Two metrics $M1$ & $M2$ were tested:

$$M1 = \sqrt{\frac{1}{2}\dot{\gamma}^2 + Bn\dot{\gamma}}, \qquad M2 = \sqrt{M1^2 + Reu^2}.$$

The second metric includes inertial effects. However, in practice the flows considered did not generate significant additional gradients due to inertial effects, we didn't see any significant improvement from $M2$ compared $M1$ and thus use $M1$ for all results below (as for the Stokes flow in [209]). Basically this metric causes the mesh generator to refine the mesh close to yield surfaces, where the second derivative of velocity is discontinuous. We

Algorithm 2 Uzawa algorithm for inertial flow

Initiate the variables: $\mathbf{u}^{-1} = \mathbf{u}^0 = 0, \quad \mathbf{T}^0 = \gamma^0 = 0.$
Solve (5.11)-(5.14) with $\mathbf{g} = (1, 0)^T$ to give $(\mathbf{u}^*, p^*)$.
Compute the areal flow rate through the channel due to $\mathbf{u}^*$:

$$Q^* = \int_0^{y_w} u^*(x, y)\ \mathrm{d}y.$$

Note that solving (5.11)-(5.14) with $\mathbf{g} = (1/Q^*, 0)^T$ gives unit areal flow rate.

for $n = 0, \ldots\ n_{max}$ **do**
  1-Solve the generalized Stokes problem at step n:
  Let $\tilde{\mathbf{u}} = 2\mathbf{u}^n - \mathbf{u}^{n-1}$
  Compute characteristics: $\mathbf{X}^n(\mathbf{x}) = \mathbf{x} - \tilde{\mathbf{u}}\Delta t,\ \mathbf{X}^{n-1}(\mathbf{x}) = \mathbf{x} - 2\tilde{\mathbf{u}}\Delta t$
  Define $\mathbf{g}$ in (5.11) by:

$$\mathbf{g} = \nabla \cdot (\mathbf{T}^n - a\gamma^n) + Re\frac{4\mathbf{u}^n(\mathbf{X}^n) - \mathbf{u}^{n-1}(\mathbf{X}^{n-1})}{2\Delta t}. \tag{5.15}$$

  Solve (5.11)-(5.14) to give $(\mathbf{u}^{n+1}, p^{n+1})$.
  2-Modify the solution to give unit areal flow rate:
  Let $f^{n+1} = (1 - Q^{n+1})/Q^*$ where $Q^{n+1} = \int_0^{y_w} u^{n+1}\ \mathrm{d}y$
  Update $(\mathbf{u}^{n+1}, p^{n+1}) = (\mathbf{u}^{n+1}, p^{n+1}) + f^{n+1}(\mathbf{u}^*, p^*)$.
  3-Update relaxed strain rate:

$$\gamma^{n+1} = \begin{cases} 0 & |\mathbf{T}^n + a\dot{\gamma}(\mathbf{u}^{n+1})| < B \\ (1 - \frac{B}{|\mathbf{T}^n + a\dot{\gamma}(\mathbf{u}^{n+1})|})\frac{\mathbf{T}^n + a\dot{\gamma}(\mathbf{u}^{n+1})}{1+a} & \text{otherwise} \end{cases}$$

  4-Update stress Lagrange multiplier:

$$\mathbf{T}^{n+1} = \mathbf{T}^n + a(\dot{\gamma}(\mathbf{u}^{n+1}) - \gamma^{n+1})$$

  if $\min(\|\dot{\gamma}(\mathbf{u}^{n+1}) - \gamma^{n+1}\|_{L^2}, \|\mathbf{u}^{n+1} - \mathbf{u}^n\|_{L^2})/\Delta t \leq 10^{-6}$ **then**
    Stop the n loop
  end if
end for

perform 4 cycles of adaptation. A typical computation starts with a mesh of 8000-10,000 points and the last adapted mesh may have up to 150,000 points. Further details of the mesh adaptivity may be found in [36, 37].

The modifications of (5.11)-(5.14) to fit our problem are two-fold. Firstly, since (5.11) is linear and the boundary conditions are homogeneous, we are able to enforce the fixed flow rate constraint (5.10) in step 2 of the algorithm. Secondly, we have combined time-stepping for the Uzawa iteration with that for the time advance, as a means of accelerating convergence. This *pseudo-timestepping* does not therefore compute an actual solution to any time-dependent problem at intermediate timesteps. However, if $\|\mathbf{u}^{n+1} - \mathbf{u}^n\|_{L^2}/\Delta t \to 0$ the converged solution is a steady inertial flow, as required.

In general, adding the yield stress increases the viscosity and is thus expected to stabilize the flow (i.e. hydrodynamically). We expect therefore that the velocity residual $\|\mathbf{u}^{n+1} - \mathbf{u}^n\|_{L^2}/\Delta t$ should converge more easily for large B at significant Re. This is indeed what we observe. Figure 5.3 shows the decay of the velocity residual with iterations n at two different Re and for 4 increasing values of B with $(h, \delta) = (4, 0.25)$. We do not know the limit of stability for a Newtonian fluid in this geometry, but see that the velocity residual does not decay for $B = 0$ or $B = 1$ at $Re = 2000$. This is evidence that the flow is unsteady for these parameters, but as remarked above the actual computed velocity in these cases does not have physical meaning.

For all results presented in this chapter the velocity residual is converged ($\leq 10^{-6}$) and we may assume the flow is steady. The code has been benchmarked against the published results for the lid-driven cavity flow problem for both Newtonian and Bingham fluids. For $Re = 1000$ and $B = 0$, Fig. 5.4a presents the comparison with the Newtonian results of Ghia et al. [107]. Our results also compare well with those of Syrakos et al. [224] for $Re = 1000$ and $B = 10$, but not with those of Vola et al. [241] for the same parameters; see Fig. 5.4b. As a second check we have recomputed the flows using a finite volume method on regular rectangular mesh, implemented in the code PELIGRIFF (see e.g. [203]). We again reproduce the results of [107, 224] but not [241].

For a given geometry we have computed two types of flow. Firstly, with

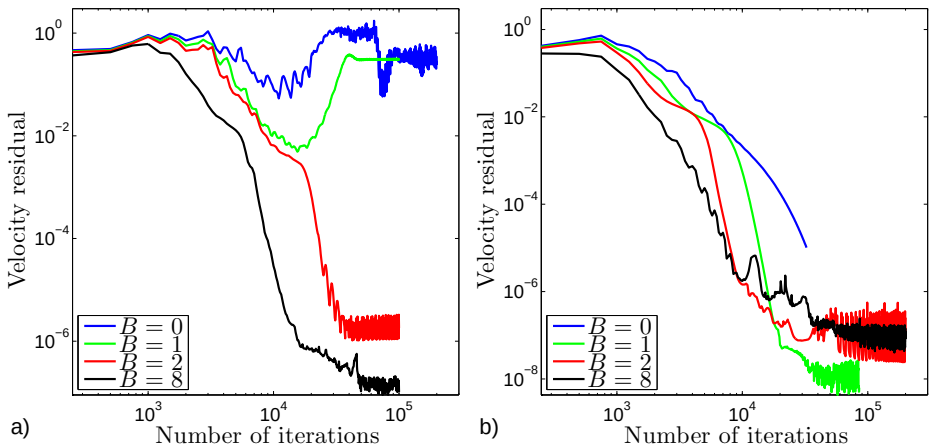

Figure 5.3: Decay of the velocity residual $\|\mathbf{u}^{n+1} - \mathbf{u}^n\|_{L^2}/\Delta t$ for the washout $(h, \delta) = (4, 0.25)$ at increasing $B = (0, 1, 2, 8)$: (a) $Re = 2000$; (b) $Re = 500$.

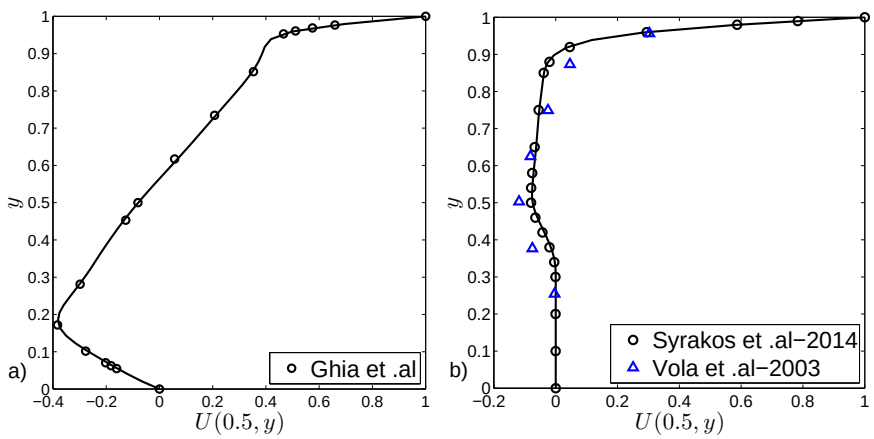

Figure 5.4: Validation of our code with published results from the lid-driven cavity flow. Plots show the horizontal velocity component, $U(0.5, y)$, along the centre of the cavity. a) Comparison with Ghia et al. [107] for $Re = 1000$, $B = 0$. b) Comparison with Syrakos et al. [224] and with Vola2003 et al. [241] for $Re = 1000$, $B = 10$.

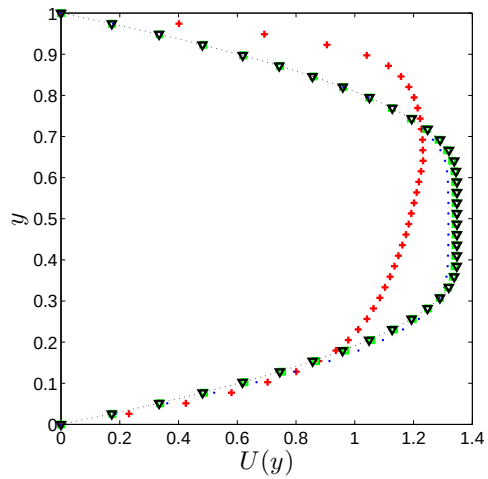

Figure 5.5: Convergence of the entrance velocity profile $u(-0.5\delta^{-1} - l_e, y)$ to the plane Poiseuille solution as the entrance length $l_e = l_d$ increases. The black dotted line shows the plane Poiseuille flow: $(Re, B, h, \delta^{-1}) = (200, 2, 10, 10)$ and entrance lengths are $l_e = (0, 2, 5, 10)$ indicated by markers $(+, \bullet, \square, \triangle)$, respectively.

$l_e = l_d = 0$ and periodic conditions imposed on the velocity at the two ends of the channel. Inevitably these flows are strongly asymmetrical. Although not relevant for the washout application, these do provide a baseline for the degree of asymmetry in the velocity due to the geometry. The second type of flow is computed with the inflow/outflow conditions discussed earlier and with $l_e = l_d$ increased until the entry and exit flows agree with the plane Poiseuille flow solution $U_{Poiseuille} = U(y)$ to within a tolerance: $\|u - U_{Poiseuille}\|_{L^\infty} \leq 0.002$ at $x = \pm 0.5\delta^{-1} \pm l_e$. An example of the evolution in $u(-0.5\delta^{-1} - l_e, y)$ with l_e is shown in Fig. 5.5, with analogous results at $x = 0.5\delta^{-1} + l_d$.

5.4 Results

Example computed results are shown below in Fig. 5.6 for fixed $(h, \delta, B) = (2, 0.25, 5)$ and for increasing $Re = 0,\ 50,\ 100,\ 200$. We show colourmaps of the speed and pressure, for both the periodic geometry ($l_e = l_d = 0$) and the

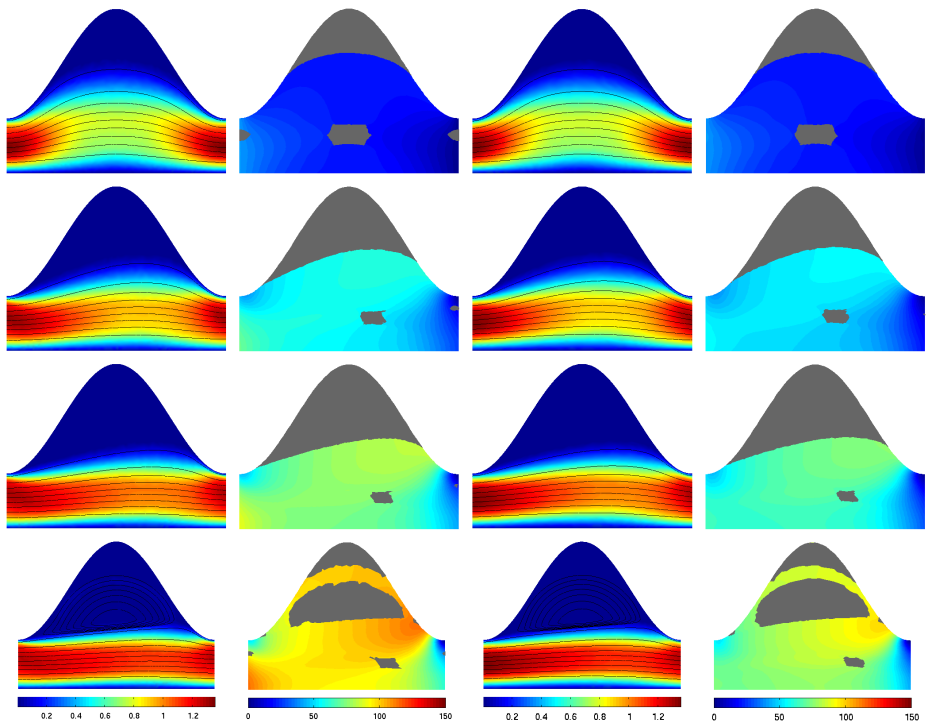

Figure 5.6: Colourmaps of the flow speed with streamlines and pressure compared for periodic washout (two left columns) with washout that has entrance length (two right columns). Parameters are $(h, \delta, B) = (2, 0.25, 5)$ and $Re = 0,\ 50,\ 100,\ 200$, from top to bottom. The gray regions indicate unyielded fluid.

fully developed inflow/outflow ($l_e = l_d = 10$). For the latter computations we only display results within the washout length, in order to aid comparison. We note that the differences in velocity field between periodic and full developed flows are relatively minor. At lower Re the streamlines tend to meander into the washout, whereas at higher Re there is a tendency to bypass the washout and the streamlines tend to straighten. The differences in pressure are more significant, but mostly manifest outside of the washout. The net pressure drop across the washout appears to increase with Re and the variations in pressure across the washout are more extreme in the fully developed case. Neither effect is unexpected.

The most noticeable feature concerns the position and size of the static plug region within the washout. Contrary to intuition, increases in Re appear to increase the size of stationary plug initially, before eventually the increased stresses result in a smaller stationary plug. At the same time, we observe that although the large Re flows have mobilized the fluid within the lower part of the washout, the fluid remains largely unyielded and continues to recirculate within the washout. We show a second set of results for $(h, \delta, B) = (1, 0.25, 5)$ (reduced h) in Fig. 5.7, again for $Re = 0,\ 50,\ 100,\ 200$ but only for the fully developed washout. We see a similar trend in the size of the static plug and in straightening of the streamlines as Re is increased at constant B.

We see that this process also involves significant changes in the distribution of stresses within the washout region. The size of extensional stresses in the upstream part of the washout decreases with Re as the plug grows. In [209] we saw that $\sigma_{yy} \approx$ constant, within the central part of the plug/washout region at $Re = 0$. Here inertia results in complex distributions of all stress components, breaking the symmetry of the $Re = 0$ flows.

5.4.1 Flow rate effects

We have seen that the main surprising effect above is to increase the size of the static plug region in the washout, with increasing Re at constant B. Typically in hydraulic flows, we interpret increasing Re as an increasing flow rate. However, here we see that increasing flow rate (hence $\hat{U}_0$) would result in decreasing B, unless one of the other parameters is also varied. Thus, we must interpret the above results with increasing Re as either: (i) increasing $\hat{\rho}$, or (ii) increasing $\hat{U}_0$ and proportionately increasing $\hat{\tau}_Y$. In the latter case it is intuitive that the size of static plug layer may increase.

To investigate further and to make the work more relevant to the cementing application, we study the effect of increasing flow rate independently. As $\hat{U}_0$ appears linearly in both Re and B, this corresponds to varying $\hat{U}_0$ at con-

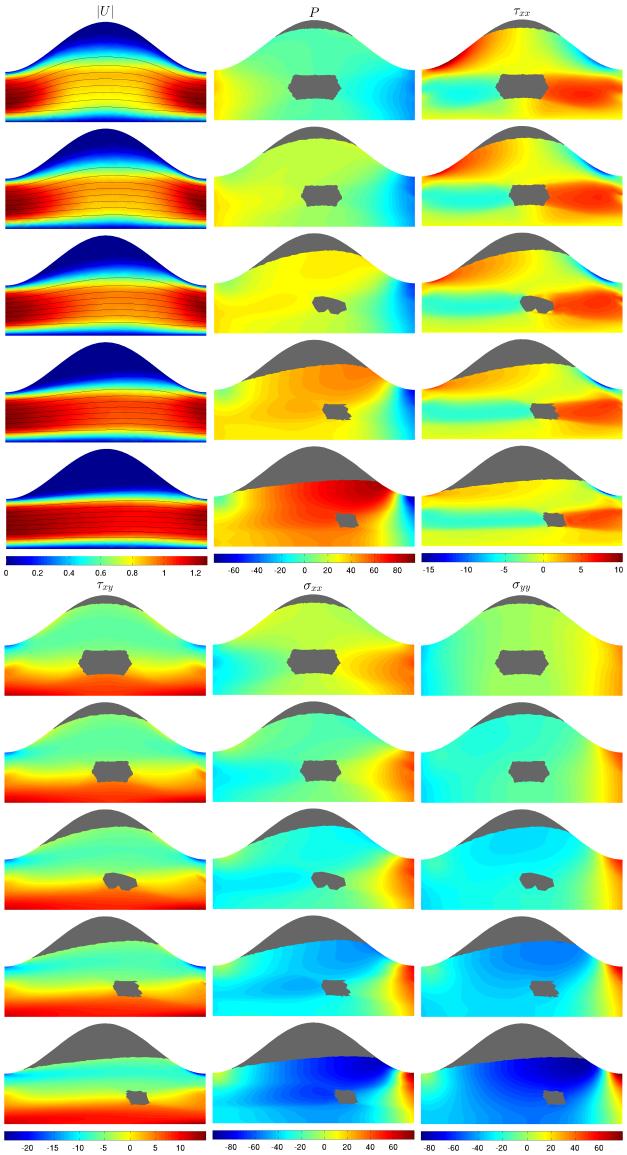

Figure 5.7: Colormaps of the flow variables, restricted to the washout region for $(h, \delta, B) = (1, 0.25, 5)$. At the top of the figure the columns show speed, pressure and τ_{xx}; the columns at the bottom of the figure show τ_{xy}, σ_{xx} and σ_{yy}, from left to right. The rows show $Re = 0,\ 50,\ 100,\ 200,\ 500$, from top to bottom. The gray regions indicate unyielded fluid.

stant Hedström number:

$$He = ReB = \frac{\hat{\rho}\hat{\tau}_Y \hat{D}^2}{\hat{\mu}^2}, \tag{5.16}$$

i.e. as we increase Re we adjust $B = He/Re$. Note that He depends only on the fluid properties and flow geometry, with no dependence on $\hat{U}_0$. To study flow rate effects we start with fixed $He = 500$, which is in the range of Hedström numbers for typical drilling muds and cementing geometries.

We have conducted a parameteric study over (h, δ, Re)-space with ~ 200 cases computed. The range of parameters considered was:

$$0.25 \leq h \leq 40, \qquad 0.05 \leq \delta \leq .5, \qquad 10 \leq Re \leq 500,$$

all for fixed $He = 500$. Smaller sets of results were then computed at different He. Figure 5.8 shows the effect of increasing flow rate at $(h, \delta) = (1, 0.25)$ and $He = 500$. We again observe the straightening of the streamlines as the flow rate is increased from zero. The static plug region in the washout first decreases in area, then increases, up until an intermediate range of Re, then finally in this case disappears. This demonstrates that the previously observed effects are a result of changes in the flow variables and not increases in yield stress. This of course has industrial significance as the usual perception is that increasing the flow rate will be more effective at conditioning the drilling mud. This appears to be false for a significant range of flow rates.

For the same washout geometry we study in Fig. 5.9 the distribution of pressure (averaged in y across the channel) along the channel and through the washout as the flow rate increases at fixed $He = 500$. Firstly, we see that both before and after the washout the average pressure converges relatively quickly to a linear variation that matches that of the relevant plane Poiseuille flow (marked with a broken line in Fig. 5.9). The pressure deviation from the Poiseuille flow is clearly asymmetric (in x) upstream and downstream of the washout. The entry length is relatively short compared to the development length (after the washout). We also observe that although at smaller Re the average pressure decreases monotonically through the washout, at larger Re

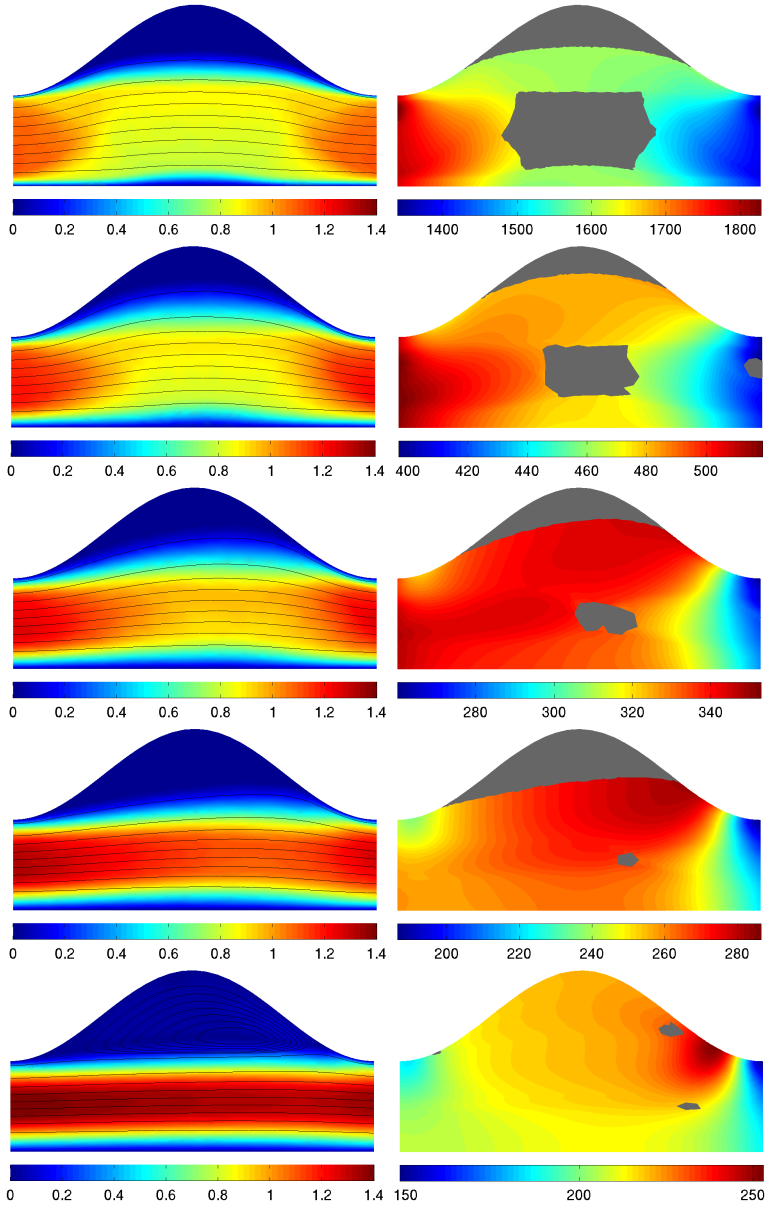

Figure 5.8: Effects of increasing flow rate at $(h, \delta) = (1, 0.25)$ and $Re = 10,\ 50,\ 100,\ 200,\ 500$ from top to bottom, at fixed $He = 500$. Left: velocity magnitude and streamlines; right pressure with unyielded regions shown as gray.

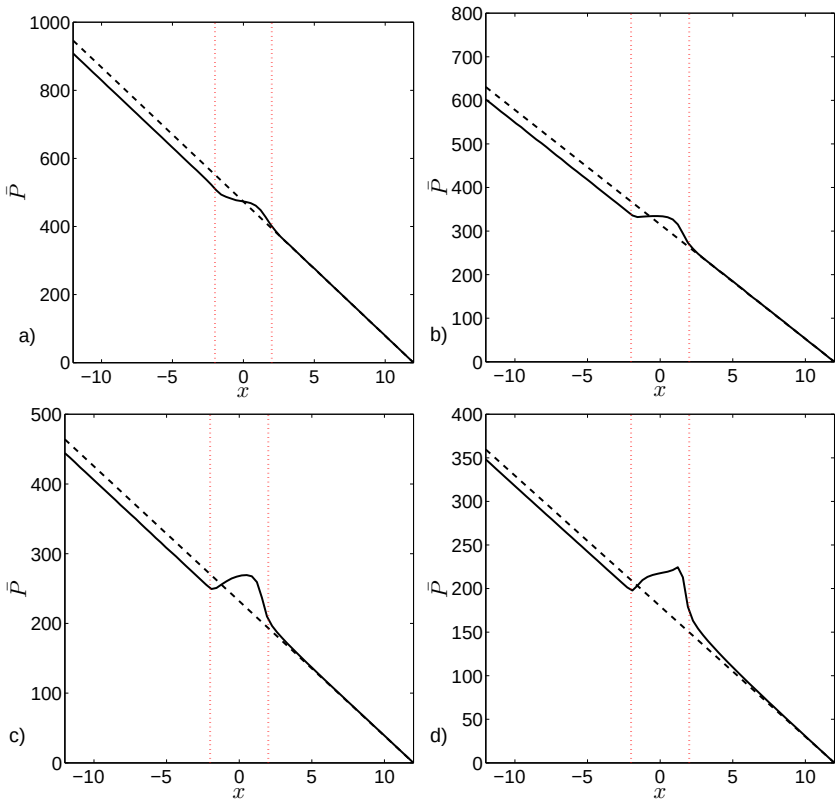

Figure 5.9: Average pressure along the channel (black) compared with the Poiseuille flow pressure (broken line) as the flow rate increases. $(h, \delta^{-1}) = (1, 4)$ and $Re = 50,\ 100,\ 200,\ 500$ with fixed $He = 500$. The vertical dotted lines marks the washout start and end.

(flow rate) the pressure increases in the washout. This gain in pressure suggests a transfer from the dynamic head to the pressure head due to the expansion: frictional losses are insufficient to decrease the pressure.

The offset between the broken and solid lines in Fig. 5.9 (at the very left of each plot) indicates the net effect of the washout on the frictional pressure losses. This *washout* Δp is positive, meaning that the frictional pressure losses are reduced by the washout. We illustrate in Fig. 5.10 the variation in washout Δp with Re at fixed $He = 500$ for 2 geometries. As well

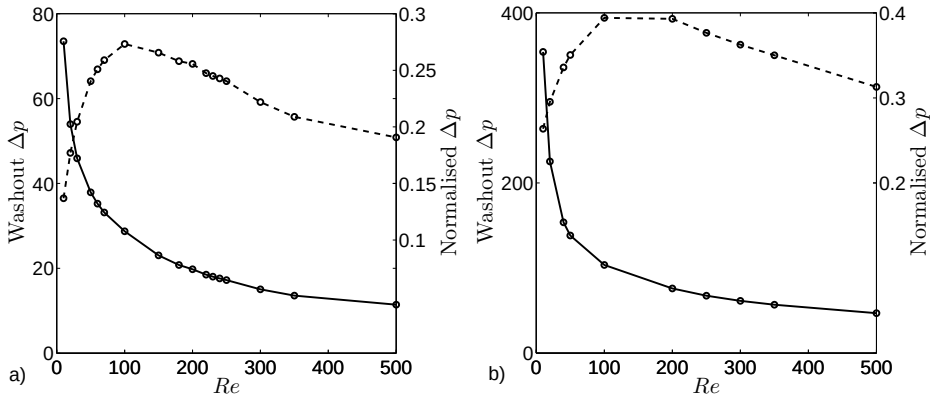

Figure 5.10: Pressure drop offset due to washout with increasing Re at fixed $He = 500$. The solid line shows the pressure drop and the broken line shows the normalized value with the pressure drop, normalized with the Poiseuille flow pressure drop over the length of washout. a) $(h, \delta) = (1, 0.25)$ and b) $(h, \delta) = (1, 0.1)$.

as the washout Δp we present a normalised Δp, for which we have scaled the washout Δp with the pressure drop over a uniform channel of equivalent length to the washout. These plots show that with increasing flow rate (Re) the offset is reduced, i.e. the pressure drop gets closer to that of the plane Poiseiulle flow. This might be expected phenomenologically as for large Re we have seen that the streamlines straighten. The normalized Δp shows a maximum at an intermediate Re.

The effects of flow rate on the static plug within the washout and on conditioning are illustrated more clearly in Fig. 5.11, for 3 different washout geometries. In [209] we have defined the *flowing area* as that part of the washout that is non-stationary. As we have seen here, even when the fluid begins to move it does not necessarily leave the washout: typically there are significant parts of the washout in which the yielded fluid still recirculates. We therefore define the *displaced area* as that part of the washout that is actually removed from the washout. By definition the displaced area is always less than the flowing area. From the industrial perspective, drilling mud that is flowing but not displaced would be to some extent conditioned

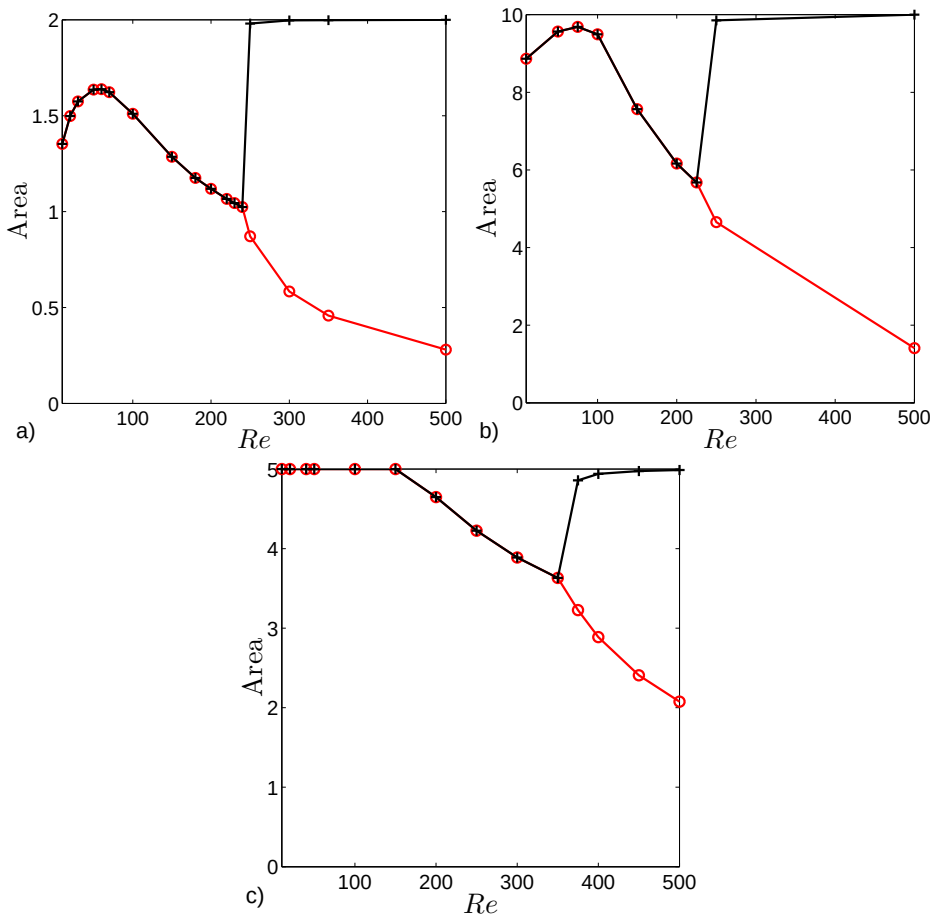

Figure 5.11: Flowing area (black, +) and displaced area (red, ◯) variations with increasing Re at fixed $He = 500$. (a) $(h, \delta) = (1, 0.25)$ (b) $(h, \delta) = (2, 0.1)$ (c) $(h, \delta) = (1, 0.1)$

(sheared) but is not replaced during the circulation phase. Also the degree of shearing in a recirculation zone is questionable. First we often see significant plugs within the recirculation zone. Second, the strength of the recirculation zone is generally very weak and decreases with depth into the washout if very deep, e.g. see the secondary vortices in [209] and the analogy with [166].

We observe in Fig. 5.11a & b similar qualitative behaviour for the first 2 geometries. As Re increases from zero the flowing and displaced areas

initially coincide and increase (i.e. initially increasing flow rate improves conditioning). A first critical Re is attained when both flowing and displaced areas attain a local maximum. This appears to approximately coincide with the onset of the pressure increase in the washout. Further increases in Re result in decreasing flowing and displaced areas until a second critical Re is attained. At the second critical Re a part of the washout fluid begins to move in a recirculation zone. The flowing area thus increases rapidly (essentially there is a jump), whereas the displaced area continues to decrease with Re. Throughout this regime the streamlines are continually straightened and the main flow appears to bypass the washout. For these two geometries the washout depth is modest and once recirculation starts the flowing area quickly converges to the full area of the washout. For a deeper washout this convergence is not immediate, but occurs in all cases as Re increases. This is because at fixed He increasing Re means decreasing B and at low enough B there is no static fluid in the washout.

A different type of behaviour is seen in Fig. 5.11c. Here we observe that the flowing and displaced areas are constant and equal for low Re, but are also equal to the washout area. This can be understood with reference to [208] in which the onset of static regions was studied in wavy-walled channels. It was observed that (for $Re = 0$) when $h\delta < (h\delta)_c$, no static fluid was found in the deepest part of the channel, even as $B \to \infty$, i.e. there is a minimal slope of the washout wall required to have static fluid and the relatively shallow washout in Fig. 5.11c does not exceed the minimum.

At a fixed He by letting $Re \to 0$ we have $B \to \infty$ and in this limit there are only two possibilities: $h\delta$ is less or greater than the critical $(h\delta)_c$. For $(h\delta)_c < h\delta$ we find static fluid at washout for $Re = 0$ (Fig. 5.11a & b). By increasing Re the shear stress over this static region increases and the displaced area increases until the first local maximum. On the other hand, for $h\delta < (h\delta)_c$ there is no static fluid at the washout wall as $Re \to 0$ (Fig. 5.11c). For such cases, as Re increases the streamlines tend to parallelize and the size of extensional stresses in the washout area drops. Somewhat counter-intuitively, a static region appears in the washout as Re increases! Consequently, the flowing area and displaced area decrease above

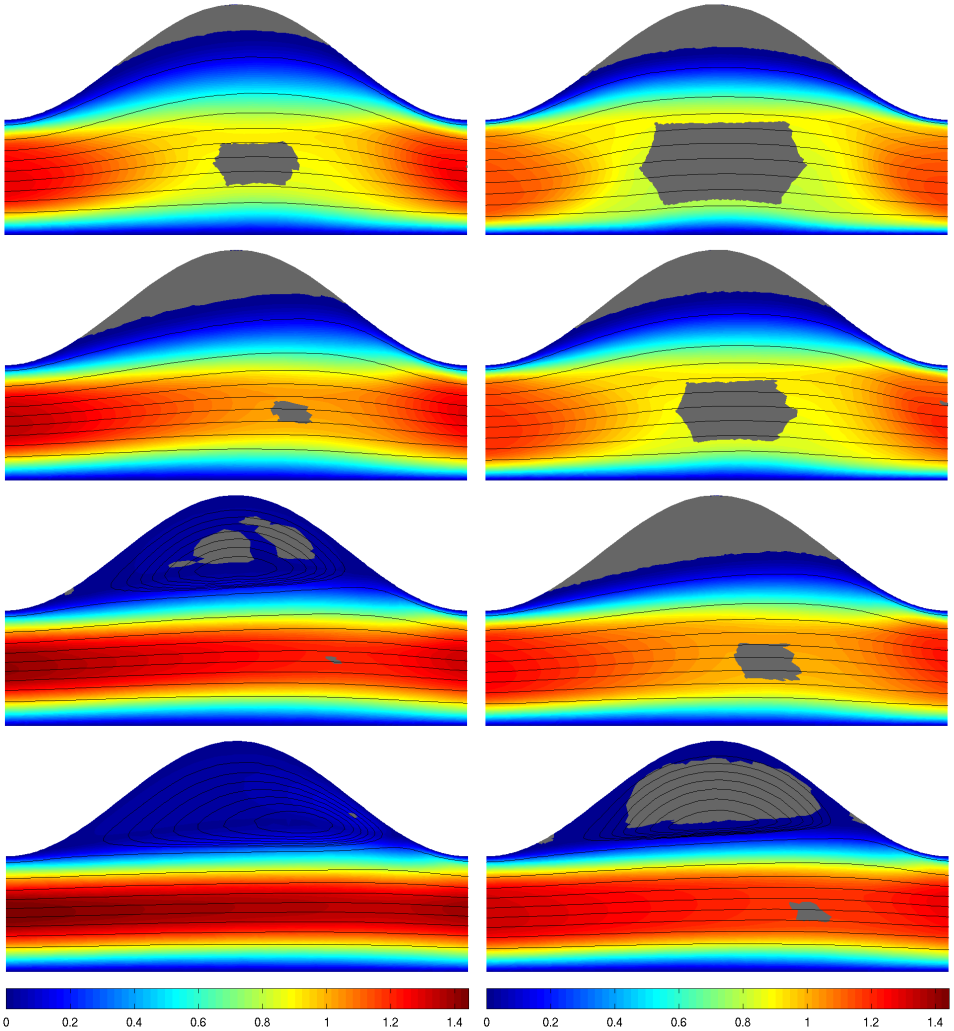

Figure 5.12: Effects of increasing flow rates at fixed He. The inertial effects are controlled by $Re = 50,\ 100,\ 200,\ 400$ (top to bottom) and geometric variables are $(h, \delta) = (1, 0.25)$. The gray areas denote unyielded fluid. Left column: $He = 200$, right column: $He = 1000$.

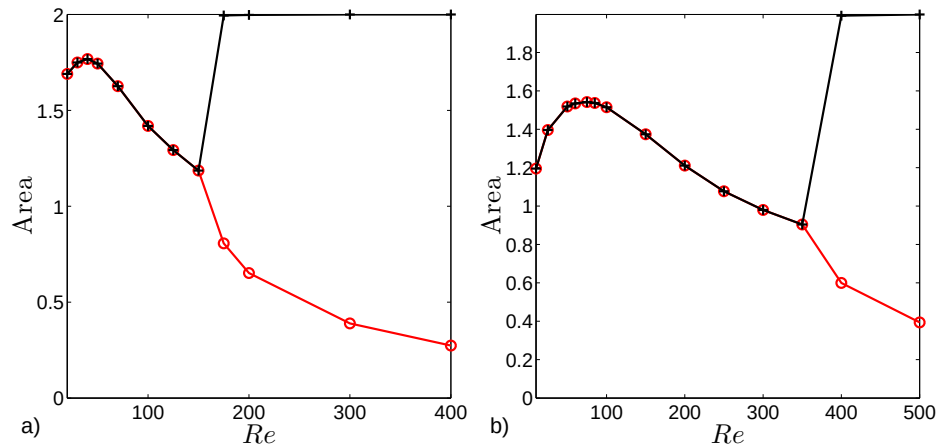

Figure 5.13: Flowing area (black, +) and displaced area (red, ◯) variation with increasing Re for $(h, \delta) = (1, 0.25)$ and different fixed Hedström numbers: (a) $He = 200$ (b) $He = 1000$

this first critical Re. With growth of the static region with Re we again reach a second critical Re, above which the fluid in the washout starts to recirculate and the flowing area rapidly increases.

5.4.2 Varying He

The effects illustrated above for increasing flow rate are also found at other He. Figure 5.12 shows the speed colourmap and streamlines for two other $He = 200,\ 1000$ for increasing flow rates ($Re = 50,\ 100,\ 200,\ 400$ at fixed He), with $(h, \delta) = (1, 0.25)$. The effects are qualitatively similar to those at $He = 500$. The effects on flowing and displaced areas at $He = 200,\ 1000$ are shown in Figure 5.13 and mimic that shown above for $He = 500$. Both critical Re appear to be increased with increasing He. It is worth noting that for the examples shown, with $h = 1$ the washout is not very deep. The maximum washout area is 2 and once recirculation starts the stationary layer is effectively removed (the flowing area is approximately 2 after the second critical Re). In deeper washouts this is not the case at all: recirculation zones co-exist with significant stationary layers deeper into the washout.

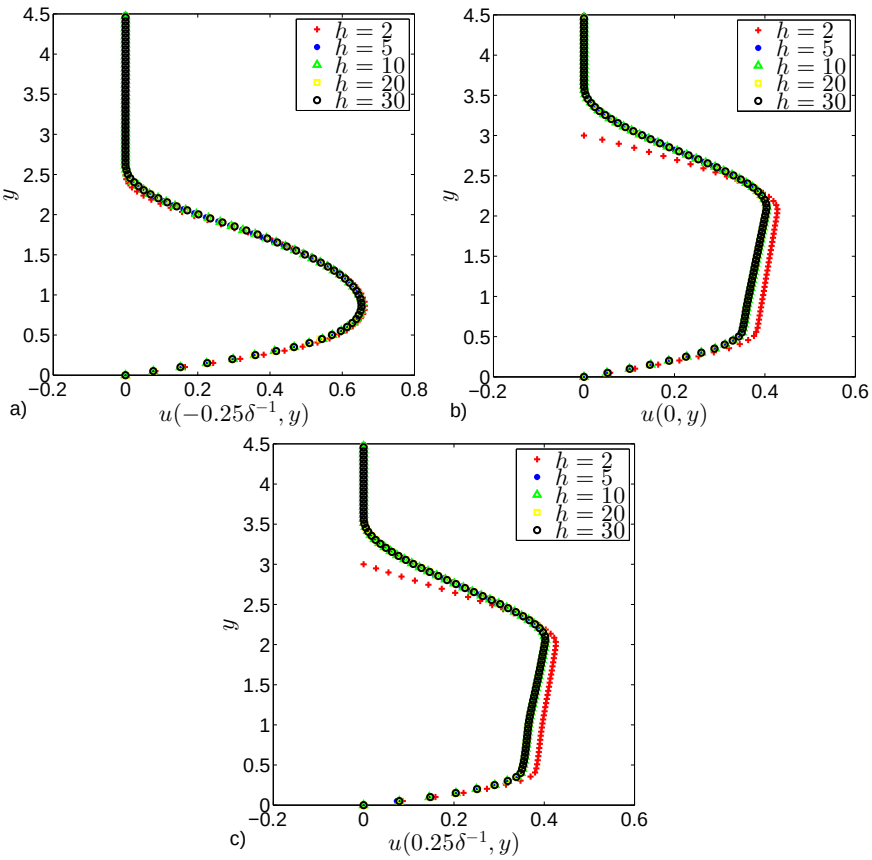

Figure 5.14: Variation of the x-component of velocity $u(x, y)$ with increasing h at a) $x = -0.25\delta^{-1}$, b) $x = 0$, c) $x = 0.25\delta^{-1}$ for a square washout: $(Re, B, \delta) = (100, 5, 0.1)$.

5.4.3 Effects of washout shape

In [209] one of the main results was the discovery at $Re = 0$ that for deep washouts and at large yield stresses the flow self-selects its flowing region. The flowing region was found to become invariant as h is increased and between different washout geometries. Finally, a square washout shape was found to have the maximal stationary regions, of all washouts considered with the same (h, δ). In moving to inertial flows we may expect similar effects, but must be more cautious with regard to washout shape. For example, a square (or angular) washout at large Re is likely to shed vortices

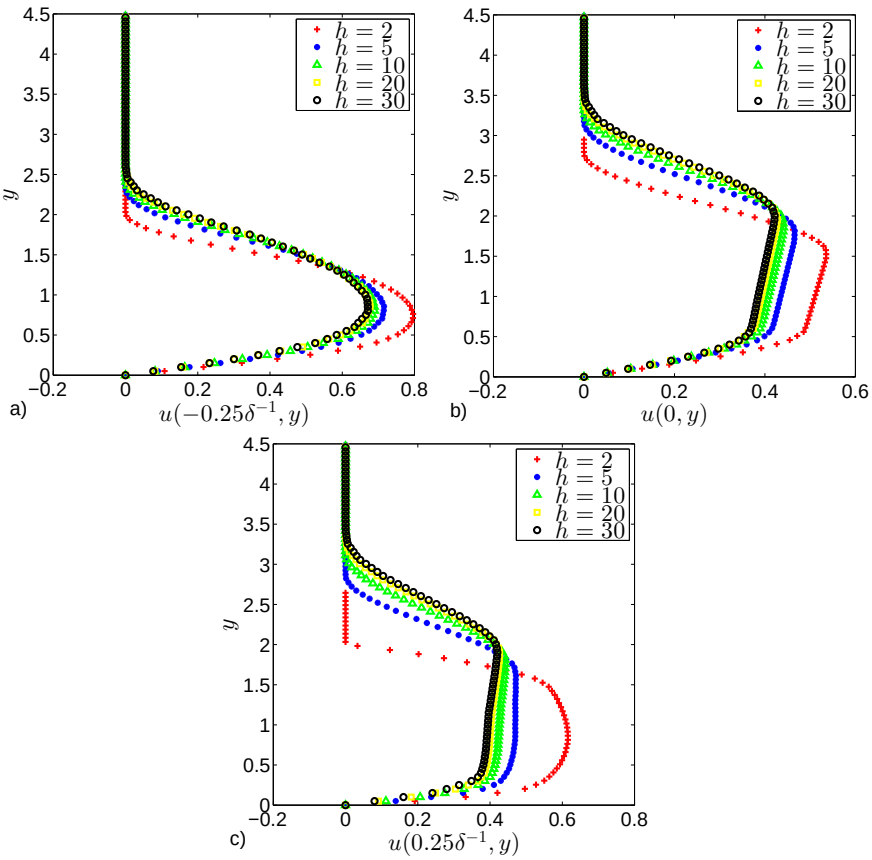

Figure 5.15: Variation of the x-component of velocity $u(x, y)$ with increasing h at a) $x = -0.25\delta^{-1}$, b) $x = 0$, c) $x = 0.25\delta^{-1}$ for a sinusoidally wavy washout: $(Re, B, \delta) = (100, 5, 0.1)$.

at the corners and is likely to become unsteady at lower Re than a smoother washout. Secondly, we have seen that inertial flows transition to a recirculatory regime occurs at a given Re. This transition and the shape of any detached plug region within the recirculating region are likely to be sensitive to washout shape.

We first establish that as h increases, steady flows attain an invariant velocity profile. Figure 5.14 shows the x-component of velocity $u(x, y)$, with increasing h at $x = -0.25\delta^{-1},\ 0,\ 0.25\delta^{-1}$ for a square washout: $(Re, B, \delta) = (100, 5, 0.1)$. We see that as h significantly exceeds the width of the flowing

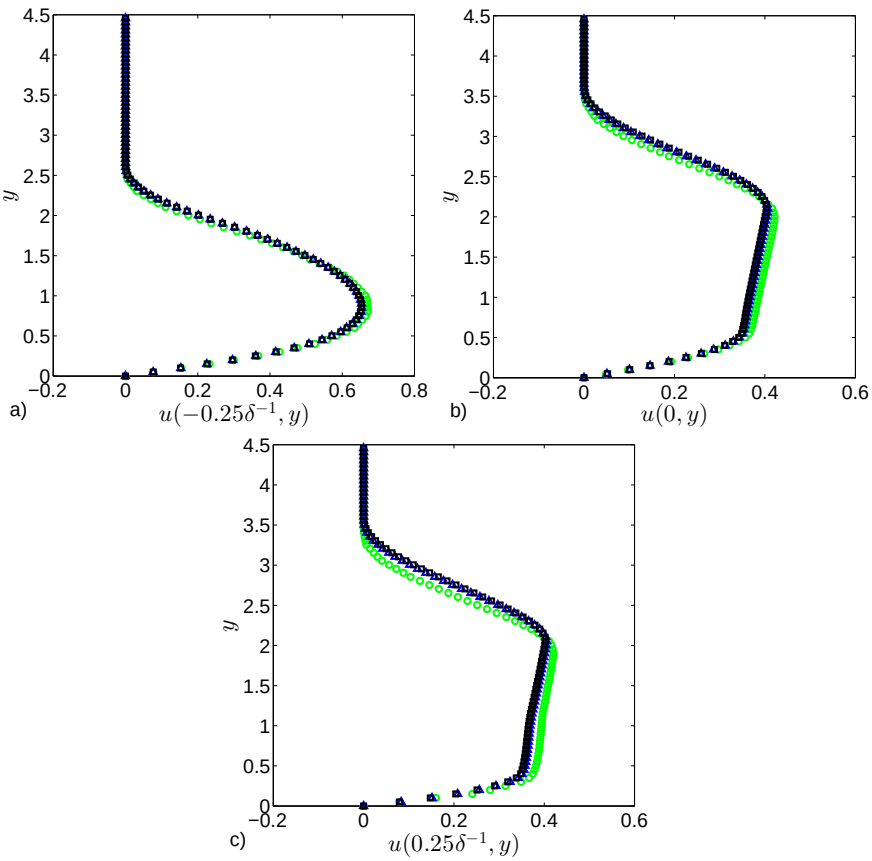

Figure 5.16: comparison of x-component of velocity $u(x, y)$ at a) $x = -0.25\delta^{-1}$, b) $x = 0$, c) $x = 0.25\delta^{-1}$ for $(Re, B, h, \delta) = (100, 5, 30, 0.1)$, between three different washout shapes. The markers are: $\square$, expansion-contraction/square washout; $\triangle$, linear variation/triangular washout; $\bigcirc$, wavy sinusoidal washout.

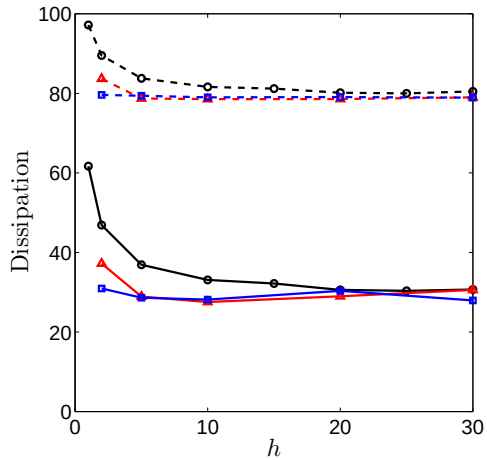

Figure 5.17: Plot of viscous (solid line) and plastic (broken line) dissipation functionals for $(Re, B, \delta) = (100, 5, 0.1)$ and different types of washouts. The markers are: $\square$, expansion-contraction/square washout; $\triangle$, linear variation/triangular washout; $\bigcirc$, wavy sinusoidal washout.

region the velocity appears to converge. Figure 5.15 shows analogous results but for a wavy channel. The velocity field again converges at large h. Finally, Fig. 5.16 compares the velocity profiles at the same x-positions for three different washout geometries of wavy, triangular and square. We can see that square and triangular shapes are close, but the wavy profile has a visible difference and needs higher h to catch up. At any rate the convergence of these is apparently slower than in the non-inertial flows of [209] and this is probably due to the variations along the channel.

A different way of assessing the convergence of the solutions, with large h and/or comparing between geometries, is to evaluate the viscous and plastic dissipation functionals within the washout section of the channel. These functionals include of course extensional strain rates and hence variations along the channel. Figure 5.17 illustrates this variation and although we can see that the dissipation functionals are converging the convergence is relatively slow with h, i.e. considering that the velocity is static in the upper part of the washout at relatively small h for intermediate x. The difference

in dissipation functionals comes mainly from the entry/exit regions of the washout which are sensitive to geometry.

5.5 Discussion and summary

We have presented a largely computational study of steady inertial flows of a Bingham fluid through 2D "washout" geometries, representing longitudinal sections of a narrow eccentric annulus; see Fig. 5.1. This study extends Chapter 4 (and [209]) into the inertial regime, thus giving a more comprehensive picture of effects that occur in circulation phase of cementing of oil wells.

The computations achieve steady state via a time-dependent iteration. We observed that the effect of having a yield stress was to increase the range of Reynolds number Re for which a steady solution could be found, hinting at an increase in stability of the flow with B, as would be expected. This effect was not quantified.

We investigated the effects of increasing Re on converged steady laminar flows. Some effects observed were largely predictable. Increasing Re results in a fore-aft asymmetry in symmetric washout shapes. Increasing Re can lead to an increase in averaged pressure in the expanding part of the washout. Entry/exit development lengths did not have a major effect on the flow within the washout itself.

Increasing Re was studied for fixed Bingham number B and for fixed Hedström number $He = ReB$. The latter represents an increase in flow rate for fixed geometry and fluid properties. In both cases we observed that the variation in flowing area of the washout (i.e. that area that is mobilized) was non-monotone. Depending on the slope of the washout walls $h\delta$, at $Re = 0$ stationary fluid was either present at the walls or not (for sufficiently shallow washouts). Increasing Re resulted in a straightening of the streamlines through the washout region, in the main part of the channel.

At fixed He, the flowing area initially either increased (static layers present at $Re = 0$) or remained constant (equal to the washout area: mobile at $Re = 0$) up until a 1st critical value of Re after which the flowing area

decreased. In this regime of decreasing Re the results are quite counterintuitive and contrary with the industrial perception that pumping faster will circulate/condition the mud better. Note that in some cases increasing Re results in static washout regions when there are none at $Re = 0$!

At higher value of Re, on passing a second critical value, we observe the onset of zones of recirculation within the washout. The flowing area thus increases but the area of washout in which fluid is displaced during conditioning continues to decrease. For the examples we have studied the two critical values of Re cover a range of 100's (see e.g. Figs. 5.11 & 5.13), meaning that these effects are not marginal. Overall this shows that a more careful design of the recirculation/conditioning phase of primary cementing would be fruitful.

We also studied the effects of washout geometry in a targeted way. In [209] the washout geometry was observed to have little effect on flowing area geometry for sufficiently large B and h. The same phenomena was observed again at large h over a range of different washout geometries. We examined convergence of the velocity profiles and dissipation rates, for different shapes as h is increased. Thus, the self-selection of flowing area still remains valid for $Re > 0$ in steady laminar flows over the range of parameters considered. However, we noted that convergence was slower than for $Re = 0$ and retain some caution in using reference geometries (such as the square washout in [209]) with sharp corners since these are likely to be vulnerable to inertial instabilities induced by geometry, e.g. vortex shedding.

Our attention is now focused in two future directions. Firstly, the problem of fluid-fluid displacement through similar geometries as considered here requires study. These flows are typically complicated by both density and rheology differences between the fluids. Even for iso-density displacements it is known that static layers can result as a less viscous fluid by-passes an in-situ yield stress fluid; e.g. [9]. Including a density difference increases the flow complexity but also makes questionable the 2D assumptions made here, as buoyancy, eccentricity and inclination in geometries such as Fig. 5.1 almost certainly will promote azimuthal displacement flows. Nevertheless, the 2D study of displacement is the next logical step and our progress on this

problem is outlined next in Chapter 6. The second direction planned for the future is to study 3D geometries. Not only are primary cementing displacements likely to become more 3D, but other important cementing geometries are also inherently 3D. An example being the setting of abandonment plugs in milled out wellbores, e.g. [46].

Chapter 6

Displacement flow

In this chapter we begin to consider the displacement of a yield stress fluid through washout geometries related to the primary cementing flow in oil/gas well construction. First we review the relevant literature and formulate the problem to solve. Then we discuss some of the computational challenges and present a set of initial results for the displacement of Bingham fluid by a Newtonian fluid in a square washout geometry.

6.1 Introduction

Two-fluid and displacement flows have been subject of vast interest in fluid mechanics research, both due to the many applications and to having rich theoretical aspects. For better clarity in what follows, we call the **displacing fluid** the *invading fluid* and the **in situ or displaced fluid** the defending fluid.

Perhaps the most well know phenomenon in displacement flows is the Saffman–Taylor instability [211] that happens when the invading fluid is less viscous and fingers into the defending fluid. Examples include secondary and ternary oil recovery. The Rayleigh–Taylor instability [218] occurs when the density difference between fluids is mechanically unstable, i.e. heavy fluid above light fluid. Examples are nuclear explosion, mushroom clouds from volcanic eruptions and supernova astrophysical explosions. The Kelvin-

Helmholtz [89] is an archetypical instability that occurs at the interface of two fluids, moving at different velocities (e.g. in shear flow, although the origins are inviscid), and results in astounding vortex shapes such as in cloud formations, Jupiter's Red Spot and the Sun's corona. Thus, two-fluid flows have triggered considerable research in hydrodynamic stability theory with many applications.

One reason for the rich dynamics of two-fluid systems comes from the contrast in physical parameters of the fluids (e.g. density, viscosity, etc...), across the *interface*. For immiscible fluids surface tension is also present and can strongly affect the interface dynamics, while for miscible fluids mixing occurs. Due to this diversity, there is enormous amount of work in the literature of two-fluid and displacement flows, that would require an extensive review. However, with primary cementing as our principal motivation we limit our review to those displacement flows in confined geometries with the possibility of having residual layers of defending fluid. In the primary cementing process, the (in-situ) defending fluid is a drilling mud and the invading fluid is either a cement slurry or a spacer fluid. All these fluids may be considered to be shear-thinning yield stress fluids.

The industrial difficulty stems from the possibility of the defending drilling fluid remaining behind in the well after displacement. In this chapter we will consider a simplified model of the primary cementing flow in a 2D rectangular washout. The geometry is initially filled with defending fluid and invading fluid displaces it as it is pumped from upstream. The fraction of the defending fluid which is eventually displaced is called displacement efficiency: $\eta \in [0\ 1]$, which ideally should increase to 1 over the course of the displacement flow. The displacement efficiency is however a simplified indicator of a wide range of complex behaviours. Here we start to explore some of these behaviours in washout geometries.

One type of displacement flow with residual layers are gas displacement flows, which have application in injection molding, enhanced micro filtration [144], ... In displacement flow of two Newtonian fluids in a uniform channels, residual wall layers can exist over very long times only when the displacing fluid is inviscid. Otherwise the residual wall layers will drain over time

due to viscous shear stresses exerted at the interface and the displacement efficiency asymptotes to 1. This means that permanent residual layer is only possible when the invading fluid has zero viscosity. The gas displacement of a Newtonian fluid in a pipe was first studied experimentally by Taylor [231]. As well as predictions of residual layer thickness he suggested three possible configurations of the stream lines around the interface. Cox [73] gave more explanations and the predictions of the streamline shapes were confirmed numerically by Soares et al. [222]. Dimakopoulos and Tsamopoulos [83] studied numerically the inertial gas displacement flow in straight tubes and in a contraction. They showed that increasing the gas pressure does not affect the thickness of deposited layer and shape of the advancing bubble in straight tubes and only makes the process faster.

There are also some gas displacement studies of non-Newtonian fluids. Dimakopoulos and Tsamopoulos have numerically investigated these flows for several cases: displacement of viscoplastic [84] and viscoelastic [85] fluids in straight and contraction geometries, gas displacement of viscoplastic fluid in expansion-contraction geometry [86]. De Sousa et al. [76] investigated gas displacement of shear-thinning and viscoplastic fluids numerically. They observed that by decreasing the shear thinning index or yield stress the thickness of deposited residual layer decreases.

All of the above mentioned works are for immiscible fluids and surface tension is important. In primary cementing it is common to use a spacer fluid that is chemically compatible with both the drilling mud and cement slurry. Commonly the fluids are water-based and miscible. Despite being miscible, the molecular diffusivity between fluids is generally very low. Hence sharp interfaces exist in displacement flows and significant mixing occurs only if the flow becomes chaotic. This limit of zero molecular diffusion of miscible flows is interesting as it is mathematically the same as the limit of zero surface tension of immiscible fluids. So this type of flow stands in the mid-ground between miscible and immiscible displacements.

One approach to modelling cementing is to consider the wellbore and casing as two eccentrically arranged pipes separated by a thin gap, varying slowly in the azimuthal and axial directions. This approach leads to

a Hele-Shaw approximation for the flow. This kind of flow has been studied e.g. Alexandrou and Entov [5] who study the fingering of inviscid fluids for Bingham and other non-Newtonian fluids. This type of model has also been extensively used for the study of primary cementing in our group; see [33, 47, 48, 153, 189]. This model gives valuable information about displacement flow. However, the basic flow unit considered is the flow of a single fluid in a slowly varying channel, which therefore cannot have stationary layers at the wall, i.e. the Hele-Shaw approach involves averaging across a narrow gap. Static fluids in this type of model only happens when the pressure gradient is insufficient to mobilize the entire fluid in the gap, which is a different mechanism from getting static fluid at the wall due to geometrical non-uniformity.

The most relevant works are those considering the displacement of viscoplastic fluid by another fluid, with a focus on static wall layers. Allouche et al. [9] carried out a detailed study of static layers in displacement flow of two iso-density viscoplastic fluids in plane channel. Using a lubrication model they give sufficient conditions to have no static wall layer, which depends on two dimensionless parameters: the displacing fluid Bingham number and the ratio of the yield stress of the two fluids. If these conditions are not met, an upper bound (h_{max}) for the static wall layer thickness can be derived. However, comparing their theoretical estimates with 2D computations of the actual thickness of residual layers revealed that h_{max} is too conservative. By analyzing the streamline configuration close to the steady displacing front, a new recirculating thickness h_{circ} was derived which is in close agreement with the 2D computations. Frigaard et al. [103] studied steady front displacement of iso-density fluids theoretically and showed that for a given shape of displacing front static layers with different thickness can exist. Thus they concluded that the final thickness of layers depends on transients, not the steady solution. Frigaard et al. [104] considered two-layer axial flows of iso-density viscoplastic fluids. They derived two variational principles for these flows: strain rate minimization and stress maximization principles. The strain rate minimization leads to existence and uniqueness results for this class of flow. The stress maximization principle leads to a

number of qualitative results. For example it is shown that using stress maximization principle, an interface shape optimization problem for maximal wall static layer is obtained. Wielage and Frigaard [249] studied the same problem as in [9], but with two improvements. First, they used the augmented Lagrangian method, rather viscosity regularisation, in order to compute (truly) static layers. Secondly, they extended their simulations for significantly longer times to make sure that slower transients do not change the static layer thickness. In addition they studied the combined effects of inertia and pulsation of the displacing flow, on the static wall layers shape and efficiency of displacement.

By looking at the work published that addresses primary cementing displacement flows, we see that all of the studies concerning static layers on the walls are performed in uniform channels: the effect of non-uniformity in the geometry has not been considered in the context of displacements. In this chapter we start to consider this problem.

6.2 Model problem

A full study of the cement-drilling mud displacement flow is extremely complicated. Rheologically, both fluids are usually modeled as Herschel-Bulkley fluids. The density can be quite different and in reality the well might be inclined at any angle relative to gravity. Adding geometrical parameters to these degrees of freedom, we would end with a problem of at least 10 dimensionless parameters, which is very hard to study.

To simplify, we consider iso-density displacement flow of a Bingham fluid by a Newtonian. Having iso-density fluids we neglect both gravity and inclination. Further, we only use the square shape as a washout geometry. This is the simplest displacement flow for which we are likely to have static residual regions attached to the walls and within the washout, and for which the two fluids have some rheological freedom and relevance.

With these simplifications, we consider the flow geometry as shown in Figure 6.1. The unsteady Navier-Stokes equations and the mass conserva-

tions govern the flow, as usual. In dimensional form these are:

$$\hat{\rho}(\frac{\partial \hat{\mathbf{u}}}{\partial t} + \hat{\mathbf{u}}.\nabla\hat{\mathbf{u}}) = -\nabla\hat{p} + \nabla.\hat{\boldsymbol{\tau}}, \tag{6.1}$$

$$\nabla.\hat{\mathbf{u}} = 0. \tag{6.2}$$

These equations hold for the entire flow domain of the invading/defending fluids. The difference comes in the stress divergence term for each fluid. For parts of the domain filled with invading fluid (cement or spacer)

$$\hat{\tau}_{ij} = \hat{\mu}_i\hat{\dot{\gamma}}_{ij}, \tag{6.3}$$

and for parts of the domain filled with the defending fluid (drilling mud)

$$\hat{\tau}_{ij} = (\hat{\mu}_d + \frac{\hat{\tau}_y}{\hat{\dot{\gamma}}(\hat{\mathbf{u}})})\hat{\dot{\gamma}}_{ij} \Leftrightarrow \hat{\tau} > \hat{\tau}_y, \tag{6.4}$$

$$\hat{\dot{\gamma}}_{ij} = 0 \Leftrightarrow \hat{\tau} \leq \hat{\tau}_y. \tag{6.5}$$

Here $\hat{\mu}_i, \hat{\mu}_d$ are the viscosities of invading and defending fluids and $\hat{\tau}_y$ is yield stress of the defending fluid. If the fluids domains are independent, then we also have an interface, say $\hat{F}(\hat{\mathbf{x}}, \hat{t}) = 0$, that is advected with the flow, via a kinematic equation. At the interface the velocity is continuous. We also should have continuous traction vector along the interface:

$$(-\hat{p} + \hat{\boldsymbol{\tau}})_{invading}.\mathbf{n}_s = (-\hat{p} + \hat{\boldsymbol{\tau}})_{defending}.\mathbf{n}_s, \tag{6.6}$$

where the left and right sides are evaluated using (6.3) and equations (6.4-6.5) respectively ($\mathbf{n}_s$ is the unit normal vector to the interface). An alternate description (adopted below) is to consider the fluid phases to be defined by a scalar concentration (i.e. volume fraction), that is advected and diffuses (and then consider the limit of small diffusivity).

Geometrical parameters for the flow are the width $\hat{D}$ of the channel, depth $\hat{H}$ and length of washout $\hat{L}$. As with the inertial flows in Chapter 5, there is also entrance/exit development length $\hat{l}$, see Figure 6.1. To make the equations dimensionless we use these scales: mean velocity in the uniform

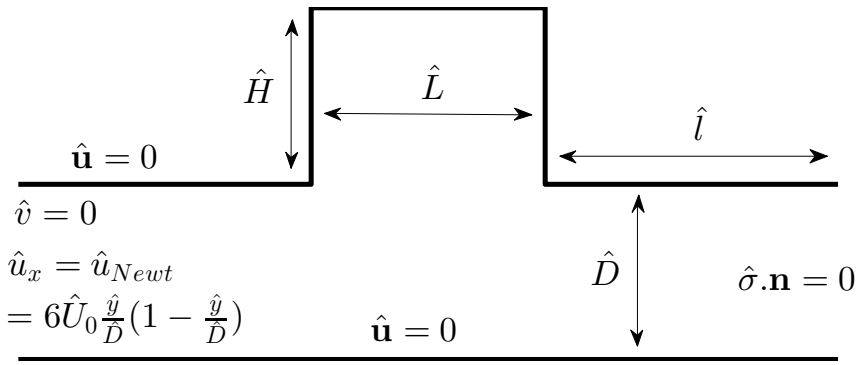

Figure 6.1: Problem domain, geometrical dimensions and boundary conditions used for displacement flow

channel $\hat{U}_0$ for velocity, $\hat{\mu}_d\hat{U}_0/\hat{D}$ for stresses and $\hat{D}$ for lengths. With these scales the non-dimensional equations are:

$$Re(\frac{\partial \mathbf{u}}{\partial t} + \mathbf{u}.\nabla\mathbf{u}) = -\nabla p + \nabla.\boldsymbol{\tau}, \tag{6.7}$$

$$\nabla.\mathbf{u} = 0. \tag{6.8}$$

The constitutive law for the invading fluid (cement slurry or spacer) becomes:

$$\tau_{ij} = M\dot{\gamma}_{ij}, \tag{6.9}$$

and for the defending fluid (drilling mud):

$$\tau_{ij} = (1 + \frac{B}{\dot{\gamma}(\mathbf{u})})\dot{\gamma}_{ij} \Leftrightarrow \tau > B, \tag{6.10}$$

$$\dot{\gamma}_{ij} = 0 \Leftrightarrow \tau \leq B. \tag{6.11}$$

Dimensionless dynamic parameters of the problem are the Reynolds number, $Re = \hat{\rho}\hat{U}_0\hat{D}/\hat{\mu}_d$, the Bingham number $B = \hat{\tau}_y\hat{D}/\hat{\mu}_d\hat{U}_0$, and the viscosity ratio $M = \hat{\mu}_i/\hat{\mu}_d$, of invading to defending fluid. The dimensionless geometric parameters are the maximum washout depth, $H = \hat{H}/\hat{D}$, the washout length $L = \hat{L}/\hat{D}$, and the development length, $l = \hat{l}/\hat{D}$. Following Chapter 5 we fix the development length to $l = 10$.

For boundary conditions we have no-slip on the top/bottom walls. At the inflow a Poiseuille velocity profile of Newtonian fluid is prescribed such that the non-dimensional flow rate $Q = 1$ (as velocities scaled with mean velocity). And at the outlet zero stress boundary condition is applied, see Figure 6.1.

We use the augmented Lagrangian method for solution of this problem as before and we do not repeat the details here. The rest of the numerical scheme, including surface tracking and Navier-Stokes problem, is explained in the following sections.

6.3 Numerical method for interface tracking: VOF

Interface tracking is the major challenge that one faces in the numerical solution of the two fluid systems. The methods used can be mainly grouped into **Lagrangian** and **Eulerian**, with some others that use both in a hybrid way.

In Lagrangian methods the interface is tracked directly using a set of points which are advected with the velocity field. The advantage is that interface tracking is accurate and simple, as we directly follow the position. Also computing the normal vector to the interface is also more accurate. However the problem is that it is hard to capture merging or break-up of the interface, e.g. a bubble which breaks up or two bubbles that merge.

On the other hand Eulerian methods do not directly track the interface, instead a passive scalar field is used which is advected with the velocity field on a mesh, and the interface shape is implicitly inferred from the field. Volume of fluid (VOF) [119], level set [2] and phase field [248] are examples of Eulerian interface tracking methods. The main advantage is that merge/break-up of the interface is easily tracked. On the other hand, since these methods filter some information about the interface, we cannot reconstruct the shapes of the interface as accurate as with Lagrangian methods. This is a motivation for using hybrid approaches which try to mix both of these.

If the specific problem of study does not involve merge/break-up Lagrangian method is easy and advantageous, however this is not the case for the displacement flows that we are interested in. Here the flow phenomena to be studied are unknown at the outset. Thus we use the VOF method. In this method a scalar field c is defined as the fraction of the volume of each cell in the mesh which is occupied by one fluid, see Figure 6.2. Obviously we have $c \in [0\ 1]$. The equation for evolution of c would be

$$\frac{Dc}{Dt} = \frac{\partial c}{\partial t} + \mathbf{u}.\nabla c = 0. \tag{6.12}$$

By using incompressibility $\nabla.\mathbf{u} = 0$ we can write the equation in conservative form

$$\frac{\partial c}{\partial t} + \nabla.(c\mathbf{u}) = 0. \tag{6.13}$$

The advantage of this form is that if we use Finite Volume methods for solution, then it is guaranteed to conserve the volume of fluids at the discrete level.

Having discrete conservation of c is good, but more is required. The other important properties of c are: (a) it should preserve a sharp transition from 0 to 1 around the interface; (b) The range of c should remain $[0\ 1]$, as it has no physical meaning to have $c < 0$ or $c > 1$. This problem of conservation laws with sharp changes has been well studied. If we use conventional flux computation schemes we either get too much dissipation of c, i.e. smearing of the interface or often get overshoots of c to outside of the physical range. One solution is to use special flux computation schemes such as **MUSCL**, which stands for Monotone Upstream-centred Schemes for Conservation Laws.

For our problem we use the van-Leer limiter which is designed for structured meshes only. Generally MUSCL schemes are much more complicated for unstructured meshes. Since for our problem, in this simplified geometry, using structured is adequate, we avoid those complications. We outline the scheme for a simple 1D flow in x direction as shown in Figure 6.3. Equation

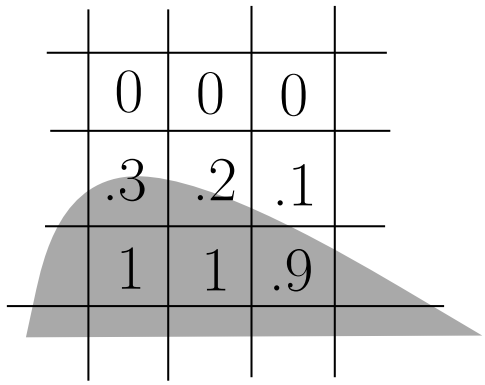

Figure 6.2: Volume fractions values assigned to each cell in VOF

(6.13) for this flow simplifies to

$$\frac{dc}{dt} + \frac{d(cu)}{dx} = 0, \tag{6.14}$$

where u is the velocity in positive x direction. Integration over cell i yields the finite volume form

$$\frac{d}{dt}\int_i c\ dx + \int_i \frac{d(cu)}{dx}\ dx = 0, \tag{6.15}$$

$$\frac{d}{dt}\int_i c\ dx + \frac{(cu)_{i+1/2} - (cu)_{i-1/2}}{\Delta x} = 0. \tag{6.16}$$

We need to compute the fluxes $(cu)_{i+1/2}, (cu)_{i-1/2}$ on faces of control volume. The 1D MUSCL scheme computes the flux $F_{i+1/2}$ on the face $i+1/2$ of cell i as

$$F_{i+1/2} = u_{i+1/2}[c_i + \psi(r_{i+1/2})(c_i - c_{i-1})], \tag{6.17}$$

$$r_{i+1/2} = \frac{c_{i+1} - c_i}{c_i - c_{i-1}}. \tag{6.18}$$

The function ψ is called flux limiter and $r_{i+1/2}$ shows the ratio of jump

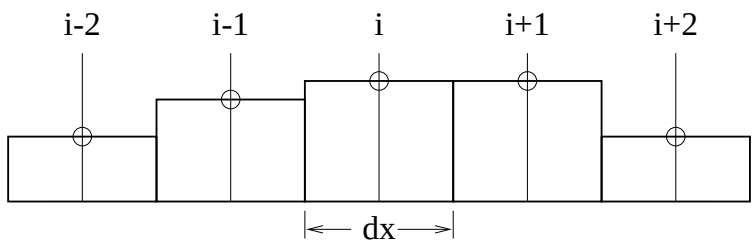

Figure 6.3: A 1D domain and its finite volume discretization. Figure courtesy of C. Olivier-Gooch

across the boundaries of c. For the van-Leer limiter we use:

$$\psi(r) = \begin{cases} 0 & \Leftrightarrow r \leq 0, \\ \dfrac{2r}{1+r} & \Leftrightarrow r > 0. \end{cases} \tag{6.19}$$

With this type of computing fluxes we will have both sharp boundaries and keeping the scalar in the physical range [0 1].

To extend this method for 2D we simply apply the above scheme in each direction separately. This is possible as we use a structured rectangular grid. The van-Leer scheme cannot be applied to an unstructured grid in this simple format. The 2D equation in discrete form becomes

$$\frac{c_{i,j}^{n+1} - c_{i,j}^{n}}{\delta t} + \frac{F_{i+1/2,j}^{n} - F_{i-1/2,j}^{n}}{\Delta x_{i,j}} + \frac{F_{i,j+1/2}^{n} - F_{i,j-1/2}^{n}}{\Delta y_{i,j}} = 0, \tag{6.20}$$

where δt is time step, $\Delta x_{i,j}, \Delta y_{i,j}$ are the sizes in x, y directions of cell i, j. All $F_{k,l}$ fluxes are computed as explained for the 1D case.

One important issue with VOF that we didn't discuss here is interface reconstruction. A variety of ways have been proposed such as SLIC [179], PLIC [255], LVIRA [197] and others. This has applications when we want to obtain the interface normal and curvature for computation of surface tension effects. As we consider miscible flows no surface reconstruction is necessary and we basically ignore these features. Also another limitation is that VOF cannot be used for systems with three or more fluids.

6.4 Numerical method for the solution of the Navier-Stokes equation with an interface

The VOF method for tracking of the interface was explained in the previous section. Now to solve the displacement flow, the Navier-Stokes should be coupled with this equation. Generally speaking, the coupling can be strong or weak. In the former method both equations are solved together in each time step, while in the latter each equation is solved sequentially within each time step and the information is transferred between them.

We use weak coupling of VOF/Navier-Stokes equations and also include the ALG2 of the augmented Lagrangian method (1) in Navier-Stokes solution. In the version of ALG2 that we have used so far, a generalized Stokes problem arises at each iteration. The Stokes problem includes two new tensor fields: the Lagrange multiplier, $\mathbf{T}$, and the relaxed strain rate, $\boldsymbol{\gamma}$. We use a Finite Element Method to solve the Stokes problem. A first order Euler time discretization is used. Pressure and viscous terms are implicitly assembled. The inertial term is first linearized using the convective velocity field of the previous iteration, then it is considered implicitly and a standard finite element assembly is used for it. In summary the discrete form of the generalized Stokes equation is

$$Re(\frac{\mathbf{u}^{n+1}-\mathbf{u}^{n}}{\Delta t}+\mathbf{u}^{n}.\nabla\mathbf{u}^{n+1})=-\nabla p^{n+1}+a\nabla.(\dot{\gamma}(\mathbf{u}^{n+1}))+\nabla.(\mathbf{T}^{n}-a\boldsymbol{\gamma}^{n}). \tag{6.21}$$

The parameter $a > 0$ is the augmentation parameter which should be set. We use $a = 10$. The weak form of this equation is solved using the PELICANS [135] finite element framework. This code has been used within our group for several years for solution of many types of displacement flows in uniform channels.

By using VOF the sharp variation of color scalar from 0 to 1 is smoothed somewhat. For intermediate values of c we need to use some value for the physical parameters. Instead of two constitutive relations (6.3)–(6.5), we

use linear interpolation:

$$\tau_{ij} = (M(c) + \frac{B(c)}{\dot{\gamma}(\mathbf{u})})\dot{\gamma}_{ij} \Leftrightarrow \tau > B(c), \tag{6.22}$$

$$\dot{\gamma}_{ij} = 0 \Leftrightarrow \tau \leq B(c), \tag{6.23}$$

$$B(c) = (1-c)B, \tag{6.24}$$

$$M(c) = cM + (1-c). \tag{6.25}$$

We take $c = 1$ as the invading fluid, for which the above model reduces to (6.3), and for $c = 0$ this gives the defending fluid rheology (6.4)–(6.5).

Algorithm 3 Solution algorithm for two fluid Navier-Stokes flow

Let $\mathbf{u}^0, p^0, c^0, \mathbf{T}^0, \boldsymbol{\gamma}^0$ and Δt given
while End time not reached **do**
  Compute approximate δt of color transport equation from CFL condition (6.26). Then set $n = \lceil \Delta t/\delta t \rceil$ and $\delta t = \Delta t/n$
  for $i = 1 : n$ **do**
    Advance c by solving (6.20)
  end for
  repeat ▷ Conventional ALG2 (1) iterations
    1- Using the updated c^{n+1} solve (6.21)
    2- Set

$$\gamma_{ij}^{n+1} = \begin{cases} 0 & |T_{ij}^{n-1} + a\dot{\gamma}_{ij}(\mathbf{u}^{n+1})| \leq B(c) \\ (1 - \frac{B(c)}{|T_{ij}^{n-1} + a\dot{\gamma}_{ij}(\mathbf{u}^{n+1})|})\frac{T_{ij}^{n-1} + a\dot{\gamma}_{ij}(\mathbf{u}^{n+1})}{M(c)+a} & \text{otherwise} \end{cases}$$

    3- Set

$$T_{ij}^{n+1} = T_{ij}^{n} + a(\dot{\gamma}_{ij}(\mathbf{u}^{n+1}) - \gamma_{ij}^{n+1})$$

  until $|\gamma_{ij}^{n+1} - \dot{\gamma}_{ij}(\mathbf{u}^{n+1})|_{L^2} \leq 10^{-6}$ or 300 iterations reached
end while

The time step restriction is coming from explicit solving of the color function for VOF. So we need a CFL condition taken as

$$\delta t \leq A_{CFL} \frac{\min\{\Delta x, \Delta y\}}{\max|u_x| + \max|u_y|}. \tag{6.26}$$

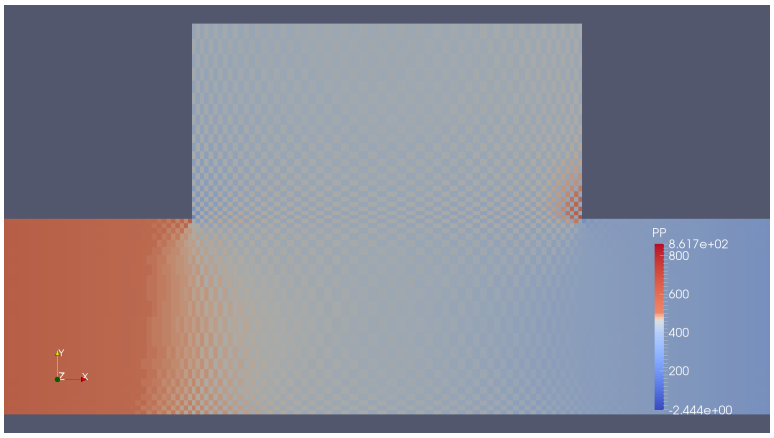

Figure 6.4: Checker-board pattern of pressure field due to violation of Inf-Sup condition.

We usually use $A_{CFL} = .2 - .3$ range. The Navier-Stokes part is less restrictive in terms of the time step, in comparison to the VOF part. With this fact, to save computational cost, the c-transport equation is advanced over several smaller time steps and then the Navier-Stokes is solved with one bigger time step. The overall solution procedure is summarized in Algorithm 3.

Numerical issues encountered and solutions

Despite the fact the two fluid solver presented has been used in our group successfully for several years, we had issues when we applied to our problem. First, all of the previous problems studied had a uniform channel as geometry. Second, the type of elements used for velocity, pressure, multiplier and color were standard $Q1, Q0, Q0$ and $Q0$ elements respectively, see Figure 6.5. It is known that the $Q1, Q0$ element pair does not satisfy the inf-sup compatibility condition. The practical consequence of this is that the the pressure field may show some spatial oscillations (checkerboard modes). However, as discussed in [249], this has not been observed for the displacement flows that have been studied to date. When we used the same solver for our case, oscillatory pressure fields showed up in the washout section,

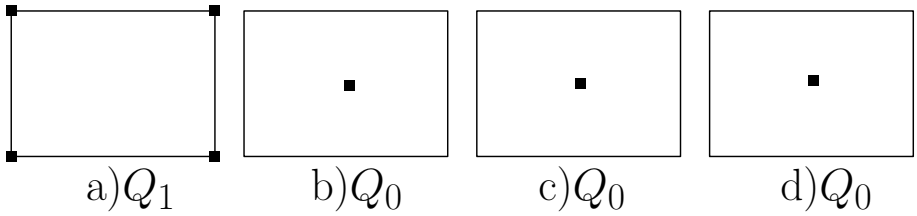

Figure 6.5: The original element types used for displacement flows a) velocity, b) pressure, c) multiplier, and d) color spaces

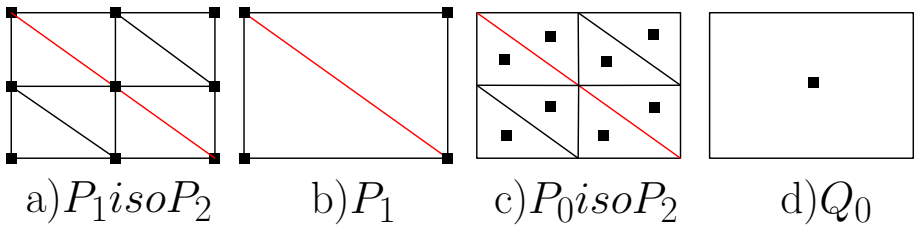

Figure 6.6: The modified elements for Inf-Sup compatibility. a) velocity, b) pressure, c) multiplier, and d) color spaces. The red line shows rectangle divided to two triangular elements.

see Figure 6.4 for example. A very interesting checkerboard type pattern is obvious in this figure.

Consequently to solve this problem an improved choice of elements was needed. For Bingham flows an ideal set of elements for unstructured triangular grids could be $P_1 isoP_2$, P_1 and $P_0 isoP_2$ for velocity, pressure and multiplier spaces, respectively. For Stokes equations the Taylor-Hood elements $P_2 - P_1$ are popular, e.g. [30]. However, as the second derivative of the velocity field of Bingham flows is not necessarily continuous, higher order elements may not increase the accuracy, so cheaper elements are preferred.

One issue was that our solver for c was limited to quadrilateral meshes, so we kept the main mesh as rectangular for the VOF solver, but each rectangle was split internally into two triangles for the Navier-Stokes part, see Figure 6.6. This looked fine, but on implementation the VOF solver was observed to overshoot, giving $c > 1$ in some parts of the domain, especially around the corners of the washout. This problem took a long time to resolve. Eventually it was concluded that this had been due to not having

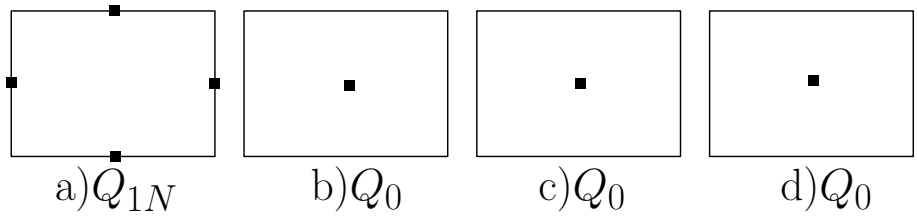

Figure 6.7: The elements set with discrete divergence free property. a) velocity, b) pressure, c) multiplier, and d) color spaces.

a divergence free velocity field, at the discrete level, on elements of the c-space. To explain this further, there is no direct discrete guarantee that the integral $\int \mathbf{u}.\mathbf{n}$ around the domain of the element in Figure 6.6d, evaluated using the velocity nodes in Figure 6.6a, would **exactly** be equal to zero. When this property does not exist at the discrete level, (6.13) would not be equal to (6.12) at the discrete level. This is because we assumed $\nabla.\mathbf{u} = 0$ to convert the original color equation (6.12) to (6.13). This discrepancy in discrete level can lead to $c > 1$ as we were observing.

The remedy to the c overshoot issue is to use elements that guarantee that the discrete level is divergence free. We used a new set: Q_{1N} non-conforming and Q_0, respectively for velocity and pressure [204], with Q_0, Q_0 for multiplier and color elements; see Figure 6.7. The new combination of velocity/pressure elements gives the discrete divergence free condition and no more observations of color overshoot were made. On the other hand the draw back of using a non-conforming velocity space is that the accuracy is lower compared to the $P_1 iso P_2$ space, which is linear.

6.5 Validation with previous steady computations

As noted, the displacement code has been previously used within our group for study of several flows and we had good level of confidence. However to validate the new elements, we compared with the results of the steady inertial computations (calculated with FreeFEM++ on unstructured triangular meshes plus mesh adaptation) of Chapter 5. For this purpose we allow the

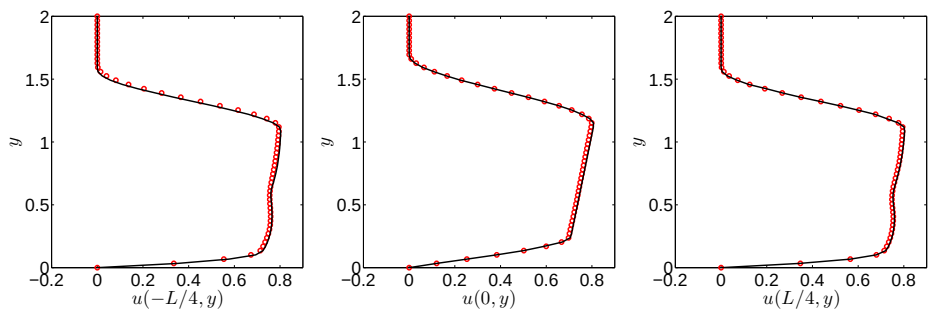

Figure 6.8: x-velocity profiles $u(x, y)$ at three sections of the washout (left to right): $x = -L/4,\ 0,\ L/4$. The displacement solver (red circles) is compared with the steady inertial solutions of the flow computed using FreeFEM++ with mesh adaptation (solid lines). The rows are $Re = 10$, all with $He = 500$.

same Bingham fluid to displace itself in a square washout $H = 1,\ L = 4$ for long enough time to reach steady state. The comparisons of velocity profiles at three equally spaced sections of the washout are shown in Figures 6.8,6.9,6.10,6.11 and 6.12. We fix the Hedström number $He = 500$ (recall $He = Re \times B$ as in Chapter 5), and vary five Reynolds numbers: $Re = 10,\ 50,\ 100,\ 200,\ 500$. We observe that the results match well. The validity of displacement code with the new Q_{1N} elements is thus reinforced.

6.6 Preliminary computational results

The dimensionless parameter space of problem consists of (H, L, B, Re, M), i.e. five dimensionless parameters. As we saw in Chapter 5, practically the Reynolds and Bingham numbers do not change independently in the process, as the mean velocity (pumping speed) is the main independent variable in field conditions. Hence we replace B with Hedström number $He = Re \times B$ and consider the space as $(H,\ L,\ Re,\ He,\ M)$.

As time was limited for this preliminary study, we only present initial results over a limited range of parameters. First we fixed $He = 500$ to reduce one parameter and as this is in the range of field conditions. Based on experience from the previous chapter we performed a parametric study

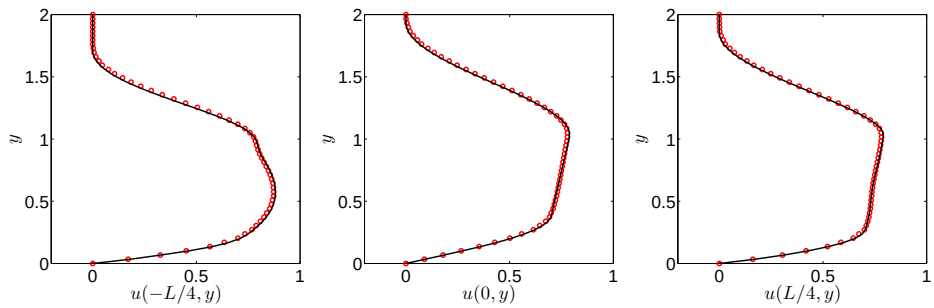

Figure 6.9: x-velocity profiles $u(x, y)$ at three sections of the washout (left to right): $x = -L/4,\ 0,\ L/4$. The displacement solver (red circles) is compared with the steady inertial solutions of the flow computed using FreeFEM++ with mesh adaptation (solid lines). The rows are $Re = 50$, all with $He = 500$.

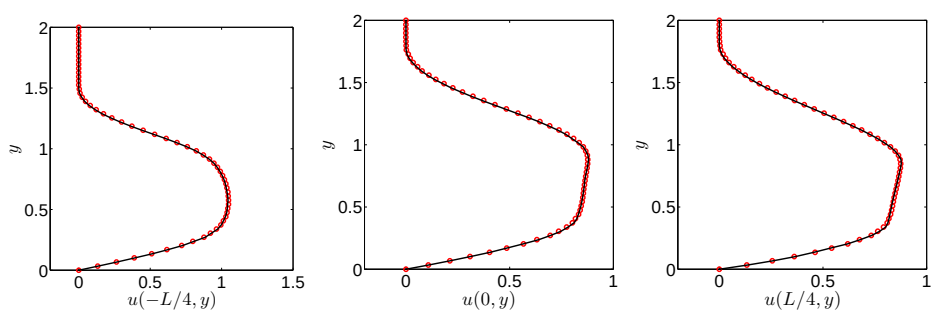

Figure 6.10: x-velocity profiles $u(x, y)$ at three sections of the washout (left to right): $x = -L/4,\ 0,\ L/4$. The displacement solver (red circles) is compared with the steady inertial solutions of the flow computed using FreeFEM++ with mesh adaptation (solid lines). The rows are $Re = 100$, all with $He = 500$.

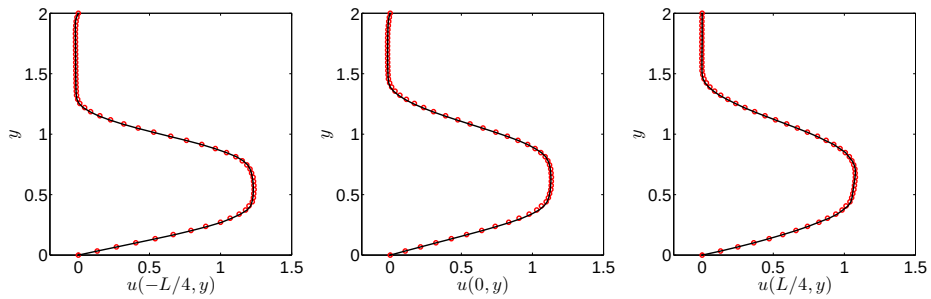

Figure 6.11: x-velocity profiles $u(x, y)$ at three sections of the washout (left to right): $x = -L/4,\ 0,\ L/4$. The displacement solver (red circles) is compared with the steady inertial solutions of the flow computed using FreeFEM++ with mesh adaptation (solid lines). The rows are $Re = 100$, all with $He = 500$.

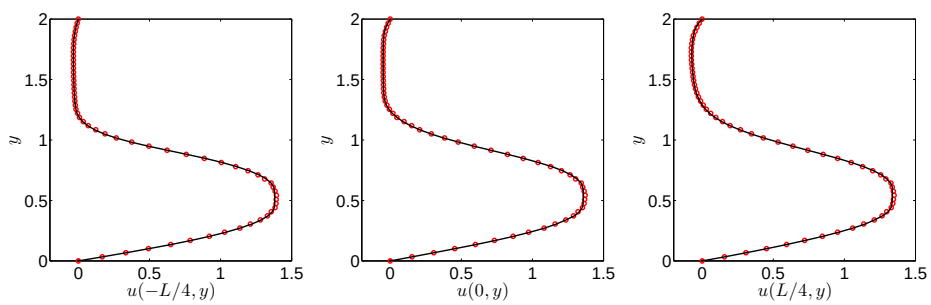

Figure 6.12: x-velocity profiles $u(x, y)$ at three sections of the washout (left to right): $x = -L/4,\ 0,\ L/4$. The displacement solver (red circles) is compared with the steady inertial solutions of the flow computed using FreeFEM++ with mesh adaptation (solid lines). The rows are $Re = 500$, all with $He = 500$.

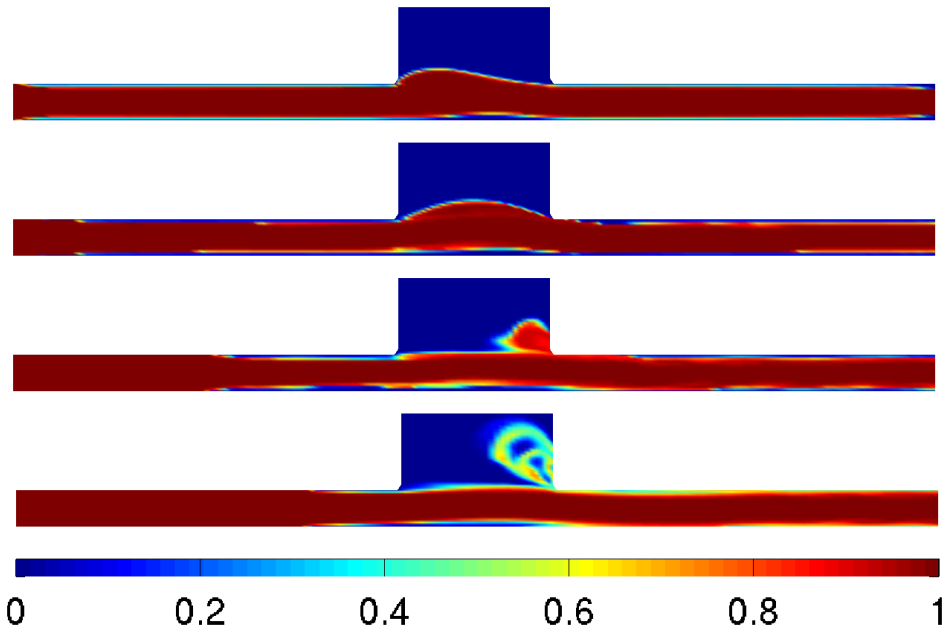

Figure 6.13: Colormaps of c for $H = 2,\ L = 4,\ M = 0.1$ and $Re = 10,\ 50,\ 100,\ 200$ from top to bottom. The flow is from left to right and the times are $\bar{t} = 4,\ 4,\ 4,\ 4$

over the following ranges:

$$H = 2, 5, 10 \quad L = 4, 10, 20 \quad Re = 10, 50, 100, 200 \quad M = 0.1, 0.3, 3, 9, 27 \tag{6.27}$$

As the viscosity ratio (M) is a new parameter and we have less intuition about the effects, more points were used for M. The displacement flow is generally unsteady, but in some cases at long times it converges to a steady flow. In comparing between flows we have tried where possible to do so at a sufficiently long time for the flow to become steady. The *average passage time* is

$$t_{pass} = \frac{\hat{U}_0}{\hat{L} + 2\hat{l}}, \tag{6.28}$$

which is simply the time to travel the domain length at the mean velocity. Equally, after $t = t_{pass}$ a volume equal to the uniform channel volume

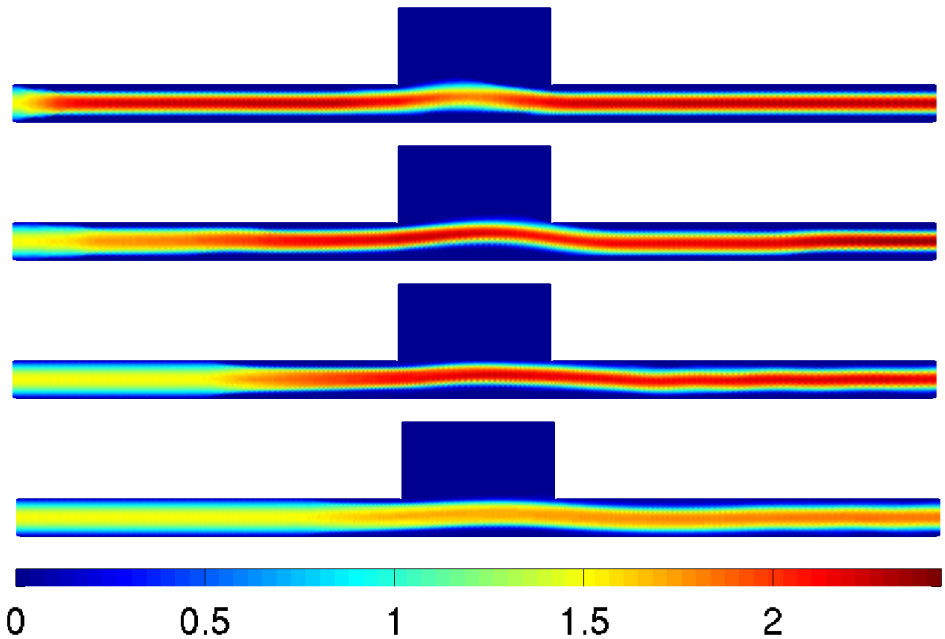

Figure 6.14: The speed colormap for $H = 2,\ L = 4,\ M = 0.1$ and $Re = 10,\ 50,\ 100,\ 200$ from top to bottom (the same flows as Figure 6.13).

(i.e. neglecting the washout) has been pumped.

To compare flows, we find that the stable displacements are usually realised after , we do so after a few t_{pass}, and that if unstable at e.g. $t = 3t_{pass}$, the flow remains unstable. Thus, we define a new time scale for presenting our results:

$$\bar{t} = \frac{t}{t_{pass}}. \tag{6.29}$$

The usual simulation time for the results we present is at $\bar{t} = 5$. However, some of the unstable flows are presented for shorter times as the time step for the simulations was shorter and computational times longer (and we had limited computational resources).

First we show a few example cases and look at the general trends of the results. Note that $He = 500$ for all results of this chapter, so this means that by increasing Re the the Bingham number B decreases. Figure 6.13 shows

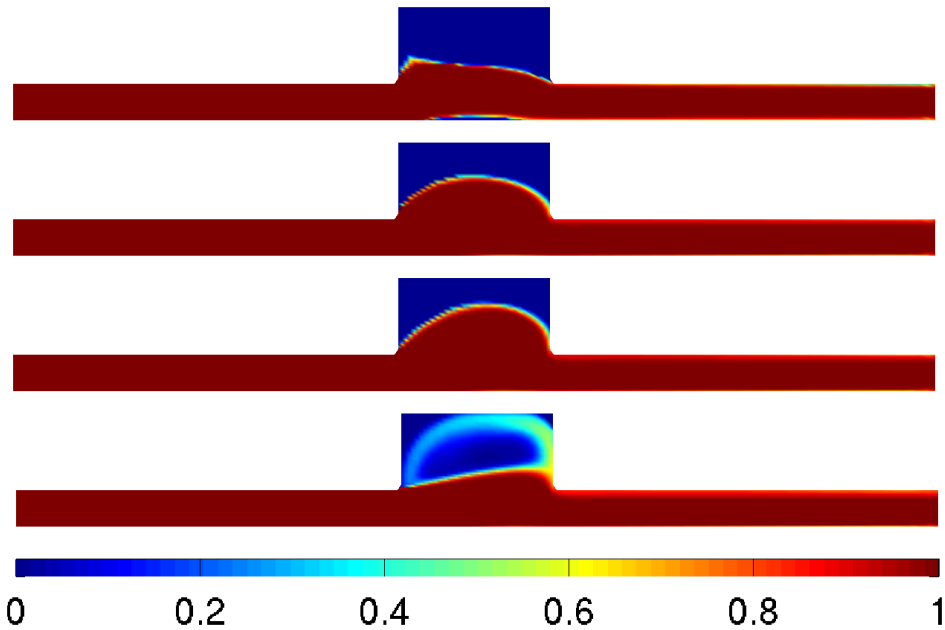

Figure 6.15: Colormaps of c for $H = 2,\ L = 4,\ M = 9$ and $Re = 10,\ 50,\ 100,\ 200$ from top to bottom and times are $\bar{t} = 4,\ 4,\ 4,\ 4$.

colormaps of c for $H = 2,\ L = 4,\ M = 0.1$ with $Re = 10,\ 50,\ 100,\ 200$, increasing from top to bottom. We observe at the lower Re, the asymmetry in the washout orients upstream towards the entry of the washout. By increasing Re the asymmetry move to the downstream/exit side of the washout. Interestingly for $Re = 50$ the flow is almost symmetric. We see that from $Re = 10$ to 50, washout displacement efficiency increases and then decreases. This is consistent with the results in Chapter 5, where we found that increasing inertia helps to circulate more fluid, up to some Re_c, and then degrades the displacement efficiency.

One new feature compared to single fluid flows is the static layers on the entry/exit development sections. These can appear if the invading fluid exerts a shear stress on the walls of the channel less than the defending fluid yield stress. For our study the invading fluid is Newtonian and the minimal

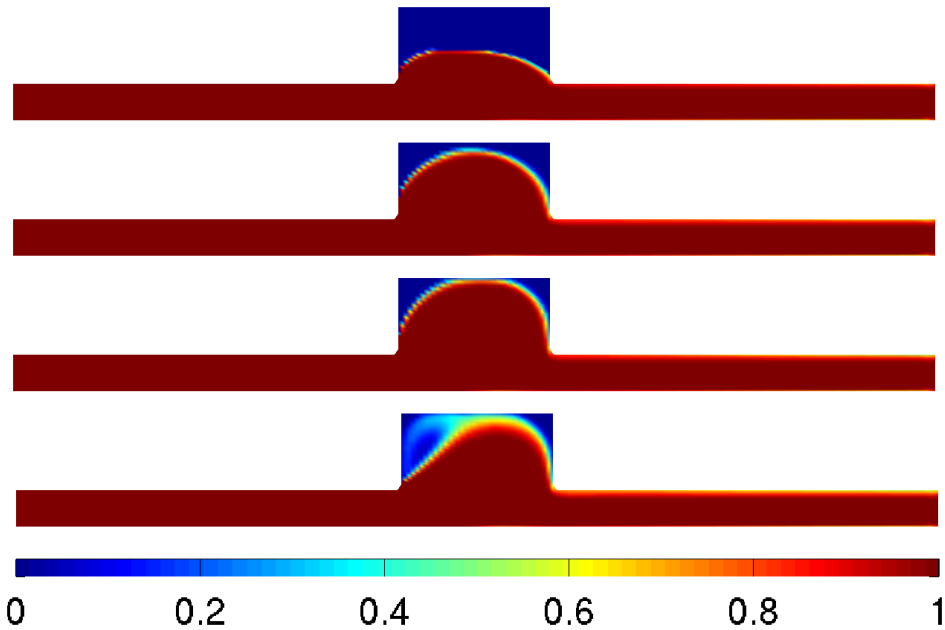

Figure 6.16: Colormaps of c for $H = 2,\ L = 4,\ M = 27$ and $Re = 10,\ 50,\ 100,\ 200$ from top to bottom and the times are $\bar{t} = 4,\ 4,\ 4,\ 4$.

wall shear stress is:

$$u(y) = 6y(1-y) \Rightarrow \tau_w = M\frac{du}{dy}|_{y=0} = 6M. \tag{6.30}$$

This leads to the following simple condition needed for static layers on the walls of the channel:

$$6M \leq B. \tag{6.31}$$

This means that if $6M \geq B$ then no static layers should exist on the channel walls for long times. With our current range of B this means for $M = 9$ & 27 we should have no static layers in the development sections and indeed we find this. In Figure 6.13 there is a static layer in development section for all Re while for $M = 9,\ 27$ (Figures 6.15 & 6.16) no static layer exists. We consistently get the same result for other cases as well.

A second related new feature in these flows, compared to the single

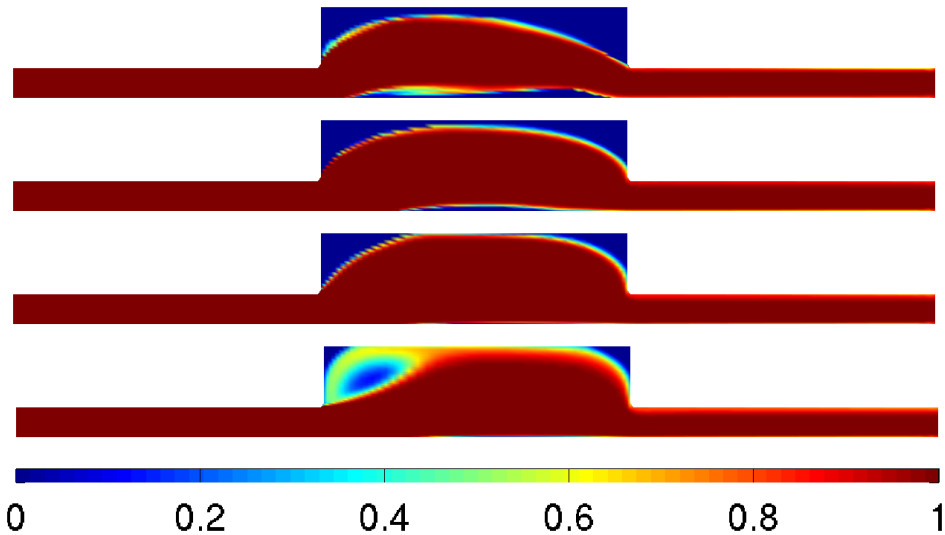

Figure 6.17: Colormaps of c for $H = 2,\ L = 10,\ M = 9$ and $Re = 10,\ 50,\ 100,\ 200$ from top to bottom and times are $\bar{t} = 5,\ 5,\ 5,\ 5$.

fluid flow, is that a static layer may sometimes appear on the straight wall opposite the washout section. This is probably due to the same mechanism as in the development channels, i.e. as the flow width widens in the washout section, the shear stress on the walls reduces and static layers emerge that can be thicker than in the development sections. It is even possible that the washout section can have static layers while the development sections are clean, e.g. see Figure 6.15 for $Re = 10$ (top figure).

A rather beautiful phenomenon that we observe in Figure 6.13 for $Re = 100,\ 200$ is frozen chunks of the invading fluid in the washout. Basically during the initial phase of displacement some part of the invading fluid penetrates in the washout, but inertia is not high enough to sustain the washout flow. Hence the trapped chunk of the fluid comes to rest in finite time, due to yield stress in the surrounding fluid. We can confirm the fluid is trapped by looking at the c and speed colormaps together, as in Figure 6.14.

Figure 6.15 shows the same geometry but the viscosity of the invading fluid is increased to $M = 9$. First we see that the static layers in the

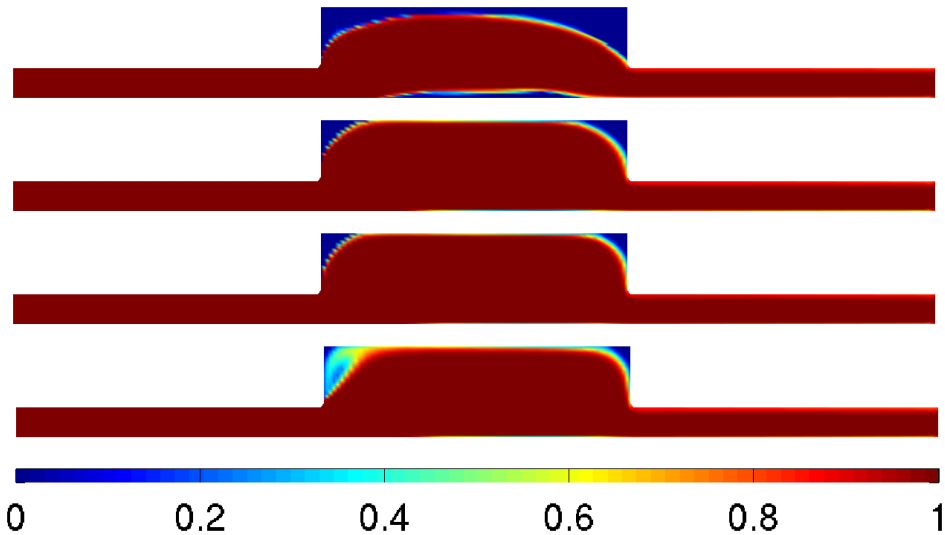

Figure 6.18: Colormaps of c for $H = 2,\ L = 10,\ M = 27$ and $Re = 10,\ 50,\ 100,\ 200$ from top to bottom and the times are $\bar{t} = 5,\ 5,\ 5,\ 5$.

development sections are completely displaced compared to $M = 0.1$ as (6.31) predicts. We see that increased shear due to higher viscosity has also significantly helped to displace more fluid in the washout section as well. The flow pattern for $Re = 200$ is interesting, there is a recirculation pattern in the washout consisting of an outer ring of mixed fluids and an inner uncontaminated region of defending fluid. Figure 6.16 shows a further increase of viscosity to $M = 27$. Now we get very good displacement of the washout for $Re = 100$. The invading fluid touches the upper wall of the washout. This good displacement is accomplished by the high shear stresses developed due to increased invading fluid viscosity. For $Re = 200$ the fluid penetrates deep into washout too. However, high inertia forces the invading fluid more to the downstream side of the washout. The big vortex that had filled the whole washout reduces in size and shifts to the upstream side of the washout, yet it has kept the ring/uncontaminated core structure.

Now we consider increasing L. Figure 6.17 shows $H = 2,\ L = 10,\ M = 9$; compare with Figure 6.15. Interestingly, we see that now the invading

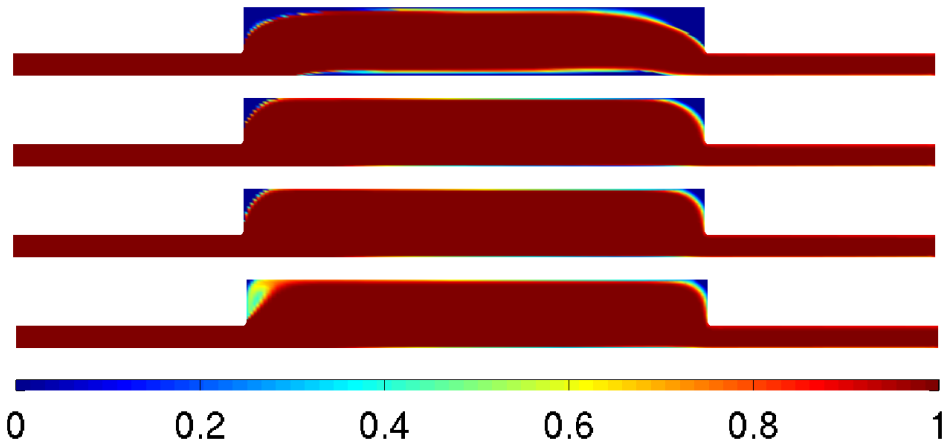

Figure 6.19: Colormaps of c for $L = 20$ and the rest of parameters the same as Figure 6.18. Flow demonstrates a steady full displacement.

fluid penetrates considerably deeper into the washout for all ranges of Re. This relates to neither viscous nor inertial effects. Indeed it appears to be due to giving these forces enough length to develop their full impact on the washout. Presumably development length depends on M and Re. In Figure 6.18 the viscosity is increased to $M = 27$ and we can notice that for larger M this length is shorter. Another message of this figure is that for $Re = 50, 100, 200$ a full displacement of the washout is achieved. By full we mean that the invading fluid has totally displaced the defending fluid after the development length. To better demonstrate this, Figure 6.19 shows continuation of the washout length to $L = 20$ which indicates a full displacement.

This type of displacement is very desirable and clearly occurs in the stable slow flow limit when two conditions are met:

1. The length of the washout is long enough to let the flow develop, which is realised for $L/(1+H) \gg \mathcal{O}(1)$ at least. We have not studied this in more quantitaive detail.

2. Viscosity should be high enough for the shear stress on the wall to

exceed B. Following the same method that led to (6.31), we find

$$\tau_{wall} = \frac{6M}{(1+H)^2} = B \Longrightarrow M = \frac{B(1+H)^2}{6}, \tag{6.32}$$

as the minimum required viscosity ratio M to achieve full displacement.

This shows quadratic growth of the required viscosity with depth of washout, which may be prohibitive in practice. In general we can expect the displacement flow to develop into a simple Poiseuille flow with/without static layer on the wall, if the washout is long enough.

Recall that the above analysis neglects inertia and consequently should be true only when viscosity is dominant. When inertia and viscous forces are nearly balanced and the flow is still stable, inertia can significantly impact the residual layer thickness and displacement in long washouts. Good examples are Figure 6.20d and Figure 6.21b, in both inertia has caused the flow to curve out a wavy static layer on the walls. The amplitude of the wave increases with inertia. This effect of inertia is apparently very unstable, i.e. by small change in initial condition the static layer pattern can greatly vary.

So far most of the results we explored were in the large M low Re range of our parameter space, where viscous stresses are dominant and we get smooth stable displacements. We also see many unstable flows in our results, when Reynolds is high enough and the viscosity ratio is low. Figure 6.22 shows colormaps of c for $H = 2,\ L = 10,\ M = 0.1$ and the sequence $Re = 10,\ 50,\ 100,\ 200$. We observe that for $Re = 10$ the flow is obviously stable, while for $Re = 100,\ 200$ the flow is fully unstable. The $Re = 50$ flow appears somewhat transient but is actually stable.

Another example of unstable flow was already shown in Figure 6.21. The flow is stable for $Re = 10,\ 50$ and by increasing inertia the flow becomes unstable at $Re = 100$. Note $\bar{t} = 3.4$, so enough time has passed to conclude the flow is unstable. For $Re = 200$ we have shorter $\bar{t} = 1.5$, as numerical solution of unstable flows takes a very long time, due to the smaller time steps and greater number of iterations needed to converge at each time step.

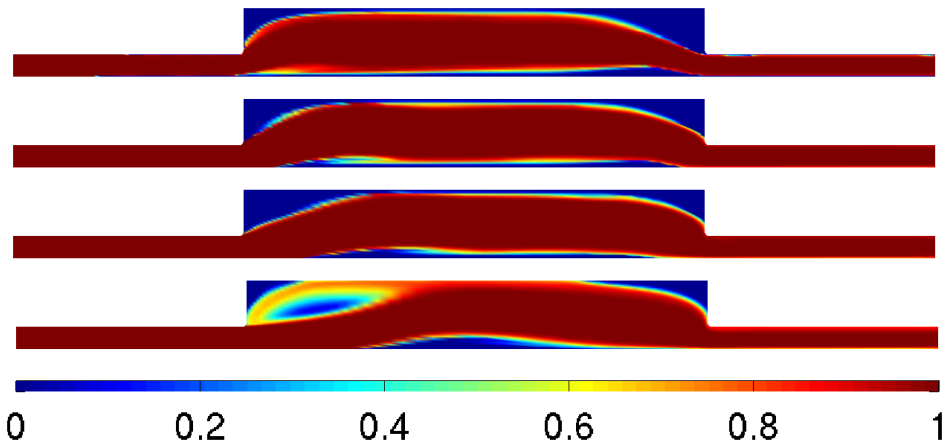

Figure 6.20: Colormaps of c for $H = 2,\ L = 20,\ M = 3$ and $Re = 10,\ 50,\ 100,\ 200$ from top to bottom and snapshot times are $\bar{t} = 6,\ 6,\ 6,\ 6$.

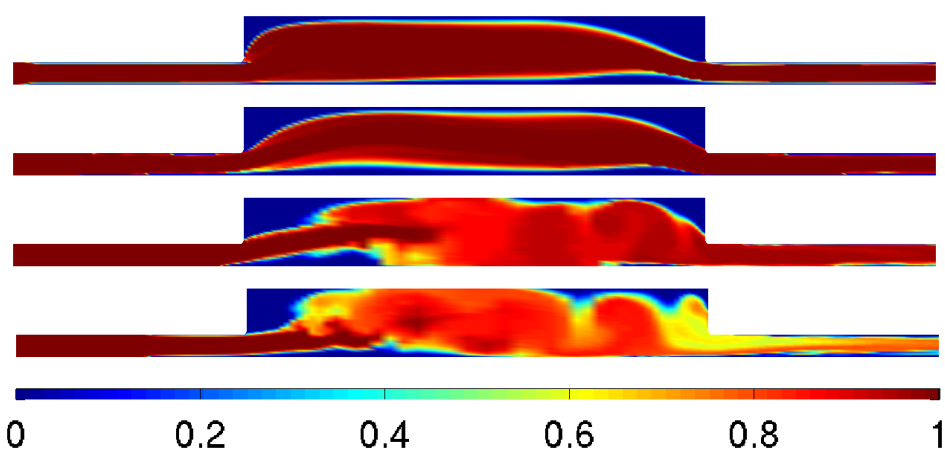

Figure 6.21: Colormaps of c for $H = 2,\ L = 20,\ M = 0.3$ and $Re = 10,\ 50,\ 100,\ 200$ from top to bottom and times are $\bar{t} = 6,\ 6,\ 3.42,\ 1.5$.

Anyway, as the Reynolds number is higher we can infer that it will remain unstable just like the $Re = 100$ case. We see that when unstable flow happens the mixing of fluids is very strong and a good displacement occurs through the washout, except at the corner region close to the entrance. Here lower Reynolds flows achieve a better displacement, for example compare $Re = 100$ with $Re = 10$ in Figure 6.21.

Looking at the time evolution of an unstable displacement flow, we can divide it into two periods as follows. (a) The initial phase when an unstable finger of the invading fluid moves forward until it reaches the exit of the domain. Most of the displacement happens in this phase by pushing and viscous drag as the main mechanisms of displacement. (b) The second phase starts after the invading fluid has reached the exit. At this point a channel has been opened through the defending fluid, usually with irregularly shaped static layers due to unsteadiness and instability; e.g. Figure 6.23g. Then the invading fluid largely flows along this channel, just as in a single unstable Newtonian flow. The flow can still wash some stagnant material out of the domain by: (i) shearing of static layers; (ii) yielding of chunks of the fluid and transporting it away. The former happens for the smoother layers where the surface is mainly aligned with the flow, and takes place over a long time scale. The latter mainly occurs for rough shaped stagnant surfaces, usually carried away by a pulse of flow with higher velocity, and takes place over the convective time scale. Most often the jagged surfaces are smoothed quickly by yielding and then slowly washed. This second phase of displacement continues until the residual stagnant zones are strong enough to resist all the unstable forces. Commonly the corners of the washout are the only locations that can keep a noticeable amount of stagnant fluid and some small bits of fluid may survive elsewhere.

We can observe the two phases of unstable displacement in Figure 6.23 which shows the evolution of c for $H = 2,\ L = 20,\ Re = 100,\ M = 0.3$. The first phase is completed at $\bar{t} = 1.3$ (label g in figure) where invading fluid has reached the exit. We see two domes of stagnant fluid on the bottom wall at this point. The larger one close to the washout entry and the smaller one close to the exit (circled in figure), and some thin layers on the development

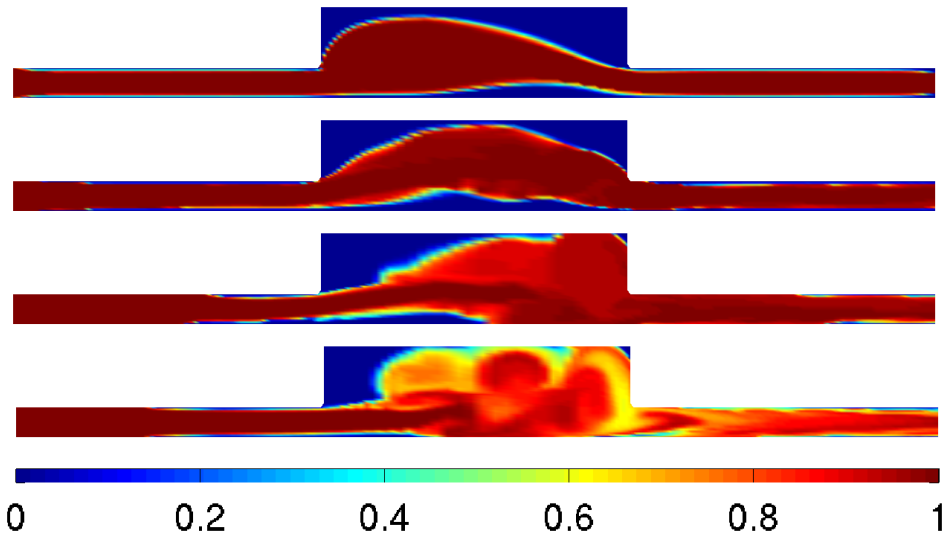

Figure 6.22: Colormaps of c for $H = 2,\ L = 10,\ M = 0.1$ and $Re = 10,\ 50,\ 100,\ 200$ from top to bottom and times are $\bar{t} = 5,\ 5,\ 3.7,\ 1.84$.

sections. Note that after this point the bulk of the flowing channel does not change and only the domes and development section layers are washed out, mostly by a shearing mechanism. There are some spots that we may infer more of yielding type mechanism e.g. from (g) to (h) for the smaller dome or the tail of bigger dome from (j) to (k) (circled in figure). We see that the static fluids at corners of the washout have kept their shape virtually unchanged, especially the region at the washout entrance. The yielding mechanism is shown nicely in Figure 6.24 which shows two snapshots of c for a case where we can easily see yielding and transportation of a chunk of fluid.

On the other hand, stable displacements have only the one phase, and this is similar to the first phase of unstable displacements, i.e. the invading fluid pushes and drags the defending fluid out of the domain. However, after the invading fluid reaches the exit, very little additional displacement happen by shearing mechanism and there is no yielding of chunks of fluid, unlike the unstable displacement. Figure 6.25 shows a typical stable displacement

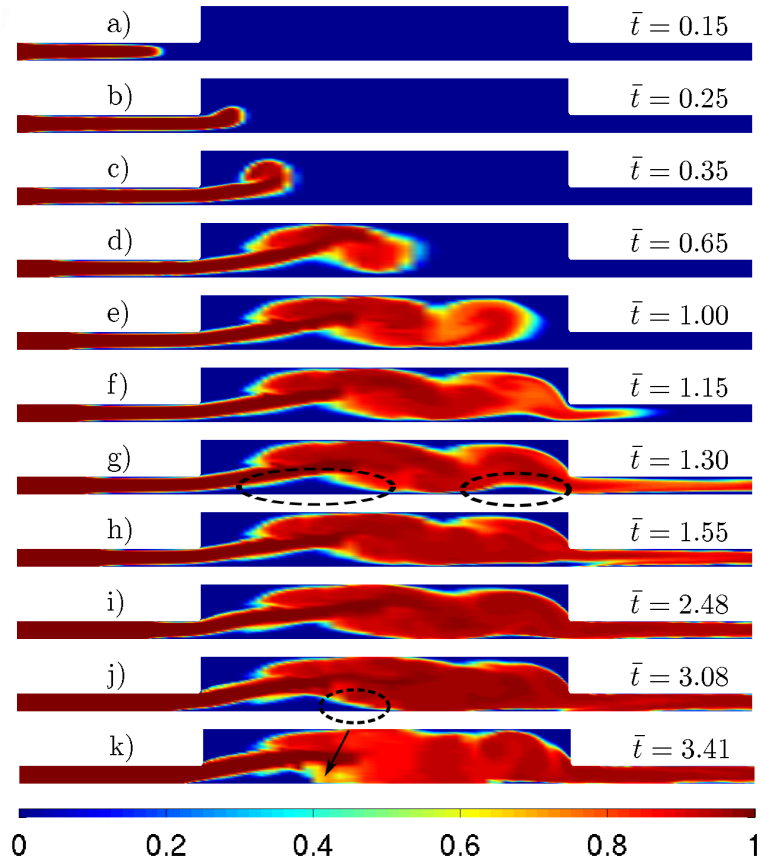

Figure 6.23: The evolution of c for $H = 2,\ L = 20,\ Re = 100,\ M = 0.3$

progressing. We can see that practically no further displacement happens after the fluid has reached the exit at $\bar{t} \approx 2.19$ (label (i) in Figure 6.25), nor even much later at $\bar{t} = 7.11$ (label (j) in Figure 6.25).

The effect of L on unsteady behaviour of the flow is also interesting. For example, compare the flows in Figure 6.13 and Figure 6.22, in which the length of washout L has increased from 4 to 10. The flow has changed from the frozen stable pattern to an unstable flow for both the cases of $Re = 100$ & 200. It appears that the longer L allows the instability enough time to grow, while in the shorter length the instability is damped, i.e. these

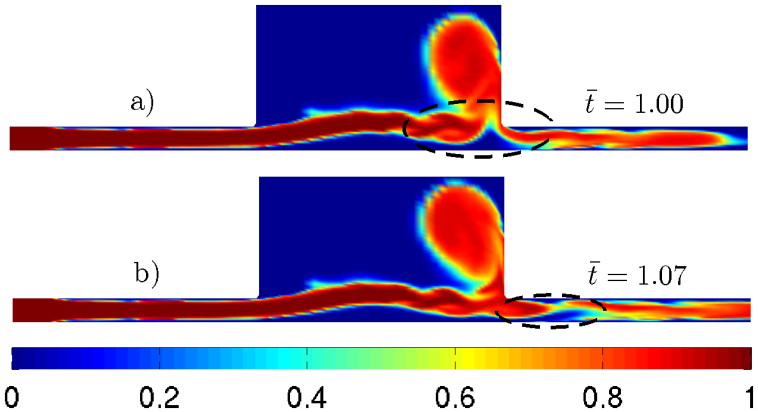

Figure 6.24: The stagnant fluid circled in a) is displaced by yielding, and can be tracked in b). Parameters are $H = 5,\ L = 10,\ Re = 100,\ M = 0.1$

are advectively unstable. This is very much like the stable displacement examples we saw before, in that increasing L enabled the flow to penetrate much deeper into the washout (growth of amplitude). This suggests that L plays a vital role as a development length for the local flow in the washout and that flow development depends critically on Re. Further study of this is needed.

Another example of the stabilizing effect of L can be observed in Figure 6.26, in which L is reduced from 20 in Figure 6.21 to 10. Note it can be also viewed as the increased viscosity ratio version of Figure 6.22, from $M = 0.1$ to $M = 0.3$. In either case we observe that the flow at $Re = 100$ has become stable. The flow appears to be unstable, judging solely from the distribution of c at $\bar{t} = 5$, but the speed colormap in Figure 6.27 shows a smooth channel of mobile fluid with no evidence of instability. The frozen pattern surrounding the flow path is a signature of some early instability growth in the flow, topologically analogous to Kelvin-Helmholtz type. Regarding other Re values we see that $Re = 10,\ 50$ are stable in Figures 6.21, 6.22 and 6.26. At $Re = 10$ there is minimal difference between the figures and for $L = 20$ it appears to be an extended version of $L = 10$. For $Re = 50$ increasing $M = 0.1$ to $M = 0.3$ has made the flow smoother, also the ef-

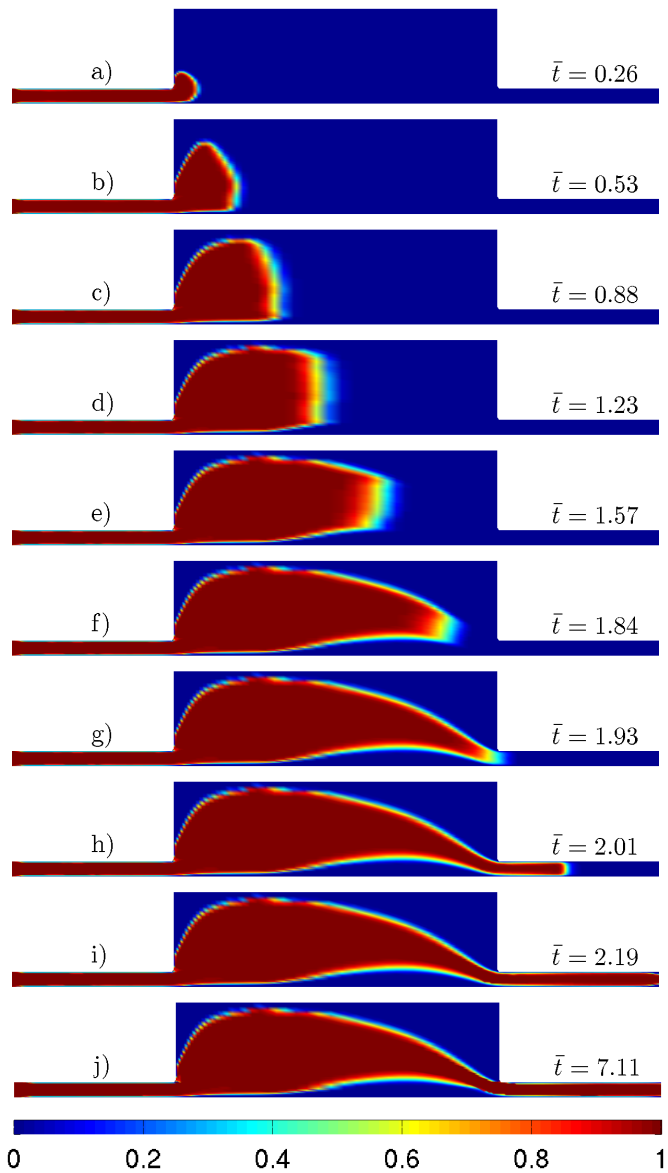

Figure 6.25: Progress of c for a stable displacement. $H = 5$, $L = 20$, $Re = 10$, $M = 0.3$.

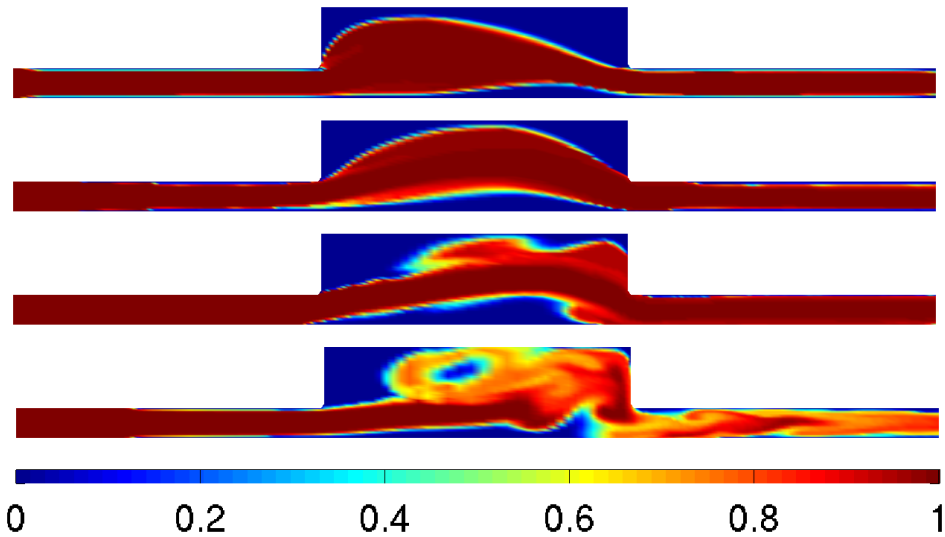

Figure 6.26: Colormaps of c for $H = 2,\ L = 10,\ M = 0.3$ and $Re = 10,\ 50,\ 100,\ 200$ from top to bottom and times are $\bar{t} = 5,\ 5,\ 5,\ 1.3$.

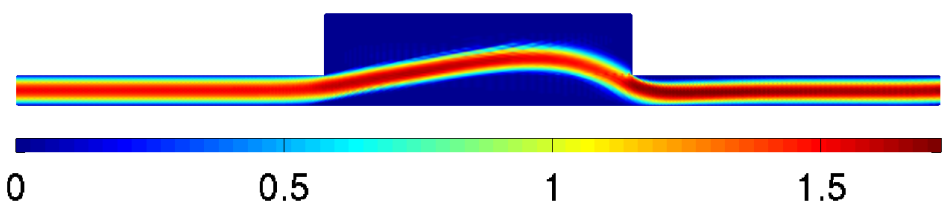

Figure 6.27: Colormap of the speed for $H = 2,\ L = 10,\ Re = 100,\ M = 0.3$

fect of increased L allows inertia to create a wavy static layer. We see that $Re = 200$ is high enough such that the flow is unstable in all three cases. Having said all this, recall that if we increase M sufficiently we get stable displacements again, e.g. see Figure 6.17 and Figure 6.20.

Concerning the effect of H, for stable displacements and if H is sufficiently large we see similar results as with self-selection in single fluid flows. Perhaps *self-selection* is inappropriate as a term for displacement as here as flow is unsteady and initial conditions can certainly affect the flow. In-

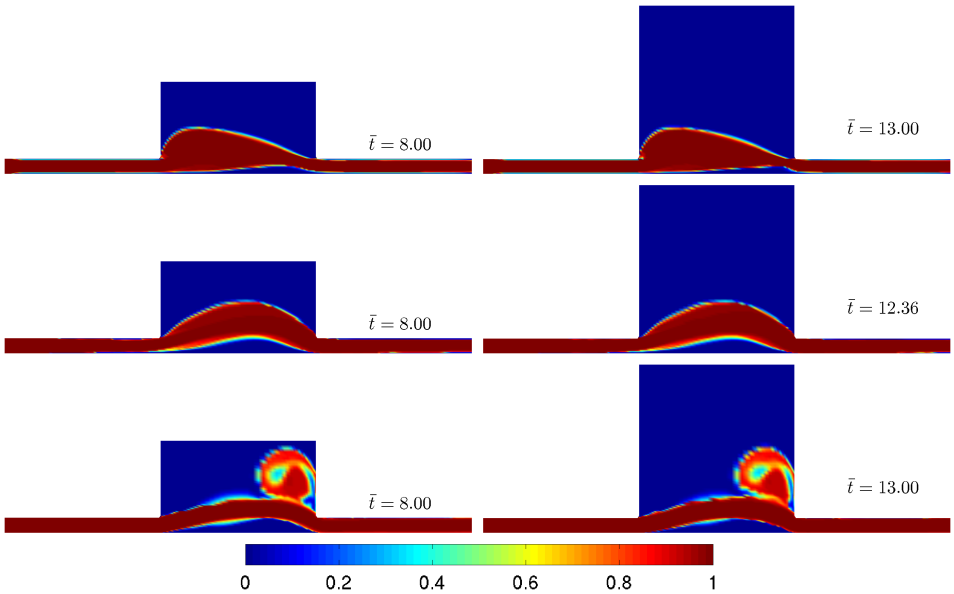

Figure 6.28: Comparing the effect of increasing H on final shape of the displacement. Colormaps of c are shown. Left column $H = 5$ and right column $H = 10$. Rows from top to bottom: $Re = 10,\ 50,\ 100$ and $L = 10,\ M = 0.3$.

stead we can say that we observe invariance of the final steady displacement shape, as in the single fluid flows. This is illustrated in Figure 6.28 where we compare the final flow shapes for two values of $H = 5,\ 10$ over the range of $Re = 10,\ 50,\ 100$, (for other parameters $L = 10,\ M = 0.3$). We see that for fully stable flows at $Re = 10,\ 50$, the same shapes are clearly obtained at both H. There are some subtle differences which could be due to the times of comparison not being identical. However for $Re = 100$ we see frozen fluid pieces which are quite different. This can be also due to that $H = 5$ is not large enough for this case to be compared.

For unstable flows we observe that increasing H lead to a cavity like configuration, such as shown in Figure 6.29, in which a big vortex resides in the washout and the invading fluid jet travels nearly in a straight path from upstream to downstream of the washout, with parts of invading fluid occasionally detaching and entering the washout vortex structure. In this case

most of the circulation is made up of the defending fluid and displacement is much weaker compared to smaller $H = 2,\ 5$ values which attain relatively high displacement efficiency. Sever inertia is clearly making things worse for deep washout of $H = 10$. Increasing viscosity is one way to get better displacement as we saw before. Figure 6.30 shows the outcome of increasing $M = 0.3$ to $M = 27$ for this washout. Certainly we see much improvement in displacement efficiency, though at a much higher energy cost (pump power) due to high viscosity. In addition it might not be possible to attain $M = 27$ in practice.

So it looks very difficult to achieve a good displacement efficiency for long and deep washouts like $H = 10,\ L = 20$, as neither of high inertia or large viscosity are useful or practical. On the other hand, industrially, deep and long washouts are the ones which we do really worry about. The borehole of these washouts are prone to collapse and gas invasion, also fluid migration can happen between formation layers due to long length. Consequently it is crucial to find ways to accomplish better displacement without brutely increasing viscosity.

In the following we give an idea on how to improve the displacement for these *long-deep* washouts. We did not have time to actually examine it, however it is based on the observations we have had so far, and intuitively looks to be correct.

First we should revisit a trend in the results that was briefly mentioned and elaborate more on it. Figure 6.31 nicely shows it in our model long-deep washout case. Basically it shows the results for $Re = 10,\ 50,\ 100$ of the same washout we considered ($H = 10,\ L = 20,\ M = 0.3$). First note that actually all the lower Re flows get better displacement than $Re = 200$, consistent with results of Chapter 5 that we observed too much of inertia becomes harmful. This is not new, however the new phenomenon here is the shift of flow asymmetry from fore (close to entrance) to aft (close to exit) as Reynolds is elevated from $Re = 10$ to $Re = 50$ and $Re = 100$. This can be observed in other earlier results e.g. Figures 6.28, 6.26, 6.22 and 6.13.

Fore asymmetry is particularly interesting, it happens at low Re values and it seems that for sufficiently large H we get an interesting shape in-

variance relative to M. Basically the opening portion of the flow (where it widens up to the maximum width) becomes virtually constant and the converging portion responses to M variation. Figure 6.32 shows the sequence $M = 0.1,\ 0.3,\ 3,\ 9,\ 27$ and $Re = 10$ for our long-deep washout. We can see that the flow portion at the left of dashed line is remarkably neutral to the two orders of magnitude of change in M from 0.1 to 27. The evident difference is in the flow width in the converging portion of flow. We see that for $M = 0.1$ the flow width quickly narrows down from the maximum (after the dashed line) to the development section width, while for $M = 27$ the flow keeps wider and reaches the exit of washout with a larger width than the development section. This is expected as higher M means more viscous drag, however it looks that at the beginning of the washout where flow is expanding, pushing forces play the key role in displacement and viscous drag is relatively smaller. This could be due to a great pressure imbalance experienced by the flow over the sudden expansion at the beginning of the process. We remind that in Figure 6.32 $\bar{t} \geq 7$ for all of the cases, therefore we have confidence in these as final flow structures. Lastly we should say that this invariance at low Re can also be observed for smaller expansion ratios as well to some extent, but not as nicely as larger H. Figure 6.33 shows variation of flow by M for $H = 2,\ L = 10,\ Re = 10$. Again we can see the shape of flow is not changing much at the opening portion of washout where the flow is expanding (left of dashed line).

With these preliminaries we can revisit the problem. As long-deep washouts are the most industrially concerned ones we would like to accomplish a good displacement such as in Figure 6.30 with large $M = 27$, however this large viscosity ratio could be impractical, both due to enormous pumping energy needed and also being able to actually make or get ready such fluids. On the other hand, we observed that for smaller M values at low Re we get a strong asymmetry which locally gives a good displacement at the washout entrance. Also as Re is increased the asymmetry moves to the downstream of washout and we get better displacement there. For higher Re unstable flow can mobilize additional stagnant fluid on the casing (straight wall) and also at down stream of the washout, however it should

not pass certain limit or we get a big vortex configuration as observed before, worsening the displacement.

Putting together these pieces, we propose the following strategy to obtain a displacement similar to Figure 6.30 in a long-deep washout, but with a low M:

1. Pump at low $Re = Re_l$ (e.g. 10) for a period of $\mathcal{O}(t_{pass})$.
2. Slowly increase Re to higher value Re_h over $\mathcal{O}(t_{pass})$ time frame. The flow should be still stable at Re_h.
3. Increase Re to unstablize the flow and keep this for another $\mathcal{O}(t_{pass})$.

With this strategy we will do a sweep of washout, continuously displacing fluid from upstream to downstream as observed in Figure 6.31. At the final step the unstable flow can wash away even more stagnant fluid by the yielding and shearing mechanisms explained before, but the range of Re should be controlled to avoid falling in the circulation regime. Remind that the time scales of $\mathcal{O}(t_{pass})$ are essential for each step of this process as they ensure we have some type of quasi-steady like flow. Otherwise if we rapidly level up the Re, the flow will not have enough time to displace in the patterns that we see for the steady flows in Figure 6.31.

On the top of these good properties, interestingly we can see that the maximum depth of penetration into washout for each of the flows in Figure 6.31 is roughly the same as Figure 6.30 that we have $M = 27$. Thus, this process potentially can achieve the same displacement as large viscosity case of $M = 27$.

Note that the proposed process is practical and can be used out of the box, as increasing Re simply means to pump faster in the field. Usually operators have some idea about the range of Re for having laminar or turbulent flow and primarily t_{pass} is the parameter that should be estimated. For this we need information about the length of washout that is becoming more available these days via the use of new measurement technologies.

Last but not least, we should say that it has been previously concluded in [103] that for uniform geometries, the transient behaviour of displacement

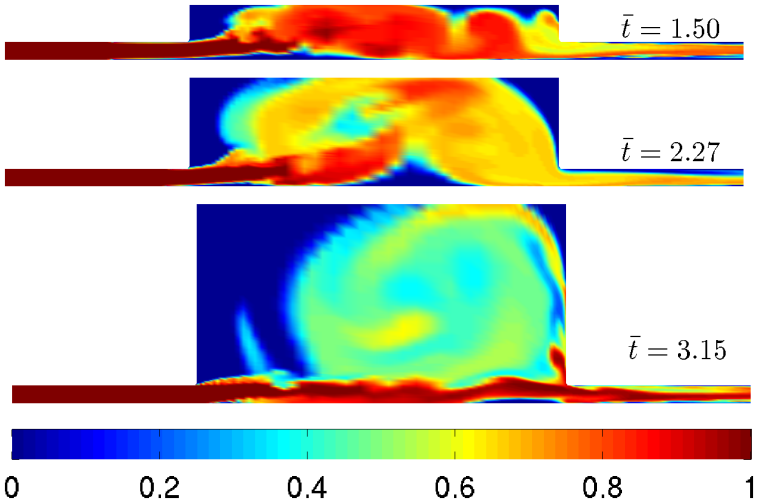

Figure 6.29: The effect of increasing H in unstable flows. $L = 20, Re = 200, M = 0.3$ and from top to bottom $H = 2, 5, 10$.

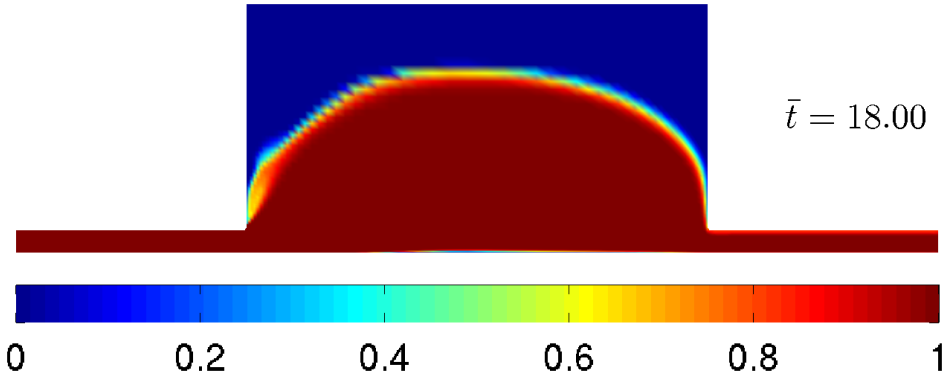

Figure 6.30: Colormap of c for $H = 10,\ L = 20,\ Re = 200,\ M = 27$

flow can have significant impact on the removal of stagnant fluids. Here we proposed a transient process for non-uniform geometries to enhance displacement efficiency.

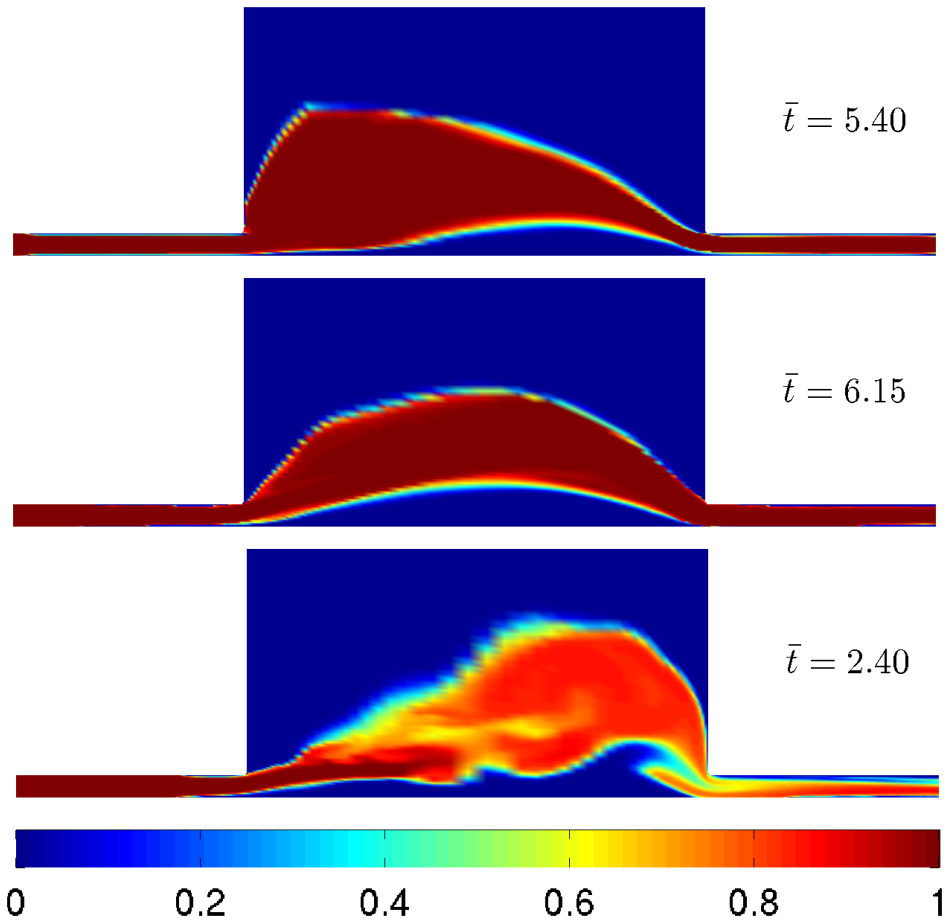

Figure 6.31: Colormaps of c for $H = 10,\ L = 20,\ M = 0.3$ and from top to bottom $Re = 10,\ 50,\ 100$.

6.6.1 Discussion and summary

We have developed and benchmarked a numerical code that is capable of resolving 2D displacement flows of non-Newtonian fluids in complex washout geometries. Although we have considered only iso-dense fluids and a Newtonian fluid displacing a Bingham fluid, there is no reason to suspect that the code will not work adequately for other fluid types and with buoyancy.

Even for the simple geometry considered and the simplified rheologies, 5 dimensionless groups govern the flow. Due to the transient nature of a

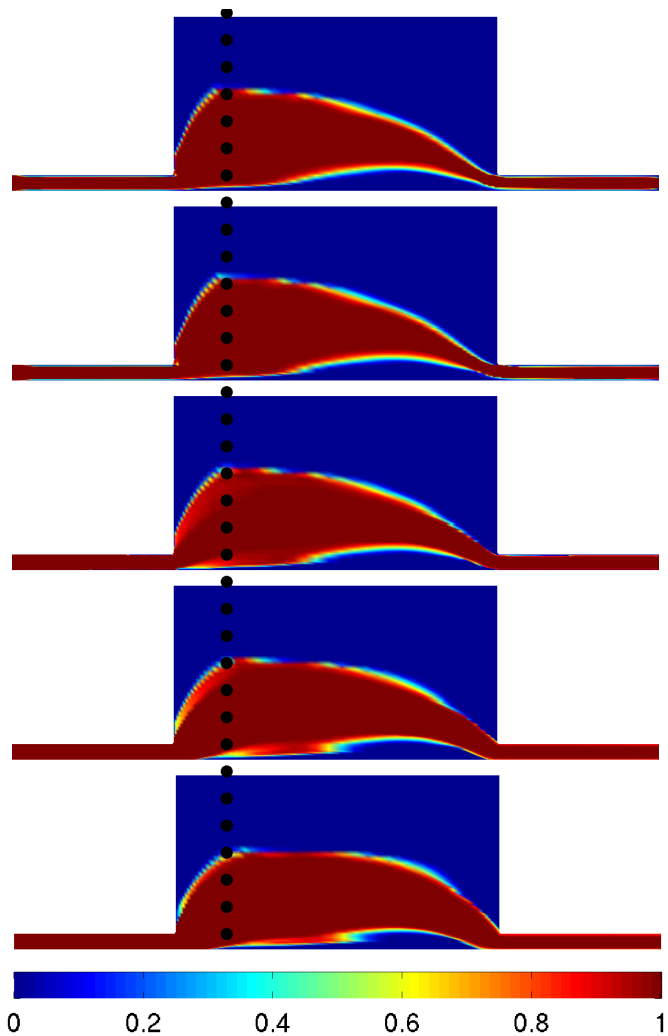

Figure 6.32: Colormaps of c for increasing $M = 0.1,\ 0.3,\ 3,\ 9,\ 27$ from top to bottom and $H = 10,\ L = 20,\ Re = 10$. Times are $\bar{t} = 7.4,\ 9.4,\ 8.9,\ 11.5,\ 10$ respectively

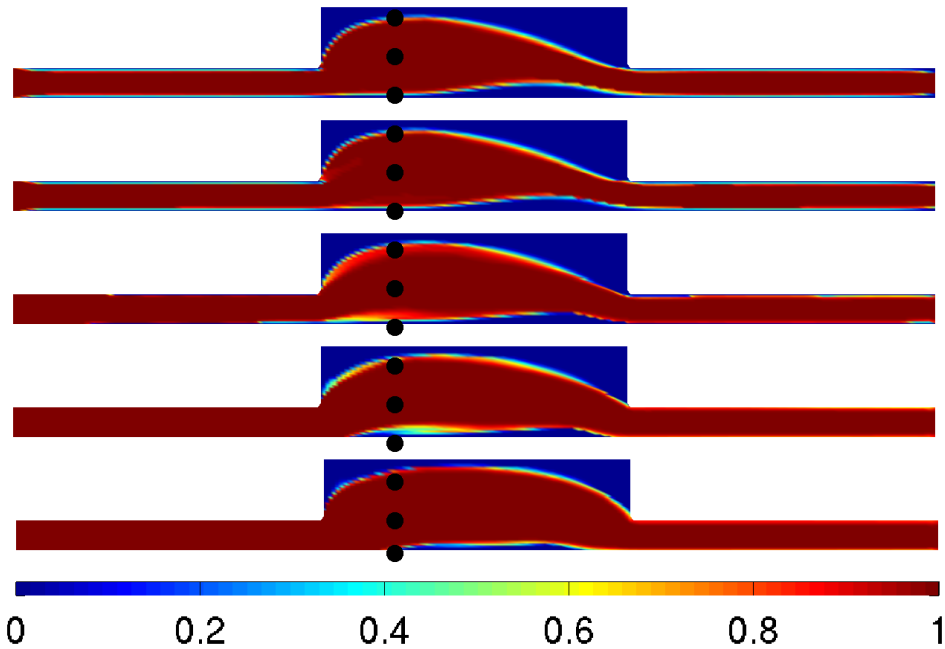

Figure 6.33: Colormaps of c for increasing $M = 0.1,\ 0.3,\ 3,\ 9,\ 27$ from top to bottom and $H = 2,\ L = 10,\ Re = 10$. Times are $\bar{t} = 5$ for all.

displacement, the end-time for comparison is also important. Thus, the degree of complexity is high even for our present results. Therefore, it is appropriate to consider our results as preliminary and our parametric ranges are far from comprehensive. Nevertheless, a number of interesting features have been observed. These include the following.

- Static layers of fluid can exist permanently in the washout and development sections, depending on the dimensionless parameters. Contrary to the single fluid flows studied in Chapter 4 & Chapter 5 static layers can also exist on the (straight) casing wall along the length of the washout, i.e. mobility of the single phase flow during recirculation does not guarantee mobility during the displacement phase.

- We can have both stable and unstable displacements. In the former case viscous forces are dominant (low Re, high M). The defending fluid

is slowly displaced by a combination of pressure forces and viscous drag, leading to smooth, well shaped static residual layers. In the latter case the flow remains unstable throughout the displacement, strong mixing of the fluids can happen and the static layers are more irregularly shaped.

- The stable displacement takes place in one stage while the unstable one can be divided into two stages. In stable displacements the invading fluid displaces the defending fluid steadily until it reaches the domain exit, afterwards no more (or very little) displacement happens and the flow remains steady. In unstable displacements, first an unstable invading fluid displaces the defending fluid and reaches the exit. In the second stage the flow remains unsteady and continues to wash and transport parts of defending fluid out of the domain.

- In stable displacements along sufficiently long washouts, if the viscosity of invading fluid is large we can get a full displacement of the defending fluid throughout the washout, except for small regions at the corners of the washout. We have developed an estimate for the minimum required viscosity ratio to accomplish this.

- When viscous and inertial forces are closely balanced and the flow is still stable, inertia can considerably influence the topography of static layers. For example in the long washouts, it may create wavy shaped static layers. This type of effect is rather sensitive to the flow conditions: small changes might lead to great variation, partly it depends on inertia and partly since the flow is irreversible.

- In stable displacements when inertial effects are high enough a recirculating vortex can exist in the depth of the washout. The structure of the vortex is interesting: it consists of an uncontaminated core of defending fluid plus a surrounding ring of mixed fluids. This seems to be the only case for which we get non-static defending fluid remaining in the washout zone for long time.

- The yield stress has interesting effects on the stability of the flow. Sometimes the displacement starts in an unstable mode at the beginning and the amplitude of instabilities grow for a while, however the yield stress eventually damps the instabilities and it seems that eventually we get a stable displacement, at least for the parameters tested. Fascinating patterns that indicate the early unsteadiness of the flow can be frozen into the flow by the yield stress of the displaced fluid.

- In addition to dynamic parameters of the problem i.e. Re and M, we observed that the length of the washout can also play a role in determining stability or instability of the flow.

- Generally, by increasing inertial effects the asymmetry of the flow increases.

- In the low Re limit we saw that the displacement pattern in the local region very close to the entrance to the washout is approximately invariant with respect to M. We postulate that this is primarily caused by the large pressure imbalance on the fluid, due to the sudden expansion of the flow. However this needs more investigation.

- We observed some evidence of the similarity of self-selection of the flowing area, for large enough H and B, i.e. when the washout is adequately deep. This is peraps better described as a flow invariance. The displacement must be stable to achieve this.

In terms of the practical application to cementing, the following observations appear relevant.

- Increasing the viscosity ratio M of invading to defending fluid always leads to better displacement. This is achieved by increased drag force on defending fluid. In fact if the washout is long enough and M is large enough we can achieve full displacement of the washout (except for small corner regions). However the required M is quite restrictive, as it quadratically grows with the depth of the washout.

- We observed in Chapter 5 and here again that increasing inertia does not always lead to better displacement. For long-deep washouts we observed that highly inertial flow leads to a flow structure in which the invading fluid is simply traveling in a roughly straight line from upstream to downstream, leaving a large vortex of mixed fluids circulating within the washout. For smaller inertia the invading fluid penetrates deeper into the washout and better displacement is achieved. This is contrary to general idea in the industry that the higher inertia always results in better displacement.

- The low Re flows achieve better displacement at the entrance (upstream) area of the washout, i.e. compared to higher Re flows. Higher Re flows generally achieve better displacement in the exit (downstream) region.

- Finally, based on the behaviour of the displacement flows observed, we have proposed a method to achieve better displacement for long-deep washouts when M is low. It is based on having a transient process in which we increase Re from low to high, during a time period of $\mathcal{O}(t_{pass})$. With this strategy we attempt to combine both the good properties of low Re displacements with those at higher Re. The former of these is better mobilization of the invading fluid at the upstream end. The latter of these improves the downstream end of the washout. However, we should be careful not to put too much inertia into the flow. This can lead to a large vortex structure in the washout, hence reducing displacement efficiency.

Chapter 7

Summary and conclusions

In this thesis we have studied the effect of geometric non-uniformities on 2D channel flows of yield stress fluids. The methodology has been mainly computational although in each specific flow we have also tried to build our physical insight and deliver easy to use predictive estimates through the use of analytical methods (asymptotics, variational methods, dimensional analysis and curve-fitting) as much as possible.

In the following concluding chapter, we first summarize the specific results, insights and novel contributions of each chapter (§7.1). Secondly, we look back at the research motivations, objectives and the overall path we took in the thesis. We try to develop a larger vision of where we were, how far we have progressed and what we see on the horizon (§7.2). Third we mention the limitations of our study and possible improvements (§7.3). Finally we end the thesis with recommendations for future research directions.

7.1 Results, insights and contributions from the individual chapters

7.1.1 Bingham fluid flow along wavy channels (Chapter 2)

1. To the best of our knowledge, this was a first study of its kind in 2D flows that was specifically targeted at understanding self-selection

behaviour in a channel geometry. We systematically studied about 500 computation covering a wide range of problem parameters (h, δ, B).

2. It was perceived that in a wavy channel, for sufficiently large $B \geq \mathcal{O}(1)$ stagnant fouling zones appear first at the widest part of the channel, when the amplitude h exceeds a critical limit h_c. These stagnant regions continue to exist and grow with increasing h. We found that h_c decreases monotonically as B increases, i.e. we get static layer at smaller h.

3. Qualitatively four types of flows were identified based on the unyielded regions arrangement: the central plug can be intact or broken and is always present in the flow, whereas static layers might be present or not. When $B \geq \mathcal{O}(1)$ we observed the following trends in the flow configuration. For $\delta = \mathcal{O}(1)$ the central plug is chiefly intact and remains so with the growth of h through the appearance of static layers. For long $\delta \ll \mathcal{O}(1)$ the central plug is intact only when $h \leq \mathcal{O}(\delta)$ and quickly breaks with increase of h, forming two islands each around a symmetry points of the channel, at the narrowest and widest sections. With further increase of h static layers appear. If static layers exist at a given h, δ, B, then they would exist for larger h, δ, B as well. For a given flow with static layer, if we keep h, B constant and decrease the δ, the static layer eventually vanishes. Conversely for a case without stagnant layer if δ is increased at constant h, B, eventually a static layer appears.

4. We observed that for sufficiently large $B \geq \mathcal{O}(1)$, a variable that describes the onset of static layers is $h\delta = \hat{H}/\hat{L}$, which is simply the average slope of the non-uniformity. This means if $h\delta \geq (h\delta)_c$ then we have static layers. We showed that this limit can be expressed as $(h\delta)_c = f(B, L)$ where the function f is predominantly determined by B and changes in δ result in weak variation. Moreover it was showed that f can be bounded by 2 curves ($f_s(B)$ & $f_n(B)$, respectively), that give sufficient and necessary values of $h\delta$

to have a static layer. These bounds are only functions of B, i.e. $(h\delta)_n = f_n(B) \leq (h\delta)_c = f(B, L) \leq (h\delta)_s = f_s(B)$. This means that, for static zones to appear, it is necessary for $h\delta$ to be at least $f_n(B)$. Conversely, if $h\delta$ is greater than $f_s(B)$ then it is guaranteed to have a static layer at the widest section of the channel. These bounds are quite close, generally differ by $\leq 15\%$ and get closer for smaller B. We have provided curve fitted expressions for $f_n(B)$ & $f_s(B)$. The existence of the necessary bound can be understood from exploring the lubrication limit, i.e. if $h\delta \ll \mathcal{O}(1)$ then the lubrication approximation is correct in describing the shear stresses near the wall and this never predicts static layers, even for $B \to \infty$; see [102]. The existence of the sufficient bound can be explained by looking at the Newtonian counter part where the increase of h results in recirculation at the widest part of the channel. At the amplitude h_{Newt}, for the onset of recirculation, we have $\tau_{xx} = \tau_{xy} = 0$ at the maximum depth of the channel wall. Therefore, if we put any amount of yield stress we should get a static layer at this amplitude. Therefore, we see that the sufficiency condition for the Bingham fluid to have a static layer should be bounded by the Newtonian condition for recirculation.

5. For moderate B when the amplitude h is increased above critical h_c changes in the position of the stagnant layer boundary quickly become insignificant. Also we observed that in this range of B & h, having different shapes of wall non-uniformities did not produce noticeably different flows in the mobile regions. These all suggested that the flowing part of the channel is inherently self-selected. We were able to show some universal scalings for our computations, though we could not give complete understanding. The flow in the narrow region between the stagnant layer and the central plug shows interesting features: both a very symmetric velocity ($u(y)$ approximately cubic) and $\sigma_{yy} \approx 0$. Exploiting these we tried to derive a semi-analytic form for the flow fields, containing only a function $F(x)$ describing streamwize variations, but were unable to derive a closed form expression for F.

6. Many of the results discussed above relate to $B \geq \mathcal{O}(1)$. We also explored the limit of small $B \ll \mathcal{O}(1)$ (Newtonian limit). We observed that this limit contains some interesting complications, so that not all the previous observations will hold, e.g. we showed a case in which a static layer is formed and then by increasing h it vanishes, being replaced by a recirculation region. With further increases of h, we observed a second vortex in some cases. The strength of the vortices decays quickly with depth and even a very small amount of yield stress $\approx .001$ can solidify the vortex into stagnant zone.

7.1.2 Fracture flow and critical pressure drop (Chapter 3)

1. We explored the validity of using Hele-Shaw/lubication approaches to developing a (nonlinear) Darcy law for flows along narrow cracks/fractures. We used two idealized geometries: a wavy and a linear wall profiles, positioned with a shift between top, bottom walls (defined via the parameter $\psi \in [0, 1]$), to create tortuosity in the flow path. Over 2000 cases were computed over the dimensionless parameter space H, L, ψ, B. We found that the Darcy-type approximation can reasonably predict pressure drop over the channel if $H/L \ll \mathcal{O}(1)$, i.e. for small variations of flow width compared to length, which is what is generally expected.

2. For thicker fractures $H/L \geq \mathcal{O}(1)$ stagnant layers appear which cause a significant error in pressure drop predictions made using Hele-Shaw/lubication approximations. As these stagnant layers are $\mathcal{O}(1)$ variations in the flowing geometry it is not surprising that $\mathcal{O}(1)$ errors emerge. Physically, we know that when self-selection takes place, the geometry of flowing region is defined by the boundaries of stagnant layers and not the original walls. Hence it seems sensible to use the self-selected boundaries for application of Hele-Shaw/lubication approximations. Using this idea, we showed that a significant improvement in pressure drop approximations can be achieved for these thick fractures. Interestingly, we observed as B (the nonlinearity) increases the Hele-

Shaw/lubication approximation using the self-selected boundaries actually improves. This is because the static layers tend to straighten the flowing region.

3. A large part of chapter was dedicated to the study of the critical pressure drop needed to start the flow in a fracture. We considered only the wavy fracture with no shift (symmetry) in this part to simplify the geometries. To be able to apply variational methods effectively to the flow onset problem we rescale the problem using the presure drop instead of the mean velocity. This replaces B with the Oldroyd number, defined as $Od = \hat{L}\hat{\tau}_y/\hat{D}\Delta\hat{P}$. This parameter compares the applied pressure along the fracture with the yield stress. There is no flow in the fracture for Od above a critical value Od_c. This limit is equivalent to taking $B \to \infty$ in the original (mean velocity) scaling. The critical Od_c is (formally) shown to be given by the ratio of pressure work to plastic dissipation in the limit as $Od \to Od_c^-$. We provide general bounds for the convergence of pressure work, viscous and plastic dissipation functionals, all derived from the variational setting.

4. The limit $Od \to Od_c^-$ has been studied both numerically and asymptotically.

   - For short fractures $L \approx \mathcal{O}(1)$ with $H \approx \mathcal{O}(1)$ we have $Od_c = 1$. Close to the zero flow limit there is a large stagnant layer filling almost the whole non-uniformity of the fracture. There is also a large intact central plug moving slowly along the centre of the fracture. Between the boundaries of these two unyielded regions there is a thin shear layer of yielded fluid which has a width of d_0 at the mid point of the symmetric fracture. By increasing B, d_0 decreases as the flow approaches a uniform channel flow, for which $Od_c = 1$. It was established, using the variational bounds and the scaling of velocity field through the shear layer that as $B \to \infty$ we have $d_0 \approx \mathcal{O}(1/B^k)$ with $1/3 \leq k \leq 2/5$ and $1 - Od \approx \mathcal{O}(1/B^{2k})$.
   - Short thin fractures in which $H \ll \mathcal{O}(1)$, have no stagnant layer

at the flow onset limit and the lubrication (Darcy) approximation can be applied with reasonable accuracy. For these $Od_c > 1$, meaning that less pressure is needed to mobilize fluid compared to the uniform channel, which shows the greatest resistance.

- Long thin fractures $L \gg \mathcal{O}(1), H \ll \mathcal{O}(1)$ have no static layers and again the lubrication approximation is fine leading to $Od_c > 1$. Using an asymptotic expansion of the lubrication approximation in this limit we established that $Od_c - Od \approx 1/B^{1/2}$.
- For both short deep and long thing fractures we were able to verify the orders of convergence of $d_0, Od_c - Od$ obtained from the analysis with numerical solutions nicely. It showed that good anisotropic mesh adaptation strategies yield very accurate results which can capture the asymptotic behaviour in the numerical solutions.
- For other cases where the fracture is not thin or short, as $B \to \infty$ a static layer exists, but only fills the fracture partially in the interval $(-x_f, x_f)$. The central plug is broken into two parts, each around the symmetry points at the narrowest and widest sections of the fracture. The narrow plug has $\mathcal{O}(1)$ size and the wider plug is wider, occupying almost the same length as the static layer. There is a thin shear layer between large plug and the static layer. Between the two plugs we find a slightly sheared pseudo-plug region. The pseudo-plug joins to the wall in a narrow layer of high shear. Based on these observations we have constructed an approximation for the plastic dissipation which depends only on x_f. Then from the velocity minimization principle (Section 1.3) we find the x_f which minimizes the dissipation. This in turn yields an estimate for Od_c. This approximation gives remarkably good results in a wide range of fracture geometries, typically $\leq 10 - 15\%$ error. Moreover, the same approximation method leads to a bound $L \leq 2\pi$ for short fractures, for which $Od_c = 1$ is predicted. Furthermore, the approximation also gives accurate

result for long-thin geometries. The error of model becomes larger when both L, H are large, which is not very relevant for fracture geometries.

5. In addition to simple fractures, we performed several computations for affine fracture geometries which are closer to the reality of geological cracks. These geometries need more focused study, however we have observed some of the trends. First we encounter similar static layer, pseudo-plug and plug regions. Secondly, for the limit of no flow nearly all the small scale wall roughness is filled with static fluid and the self-selected path has a smooth wall with some singular points. Topologically it seems that we can partition it into sections of pseudo-plugs, shear layers, plugs and static regions as we studied before.

6. Our study showed that if Darcy-type approximations are naïvely applied for the study of onset/channelization in porous media or in rough Hele-Shaw cells (2D fractures), then it would suffer significant $\mathcal{O}(1)$ errors.

7.1.3 Washout flows at $Re = 0$; Chapter 4

1. This chapter focused at an industrial problem in which geometry at first glance seems an insurmountable barrier, i.e. in general washout shapes are not predictable. However, motivated by insights from Chapter 2, we began by investigating the idea of invariance of the flowing area.

2. We systematically explored the problem of the uncertainty of washout geometries by considering four categories of wall variation, from uniform annulus wall to the maximum washout depth: (i) smooth (sine wave), (ii) linear (or triangular wave), (iii) sudden (or square-wave), and (iv) semi-fractal (koch snowflake). We studied the Stokes flow of the Bingham fluid through these washouts and computed ~ 1000 different cases over a wide range of the parameter space of the problem: (H, L, B).

3. Regarding the onset of static layers we observed strong geometry dependence. Having $B \geq \mathcal{O}(1)$, for sudden expansion we always get static zone at the corners and the same happens for semi-fractal shapes in which the small scales are quickly filled with static fluid. On the other hand, for wavy and linear shapes there is no static layer until the ratio H/L (average slope of profile) passes a critical limit, which is the same behaviour observed in Chapter 2.

4. Regarding deep washouts, we observed that for $B \geq \mathcal{O}(1)$, as H gets progressively large a single connected stagnant region fills the deepest parts of the washout, for all 4 categories of washout geometry. In each geometry changes in the boundary of the stagnant region become negligible at large H, so that eventually the flowing part of the washout is virtually self-selected.

5. To the best of our knowledge, this is the first time the correspondence between stagnant zones of a subdomain have been examined in relation to those for a larger domain (in 2D flows). In duct geometries, Mosolov and Miasnikov [169] proved that stagnant zones of the main domain will inherently remain stagnant for suitably chosen subdomain; see Figure 1.14. For equal (H, L) all of the washout domains are a subdomain of the sudden expansion one. Indeed we found that this connection is true in 2D for our computations and the stagnant zones of the sudden expansion washout remain static in other subdomain washouts, see Figure 4.11.

6. Regarding invariance, we found that for $B \geq \mathcal{O}(1)$ as $H \to \infty$ the boundary of the static fouling layer for all the different washout shapes converges to that of the sudden expansion. In other words, self-selection of the flowing area is invariant with respect to wide ranges of the underlying geometrical parameters. Practically speaking, this is very useful as the static layer of a sudden expansion washout quickly converges to its final shape, typically at $H/L \approx \mathcal{O}(1)$. We can compute the final shape of the boundary of the static region in this washout,

once only, and then use it as an approximation for other arbitrarily shaped washouts, say $y = f(x)$. Industrially, the most important situations take place when $\max f(x) \to \infty$, i.e. a very deep washout, for which we want to know the shape of the static zone. It is hard to compute very large geometries, but here we are lucky that for sudden expansions the infinite depth solution is found at $H/L \approx \mathcal{O}(1)$, which we can compute. Finally, from the domain invariance we know that the other washout solutions converge to the sudden expansion (square wave). Picking up this idea, we proposed a simple way to compute the flowing area for any given washout geometry. This quantity is itself useful in order to e.g. estimate the amount of extra cement needed to pump when displacing a washout section of the well.

7.1.4 Inertial flow in washouts; Chapter 5

1. In this chapter we studied the effect of inertia on the steady Bingham flow through model washout geometries. For this case we only used the wavy geometry, as we expected qualitatively similar effects of inertia in other (non-abrupt) geometries. The parameter space of the problem is increased to (H, L, B, Re). As in practice the flow rate (pumping speed) is the main independent physical variable used in the process, the Hedström $He = Re \times B$ number was used instead of B, to study the parameter space. This dimensionless parameter (He) is independent of velocity and for most of our computations $He = 500$ was used.

   - It was found that the yield stress has a stabilizing effect, i.e. the flow remains stable for higher values of Re.
   - As expected, we found that inertia induces asymmetry in the flow and in the shape of the static layer in the washout region.
   - Contrary to general industrial perceptions, we found that increasing inertia does not always lead to better conditioning of the washout region, meaning a smaller static zone in the washout. In fact we found that if Re passes a certain limit, then the static

region enlarges with the increase of Re. We found two trends here:

- For relatively shallow washouts which have no static region in the Stokes flow limit $Re \to 0$, there is initially no static region at small Re, but by increasing Re sufficiently, a static region emerges. This is very bad as we had perfectly mobile region and increasing inertia worsened the situation.
- For deeper washouts which have static layers in the Stokes limit $Re \to 0$, initially increasing Re helps to shrink the static layers, but only up to a critical limit Re_c. After this point increasing inertia again leads to growth of the static layers. We found in our computations that typically $Re_c \approx 100$ which shows we need only a small amount of inertia for better conditioning.

Of course, all our simulations with inertia are still laminar and relatively far from turbulent transition.

- Note as $He = Re \times B$ was fixed in our study, $Re \to 0$ means to have $B \to \infty$, so the above two types of variations can be understood by the $B \to \infty$ limit discussed in Chapter 2. We observed that as $B \to \infty$ the critical $(h\delta)_c = (H/L)_c$ for getting static layer becomes almost constant. This can help to identify the two types of washouts in the above.

7.1.5 Displacement flow; Chapter 6

In this chapter we considered a simplified model for the primary cementing by considering a Newtonian fluid to displace viscoplastic fluid. This is the simplest model which we can have static layers in the flow and there is some rheological freedom and relevance to main problem. Even with this simplified model the flow is governed by 5 dimensionless parameters.

1. Static layers of fluid can exist permanently in the washout and development sections, depending on the dimensionless parameters. Contrary

to the single fluid flows studied in Chapter 4 & Chapter 5 static layers can also exist on the (straight) casing wall along the length of the washout, i.e. mobility of the single phase flow during recirculation does not guarantee mobility during the displacement phase.

2. We can have both stable and unstable displacements. In the former case viscous forces are dominant (low Re, high M). The defending fluid is slowly displaced by a combination of pressure forces and viscous drag, leading to smooth, well shaped static residual layers. In the latter case the flow remains unstable throughout the displacement, strong mixing of the fluids can happen and the static layers are more irregularly shaped.

3. The stable displacement takes place in one stage while the unstable one can be divided into two stages. In stable displacements the invading fluid displaces the defending fluid steadily until it reaches the domain exit, afterwards no more (or very little) displacement happens and the flow remains steady. In unstable displacements, first an unstable invading fluid displaces the defending fluid and reaches the exit. In the second stage the flow remains unsteady and continues to wash and transport parts of defending fluid out of the domain.

4. In stable displacements along sufficiently long washouts, if the viscosity of invading fluid is large we can get a full displacement of the defending fluid throughout the washout, except for small regions at the corners of the washout. We have developed an estimate for the minimum required viscosity ratio to accomplish this.

5. When viscous and inertial forces are closely balanced and the flow is still stable, inertia can considerably influence the topography of static layers. For example in the long washouts, it may create wavy shaped static layers. This type of effect is rather sensitive to the flow conditions: small changes might lead to great variation, partly it depends on inertia and partly since the flow is irreversible.

6. In stable displacements when inertial effects are high enough a recirculating vortex can exist in the depth of the washout. The structure of the vortex is interesting: it consists of an uncontaminated core of defending fluid plus a surrounding ring of mixed fluids. This seems to be the only case for which we get non-static defending fluid remaining in the washout zone for long time.

7. The yield stress has interesting effects on the stability of the flow. Sometimes the displacement starts in an unstable mode at the beginning and the amplitude of instabilities grow for a while, however the yield stress eventually damps the instabilities and it seems that eventually we get a stable displacement, at least for the parameters tested. Fascinating patterns that indicate the early unsteadiness of the flow can be frozen into the flow by the yield stress of the displaced fluid.

8. In addition to dynamic parameters of the problem i.e. Re and M, we observed that the length of the washout can also play a role in determining stability or instability of the flow.

9. Generally, by increasing inertial effects the asymmetry of the flow increases.

10. In the low Re limit we saw that the displacement pattern in the local region very close to the entrance to the washout is approximately invariant with respect to M. We postulate that this is primarily caused by the large pressure imbalance on the fluid, due to the sudden expansion of the flow. However this needs more investigation.

11. We observed some evidence of the similarity of self-selection of the flowing area, for large enough H and B, i.e. when the washout is adequately deep. This is perhaps better described as a flow invariance. The displacement must be stable to achieve this.

In terms of the practical application to cementing, the following observations appear relevant.

1. Increasing the viscosity ratio M of invading to defending fluid always leads to better displacement. This is achieved by increased drag force on defending fluid. In fact if the washout is long enough and M is large enough we can achieve full displacement of the washout (except for small corner regions). However the required M is quite restrictive, as it quadratically grows with the depth of the washout.

2. We observed in Chapter 5 and here again that increasing inertia does not always lead to better displacement. For long-deep washouts we observed that highly inertial flow leads to a flow structure in which the invading fluid is simply traveling in a roughly straight line from upstream to downstream, leaving a large vortex of mixed fluids circulating within the washout. For smaller inertia the invading fluid penetrates deeper into the washout and better displacement is achieved. This is contrary to general idea in the industry that the higher inertia always results in better displacement.

3. The low Re flows achieve better displacement at the entrance (upstream) area of the washout, i.e. compared to higher Re flows. Higher Re flows generally achieve better displacement in the exit (downstream) region.

4. Finally, based on the behaviour of the displacement flows observed, we have proposed a method to achieve better displacement for long-deep washouts when M is low. It is based on having a transient process in which we increase Re from low to high, during a time period period of $\mathcal{O}(t_{pass})$. With this strategy we attempt to combine both the good properties of low Re displacements with those at higher Re. The former of these is better mobilization of the invading fluid at the upstream end. The latter of these improves the downstream end of the washout. However, we should be careful not to put too much inertia into the flow. This can lead to a large vortex structure in the washout, hence reducing displacement efficiency.

7.2 Context of the thesis

This thesis was largely dedicated to the study of a collection of yield stress fluid flows in 2D channel type geometries which are not uniform. Here we look back at the underlying motivations and how we were drawn to the study of such flows, what were our objectives and a summary of efforts we made, the current state and what we can forecast for the future.

The importance of non-uniformities in geometry on yield stress flows comes from both theoretical aspects and practical applications. The objectives of this thesis was also two fold. Firstly, we wished to extend the current understanding of qualitative aspects of non-uniform 2D channel flows, in the context of illuminating the relationship between the unevenness of the channel geometry and the yield surfaces, and in particular the emergence of static regions. Secondly as an engineering study, we wished to explore practical consequences of this understanding. In petroleum industry there are a set of problems related to well construction, such as primary cementing (washouts), squeeze cementing, hydraulic fracturing which all involve yield stress flow in non-uniform channel type geometries. In different operational contexts phenomena such as fouling ad flow/no flow become practically important and deserve consideration.

7.2.1 Scientific context

On the theoretical side, it is known that a yield stress fluid can *filter* the non-uniformities in the domain geometry via appearance of stagnant zones attached to the original boundary. Whereas prior work had observed these features in sudden expansion/contraction type of flows, where the corners are fouled, there was little understanding of why this occurs, nor appreciation that these static zones arise also in smooth geometries. Our work represents the first comprehensive study of these phenomena. This aspect of *self-selection* of the flowing domain geometry due to the yield stress is unique among all non-Newtonian fluids. Mathematically these problems are free-boundary problems, but in this specific context, the free boundaries of primary interest are those bounding regions attached to the wall (identified

by $\mathbf{u} = 0$).

An interesting characteristic of the self-selection problem is the looser coupling of it to the detailed velocity solution in the flowing region, particularly for flow/no-flow problems with yield stress fluids. In many situations, flow/no-flow problems can be expressed in a purely geometric optimization form, involving no dynamic parameter of the flow. The seminal works of Mosolov and Miasnikov [168, 169] are the best examples of rigorous mathematical analysis of self-selection and flow/no-flow problems, but only for the special class of yield stress duct flows. They considered an arbitrary duct geometry. Without solving the full velocity solution, they derived the exact value for the minimum pressure drop needed to start the flow, proved many qualitative features of the self-selected boundaries, gave bounds on the maximum velocity and various other insights (surveyed in Chapter 1).

Self-selection and flow/no-flow at $Re = 0$ are studied in idealised channels/fractures in chapters 2, 3 & 4. Although the approach is primarily computational rather than theoretical, we do begin to build a clear qualitative picture along the lines of that offered by Mosolov and Miasnikov. Firstly, the wide selection of computed results give a panoramic view of how the unyielded regions develop as (H, L, B) are varied, as well as quantitative data on the velocity and stres fields. We have seen in a systematic way that self-selection occurs and that some features are shared with the simpler duct flows. For example, as the depth of washouts (or wave amplitude) increases, the invariance of the self-selected yield surface bounding the static regions is a noticeable feature. The flow domains at larger H include those at smaller H and, as with [168, 169] it seems that the velocity and stress field for the smaller domain can be extended to the larger domain, by enlarging the static regions into the depths of the channel/fracture unevenness. This does however appear to require $B \sim \mathcal{O}(1)$, as shown by the limit $B \to \infty$, studied in 2.

In various parts of the thesis we have produced reduced models, curve fits and universal scalings relating different features of these flows. Undoubtedly these results have individual practical utility, e.g. in predicting flow features. However, it is fair to say that a more complete understanding has eluded

us, except via computation.

In terms of flow/no-flow, we have formulated the problem in the proper variational context in Chapter 3, (i.e. in defining Od_c), but have not attempted to characterize the functional optimization problem in a geometric way, although for channels with some symmetry the geometric character of the flows is evident. Considering the analysis of Chapter 3, we looked at 3 types of fracture. The short and deep fractures behaved as the uniform channel and the long-thin fractures had a yield limit that is also easily interpreted as a geometric average. However, the intermediate shaped fractures had Od_c computed containing significant contributions from both thin layers (at the walls and separating the widest plug from the stagnant regions) and from the pseudo-plug region. The latter region does not vanish as $Od \to Od_c$. This makes the flow/no-flow problem harder to characterize in such a universal way as was possible for uniaxial duct flows in [168, 169], where the limiting flows always contain thin (*boundary-layer*) shear regions separating mobile and stagnant regions. For the 2D flows, in order to progress (either geometrically or in other ways) it seems that the main barrier is to understand these pseudo-plug regions.

A slightly different perspective on the results of the early part of the thesis is to view 2 & 3 in the context of the earlier studies of [102, 199]. Together, these build a complete picture of the symmetric periodic wavy-walled channel flow at $Re = 0$, which for Newtonian fluids is a classical type of flow. At fixed yield stress and length, increasing the amplitude sees initially an intact central plug region, then breaking of the central plug ([102, 199]). At larger amplitudes H we see the start of fouling in the deepest parts of the channel, then the boundary of the fouling region becoming progressively invariant as $H \to \infty$ (contributions of this thesis). Similarly, for fixed geometry (and pressure drop) we have seen that increasing the yield stress can lead first to fouling (depending on the geometry) and then to a thickening of the fouled region. As the yield stress approaches a critical value the flow stops.

We may infer that these features of the symmetric wavy-walled channel will carry over qualitatively to other symmetric geometries (e.g. the trian-

gular wave). On the other hand we have also seen very interesting flows in simplified geometries on introducing the shift ψ in 3, e.g. those with asymmetrical plug regions connected by thin strands of unyielded material. Such flows and the differences in flow/no-flow for asymmetric geometries are challenging areas for study that have been exposed in this thesis.

In the Stokes flow context we have used tried and tested computational methods. Although the methods are advanced we have implemented only small changes from those developed in the literature. We have universally used the augmented Lagrangian method, as much of the thesis concerns predicting yield surfaces and unyielded plug regions, for which this is the only reliable general computational method. The computations do however demonstrate the following.

- The effectiveness of the implemented anisotropic adaptive meshing techniques with the augmented Lagrangian method in determining complex yield surfaces.

- The feasibility of using such 2D computations in conducting parametric studies over wide parameter ranges to elucidate physical features in an empirical fashion, i.e. the computation is our experiment.

- Through careful use in parallel with analytical methods, the ability of these methods to quantify yield limits of the flow is established, e.g. in 3 the numerically evaluated asymptotic convergence rates of the dissipation conform to the variational analysis bounds.

Chapters 5 & 6 moved away from the Stokes flows. Due to parametric complexity our studies here have been less comprehensive. Some features of the inertial flow are analogous to those observed with Newtonian fluids, e.g. the breaking of fore-aft symmetry of the flow, the need to include a development length, etc. To some extent we also saw that the self-selection and universality principles of the Stokes flow extended to the inertial regimes. Some displacement features such as the static wall layers also feature in geometrically simpler studies. The contributions from these chapters are mostly however of industrial relevance.

7.2.2 Industrial context

On the industrial application side there are many important problems involving yield stress fluids and duct flows. Here we group into two categories for which the results of the thesis have a direct impact.

Firstly, there are flows in which self-selection of stagnant regions is of importance. For many of these flows the ideal situation is to minimise the extent of fouling or to eliminate it.

- In the context of primary cementing, the main driver is mud-removal. Drilling mud that is left behind in a well, attached to the walls or otherwise, can form a porous conduit along the length of the well allowing formation fluids to connect hydraulically to surface. We have studied simplified 2D models of washouts (see below).

- In the setting of cement plugs for well abandonment, some jurisdictions regulate for the well casing to be milled out and for a cement plug to be set across the cut casings, sealing into the formation. These geometries are effectively deep and long washouts.

- Some of the existing work identifying stagnant regions focused at abrupt expansion and contraction geometries. Although benchmark problems, their origin comes from polymer processing applications e.g. in extrusion. Capillary rheometry also has similar geometries, where the fluid is pushed along the main barrel before entering the (much narrower) extrusion section. Thick pastes are one example of yield stress fluids handled in this way. Thinner fluids tend to have recirculation zones at the contraction, which compromise the measurement accuracy. Thus, for yield stress fluids its important to be able to estimate the extent of the stagnant corner regions.

- In hydraulic fracturing, after the pumping pressure is relaxed, the fracture closes on the proppant laden frac fluid. Some of the fluids used are viscous gels and although chemical breaker compounds are also pumped, designed to be released mechanically via the closing of the fracture, it is unclear to what degree gels in the fracture are

actually broken down. The flow-back phase is where the initial flow from the fracture is used to clean the frac fluids from the well. Here, it is of interest to estimate the amount of frac fluid that might still remain trapped in the fracture.

- An important family of applications arises in the processing of food products (and other organic products that come into human contact, e.g. cosmetic and pharmaceutical). Here stagnant zones in processing machinery provide potential bacterial growth sites, with consequent health hazards.

- Finally, in designing industrial mixers for slurries and pastes, it is of great interest to determine stagnant zones as they dictate the maximum efficiency of the mixing process.

Secondly, we have applications involving the flow/no-flow limit.

- In the context of squeeze cementing we apply an over-pressure drop to a thin cement slurry in order to drive it into an unknown crack/fissure. With some estimates of the crack width, unevenness and depth we would like to predict how deeply the slurry penetrates before the yield stress causes it to stop flowing.

- Sealing: in a more general context than above, other oil and gas processes involve a physically similar procedure. These include (i) pumping lost circulation fluids during drilling of wells, to seal ongoing leaks; (ii) sealing of old fractures and cracks near the wellbore to prepare a reservoir for CO_2 storage.

- Similar penetration problems (of yield stress fluids into porous media/cracks) occur in the construction industry, e.g. silicon sealant around windows placements, damp-proofing of brick houses, etc ...

- The hydraulic fracturing flow-back problem (described above) involves first mobilizing frac fluids.

- The washout flows considered as part of the recirculation phase first have to break circulation (flow/no-flow) by applying sufficient pump pressure.

- Finally, if we move away from uneven duct flows, there are many other situations in which flow/no-flow is important, e.g. settling of particles.

Chapters 4–6 were a step by step study of the industrial problem of residual drilling mud in oil & gas washout sections. Starting with Stokes flow we included inertial effects and finally also displacement flows. The universality of the fouling regions led us in Chapter 4 to propose methods to estimate the degree of fouling, based on the square washout. In Chapter 5, we showed that inertia, counter intuitively to industrial perceptions, may result in larger static zones. Also this study exposed the need to differentiate between mud that is yielded but recirculates slowly in the washout, and mud that is displaced from the washout, i.e. what is important: trapped fluid or conditioned fluid, and what is needed to condition? For displacement flows (Chapter 6), we proposed a simple idea to improve the efficiency of displacement in long washouts by controlling the pumping speed with time. This would use less energy compared to a fully turbulent displacement and can achieve better displacement.

Early on we decided to restrict our treatment of washouts. First, we considered yield stress fluids only of Bingham type. Secondly, we considered only 2D sections of the cemented annulus. Although limiting, our results have surprising richness and have exposed features of practical importance. Fully 3D simulations seem to be beyond our current computational abilities and are very time consuming. However, in particular once we consider displacement flows and fluids of differing density, it seems apparent 3D effects will be important.

Chapter 3 gave a comprehensive study of the effectiveness of using lubrication/Hele-Shaw type of approximations for predicting the pressure drop along uneven channels. These approaches are commonly used as extensions of Darcy's law into nonlinear filtration regimes. We showed that the strict application of these approximations is rather limited to $H/L \ll 1$. A main cause of this

limitation is that the onset of fouling induces significant geometric changes in the flowing region. We showed that naïve application of the Darcy-law approach, would result in $\mathcal{O}(1)$ errors. Knowing the self-selected boundary allows us to reduce this error significantly.

Chapter 3 also gave an analysis of flow/no-flow limits for uneven channel/fracture flows. Knowing the distribution of Od_c and range of variation with H and L is helpful in designing invasion processes. Although porous media are irregular, some statistical estimates of the geometry is sometimes available (from core samples or from nearby wells), so that potentially one could include these into estimates of Od_c.

7.3 Limitations

Inevitably, there are limitations and simplification in any research direction, and here we mention some of the issues.

7.3.1 Rheological idealizations

For all of our studies, we used the Bingham model. It is the simplest rheological model of a yield stress fluid, but as such it conveys only the most important feature of these fluids: the yielding. In practice, fluids rarely fit to Bingham model well and a more realistic version is the Herschel-Bulkley model (provided the range of strain rates is limited). Further, for drilling mud conditioning flow studied in Chapters 4 & 5 thixotropy is an important issue that is neglected. Depending on operational situations, there is a often significant delay from the end of drilling until the start of conditioning. In this period, the gel structure of mud builds up and the yield stress may significantly increase.

7.3.2 Experimental study

There are relatively few experimental works reporting viscoplastic fluid flow in a nonuniform channel type geometry. The only relevant experimental work we have found are those by Souza Mendes et al. [79], Jay et al. [138, 139] and Hammad et al. [115], all of which consider axisymmetric expansion/-

contraction type geometries.

It would be advantageous to conduct some experiments to verify how much our simplifications make sense in reality. Some initial collaborative work on a wavy-walled setup has been initiated (with T. Burghelea from Nantes, France). Early results showed some degree of asymmetry, e.g. as in the figures of [79]. Unfortunately, this work has not been continued at the present time.

7.3.3 Computations

First, we were able to obtain good high quality computations for may of the steady Stokes flows, as we were able to capture analytic asymptotic results in Chapter 3 with computations. However, it is known that augmented Lagrangian method has a slow convergence rate, especially when the plastic part is highly dominating [256]. Consequently if one wants accurate results it takes a relatively long time to converge. Therefore, using an algorithm with higher convergence rate, such as [232], which is only recently proposed would be a big help.

Another limitation was that we could not find a unified numerical platform which serves all of our requirements for boundary conditions, element types, meshing, ... Consequently we used four different types of codes which is a big burden to manage and is inefficient in the duplication of effort. For example we re-implemented the augmented Lagrangian method twice: once from Chapter 2 to Chapter 4 and again for Chapter 5. Ideally it would be good to find a unified platform.

7.4 Future directions

Besides addressing the limitations mentioned above, we consider the avenues below for future work in this area.

- Considering flow/no-flow problems, one possible approach might be to reduce the variational principles to a simpler form for some special case e.g. $u_y \ll u_x$ and then try to extract useful information directly. Another possible avenue for using variational principles could be deriving

some kind of reduced computational algorithm which only tracks the boundaries of stagnant zones, even for special cases e.g. channel flows. Recall here that the onset problems naturally take the form of some kind of geometric optimization problem. In Mosolov and Miasnikov finding the value of K (see Equation 1.67) reduced the critical flow/no-flow problem to a maximization of the ratio of perimeter to area in subdomains of the duct. Within [104] a form of geometric optimization problem was derived for finding the local shape of displacement front and in Chapter 3 equation (3.38) is the solution of a geometric optimization problem again. Therefore it seems probable to be able to derive e.g. an iterative geometric optimization algorithm which starts with the boundary of the channel and in each iteration modifies its shape until converges to the final self-selected boundary. This would be a great method e.g. in Chapter 3 to estimate the pressure drop for affine fractures which have complicated geometry.

- In Chapter 2 where we investigated the features of self-selection, one of the ideas that we tried was to look at the variation of the curvature of yield surface and the angle at which it meets the wall. Even though we were using mesh adaptation using our data to determine these parameters was not possible. Instead, using an approach like Szabo & Hassager [225] could be effective. Basically we should assume the overall shape of unyielded regions and then correct them iteratively. This method, although not universally applicable, generally gives very accurate results, and here we have the initial estimates of the yield surface from the current computations.

- We did not do axisymmetric computations, nor 3D computations. Both geometries could be interesting to study and practically useful. In particular, we note that most existing experimental results concern axisymmetric geometries.

- In the last chapter we were limited to rectangular geometries due to our VOF solver. It would be better to lift this limitation so that

other types of washout walls can be studied. As we had short time for the last chapter, we were unable not make a complete study. The computations should be done for much wider range of parameter and also longer times.

Bibliography

[1] S. S. Abdali. Entry and exit flows of Bingham fluids. *J. Rheol.*, 36(2):389, Feb 1992. 38, 47

[2] D. Adalsteinsson and J. A. Sethian. A fast level set method for propagating interfaces. *Journal of Computational Physics*, 118(2):269277, May 1995. 212

[3] U. E. P. Agency. http://www2.epa.gov/hfstudy/hydraulic-fracturing-water-cycle, retrieved 2015-11-05. xi, 9

[4] T. Al-Fariss and K. L. Pinder. Flow through porous media of a shear-thinning liquid with yield stress. *Canadian Journal of Chemical Engineering*, 65(3):391–405, 1987. 92

[5] A. Alexandrou and V. Entov. On bubble rising in a hele–shaw cell filled with a non-newtonian fluid. *European Journal of Applied Mathematics*, 15(03):315–327, 1997. 208

[6] A. N. Alexandrou, E. Duc, and V. Entov. Inertial, viscous and yield stress effects in Bingham fluid filling of a 2-D cavity. *Journal of Non-Newtonian Fluid Mechanics*, 96(3):383403, Jan 2001. 38

[7] A. N. Alexandrou, G. C. Florides, and G. C. Georgiou. Squeeze flow of semi-solid slurries. *Journal of Non-Newtonian Fluid Mechanics*, 193:103115, Mar 2013. 38

[8] A. N. Alexandrou, T. M. McGilvreay, and G. Burgos. Steady herschelbulkley fluid flow in three-dimensional expansions. *Journal of Non-Newtonian Fluid Mechanics*, 100(1-3):7796, Sep 2001. 48

[9] M. Allouche, I. A. Frigaard, and G. Sona. Static wall layers in the displacement of two visco-plastic fluids in a plane channel. *Journal of Fluid Mechanics*, 424:243277, Dec 2000. 154, 178, 203, 208, 209

[10] R. A. Almehaideb. Asphaltene precipitation and deposition in the near wellbore region: a modeling approach. *Journal of Petroleum Science and Engineering*, 42(2-4):157170, Apr 2004. 54

[11] A. Ambari, M. Benhamou, S. Roux, and E. Guyon. Distribution des tailles de pores d'un milieu poreux déterminée par l'écoulement d'un fluide á seuil. *Comptes rendus de l'Académie des sciences. Série 2, Mécanique, Physique, Chimie, Sciences de l'univers, Sciences de la Terre*, 311(11):1291–1295, 1990. fre. 92

[12] J. S. Anya M. Hillery, Andrew W. Lloyd. *Drug Delivery and Targeting: For Pharmacists and Pharmaceutical Scientists*. CRC Press, 2001. 298

[13] H. A. Ardakani, E. Mitsoulis, and S. G. Hatzikiriakos. Thixotropic flow of toothpaste through extrusion dies. *Journal of Non-Newtonian Fluid Mechanics*, 166(21-22):12621271, Nov 2011. 39

[14] C. Atkinson and K. El-Ali. Some boundary value problems for the Bingham model. *Journal of Non-Newtonian Fluid Mechanics*, 41(3):339363, Feb 1992. 46

[15] M. Balhoff, D. Sanchez-Rivera, A. Kwok, Y. Mehmani, and M. Prodanović. Numerical algorithms for network modeling of yield stress and other non-Newtonian fluids in porous media. *Trans. Porous Media*, 93(3):363–379, 2012. 92

[16] M. Balhoff and K. E. Thompson. Modeling the steady flow of yield-stress fluids in packed beds. *AIChE J.*, 50(12):3034–3048, 2004. 92

[17] N. Balmforth and R. Craster. A consistent thin-layer theory for Bingham plastics. *Journal of Non-Newtonian Fluid Mechanics*, 84(1):6581, Jul 1999. 19, 21, 93, 124, 311, 312

[18] N. J. Balmforth, A. S. Burbidge, R. V. Craster, J. Salzig, and A. Shen. Visco-plastic models of isothermal lava domes. *Journal of Fluid Mechanics*, 403:3765, Jan 2000. 21

[19] N. J. Balmforth and R. V. Craster. Dynamics of cooling domes of viscoplastic fluid. *Journal of Fluid Mechanics*, 422:225248, Nov 2000. 22

[20] N. J. Balmforth, R. V. Craster, and R. SASSI. Shallow viscoplastic flow on an inclined plane. *Journal of Fluid Mechanics*, 470, Oct 2002. 21

[21] N. J. Balmforth, I. A. Frigaard, and G. Ovarlez. Yielding to stress: Recent developments in viscoplastic fluid mechanics. *Annual Review of Fluid Mechanics*, 46(1):121146, Jan 2014. 91, 348

[22] G. I. Barenblatt, V. M. Entov, and V. M. Ryzhik. *Theory of fluid flows through natural rocks*. Norwell, MA (USA); Kluwer Academic Publishers, 1989. 91

[23] H. A. Barnes. The yield stressa review or everything flows? *Journal of Non-Newtonian Fluid Mechanics*, 81(1-2):133178, Feb 1999. 15, 348

[24] H. A. Barnes and K. Walters. The yield stress myth? *Rheol Acta*, 24(4):323326, Jul 1985. 15

[25] L. L. Baxter and R. W. DeSollar. A mechanistic description of ash deposition during pulverized coal combustion: predictions compared with observations. *Fuel*, 72(10):14111418, Oct 1993. 54

[26] M. Beaulne and E. Mitsoulis. Creeping motion of a sphere in tubes filled with herschelbulkley fluids. *Journal of Non-Newtonian Fluid Mechanics*, 72(1):5571, Sep 1997. 300

[27] A. Beck and M. Teboulle. A fast iterative shrinkage-thresholding algorithm for linear inverse problems. *SIAM Journal on Imaging Sciences*, 2(1):183202, Jan 2009. 33

[28] M. Bercovier and M. Engelman. A finite-element method for incompressible non-newtonian flows. *Journal of Computational Physics*, 36(3):313–326, 1980. 34, 37, 154, 320

[29] M. Bercovier, M. Engelman, M. Fortin, and N. Goldberger. Simulation of forming processes by FEM with a Bingham fluid model. *Int. J. Numer. Meth. Fluids*, 6(4):197218, Apr 1986. 37

[30] M. Bercovier and O. Pironneau. Error estimates for finite element method solution of the stokes problem in the primitive variables. *Numerische Mathematik*, 33(2):211224, Jun 1979. 219

[31] A. N. Beris, J. A. Tsamopoulos, R. C. Armstrong, and R. A. Brown. Creeping motion of a sphere through a Bingham plastic. *Journal of Fluid Mechanics*, 158(-1):219, Sep 1985. 29, 37, 300

[32] E. C. Bingham. *Fluidity and plasticity.* McGraw-Hill, 1922. 11

[33] S. Bittleston, J. Ferguson, and I. Frigaard. Mud removal and cement placement during primary cementing of an oil well. *Journal of Engineering Mathematics*, 43(2/4):229253, 2002. 93, 145, 208

[34] J. Blackery and E. Mitsoulis. Creeping motion of a sphere in tubes filled with a Bingham plastic material. *Journal of Non-Newtonian Fluid Mechanics*, 70(1-2):5977, May 1997. 38, 300

[35] J. Bleyer and P. Coussot. Breakage of non-Newtonian character in flow through a porous medium: Evidence from numerical simulation. *Phys. Rev. E*, 89:063018, Jun 2014. 92, 94

[36] H. Borouchaki, P. L. George, F. Hecht, P. Laug, and E. Saltel. Delaunay mesh generation governed by metric specifications. part i. algorithms. *Finite Elements in Analysis and Design*, 25(1-2):6183, Mar 1997. 61, 99, 156, 184

[37] H. Borouchaki, F. Hecht, and P. J. Frey. Mesh gradation control. *Int. J. Numer. Meth. Engng.*, 43(6):11431165, Nov 1998. 61, 156, 184

[38] E. Bouchaud. Scaling properties of cracks. *J. Phys.: Condens. Matter*, 9(21):43194344, May 1997. 98

[39] J. Boujlel and P. Coussot. Measuring the surface tension of yield stress fluids. *Soft Matter*, 9(25):5898, 2013. 347

[40] K. Boukir, Y. Maday, B. Mtivet, and E. Razafindrakoto. A high-order characteristics/finite element method for the incompressible navier-stokes equations. *Int. J. Numer. Meth. Fluids*, 25(12):14211454, Dec 1997. 182

[41] A. Bourgoyne. *Applied Drilling Engineering.* Society of Petroleum Engineers, 1986. 55, 146

[42] E. Buckingham. On plastic flow through capillary tubes. *Proc. Am. Soc. Test. Mater*, 21:1154–1156, 1921. 18

[43] G. R. Burgos and A. N. Alexandrou. Flow development of herschelbulkley fluids in a sudden three-dimensional square expansion. *J. Rheol.*, 43(3):485, 1999. 48

[44] G. R. Burgos, A. N. Alexandrou, and V. Entov. On the determination of yield surfaces in Herschel-Bulkley fluids. *J. Rheol.*, 43(3):463, 1999. xii, 18, 35, 36, 176

[45] J. C. Burns and T. Parkes. Peristaltic motion. *Journal of Fluid Mechanics*, 29(04):731, Sep 1967. 54

[46] K. Campbell, R. Smith, et al. Permanent well abandonment. *The Way Ahead*, 9(03):25–27, 2013. 204

[47] M. Carrasco-Teja and I. A. Frigaard. Displacement flows in horizontal, narrow, eccentric annuli with a moving inner cylinder. *Phys. Fluids*, 21(7):073102, 2009. 208

[48] M. Carrasco-Teja and I. A. Frigaard. Non-Newtonian fluid displacements in horizontal narrow eccentric annuli: effects of slow motion of the inner cylinder. *Journal of Fluid Mechanics*, 653:137173, Jun 2010. 208

[49] M. Carrasco-Teja, I. A. Frigaard, B. R. Seymour, and S. Storey. Viscoplastic fluid displacements in horizontal narrow eccentric annuli: stratification and travelling wave solutions. *Journal of Fluid Mechanics*, 605, May 2008. 145

[50] F. Caton and C. Baravian. Plastic behavior of some yield stress fluids: from creep to long-time yield. *Rheologica Acta*, 47(5-6):601–607, 2008. 15

[51] L. Chambers, K. Stokes, F. Walsh, and R. Wood. Modern approaches to marine antifouling coatings. *Surface and Coatings Technology*, 201(6):36423652, Dec 2006. 54

[52] G. G. Chase and P. Dachavijit. Incompressible cake filtration of a yield stress fluid. *Sep. Sci. Technol.*, 38(4):745–766, 2003. 92

[53] G. G. Chase and P. Dachavijit. A correlation for yield stress fluid flow through packed beds. *Rheol Acta*, 44(5):495501, Apr 2005. 92

[54] X. Chateau, G. Ovarlez, and K. L. Trung. Homogenization approach to the behavior of suspensions of noncolloidal particles in yield stress fluids. *J. Rheol.*, 52(2):489, 2008. 301

[55] P. Chaudhuri, L. Berthier, and L. Bocquet. Inhomogeneous shear flows in soft jammed materials with tunable attractive forces. *Phys. Rev. E*, 85(2), Feb 2012. 15

[56] M. Chen, W. Rossen, and Y. C. Yortsos. The flow and displacement in porous media of fluids with yield stress. *Chem. Eng. Sci.*, 60(15):4183 – 4202, 2005. 92

[57] T. Chevalier, C. Chevalier, X. Clain, J. Dupla, J. Canou, S. Rodts, and P. Coussot. Darcy's law for yield stress fluid flowing through a porous medium. *J. Non-Newtonian Fluid Mech.*, 195(0):57 – 66, 2013. 92

[58] T. Chevalier, S. Rodts, X. Chateau, J. Boujlel, M. Maillard, and P. Coussot. Boundary layer (shear-band) in frustrated viscoplastic flows. *EPL (Europhysics Letters)*, 102(4):48002, May 2013. 94

[59] T. Chevalier and L. Talon. Generalization of Darcy's law for Bingham fluids in porous media: From flow-field statistics to the flow-rate regimes. *Phys. Rev. E*, 91:023011, Feb 2015. 92

[60] Y. Chew, W. Paterson, and D. Wilson. Fluid dynamic gauging: A new tool to study deposition on porous surfaces. *Journal of Membrane Science*, 296(1-2):2941, Jun 2007. 54

[61] G. Christian and P. Fryer. The effect of pulsing cleaning chemicals on the cleaning of whey protein deposits. *Food and Bioproducts Processing*, 84(4):320328, Dec 2006. 54

[62] X. Clain. *Étude expérimentale de l'injection de fluides d'Herschel-Bulkley en milieux poreux*. PhD thesis, Université Paris-Est, 2010. 92

[63] I. Cohen. Using selective withdrawal to coat microparticles. *Science*, 292(5515):265267, Apr 2001. 298

[64] P. A. Cole, K. Asteriadou, P. T. Robbins, E. G. Owen, G. A. Montague, and P. J. Fryer. Comparison of cleaning of toothpaste from surfaces and pilot scale pipework. *Food and Bioproducts Processing*, 88(4):392400, Dec 2010. 54

[65] P. Coussot. *Rheometry of Pastes, Suspensions, and Granular Materials*. Wiley-Blackwell, Jan 2005. 13, 348

[66] P. Coussot. *Rheometry of Pastes, Suspensions and Granular Materials: Applications in Industry and Environment.* Wiley-Interscience, 2005. 91

[67] P. Coussot. Yield stress fluid flows: A review of experimental data. *Journal of Non-Newtonian Fluid Mechanics*, 211:3149, Sep 2014. 91, 348

[68] P. Coussot, Q. D. Nguyen, H. T. Huynh, and D. Bonn. Avalanche behavior in yield stress fluids. *Physical Review Letters*, 88(17), Apr 2002. 14

[69] P. Coussot, Q. D. Nguyen, H. T. Huynh, and D. Bonn. Viscosity bifurcation in thixotropic, yielding fluids. *J. Rheol.*, 46(3):573, 2002. 14

[70] P. Coussot, J. S. Raynaud, F. Bertrand, P. Moucheront, J. P. Guilbaud, H. T. Huynh, S. Jarny, and D. Lesueur. Coexistence of liquid and solid phases in flowing soft-glassy materials. *Physical Review Letters*, 88(21), May 2002. 15

[71] P. Coussot, H. Tabuteau, X. Chateau, L. Tocquer, and G. Ovarlez. Aging and solid or liquid behavior in pastes. *J. Rheol.*, 50(6):975, 2006. 15

[72] P. Coussot, L. Tocquer, C. Lanos, and G. Ovarlez. Macroscopic vs. local rheology of yield stress fluids. *Journal of Non-Newtonian Fluid Mechanics*, 158(1-3):8590, May 2009. 15, 301

[73] B. G. Cox. On driving a viscous fluid out of a tube. *Journal of Fluid Mechanics*, 14(01):81, Sep 1962. 207

[74] R. V. Craster. Solutions for hershcel-bulkley flows. *Q J Mechanics Appl Math*, 48(3):343374, 1995. 176

[75] A. R. de Castro, A. Omari, A. Ahmadi-Sénichault, and D. Bruneau. Toward a new method of porosimetry: Principles and experiments. *Transp. Porous Media*, 101(3):349–364–, 2014. 92

[76] D. A. de Sousa, E. J. Soares, R. S. de Queiroz, and R. L. Thompson. Numerical investigation on gas-displacement of a shear-thinning liquid and a visco-plastic material in capillary tubes. *Journal of Non-Newtonian Fluid Mechanics*, 144(2-3):149159, Jul 2007. 207

[77] P. R. de Souza Mendes. Modeling the thixotropic behavior of structured fluids. *Journal of Non-Newtonian Fluid Mechanics*, 164(1-3):6675, Dec 2009. 14

[78] P. R. de Souza Mendes. Thixotropic elasto-viscoplastic model for structured fluids. *Soft Matter*, 7(6):2471, 2011. 14

[79] P. R. de Souza Mendes, M. F. Naccache, P. R. Varges, and F. H. Marchesini. Flow of viscoplastic liquids through axisymmetric expansionscontractions. *Journal of Non-Newtonian Fluid Mechanics*, 142(1-3):207217, Mar 2007. 48, 56, 57, 94, 147, 160, 177, 270, 271

[80] E. J. Dean, R. Glowinski, and G. Guidoboni. On the numerical simulation of Bingham visco-plastic flow: Old and new results. *Journal of Non-Newtonian Fluid Mechanics*, 142(1-3):3662, Mar 2007. 33

[81] B. Deglo De Besses, A. Magnin, and P. Jay. Viscoplastic flow around a cylinder in an infinite medium. *Journal of Non-Newtonian Fluid Mechanics*, 115(1):2749, Oct 2003. 300

[82] Y. Dimakopoulos, M. Pavlidis, and J. Tsamopoulos. Steady bubble rise in herschelbulkley fluids and comparison of predictions via the augmented lagrangian method with those via the papanastasiou model. *Journal of Non-Newtonian Fluid Mechanics*, 200:3451, Oct 2013. 39, 40, 300

[83] Y. Dimakopoulos and J. Tsamopoulos. Transient displacement of a Newtonian fluid by air in straight or suddenly constricted tubes. *Phys. Fluids*, 15(7):1973, 2003. 207

[84] Y. Dimakopoulos and J. Tsamopoulos. Transient displacement of a viscoplastic material by air in straight and suddenly constricted tubes. *Journal of Non-Newtonian Fluid Mechanics*, 112(1):4375, May 2003. 207

[85] Y. Dimakopoulos and J. Tsamopoulos. On the gas-penetration in straight tubes completely filled with a viscoelastic fluid. *Journal of Non-Newtonian Fluid Mechanics*, 117(2-3):117139, Feb 2004. 207

[86] Y. Dimakopoulos and J. Tsamopoulos. Transient displacement of Newtonian and viscoplastic liquids by air in complex tubes. *Journal of Non-Newtonian Fluid Mechanics*, 142(1-3):162182, Mar 2007. 38, 207

[87] T. Divoux, C. Barentin, and S. Manneville. From stress-induced fluidization processes to herschel-bulkley behaviour in simple yield stress fluids. *Soft Matter*, 7(18):8409, 2011. 15

[88] G. Drazer and J. Koplik. Permeability of self-affine rough fractures. *Phys. Rev. E*, 62:8076–8085, 2000. 93

[89] P. Drazin. *Introduction to hydrodynamic stability.* Cambridge University Press, 2002. 206

[90] N. Dubash and I. Frigaard. Conditions for static bubbles in viscoplastic fluids. *Phys. Fluids*, 16(12):4319, 2004. 300

[91] N. Dubash and I. Frigaard. Propagation and stopping of air bubbles in carbopol solutions. *Journal of Non-Newtonian Fluid Mechanics*, 142(1-3):123134, Mar 2007. 26, 300

[92] G. Duvaut and J. L. Lions. Inequalities in mechanics and physics. *Grundlehren der mathematischen Wissenschaften*, 1976. 19, 25, 60, 99, 154

[93] K. Ellwood, G. Georgiou, T. Papanastasiou, and J. Wilkes. Laminar jets of Bingham-plastic liquids. *Journal of Rheology (1978-present)*, 34(6):787–812, 1990. 38

[94] D. Eskin, J. Ratulowski, K. Akbarzadeh, and S. Pan. Modelling asphaltene deposition in turbulent pipeline flows. *The Canadian Journal of Chemical Engineering*, 89(3):421441, Mar 2011. 54

[95] Y. Fan, N. Phan-Thien, and R. I. Tanner. Tangential flow and advective mixing of viscoplastic fluids between eccentric cylinders. *Journal of Fluid Mechanics*, 431:6589, Mar 2001. 38

[96] A. Filali, L. Khezzar, and E. Mitsoulis. Some experiences with the numerical simulation of Newtonian and Bingham fluids in dip coating. *Computers & Fluids*, 82:110121, Aug 2013. 39

[97] G. C. Florides, A. N. Alexandrou, and G. C. Georgiou. Flow development in compression of a finite amount of a Bingham plastic. *Journal of Non-Newtonian Fluid Mechanics*, 143(1):3847, Apr 2007. 38

[98] A. Fortin, D. Ct, and P. Tanguy. On the imposition of friction boundary conditions for the numerical simulation of Bingham fluid

flows. *Computer Methods in Applied Mechanics and Engineering*, 88(1):97109, Jun 1991. 39

[99] M. Fortin and R. Glowinski. *Augmented Lagrangian methods: applications to the numerical solution of boundary-value problems*. Elsevier, 1983. 19, 21, 24, 29, 30, 39, 60, 98, 154, 320

[100] I. Frigaard. Super-stable parallel flows of multiple visco-plastic fluids. *Journal of Non-Newtonian Fluid Mechanics*, 100(1-3):4975, Sep 2001. 299, 343

[101] I. Frigaard and C. Nouar. On the usage of viscosity regularisation methods for visco-plastic fluid flow computation. *Journal of Non-Newtonian Fluid Mechanics*, 127(1):126, Apr 2005. 35, 98, 154, 320

[102] I. Frigaard and D. Ryan. Flow of a visco-plastic fluid in a channel of slowly varying width. *Journal of Non-Newtonian Fluid Mechanics*, 123(1):6783, Oct 2004. 19, 22, 50, 55, 56, 58, 59, 62, 63, 64, 65, 66, 70, 93, 147, 157, 252, 265, 311, 312

[103] I. Frigaard, O. Scherzer, and G. Sona. Uniqueness and non-uniqueness in the steady displacement of two visco-plastic fluids. *Z. angew. Math. Mech.*, 81(2):99118, Feb 2001. 208, 242

[104] I. A. Frigaard, S. Leimgruber, and O. Scherzer. Variational methods and maximal residual wall layers. *Journal of Fluid Mechanics*, 483:3765, May 2003. 208, 272

[105] A. M. Gan-Calvo. Generation of steady liquid microthreads and micron-sized monodisperse sprays in gas streams. *Physical Review Letters*, 80(2):285288, Jan 1998. 298

[106] S. Ge. A governing equation for fluid flow in rough fractures. *Water Resour. Res.*, 33(1):53–61, 1997. 93, 106

[107] U. Ghia, K. Ghia, and C. Shin. High-re solutions for incompressible flow using the navier-stokes equations and a multigrid method. *Journal of Computational Physics*, 48(3):387411, Dec 1982. xx, 184, 185

[108] C. Gillham, P. Fryer, A. Hasting, and D. Wilson. Enhanced cleaning of whey protein soils using pulsed flows. *Journal of Food Engineering*, 46(3):199209, Nov 2000. 3

[109] R. Glowinski. On alternating direction methods of multipliers: A historical perspective. *Modeling, Simulation and Optimization for Science and Technology*, page 5982, 2014. 32, 34

[110] R. Glowinski and P. Le Tallec. *Augmented Lagrangian and operator-splitting methods in nonlinear mechanics*, volume 9. SIAM, 1989. 19, 21, 24, 29, 60, 98, 154

[111] R. Glowinski and J. Oden. *Numerical methods for nonlinear variational problems*, volume 52. Springer-Verlag, 1985. 19, 21, 24, 29, 60, 154, 320

[112] R. Glowinski and A. Wachs. On the numerical simulation of viscoplastic fluid flow. *Handbook of numerical analysis*, 16:483–717, 2011. 33, 37, 321

[113] T. R. Glowinski R, Lions Jacques Louis. *Numerical Analysis of Variational Inequalities*. North-Holland Pub. Co, 1981. 19, 20, 21, 24, 26, 29

[114] R. Gref, Y. Minamitake, M. Peracchia, V. Trubetskoy, V. Torchilin, and R. Langer. Biodegradable long-circulating polymeric nanospheres. *Science*, 263(5153):16001603, Mar 1994. 298

[115] K. J. Hammad, M. V. Otugen, G. C. Vradis, and E. B. Arik. Laminar flow of a nonlinear viscoplastic fluid through an axisymmetric sudden expansion. *J. Fluids Eng.*, 121(2):488, 1999. 48, 270

[116] E. Hasegawa and H. Izuchi. On steady flow through a channel consisting of an uneven wall and a plane wall: Part 1. case of no relative motion in two walls. *Bulletin of JSME*, 26(214):514520, 1983. 54

[117] F. Hecht. Bidimensional anisotropic mesh generator. Technical report, INRIA, 1997. 350

[118] F. Hecht. New development in freefem++. *Journal of Numerical Mathematics*, 20(3-4), Jan 2012. 99, 182

[119] C. Hirt and B. Nichols. Volume of fluid (vof) method for the dynamics of free boundaries. *Journal of Computational Physics*, 39(1):201225, Jan 1981. 212

[120] K. Hohenemser and W. Prager. ber die anstze der mechanik isotroper kontinua. *Z. angew. Math. Mech.*, 12(4):216226, 1932. 11

[121] Y. Holenberg, O. Lavrenteva, A. Liberzon, U. Shavit, and A. Nir. Ptv and piv study of the motion of viscous drops in yield stress material. *Journal of Non-Newtonian Fluid Mechanics*, 193:129143, Mar 2013. 300

[122] G. M. Homsy. Viscous fingering in porous media. *Annual Review of Fluid Mechanics*, 19(1):271311, Jan 1987. 3

[123] S. Hormozi, G. Dunbrack, and I. A. Frigaard. Visco-plastic sculpting. *Phys. Fluids*, 26(9):093101, Sep 2014. 299, 343

[124] S. Hormozi and I. Frigaard. Nonlinear stability of a visco-plastically lubricated viscoelastic fluid flow. *Journal of Non-Newtonian Fluid Mechanics*, 169-170:6173, Feb 2012. 299

[125] S. Hormozi, D. Martinez, and I. Frigaard. Stable core-annular flows of viscoelastic fluids using the visco-plastic lubrication technique. *Journal of Non-Newtonian Fluid Mechanics*, 166(23-24):13561368, Dec 2011. 348

[126] S. Hormozi, K. Wielage-Burchard, and I. Frigaard. Multi-layer channel flows with yield stress fluids. *Journal of Non-Newtonian Fluid Mechanics*, 166(5-6):262278, Mar 2011. 299, 343

[127] S. Hormozi, K. Wielage-Burchard, and I. A. Frigaard. Entry, start up and stability effects in visco-plastically lubricated pipe flows. *Journal of Fluid Mechanics*, 673:432467, Mar 2011. 299, 343

[128] P. D. Howell, S. L. Waters, and J. B. Grotberg. The propagation of a liquid bolus along a liquid-lined flexible tube. *J. Fluid Mech.*, 406:309335, Mar 2000. 3

[129] L. Huang, J. Norman, M. Pourkashanian, and A. Williams. Prediction of ash deposition on superheater tubes from pulverized coal combustion. *Fuel*, 75(3):271279, Feb 1996. 54

[130] C. Huen, I. Frigaard, and D. Martinez. Experimental studies of multi-layer flows using a visco-plastic lubricant. *Journal of Non-Newtonian Fluid Mechanics*, 142(1-3):150161, Mar 2007. 299, 343, 348

[131] R. Huilgol. A systematic procedure to determine the minimum pressure gradient required for the flow of viscoplastic fluids in pipes of symmetric cross-section. *Journal of Non-Newtonian Fluid Mechanics*, 136(2-3):140146, Jul 2006. 56

[132] R. Huilgol and M. Panizza. On the determination of the plug flow region in Bingham fluids through the application of variational inequalities. *Journal of Non-Newtonian Fluid Mechanics*, 58(2-3):207217, Jul 1995. 39

[133] R. R. Huilgol. *Fluid Mechanics of Viscoplasticity*. Springer Science, 2015. 22, 26

[134] P. Hurez, P. Tanguy, and F. Bertrand. A finite element analysis of die swell with pseudoplastic and viscoplastic fluids. *Computer Methods in Applied Mechanics and Engineering*, 86(1):87103, Mar 1991. 39

[135] IRSN. Pelicans object-oriented framework https://gforge.irsn.fr/gf/project/pelicans/, retrieved 2015-10-21. 216

[136] N. C. J. Tsamopoulos, Y. Dimakipoulos, G. Karapetsas, and M. Pavlidis. Steady bubble rise and deformation in newtonian and viscoplastic fluids and conditions for bubble entrapment. *Journal of Fluid Mechanics*, 601, Apr 2008. 38, 300

[137] A. Jaworek. Electrostatic micro- and nanoencapsulation and electroemulsification: A brief review. *Journal of Microencapsulation*, 25(7):443468, Oct 2008. 298

[138] P. Jay, A. Magnin, and J. M. Piau. Viscoplastic fluid flow through a sudden axisymmetric expansion. *AIChE J.*, 47(10):21552166, Oct 2001. 48, 270

[139] P. Jay, A. Magnin, and J. M. Piau. Numerical simulation of viscoplastic fluid flows through an axisymmetric contraction. *J. Fluids Eng.*, 124(3):700, 2002. 48, 270

[140] G. Karapetsas and J. Tsamopoulos. Transient squeeze flow of viscoplastic materials. *Journal of Non-Newtonian Fluid Mechanics*, 133(1):3556, Jan 2006. 38

[141] I. Karimfazli, I. A. Frigaard, and A. Wachs. A novel heat transfer switch using the yield stress. *Journal of Fluid Mechanics*, 783:526566, Oct 2015. 27

[142] L. King. Deepwater horizon modelling software showed bp cement conditions unstable, November 2010. 3

[143] Z. Kountouriotis, G. C. Georgiou, and E. Mitsoulis. Numerical study of the combined effects of inertia, slip, and compressibility in extrusion of yield stress fluids. *Rheol Acta*, 53(10-11):791804, Oct 2014. 38

[144] S. Laborie, C. Cabassud, L. Durand-Bourlier, and J. Lain. Characterisation of gasliquid two-phase flow inside capillaries. *Chemical Engineering Science*, 54(23):57235735, Dec 1999. 206

[145] O. M. Lavrenteva, Y. Holenberg, and A. Nir. Motion of viscous drops in tubes filled with yield stress fluid. *Chemical Engineering Science*, 64(22):47724786, Nov 2009. 300

[146] G. Lipscomb and M. Denn. Flow of Bingham fluids in complex geometries. *Journal of Non-Newtonian Fluid Mechanics*, 14:337346, Jan 1984. 14, 20, 93, 124, 311, 314

[147] J. R. Lister. Selective withdrawal from a viscous two-layer system. *Journal of Fluid Mechanics*, 198(-1):231, Jan 1989. 298

[148] B. T. Liu, S. J. Muller, and M. M. Denn. Convergence of a regularization method for creeping flow of a Bingham material about a rigid sphere. *Journal of Non-Newtonian Fluid Mechanics*, 102(2):179191, Feb 2002. 300

[149] B. T. Liu, S. J. Muller, and M. M. Denn. Interactions of two rigid spheres translating collinearly in creeping flow in a Bingham material. *Journal of Non-Newtonian Fluid Mechanics*, 113(1):4967, Jul 2003. 300, 301

[150] I. G. Loscertales. Micro/nano encapsulation via electrified coaxial liquid jets. *Science*, 295(5560):16951698, Mar 2002. 298

[151] H. M. *Engineering aspects of the rheology of thixotropic liquids*. PhD thesis, Faculty of Mechanical Engineering, Czech Technical University of Prague, Czech Republic, 1981. 14

[152] F. Mahaut, X. Chateau, P. Coussot, and G. Ovarlez. Yield stress and elastic modulus of suspensions of noncolloidal particles in yield stress fluids. *J. Rheol.*, 52(1):287, 2008. 301

[153] S. Malekmohammadi, M. Carrasco-Teja, S. Storey, I. A. Frigaard, and D. M. Martinez. An experimental study of laminar displacement flows in narrow vertical eccentric annuli. *Journal of Fluid Mechanics*, 649:371, Apr 2010. 208

[154] A. Malevich, V. Mityushev, and P. Adler. Stokes flow through a channel with wavy walls. *Acta mechanica*, 182(3-4):151–182, 2006. 93

[155] B. B. Mandelbrot, D. E. Passoja, and A. J. Paullay. Fractal character of fracture surfaces of metals. *Nature*, 308(5961):721722, Apr 1984. 98

[156] A. Matsoukas and E. Mitsoulis. Geometry effects in squeeze flow of Bingham plastics. *Journal of Non-Newtonian Fluid Mechanics*, 109(2-3):231240, Feb 2003. 38

[157] R. McLean, C. Manry, and W. Whitaker. Displacement mechanics in primary cementing. *Journal of Petroleum Technology*, 19(02):251260, Feb 1967. 146

[158] P. R. S. Mendes and E. S. Dutra. Viscosity function for yield-stress liquids. *Appl. Rheology*, 2004. 15

[159] O. Merkak, L. Jossic, and A. Magnin. Dynamics of particles suspended in a yield stress fluid flowing in a pipe. *AIChE J.*, 54(5):11291138, 2008. 349

[160] O. Merkak, L. Jossic, and A. Magnin. Migration and sedimentation of spherical particles in a yield stress fluid flowing in a horizontal cylindrical pipe. *AIChE J.*, 55(10):25152525, Oct 2009. 349

[161] E. Mitsoulis. Fountain flow revisited: The effect of various fluid mechanics parameters. *AIChE J.*, page NANA, 2009. 38

[162] E. Mitsoulis. Fountain flow of pseudoplastic and viscoplastic fluids. *Journal of Non-Newtonian Fluid Mechanics*, 165(1-2):4555, Jan 2010. 38

[163] E. Mitsoulis, S. S. Abdali, and N. C. Markatos. Flow simulation of herschel-bulkley fluids through extrusion dies. *The Canadian Journal of Chemical Engineering*, 71(1):147160, Feb 1993. 38

[164] E. Mitsoulis and R. Huilgol. Entry flows of Bingham plastics in expansions. *Journal of Non-Newtonian Fluid Mechanics*, 122(1-3):4554, Sep 2004. 38, 47, 57, 146, 160, 176, 300

[165] E. Mitsoulis and A. Matsoukas. Free surface effects in squeeze flow of Bingham plastics. *Journal of Non-Newtonian Fluid Mechanics*, 129(3):182187, Sep 2005. 38

[166] H. K. Moffatt. Viscous and resistive eddies near a sharp corner. *Journal of Fluid Mechanics*, 18(01):1, Jan 1964. 85, 86, 146, 194

[167] P. C. F. Møller, A. Fall, and D. Bonn. Origin of apparent viscosity in yield stress fluids below yielding. *Europhys. Lett.*, 87(3):38004, Aug 2009. 15, 348

[168] P. Mosolov and V. Miasnikov. Variational methods in the theory of the fluidity of a viscous-plastic medium. *Journal of Applied Mathematics and Mechanics*, 29(3):545577, Jan 1965. ii, xii, 19, 41, 42, 44, 56, 176, 264, 265

[169] P. Mosolov and V. Miasnikov. On stagnant flow regions of a viscous-plastic medium in pipes. *Journal of Applied Mathematics and Mechanics*, 30(4):841854, Jan 1966. ii, xii, 19, 41, 42, 45, 46, 111, 176, 257, 264, 265

[170] P. Mosolov and V. Miasnikov. On qualitative singularities of the flow of a viscoplastic medium in pipes. *Journal of Applied Mathematics and Mechanics*, 31(3):609613, Jan 1967. 111

[171] M. Moyers-Gonzalez and I. Frigaard. Numerical solution of duct flows of multiple visco-plastic fluids. *Journal of Non-Newtonian Fluid Mechanics*, 122(1-3):227241, Sep 2004. 37, 56, 299, 343

[172] M. Moyers-Gonzalez, I. Frigaard, and C. Nouar. Stable two-layer flows at all re; visco-plastic lubrication of shear-thinning and viscoelastic fluids. *Journal of Non-Newtonian Fluid Mechanics*, 165(23-24):15781587, Dec 2010. 299

[173] L. Muravleva, E. Muravleva, G. C. Georgiou, and E. Mitsoulis. Numerical simulations of cessation flows of a Bingham plastic with the augmented lagrangian method. *Journal of Non-Newtonian Fluid Mechanics*, 165(9-10):544550, May 2010. 39

[174] M. F. Naccache and R. S. Barbosa. Creeping flow of viscoplastic materials through a planar expansion followed by a contraction. *Mechanics Research Communications*, 34(5-6):423431, Jul 2007. 56, 57, 147, 160, 177

[175] B. Nassar, P. R. de Souza Mendes, and M. F. Naccache. Flow of elasto-viscoplastic liquids through an axisymmetric expansioncontraction. *Journal of Non-Newtonian Fluid Mechanics*, 166(7-8):386394, Apr 2011. 56, 57, 147, 177

[176] E. B. Nelson and D. Guillot. *Well cementing*. Schlumberger, Sugar Land, Tex, 2006. 2, 5, 6, 55, 92, 145, 146, 174

[177] R. Y. Nigo, Y. M. J. Chew, N. E. Houghton, W. R. Paterson, and D. I. Wilson. Experimental studies of freezing fouling of model food fat solutions using a novel spinning disc apparatus. *Energy Fuels*, 23(12):61316145, Dec 2009. 54

[178] T. Nishimura, S. Arakawa, S. Murakami, and Y. Kawamura. Oscillatory viscous flow in symmetric wavy-walled channels. *Chemical Engineering Science*, 44(10):21372148, Jan 1989. 54

[179] W. F. Noh and P. Woodward. Slic (simple line interface calculation). *Lecture Notes in Physics*, page 330340, 1976. 215

[180] C. Nouar, C. Desaubry, and H. Zenaidi. Numerical and experimental investigation of thermal convection for a thermodependent herschel-bulkley fluid in an annular duct with rotating inner cylinder. *European Journal of Mechanics - B/Fluids*, 17(6):875900, Nov 1998. 38

[181] E. J. O'Donovan and R. I. Tanner. Numerical study of the Bingham squeeze film problem. *Journal of Non-Newtonian Fluid Mechanics*, 15(1):75–83, 1984. 34, 38

[182] G. Ovarlez, F. Bertrand, P. Coussot, and X. Chateau. Shear-induced sedimentation in yield stress fluids. *Journal of Non-Newtonian Fluid Mechanics*, 177-178:1928, Jun 2012. 301

[183] G. Ovarlez, F. Bertrand, and S. Rodts. Local determination of the constitutive law of a dense suspension of noncolloidal particles through magnetic resonance imaging. *J. Rheol.*, 50(3):259, 2006. 301

[184] G. Ovarlez, S. Cohen-Addad, K. Krishan, J. Goyon, and P. Coussot. On the existence of a simple yield stress fluid behavior. *Journal of Non-Newtonian Fluid Mechanics*, 193:6879, Mar 2013. 15

[185] F. Oviedo-Tolentino, R. Romero-Mndez, A. Hernndez-Guerrero, and B. Girn-Palomares. Experimental study of fluid flow in the entrance of a sinusoidal channel. *International Journal of Heat and Fluid Flow*, 29(5):12331239, Oct 2008. 54

[186] T. C. Papanastasiou. Flows of materials with yield. *Journal of Rheology (1978-present)*, 31(5):385–404, 1987. 34, 38, 154, 320

[187] H. C. Park, M. C. Hawley, and R. F. Blanks. The flow of non-Newtonian solutions through packed beds. *Polymer Engineering and Science*, 15(11):761773, Nov 1975. 91, 92

[188] J. Pearson and P. Tardy. Models for flow of non-Newtonian and complex fluids through porous media. *Journal of Non-Newtonian Fluid Mechanics*, 102(2):447473, Feb 2002. 91

[189] S. Pelipenko and I. A. Frigaard. Visco-plastic fluid displacements in near-vertical narrow eccentric annuli: prediction of travelling-wave solutions and interfacial instability. *Journal of Fluid Mechanics*, 520:343377, Dec 2004. 93, 145, 208

[190] T. V. Pham and E. Mitsoulis. Entry and exit flows of casson fluids. *The Canadian Journal of Chemical Engineering*, 72(6):10801084, Dec 1994. 38

[191] C. Picioreanu, J. B. Xavier, and M. C. M. van Loosdrecht. Advances in mathematical modeling of biofilm structure. *Biofilms*, 1(4):337349, 1999. 3

[192] A. Potapov, R. Spivak, O. M. Lavrenteva, and A. Nir. Motion and deformation of drops in Bingham fluid. *Ind. Eng. Chem. Res.*, 45(21):69856995, Oct 2006. 300

[193] C. Pozrikidis. Creeping flow in two-dimensional channels. *Journal of Fluid Mechanics*, 180(-1):495, Jul 1987. 84, 85, 86

[194] C. Pozrikidis. A study of peristaltic flow. *Journal of Fluid Mechanics*, 180(-1):515, Jul 1987. 54

[195] W. Prager. Mcanique des solides isotropes au del du domaine lastique. *Mmorial des sciences mathmatiques*, 87, 1937. 11

[196] W. Prager. On slow viscoplastic flow. Technical report, Studies in mathematics and mechanics, 1954. 19, 22, 24, 59

[197] Proceedings of the Fourth International Symposium on Computational Fluid Dynamics. *A volume-of-fluid interface tracking algorithm with applications to computing shock wave refraction*, 1991. 215

[198] A. Putz and I. Frigaard. Creeping flow around particles in a Bingham fluid. *Journal of Non-Newtonian Fluid Mechanics*, 165(5-6):263280, Mar 2010. 114, 117, 300

[199] A. Putz, I. Frigaard, and D. Martinez. On the lubrication paradox and the use of regularisation methods for lubrication flows. *Journal of Non-Newtonian Fluid Mechanics*, 163(1-3):6277, Nov 2009. 22, 39, 40, 50, 55, 56, 58, 59, 61, 62, 63, 64, 65, 66, 93, 126, 147, 154, 155, 156, 157, 160, 265, 311, 312, 320, 321

[200] A. M. V. Putz, T. I. Burghelea, I. A. Frigaard, and D. M. Martinez. Settling of an isolated spherical particle in a yield stress shear thinning fluid. *Phys. Fluids*, 20(3):033102, 2008. 348

[201] G. C. D. R. B. Bird and B. J. Yarusso. The rheology and flow of viscoplastic materials. *Rev. Chem. Eng*, 1983. 18

[202] A. Ragouilliaux, G. Ovarlez, N. Shahidzadeh-Bonn, B. Herzhaft, T. Palermo, and P. Coussot. Transition from a simple yield-stress fluid to a thixotropic material. *Phys. Rev. E*, 76(5), Nov 2007. 14

[203] M. Rahmani and A. Wachs. Free falling and rising of spherical and angular particles. *Phys. Fluids*, 26(8):083301, Aug 2014. 184

[204] R. Rannacher and S. Turek. Simple nonconforming quadrilateral stokes element. *Numerical Methods for Partial Differential Equations*, 8(2):97111, Mar 1992. 220

[205] O. Reynolds. On the theory of lubrication and its application to Mr. Beauchamp Tower's experiments, including an experimental determination of the viscosity of olive oil. *Phil. Trans. R. Soc. Lond.*, 177:157–234, 1886. 93

[206] N. Roquet and P. Saramito. An adaptive finite element method for Bingham fluid flows around a cylinder. *Computer Methods in Applied Mechanics and Engineering*, 192(31-32):33173341, Aug 2003. 32, 33, 39, 61, 62, 154, 156, 300

[207] N. Roquet and P. Saramito. An adaptive finite element method for viscoplastic flows in a square pipe with stickslip at the wall. *Journal of Non-Newtonian Fluid Mechanics*, 155(3):101115, Dec 2008. 61, 154

[208] A. Roustaei and I. Frigaard. The occurrence of fouling layers in the flow of a yield stress fluid along a wavy-walled channel. *Journal of Non-Newtonian Fluid Mechanics*, 198:109124, Aug 2013. 94, 99, 107, 141, 147, 161, 165, 177, 195, 321

[209] A. Roustaei, A. Gosselin, and I. Frigaard. Residual drilling mud during conditioning of uneven boreholes in primary cementing. part 1: Rheology and geometry effects in non-inertial flows. *Journal of Non-Newtonian Fluid Mechanics*, 220:8798, Jun 2015. 94, 99, 107, 141, 174, 175, 177, 178, 180, 181, 182, 188, 193, 194, 198, 201, 202, 203, 299

[210] S. Roux and H. J. Herrmann. Disorder-induced nonlinear conductivity. *Europhys. Lett.*, 4(11):1227, 1987. 92

[211] P. G. Saffman and G. Taylor. The penetration of a fluid into a porous medium or hele-shaw cell containing a more viscous liquid. *Proceedings of the Royal Society A: Mathematical, Physical and Engineering Sciences*, 245(1242):312329, Jun 1958. 205

[212] M. Sahimi. *Flow and Transport in Porous Media and Fractured Rock*. VCH Verlagsgesellschaft, 1995. 92, 98

[213] P. Saramito. *Efficient C++ finite element computing with Rheolef*. CNRS-CCSD ed., 2015. http://cel.archives-ouvertes.fr/cel-00573970, retrieved 2015-10-14. xi, 32, 61, 156

[214] P. Saramito and N. Roquet. An adaptive finite element method for viscoplastic fluid flows in pipes. *Computer Methods in Applied Mechanics and Engineering*, 190(40-41):53915412, Jul 2001. 32, 39, 56, 61, 99, 154, 156, 182, 321

[215] J. Savins. Non-Newtonian flow through porous media. *Ind. Eng. Chem.*, 61(10):18–47, 1969. 91, 92

[216] J. Schmittbuhl, S. Gentier, and S. Roux. Field measurements of the roughness of fault surfaces. *Geophysical Research Letters*, 20(8):639641, Apr 1993. 98

[217] P. S. Scott. Finite-element simulation of laminar viscoplastic flows with regions of recirculation. *J. Rheol.*, 32(4):387, 1988. 37

[218] D. Sharp. An overview of Rayleigh-Taylor instability. *Physica D: Nonlinear Phenomena*, 12(1-3):318, Jul 1984. 205

[219] J. J. d. Silva, F. H. Neff, A. M. N. Lima, and J. S. d. Rocha Neto. Hammer impact test applied for fouling detection in pipelines. *Sba: Controle & Automao Sociedade Brasileira de Automatica*, 2011. 54

[220] J. P. Singh and M. M. Denn. Interacting two-dimensional bubbles and droplets in a yield-stress fluid. *Phys. Fluids*, 20(4):040901, 2008. 300

[221] D. Smyrnaios and J. Tsamopoulos. Squeeze flow of Bingham plastics. *Journal of Non-Newtonian Fluid Mechanics*, 100(1-3):165189, Sep 2001. 38

[222] E. J. Soares, M. S. Carvalho, and P. R. S. Mendes. Immiscible liquid-liquid displacement in capillary tubes. *J. Fluids Eng.*, 127(1):24, 2005. 207

[223] T. Sochi and M. J. Blunt. Pore-scale network modeling of Ellis and Herschel-Bulkley fluids. *J. Pet. Sci. Eng.*, 60(2):105 – 124, 2008. 92

[224] A. Syrakos, G. C. Georgiou, and A. N. Alexandrou. Performance of the finite volume method in solving regularised Bingham flows: Inertia effects in the lid-driven cavity flow. *Journal of Non-Newtonian Fluid Mechanics*, 208-209:88107, Jun 2014. xx, 184, 185

[225] P. Szabo and O. Hassager. Flow of viscoplastic fluids in eccentric annular geometries. *Journal of Non-Newtonian Fluid Mechanics*, 45(2):149169, Nov 1992. 21, 28, 29, 32, 146, 153, 160, 272

[226] L. Talon, H. Auradou, and A. Hansen. Permeability of self-affine aperture fields. *Phys. Rev. E*, 82(4), Oct 2010. 98

[227] L. Talon, H. Auradou, and A. Hansen. Effective rheology of Bingham fluids in a rough channel. *Front. Physics*, 2(24), 2014. 92, 93

[228] L. Talon, H. Auradou, M. Pessel, and A. Hansen. Geometry of optimal path hierarchies. *EPL (Europhysics Letters)*, 103(3):30003–, 2013. 92

[229] L. Talon and D. Bauer. On the determination of a generalized Darcy equation for yield-stress fluid in porous media using a lattice-Boltzmann TRT scheme. *Eur. Phys. J. E*, 36(12):1–10, 2013. 92

[230] A. J. Taylor. Conduit flow of an incompressible, yield-stress fluid. *J. Rheol.*, 41(1):93, Jan 1997. 38

[231] G. I. Taylor. Deposition of a viscous fluid on the wall of a tube. *Journal of Fluid Mechanics*, 10(02):161, Mar 1961. 207

[232] C. J. P. Timm Treskatis, Miguel A. Moyers-Gonzalez. An accelerated dual gradient method and applications in viscoplasticity. *arXiv:1509.05084 [math.NA]*, 2015. 24, 33, 271

[233] D. L. Tokpavi, A. Magnin, and P. Jay. Very slow flow of Bingham viscoplastic fluid around a circular cylinder. *Journal of Non-Newtonian Fluid Mechanics*, 154(1):6576, Sep 2008. 300

[234] J. A. Tsamopoulos, M. E. Chen, and A. V. Borkar. On the spin coating of viscoplastic fluids. *Rheola Acta*, 35(6):597615, 1996. 38

[235] K. Vajravelu, S. Sreenadh, and V. Ramesh Babu. Peristaltic pumping of a herschelbulkley fluid in a channel. *Applied Mathematics and Computation*, 169(1):726735, Oct 2005. 57

[236] R. Van Houdt and C. Michiels. Biofilm formation and the food industry, a focus on the bacterial outer surface. *Journal of Applied Microbiology*, 109(4):11171131, Aug 2010. 55

[237] T. Van Pham and E. Mitsoulis. Viscoplastic flows in ducts. *The Canadian Journal of Chemical Engineering*, 76(1):120125, Feb 1998. 38

[238] G. Vinay, A. Wachs, and J.-F. Agassant. Numerical simulation of non-isothermal viscoplastic waxy crude oil flows. *Journal of Non-Newtonian Fluid Mechanics*, 128(2-3):144162, Jul 2005. 39

[239] G. Vinay, A. Wachs, and J.-F. Agassant. Numerical simulation of weakly compressible Bingham flows: The restart of pipeline flows of waxy crude oils. *Journal of Non-Newtonian Fluid Mechanics*, 136(2-3):93105, Jul 2006. 39

[240] D. Vola, F. Babik, and J.-C. Latch. On a numerical strategy to compute gravity currents of non-Newtonian fluids. *Journal of Computational Physics*, 201(2):397420, Dec 2004. 39

[241] D. Vola, L. Boscardin, and J. Latch. Laminar unsteady flows of Bingham fluids: a numerical strategy and some benchmark results. *Journal of Computational Physics*, 187(2):441456, May 2003. xx, 184, 185

[242] H. von Koch. Koch snowflake curve, http://en.wikipedia.org/wiki/Koch_snowflake. retrieved 2015-12-14. 152

[243] G. C. Vradis and M. V. Otugen. The axisymmetric sudden expansion flow of a non-Newtonian viscoplastic fluid. *J. Fluids Eng.*, 119(1):193, 1997. 48

[244] T.-S. Vu, G. Ovarlez, and X. Chateau. Macroscopic behavior of bidisperse suspensions of noncolloidal particles in yield stress fluids. *J. Rheol.*, 54(4):815, 2010. 301

[245] A. Wachs. Numerical simulation of steady Bingham flow through an eccentric annular cross-section by distributed lagrange multiplier/fictitious domain and augmented lagrangian methods. *Journal of Non-Newtonian Fluid Mechanics*, 142(1-3):183198, Mar 2007. 39

[246] I. C. Walton and S. H. Bittleston. The axial flow of a Bingham plastic in a narrow eccentric annulus. *Journal of Fluid Mechanics*, 222(-1):39, Jan 1991. 19, 21, 37, 39, 93, 124, 146, 160, 176, 311, 312

[247] Y. Wang. Finite element analysis of the duct flow of Bingham plastic fluids: an application of the variational inequality. *Int. J. Numer. Meth. Fluids*, 25(9):10251042, Nov 1997. 38, 98

[248] J. Warren and W. Boettinger. Prediction of dendritic growth and microsegregation patterns in a binary alloy using the phase-field method. *Acta Metallurgica et Materialia*, 43(2):689703, Feb 1995. 212

[249] K. Wielage-Burchard and I. Frigaard. Static wall layers in plane channel displacement flows. *Journal of Non-Newtonian Fluid Mechanics*, 166(5-6):245261, Mar 2011. 209, 218

[250] Wikipedia. en.wikipedia.org/wiki/Deepwater_Horizon_explosion. retrieved 2015-12-05. 3

[251] Wikipedia. https://en.wikipedia.org/wiki/Edwin_Drake. retrieved 2015-12-05. 2

[252] Wikipeida. https://en.wikipedia.org/wiki/Hydraulic_fracturing. retrieved 2015-12-05. 10

[253] S. Wilson. Squeezing flow of a Bingham material. *Journal of Non-Newtonian Fluid Mechanics*, 47:211219, Jun 1993. 38

[254] M. Windbergs, Y. Zhao, J. Heyman, and D. A. Weitz. Biodegradable coreshell carriers for simultaneous encapsulation of synergistic actives. *Journal of the American Chemical Society*, 135(21):79337937, May 2013. 298

[255] D. L. Youngs. Time-dependent multi-material flow with large fluid distortion. *Numerical methods for fluid dynamics*, 24:273–285, 1982. 215

[256] Z. Yu and A. Wachs. A fictitious domain method for dynamic simulation of particle sedimentation in Bingham fluids. *Journal of Non-Newtonian Fluid Mechanics*, 145(2-3):7891, Sep 2007. 39, 271, 353

[257] Y. Zhao, H. C. Shum, L. L. A. Adams, B. Sun, C. Holtze, Z. Gu, and D. A. Weitz. Enhanced encapsulation of actives in self-sealing microcapsules by precipitation in capsule shells. *Langmuir*, 27(23):1398813991, Dec 2011. 298

[258] R. Zimmerman, S. Kumar, and G. Bodvarsson. Lubrication theory analysis of the permeability of rough-walled fractures. *International Journal of Rock Mechanics and Mining Sciences & Geomechanics Abstracts*, 28(4):325331, Jul 1991. 54, 106

[259] T. Zisis and E. Mitsoulis. Viscoplastic flow around a cylinder kept between parallel plates. *Journal of Non-Newtonian Fluid Mechanics*, 105(1):120, Jul 2002. 38

[260] N. Zuidam and V. Nedovic. *Encapsulation Technologies for Active Food Ingredients and Food Processing*. Springer Science, 2010. 298

Appendix A

Macro-size drop encapsulation

The topic here does not fall within the general framework of the thesis, but does include study yield stress fluids in a slightly different setting and does have an overlap in terms of techniques used. Equally, I was not the principal contributor to the study. This work is thus included as an appendix.[1]

A.1 Introduction

Fluid encapsulation is the process of entrapping one substance within another. Typical functions of encapsulation are to isolate an aggressive component from the environment and/or deliver one component it to a particular receptor [150]. This could be beneficial in processes involving transportation, coating, site-specific drug delivery, medical imaging as well as food, cosmetic and pharmaceutical product manufacturing [12, 63, 114, 260]. Various techniques of encapsulation are proposed in the literature, e.g. [63, 105, 137, 147, 150, 254, 257], but it is not our intention to review these here. A common feature of many current techniques is that they are limited to droplet sizes governed by capillary forces, i.e. short length scales. Instead here we propose

[1] A version of this chapter has appeared as: A. Maleki, S. Hormozi, A. Roustaei & I. Frigaard. "Macro-size drop encapsulation." *J. Fluid Mech.*, **769**:482–521, (2015).

a method of encapsulation focused at macro-scale droplets, independent of capillary forces.

Yield stress (visco-plastic) fluids have the property that they do not deform unless a given yield stress ($\hat{\tau}_Y$) is exceeded. If the deviatoric stress is below the yield stress, the fluid acts like a rigid solid, resisting deformation. While in some flows this leads to unwanted features, e.g. [209], in other cases yield stress behaviour can be exploited in order to produce novel and beneficial flow features. One example of such flows, that we generalize here, is termed Visco-Plastically Lubricated (VPL) flows, in which a yield stress fluid is used to stabilize the interface in a multi-layer flow; see [100, 124–127, 130, 171]. The main focus is pressure driven duct flows in which a visco-plastic fluid adjacent to the wall lubricates a centrally positioned viscous fluid. By controlling the relative flow rate of the two fluids we can ensure that the yield stress is larger than the interfacial shear stress by a finite amount. This results in a finite unyielded region around the central fluid, preserving stability. Both linear and nonlinear stability results have been established, for Newtonian and non-Newtonian core fluids; see [100, 124, 126, 171, 172]. Experimental studies have used viscous, shear-thinning and viscoelastic core fluids; see [127, 130].

The idea of encapsulation stems from these studies. We have looked to extend the VPL concept in different ways. For example, recently in [123] we have introduced periodic perturbations to the flow rates of initially stable VPL flows, resulting in stable patterned interfaces. In [126] we have experimented numerically with different injection novel configurations in order to advect encapsulated 'letters' and 'write' in the flow. In this chapter we expand this idea by considering the encapsulation of a regularly-spaced stream of droplets evenly spaced within the plug region of a yield stress fluid flowing along a uniform duct. The main focus is to determine the size of droplets that can be encapsulated in this way, without yielding the encapsulating plug, for both plane channel and pipe configurations. Of course if instead of droplets, neutrally buoyant solid particles are transported, the particles are indistinguishable from the plug and exert no stress. On the other hand, transported droplets perturb the stress field in the encapsulating plug, ulti-

mately breaking the plug for large droplets.

In the absence of fluid motions there are many studies of settling (or rise) in stationary yield stress fluid whereby the yield stress holds a particle (droplet or bubble) stationary until a certain critical buoyancy stress is exceeded. Thus, particles and bubbles below a certain size are held in suspension. Critical yield numbers are known for many symmetric particle geometries, e.g. spheres, cylinders, ellipsoids, and can be computed with care; see [31, 198, 206, 233]. There are similar studies that address the onset of bubble propagation; see [82, 90, 91, 136]. In both cases the yield stress fluid yields locally to the particle (bubble) and in the Stokes regime propagates slowly with yielded fluid being displaced from in front of the particle (bubble) to behind. There are many interesting studies focusing at moving particles and droplets, determining drag coefficients etc., e.g. [26, 31, 34, 81, 148, 164, 233].

In so far as viscous droplets are concerned, there are fewer studies. For example, [192] computed the motion and deformation of a single droplet in a Bingham fluid under gravity. They reported approaching a quasi-steady state after a relatively large transient period. The transient period and velocity magnitude depend strongly on the Bingham number. They also observed stationary flows for sufficiently large Bingham numbers. [121] experimentally studied the fall of a Newtonian drop inside an otherwise stagnant Bingham fluid. Using a combined PTV and PIV technique, they determined the approximate position of plug interface as well as the effects of the wall on the sedimentation velocity.

Interaction of multiple droplets or bubbles in a viscoplastic media has also recently received attention [121, 145, 149, 192, 220]. In particular, [149] reported that traveling particles in a viscoplastic media exhibit negligible interaction unless they are in close proximity (less that four sphere radii). [192] examined the interaction of two drops falling under gravity in a Bingham fluid. For the case of two similar drops, they showed that within the proximity range defined in [149], the drops tend to approach to each other and coalesce. More interestingly, [220] found in their simulations that in certain arrangements, a group of bubbles can rise under conditions where a

single bubble is unable to move. In the context of our study, the proximity distance of [149] is relevant in that we also will determine a droplet spacing above which the droplets do not influence one another. However, note that our droplets do not yield the fluid encapsulating fluid, so the connection with the above studies is via locality of the stress field rather than the velocity field.

Finally, moving to large numbers of particles, bubbles or droplets we enter the realm of yield stress suspensions, foams and emulsions. Recent work has addressed the question of estimating the bulk yield stress of a yield stress suspension, according to the fraction of the dispersed phase. Theoretical developments in [54] agree reasonably well with the experimental results of [152, 183]; see also [72, 182, 183, 244]. Of course, in dealing with suspensions the dispersed phase length-scale is much smaller than that of the bulk flow, unlike here where the droplets are of the flow dimension and we focus on a continuous stream.

An overview of the chapter is as follows. In §A.2 we present the problem of study and derive the governing equations in dimensionless form. For simplicity we start with the plane channel geometry. Section A.3 considers slender droplets, showing that the yield surface is barely perturbed by the presence of the droplets. In §A.4 we compute the flow around an iso-dense droplet, determining the mechanisms of yielding as droplets grow too large for the encapsulation, and finding the maximal droplet size. Section A.5 explores the effects of a density difference on the encapsulation process. In §A.6 we generalize the foregoing results for plane channel encapsulation to the more practical pipe geometry. The chapter closes with a summary and discussion in §A.7.

A.2 Physical problem

We consider the flow of an infinite train of regularly spaced two-dimensional droplets downwards along an infinite vertical plane channel of width $2\hat{R}$. The droplets are considered to be Newtonian and are encapsulated within a visco-plastic carrier fluid, which for simplicity we model as a Bingham

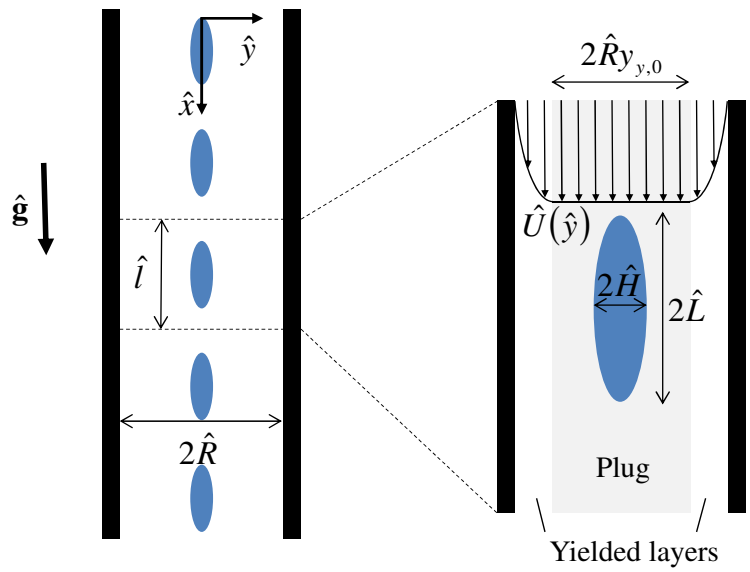

Figure A.1: Geometry of the encapsulated droplet train

fluid. Both fluids are incompressible and the areal flow is $2\hat{R}\hat{U}_0$, i.e. the mean velocity along the channel is $\hat{U}_0$. The droplets are spaced a distance $\hat{l}$ apart, each centred at $\hat{x} = k\hat{l} + \hat{U}_p\hat{t} : \ k \in \mathbb{Z}$ and have boundaries (interfaces) described by:

$$\hat{y} = \pm\hat{h}(\hat{x} - k\hat{l} - \hat{U}_p\hat{t}), \tag{A.1}$$

where $\hat{h}(0) = \hat{H}$. The length of the droplets is $2\hat{L}$ and we denote the aspect ratio of the droplet by $\delta = \hat{H}/\hat{L}$. The physical setup is shown schematically in Fig. A.1. In this chapter we adopt the convention of denoting all dimensional variables with a "hat", i.e. $\hat{\cdot}$, and all dimensionless variables without.

In the absence of the droplets the velocity of the carrier fluid adopts a uniform symmetric Poiseuille profile, which in the case of a Bingham fluid contains an unyielded "plug" region in the channel centre, of width $2y_{y,0}\hat{R}$ that translates with speed $\hat{U}_p$; see §A.2.1 later. Our objective in this chapter is to understand when this plug region may encapsulate a fluid droplet without the plug yielding. In other words, we consider the situation

in which the droplet is "frozen" into the plug, and consequently the interface between the droplet and carrier fluid does not deform. Where we refer to encapsulation we specifically mean that the droplet is held in an unyielded plug region. Much of the chapter concerns the study of when this situation may hold for a given droplet size and shape: a rudimentary analysis is given below in §A.2.3.

We shall consider flows that are periodic in $\hat{x}$ and symmetric with respect to the channel centreline $\hat{y} = 0$. We scale all lengths with $\hat{R}$, velocities with $\hat{U}_0$ and deviatoric stresses with $\hat{\mu}\hat{U}_0/\hat{R}$, where $\hat{\mu}$ is the plastic viscosity of the carrier fluid. The pressure is scaled as follows:

$$\hat{p} = \hat{p}_0 + \hat{\rho}\hat{g}\hat{x} + \frac{\hat{\mu}\hat{U}_0}{\hat{R}}p \tag{A.2}$$

i.e. p is the dimensionless modified pressure, subtracting off the static pressure $\hat{\rho}\hat{g}\hat{x}$ and a possibly time dependent pressure $\hat{p}_0(\hat{t})$.

It is assumed that the distance between droplets $\hat{l}$ is large enough for the carrier fluid to assume its undisturbed uniform Poiseuille profile between droplets, in which the plug moves with speed $\hat{U}_p$. We explore effects of varying $\hat{l}$ later. To fully exploit the symmetry of the problem, we translate to a moving frame as follows:

$$(x, y) = \left(\frac{\hat{x} - \hat{U}_p\hat{t}}{\hat{R}}, \frac{\hat{y}}{\hat{R}}\right) \tag{A.3a}$$

$$t = \frac{\hat{U}_p\hat{t}}{\hat{R}} \tag{A.3b}$$

$$(u, v) = \left(\frac{\hat{u} - \hat{U}_p}{\hat{U}_0}, \frac{\hat{v}}{\hat{U}_0}\right) \tag{A.3c}$$

In the moving frame, we consider the flow to be steady and due to periodicity consider only the domain: $(x, y) \in [-l/2, l/2] \times [-1, 1]$, where $l = \hat{l}/\hat{R}$. The droplet-encapsulating fluid interface is given by: $y = \pm h(x)$ with $h(0) = H = \hat{H}/\hat{R}$ and where $h(x) = 0$ for $|x| \geq L = H/\delta = \hat{L}/\hat{R}$. The scaled

equations of motion in the carrier fluid are:

$$0 = \frac{\partial u}{\partial x} + \frac{\partial v}{\partial y}, \tag{A.4a}$$

$$Re\left(u\frac{\partial u}{\partial x} + v\frac{\partial u}{\partial y}\right) = -\frac{\partial p}{\partial x} + \frac{\partial \tau_{xx}}{\partial x} + \frac{\partial \tau_{xy}}{\partial y}, \tag{A.4b}$$

$$Re\left(u\frac{\partial v}{\partial x} + v\frac{\partial v}{\partial y}\right) = -\frac{\partial p}{\partial y} + \frac{\partial \tau_{xy}}{\partial x} + \frac{\partial \tau_{yy}}{\partial y}, \tag{A.4c}$$

where the constitutive relations are:

$$\tau_{ij} = \left(1 + \frac{B}{\dot{\gamma}}\right)\dot{\gamma}_{ij} \Longleftrightarrow \tau > B, \tag{A.5a}$$

$$\dot{\gamma} = 0 \Longleftrightarrow \tau \leq B. \tag{A.5b}$$

Here $\dot{\gamma} = \sqrt{\dot{\gamma}_{xy}^2 + \dot{\gamma}_{xx}^2}$, is the rate of strain, $\tau = \sqrt{\tau_{xy}^2 + \tau_{xx}^2}$, is the deviatoric stress, and

$$\dot{\gamma}_{xy} = \dot{\gamma}_{yx} = \frac{\partial u}{\partial y} + \frac{\partial v}{\partial x} \tag{A.6a}$$

$$\dot{\gamma}_{xx} = -\dot{\gamma}_{yy} = 2\frac{\partial u}{\partial x} = -2\frac{\partial v}{\partial y} \tag{A.6b}$$

Two dimensionless groups are defined above: $Re = \hat{\rho}\hat{U}_0\hat{R}/\hat{\mu}$, is the Reynolds number and $B = \hat{\tau}_Y\hat{R}/\hat{\mu}\hat{U}_0$, is the Bingham number. The latter denotes the ratio of yield stress to viscous stress in the flow.

At the walls of the channel no-slip conditions are satisfied and at $x = \pm l/2$ the flow is fully developed and adopts the Poiseuille profile:

$$u(x, \pm 1) = -u_{p,0}, \qquad v(x, \pm 1) = 0, \tag{A.7a}$$

$$u(\pm l/2, y) = U_P(y) - u_{p,0}, \qquad v(\pm l/2, y) = 0, \tag{A.7b}$$

Here $U_P(y)$ denotes the fully developed plane Poiseuille profile, which has dimensionless plug speed $u_{p,0}$; see §A.2.1. Note that by virtue of the scaling,

in the translating coordinates the dimensionless velocity satisfies at each x:

$$\int_{-1}^{1} u(x,y)\ dy = 2(1 - u_{p,0}). \tag{A.8}$$

Within the droplet the scaled equations of motion are:

$$0 = \frac{\partial u}{\partial x} + \frac{\partial v}{\partial y} \tag{A.9a}$$

$$\phi Re \left(u\frac{\partial u}{\partial x} + v\frac{\partial u}{\partial y} \right) = -\frac{\partial p}{\partial x} + m\frac{\partial^2 u}{\partial x^2} + m\frac{\partial^2 u}{\partial y^2} + \chi \tag{A.9b}$$

$$\phi Re \left(u\frac{\partial v}{\partial x} + v\frac{\partial v}{\partial y} \right) = -\frac{\partial p}{\partial y} + m\frac{\partial^2 v}{\partial x^2} + m\frac{\partial^2 v}{\partial y^2} \tag{A.9c}$$

Here $\phi = \hat{\rho}_d/\hat{\rho}$ is the density ratio ($\hat{\rho}_d$ is the density of the droplet), $m = \hat{\mu}_d/\hat{\mu}$ is a viscosity ratio ($\hat{\mu}_d$ is the viscosity of the droplet), and χ is a dimensionless group:

$$\chi = \frac{(\hat{\rho}_d - \hat{\rho})\hat{g}\hat{R}^2}{\hat{\mu}\hat{U}_0}. \tag{A.10}$$

Clearly χ represents the ratio of buoyant stresses to viscous stresses; χ can be thought of as the inverse of a Stokes number.

At the interface between droplet and carrier fluid the velocity and the traction are continuous:

$$[\![\tau_{nt}]\!] = 0, \qquad \text{at} \quad y = \pm h(x), \tag{A.11a}$$

$$[\![-p + \tau_{nn}]\!] = 0, \qquad \text{at} \quad y = \pm h(x). \tag{A.11b}$$

Here the subscripts n and t on the deviatoric stress components refer to directions resolved normal and tangential to the interface. Note that we neglect capillary forces in the formulation above, as the aim is to study encapsulation via yield stress effects on a macro-scale. In §A.7 we discuss capillary effects and their comparison to the yield stress.

A.2.1 The plane Poiseuille solution $U_P(y)$

The plane Poiseuille flow solution for a Bingham fluid is straightforwardly resolved. In the fixed frame of reference the velocity is given by:

$$U_P(y) = \begin{cases} u_{p,0} & \text{if} \quad |y| \leq y_{y,0}, \\ u_{p,0}\left[1 - \dfrac{(|y| - y_{y,0})^2}{(1 - y_{y,0})^2}\right] & \text{if} \quad |y| > y_{y,0}, \end{cases} \tag{A.12}$$

The plug velocity is given by:

$$u_{p,0} = \frac{B}{2y_{y,0}}(1 - y_{y,0})^2, \tag{A.13}$$

i.e. $\hat{U}_P = \hat{U}_0 u_{p,0}$. The position of the yield surface is found from the requirement that the mean velocity is unity (recall here we have scaled with $\hat{U}_0$). This leads to the following cubic Buckingham equation:

$$y_{y,0}^3 - (3 + \frac{6}{B})y_{y,0} + 2 = 0. \tag{A.14}$$

It is not hard to show that this equation has a single root $y_{y,0}(B) \in (0, 1)$, easily computed numerically. We find that $y_{y,0}(B)$ increases monotonically and exhibits the following asymptotic behaviour:

$$y_{y,0} \sim \frac{B}{3} - \frac{B^2}{6} \quad \text{as} \quad B \to 0; \qquad y_{y,0} \sim 1 - \frac{\sqrt{2}}{B^{1/2}} + O(B^{-1}) \quad \text{as} \quad B \to \infty \tag{A.15}$$

The dimensionless yield surface position $y_{y,0}$ is sometimes called the Oldroyd number and can be used in place of B as a dimensionless group describing the base flow.

A.2.2 Inertial effects and the droplet flow

As discussed previously, the aim of the our study is to understand situations under which there may exist a droplet fully encapsulated in the unyielded plug of the encapsulating fluid. What we consider below neglects inertial effects. We now examine this assumption.

Firstly with respect to the droplet flow, for any droplet that is fully encapsulated within the plug the velocity at the interface satifies $(u, v) = 0$, as we have subtracted off the plug velocity. If we consider these conditions as the boundary conditions for the droplet domain the droplet flow problem effectively decouples from that of the carrier fluid. Using these conditions, the droplet flow has the (unique) Stokes flow solution $(u, v) = 0$, everywhere within the droplet, with

$$p = \chi x + \text{constant}. \tag{A.16}$$

The trivial solution also solves the steady inertial problem. Assuming that the plug remains unyielded we may even consider time dependent solutions for the droplet. As there is no driving force for the flow within the droplet, an energy stability analysis would show that any transients in the droplet decay to zero like $\sim \exp^{-(\phi Re/m)t}$, which is the usual viscous decay timescale of the droplet. There is no bound needed on the size of the initial condition from the perspective of the decay bound. However, transients within the droplet would induce stresses within the plug and hence the *a priori* assumption of an unyielded plug could fail for sufficiently large initial conditions. Nevertheless, it is apparent that the trivial solution is likely to be stable for a reasonable range of $Re > 0$ and we therefore consider this to represent the droplet solution.

Since the fluid in the droplet is Newtonian, the trivial solution $(u, v) = 0$, implies vanishing of the shear stresses within the droplet. Equation (A.11) therefore simplifies to the following stress conditions to be satisfied by the Bingham fluid at the interface:

$$\tau_{nt} = 0, \qquad \text{at} \quad y = \pm h(x), \tag{A.17a}$$

$$-p + \tau_{nn} = -\chi x + \text{constant}, \qquad \text{at} \quad y = \pm h(x). \tag{A.17b}$$

Assuming symmetry and locating the droplet at the origin, we may consider the constant on the right-hand side of (A.17b) to be zero.

For the carrier fluid in the absence of the droplet, the Poiseuille flow

solution is valid up to large Re, when the flow destabilizes due to turbulent transition. Departures from this solution in the droplet flow solution are likely to be associated with perturbation of the streamlines in the vicinity of the droplet. Conditions (A.17) are satisfied at the interface, which results in a perturbation of the stress field within the plug. This in turn may perturb the yield surface from its uniform value $y_{y,0}$ and the perturbed yield surface may then induce a velocity perturbation from the Poiseuille flow solution. If we suppose that the aspect ratio of the streamline perturbation is characterised by a parameter ε then the inertial terms in the x-momentum equation have size εRe and those in the y-momentum equation have size $\varepsilon^3 Re$. We may consider the inertial terms to be small if $\varepsilon Re \ll 1$, which we show later to be the case.

A.2.3 Why large droplets yield the plug

It might at first appear that the plug may sustain any droplet of size $h(x) < y_{y,0}$, since the rigid motion of the uniform plug around the droplet allows the droplet to translate at uniform speed along the channel. However, this reasoning neglects the effects of the droplet on the stress field. We consider 2 simple examples that suggest how the stresses may act to break the plug region for sufficiently large droplets.

First let us consider an iso-dense droplet ($\chi = 0$; see later in §A.5 for $\chi \neq 0$). We have seen that the undisturbed flow (no droplets) is the Poiseuille flow of §A.2.1 above, in which the frictional pressure gradient satisfies:

$$\frac{\partial p}{\partial x} = -\frac{B}{y_{y,0}}, \tag{A.18}$$

Now let us introduce a droplet within the plug region, at $x = 0$ in the translating frame. If the droplet translates uniformly, the shear stresses in the droplet are zero and the pressure in the droplet is simply $p =$ constant, (chosen to be zero). In contrast, within the yielded layer of the carrier fluid we have $p = -Bx/y_{y,0}$, varying by $\sim 2BL/y_{y,0}$ along the length of the droplet.

The stresses within the unyielded plug are indeterminate in a yield stress

fluid. Stress continuity implies that the tangential stress must vanish at the interface, whereas the total normal stress must balance the constant droplet pressure. We see that the pressure imbalance between the droplet and the yielded layer of the encapsulating fluid is of size $\sim BL/y_{y,0}$, which must somehow be absorbed by the deviatoric stresses within the plug region. Consequently, a simple order of magnitude estimate for the length of droplet that can be sustained by a visco-plastic fluid is simply:

$$y_{y,0} \gtrsim L. \tag{A.19}$$

Putting this into dimensional terms we have:

$$\frac{\hat{\tau}_Y}{\hat{G}\hat{R}} \gtrsim \frac{\hat{L}}{\hat{R}}, \quad \Rightarrow \quad \frac{\hat{\tau}_Y}{\hat{G}} \gtrsim \hat{L}, \tag{A.20}$$

where $\hat{G}$ is the frictional pressure gradient of the uniform Poiseuille flow. Since $y_{y,0} < 1$ we see that (A.19) is fundamentally a restriction on droplet area (equivalently volume in three dimensions), i.e. we expect that $LH < y_{y,0}$.

A second example considers the tangential stress distribution. Consider a droplet with slowly varying height ($\left|\frac{\partial h}{\partial x}\right| \ll 1$), encapsulated inside the plug region. Inside the plug the stress distribution is undetermined, but has to satisfy the momentum equations in (A.4). Assuming the yield surface is approximately $y_{y,0}$, we might linearly approximate:

$$\tau_{xy} \approx -B\frac{y-h}{y_{y,0}-h}, \tag{A.21}$$

i.e. satisfying the stress conditions at the droplet and yield surface. Ignoring the x-variation of h, from (A.4b) we find that $p-\tau_{xx} = -Bx/(y_{y,0}-h)$ within the plug. Outside the plug we have $p = -Bx/y_{y,0}$, and imposing continuity of normal stress across the yield surface:

$$-Bx/y_{y,0} = p - \tau_{yy} = p + \tau_{xx}, \quad \Rightarrow \quad \tau_{xx} = \frac{Bx}{2}\frac{h}{y_{y,0}(y_{y,0}-h)}. \tag{A.22}$$

Now observe that for fixed x, as $y_{y,0} - h \to 0$, $|\tau_{xx}| \to \infty$, i.e. suggesting that droplet widths may not approach arbitrarily close to the plug width.

Finally if we assume the distributions (A.21) and (A.22), on combining with the yield criterion ($\tau = B$) we predict that the plug yields along $y = \pm y_y(x)$:

$$\frac{y_y(x) - h}{y_{y,0} - h} \approx \sqrt{1 - \frac{x^2}{4}\left(\frac{1}{y_{y,0} - h} - \frac{1}{y_{y,0}}\right)^2} \tag{A.23}$$

Thus, also x is limited in such a stress distribution, i.e. $|L| < 2y_{y,0}(y_{y,0} - h)/h$, in order for the plug to remain unyielded around the droplet, or $LH < 2y_{y,0}(y_{y,0} - h)$.

The above 2 simple examples represent extremes of behaviour, indicating simply that we may expect limits on the size of encapsulated droplets. In practice the stress distributions within the unyielded plug can be any that satisfy the Stokes equations and boundary conditions.

A.3 Small-slender droplets: $h(x) \sim \delta \ll 1$

A common class of flows for which it is possible to construct analytical solutions is that in which the streamlines are nearly one-dimensional. In the problem considered, non-uniformity only arises from the droplet shape and hence we look at droplets of small aspect ratio ($H/L = \delta \ll 1$). However, the analysis above leading to (A.19) suggests that (isodense) droplets can not be encapsulated if L is larger than $y_{y,0}$. Combined with the requirement of $\delta \ll 1$ implies that $H \sim \delta \ll 1$, i.e. we consider small-slender droplets.

Assuming $h(x) \sim O(\delta)$, we develop an asymptotic approximation to the flow in the case that $\delta \ll 1$. Evidently we expect that the axial velocity will have similar size to that of the droplet free flow and the appropriate scale for y remains the channel half-width. On the other hand, since the shear stress is zero at $y = h(x)$, this suggests an $O(\delta)$ perturbation of the stress field, which may induce velocities $v \sim \delta$. In order to balance the mass conservation equation, a rescaling of x is needed. Therefore, we consider the

following rescaling:

$$x\delta = X, \quad y = Y, \quad u = U, \quad v = \delta V, \quad p\delta = P. \tag{A.24}$$

The deviatoric stresses are rescaled according to the velocity scales and implied strain rate components. This type of scaling leads to an approximation based on the yielded flow region and driven by the flow geometry. In the case of thin films, it is known that a naïve approximation of this type can lead to inconsistent results; see [146]. However, methods have been developed to correct this inconsistency in various geometries, e.g. [17, 102, 199, 246].

Using (A.24), the governing equations become

$$0 = \frac{\partial U}{\partial X} + \frac{\partial V}{\partial Y} \tag{A.25a}$$

$$0 = -\frac{\partial P}{\partial X} + \delta^2 \frac{\partial \tau_{XX}}{\partial X} + \frac{\partial \tau_{XY}}{\partial Y} \tag{A.25b}$$

$$0 = -\frac{\partial P}{\partial Y} + \delta^2 \frac{\partial \tau_{XY}}{\partial X} + \delta^2 \frac{\partial \tau_{YY}}{\partial Y} \tag{A.25c}$$

where we have for the moment ignored the inertial terms (of leading order $O(\delta Re)$ in (A.25b)). The rescaled deviatoric stress components are $\tau_{XY} = \tau_{xy}$ and $\tau_{xx} = \delta\tau_{XX}$. The constitutive relations are similar to (A.5) except with $\tau = \sqrt{\tau_{XY}^2 + \delta^2\tau_{XX}^2}$ and $\dot{\gamma} = \sqrt{\dot{\gamma}_{XY}^2 + \delta^2\dot{\gamma}_{XX}^2}$:

$$\dot{\gamma}_{XX} = 2\frac{\partial U}{\partial X}, \qquad \dot{\gamma}_{XY} = \frac{\partial U}{\partial Y} + \delta^2 \frac{\partial V}{\partial X}.$$

Also note that $\dot{\gamma}_{xy} = \dot{\gamma}_{XY}$, $\dot{\gamma}_{xx} = \delta\dot{\gamma}_{XX}$. Adopting a regular perturbation expansions in δ of form:

$$(P, U, V) = (P_0, U_0, V_0) + \delta(P_1, U_1, V_1) + \delta^2(P_2, U_2, V_2) + ...$$

we find the following expressions for the deviatoric stress components in

yielded parts of the flow

$$\tau_{XY} = \big[\frac{\partial U_0}{\partial Y} + B\ \mathrm{sgn}(\frac{\partial U_0}{\partial Y})\big] + \big[\delta\frac{\partial U_1}{\partial Y}\big] + \mathcal{O}(\delta^2) \tag{A.26a}$$

$$\tau_{XX} = 2\Big(1 + \frac{B}{|\frac{\partial U_0}{\partial Y}|}\Big)\frac{\partial U_0}{\partial X} + \mathcal{O}(\delta) \tag{A.26b}$$

Assuming the above scaling, our periodic domain becomes $X \in [-l\delta/2, l\delta/2]$, $Y \in [-1, 1]$, although we may consider only $Y \geq 0$ through symmetry. The droplet occupies $X \in [-L\delta, L\delta] = [-H, H]$ and $Y \in [-h(X), h(X))$. No slip boundary conditions are satisfied at the walls. In parts of the channel where there is a droplet, the two conditions (A.17a) & (A.17b) are satisfied at $Y = \pm h(X)$. In terms of the rescaled variables these become:

$$\tau_{XY} - \delta^2\frac{2\tau_{XX}h_X}{1 + \delta^2 h_X^2} = 0, \tag{A.27a}$$

$$P + \delta^2\frac{(1 - \delta^2 h_X^2)\tau_{XX} + 2\tau_{XY}h_X}{1 + \delta^2 h_X^2} = \chi X, \tag{A.27b}$$

where h_X is the derivative of $h(X)$ with respect to X. Ignoring the tip of the droplet $X \to \pm H$, we may assume that $|h_X| \sim O(1)$. Assuming that the droplet remains encapsulated in the plug region of the flow the stresses remain indeterminate within the plug, away from the interface.

In order to apply these conditions to deriving a perturbation solution we need at least to understand the order of magnitude of the stress components. The scales we have used are derived from the yielded region, where they are determined by the velocity scales and a leading order shear flow balance for the frictional pressure gradient. As we enter the unyielded plug, the scaling for P and τ_{XY} is likely to remain valid. However, in long-thin geometries it is known that as the plug yields the extensional stresses within the plug become of the same order as the shear stresses, i.e. this is the yielding mechanism. Examples of this feature can be found in e.g. [17, 102, 199, 246]. Therefore,

although the leading order terms in (A.27a) & (A.27b) are clear:

$$\tau_{XY,0} = 0 \quad \text{at} \quad Y = \pm h(X), \tag{A.28a}$$

$$P_0 = \chi X \quad \text{at} \quad Y = \pm h(X), \tag{A.28b}$$

at first order there may be some adjustment as we become close to breaking the plug:

$$\tau_{XY,1} - 2\delta\tau_{XX,0} = 0 \quad \text{at} \quad Y = \pm h(X), \tag{A.29a}$$

$$P_1 + \delta\tau_{XX,0} = 0 \quad \text{at} \quad Y = \pm h(X). \tag{A.29b}$$

A.3.1 $\mathcal{O}(1)$ solution in the yielded region

At leading order (A.25) and (A.26) lead to

$$\begin{aligned} 0 &= \frac{\partial U_0}{\partial X} + \frac{\partial V_0}{\partial Y} \\ 0 &= -\frac{\partial P_0}{\partial X} + \frac{\partial \tau_{XY,0}}{\partial Y} \\ 0 &= -\frac{\partial P_0}{\partial Y} \end{aligned}$$

We consider only $Y > 0$, as the flow is symmetric about the centreline. Integrating the X-momentum equation and satisfying (A.28a) gives

$$\frac{\partial U_0}{\partial Y} + B\ \mathrm{sgn}(\frac{\partial U_0}{\partial Y}) = \frac{\partial P_0}{\partial X}(Y - h) \tag{A.31}$$

The leading order position of the yield surface is denoted $Y = y_y$, which is found by equating the shear stress to the yield stress:

$$\frac{\partial P_0}{\partial X}(Y_y - h) = B\ \mathrm{sgn}(\frac{\partial U_0}{\partial Y}) = -B. \tag{A.32}$$

Integrating once more gives the velocity:

$$U_0(Y) = \begin{cases} u_p - u_{p,0} & \text{if} \quad |Y| \leq y_y, \\ u_p\left[1 - \dfrac{(|Y| - y_y)^2}{(1-y_y)^2}\right] - u_{p,0} & \text{if} \quad |Y| > y_y, \end{cases} \tag{A.33}$$

The leading order plug velocity is given by:

$$u_p = \frac{B}{2(y_y - h(X))}(1 - y_y)^2. \tag{A.34}$$

In order to find y_y, we impose the flow rate constraint across the channel, i.e.

$$\int_{-1}^{1} U_0 \, \mathrm{d}Y = 2 - 2u_{p,0}.$$

Note that the leading order velocity in the droplet is given by continuity at the interface as: $U_0 = u_p - u_{p,0}$. Integrating across the channel gives us:

$$y_y^3 - y_y(3 + \frac{6}{B}) + 2 + 6\frac{h}{B} = 0. \tag{A.35}$$

This cubic equation is similar to (A.14) and gives y_y as a function of $h(X)$ and B. It follows that u_p is also a function of both B and x. The dependence of u_p on X via $h(X)$ contradicts the idea that the plug region is rigid, i.e. this is the so-called *lubrication paradox* of [146]. The inconsistency is resolved at first order in δ.

A.3.2 $\mathcal{O}(\delta)$ solution in the yielded layer

We focus here on the yielded layer of encapsulating fluid, avoiding the tricky issue of the first order momentum balance within the unyielded plug. The idea is to correct the leading order solution, to account for the varying plug speed predicted. In this, we shall assume that $y_y(X)$ is an $\mathcal{O}(\delta)$ approximation to the position of the true yield surface at $Y = y_T$. The X-momentum balance at 1st order in the yielded layer is:

$$\frac{\partial P_1}{\partial X} = \frac{\partial^2 U_1}{\partial Y^2} \tag{A.36}$$

which requires two boundary conditions. One of these is no slip condition ($U_1(Y = 1) = 0$). The other condition can be obtained by noticing that $U(X, y_T) = 0$ provided that the spacing between droplets is long enough and the plug remains unyielded (recall that we have subtracted the pure fluid plug velocity $u_{p,0}$ from the X-component of velocity in translating to the moving frame). Therefore, the condition on U_1 is simply:

$$\equiv U_1(X, y_y) = \frac{1}{\delta}(u_{p,0} - u_p(X)) \equiv \eta. \tag{A.37}$$

This same value is adopted for all $Y < y_y$ in order to correct the plug velocity. Below we shall justify the fact that $\eta = \mathcal{O}(1)$. Note that we have imposed the condition at $y_y(X)$, which is known, rather than at $y_T(X)$. However, assuming that $y_y(X) - y_T(X) = \mathcal{O}(\delta)$, the discrepancy due to imposing at $y_y(X)$ is only at second order.

We integrate (A.36) impose the two boundary conditions and then integrate the flow rate constraint ($\int_{-1}^{1} U_1 \mathrm{d}Y = 0$) to give:

$$\frac{\partial P_1}{\partial X} = -6\eta \frac{y_y + 1}{(y_y - 1)^3} \tag{A.38}$$

and

$$U_1(X, Y) = -\eta \frac{(Y - 1)\Big(3Y + 3Y y_y - 1 - 4y_y^2 - y_y\Big)}{(y_y - 1)^3} \quad \text{if} \quad Y > y_y \tag{A.39}$$

Finally, we find y_T by imposing zero shear rate at $Y = y_T$ and expanding about $Y = y_y$ with respect to δ:

$$\frac{\partial U_0}{\partial Y}(X, y_T) + \delta \frac{\partial U_1}{\partial Y}(X, y_T) = 0 \quad \Longrightarrow \quad y_T(X) = y_y(X) - \delta \frac{\frac{\partial U_1}{\partial Y}(X, y_y(X))}{\frac{\partial^2 U_0}{\partial Y^2}(X, y_y(X))}. \tag{A.40}$$

An example of the perturbation solution is plotted in Fig. A.2a, showing $U_0(X, Y)$ and $y_Y(X)$ for an elliptical droplet with $H = 0.2$ and $\delta = 0.1$ at $B = 1$. Although H and δ are relatively large here (i.e. for what might be considered asymptotic), the idea is simply to amplify visually the fea-

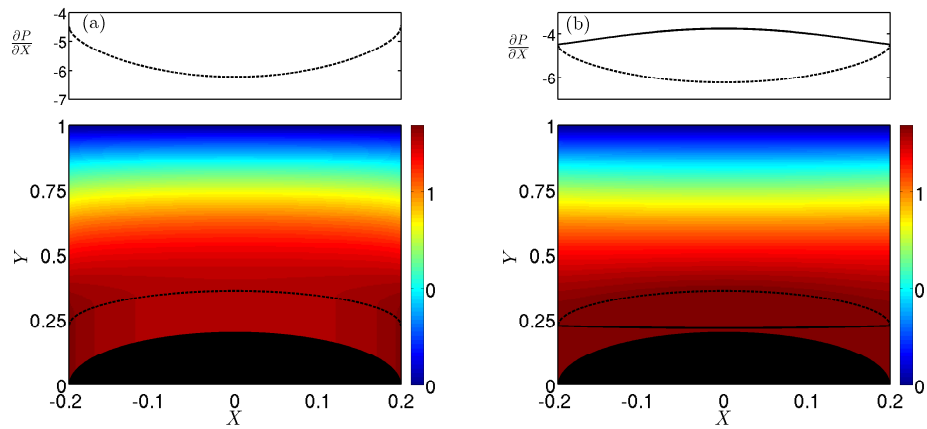

Figure A.2: Contours of the X-component of velocity obtained by the perturbation solution; $H = 0.2$, $\delta = 0.1$ and $B = 1$: a) leading order $U_0(X, Y)$; b) corrected velocity $U_0(X, Y) + \delta U_1(X, Y)$. Uncorrected yield surface position $y_y(X)$ marked with dashed line and corrected yield surface $y_T(X)$ marked with solid line. Pressure gradient for both solutions is also plotted.

tures of the perturbation solution. Fig. A.2b shows the corrected solution $U_0(X, Y) + \delta U_1(X, Y)$ and $y_T(X)$. The corresponding variations in pressure gradients are also shown on the top of each graph.

A.3.3 Size of the yield surface perturbation from $y_{y,0}$ and effects of inertia

Having now derived an expression for $y_T(X)$ we wish to examine the size of the yield surface perturbation from the Poiseuille flow yield surface, $y_{y,0}$. As previously discussed in §A.2.2, it is this quantity that dictates the size of the inertial terms that we have neglected so far.

We note that our perturbation solution has been derived under the assumption that $h(X) \sim \mathcal{O}(\delta)$ and we now define $\bar{h}(X) = h(X)/\delta$. The calculation proceeds in 2 steps. First we examine the departure of y_y from $y_{y,0}$. We write $y_y = y_{y,0} + \delta\xi_1$ and show that ξ_1 is order 1. Substituting

both y_y and $\bar{h}$ into (A.35) and expanding in powers of δ:

$$\mathcal{O}(1): \; y_{y,0}^3 - y_{y,0}(3 + 6/B) + 2 = 0, \tag{A.41a}$$

$$\mathcal{O}(\delta): \; 3y_{y,0}^2\xi_1 - \xi_1(3 + 6/B) + 6\frac{\bar{h}}{B} = 0, \qquad \Longrightarrow \qquad \xi_1 = \frac{\bar{h}}{1 + 0.5B(1 - y_{y,0}^2)} \tag{A.41b}$$

The first expression is simply the Buckingham equation (A.14), as expected. The second expression defines ξ_1. Now, since u_p is defined by y_y and h, straightforward expansion of (A.34) in powers of δ verifies that $\eta = \mathcal{O}(1)$, as has been claimed.

Secondly, we combine (A.40) and (A.41b)

$$y_T(X) - y_{y,0} = \delta\Big(\xi_1(X) - \frac{\frac{\partial U_1}{\partial Y}(X, y_y)}{\frac{\partial^2 U_0}{\partial Y^2}(X, y_y)}\Big). \tag{A.42}$$

Substituting the expressions for the derivatives of the perturbation velocity (following considerable algebra):

$$y_T - y_{y,0} = \delta\left[\xi_1 - \frac{y_{y,0} + 2}{y_{y,0} - 1}\frac{[y_{y,0}\xi_1 + y_{y,0}\bar{h} + \xi_1 - \bar{h}]}{y_{y,0}}\right] + \mathcal{O}(\delta^2) \tag{A.43}$$

and then if we substitute for ξ_1 from (A.41b), we find:

$$y_T - y_{y,0} = \delta\bar{h}\left[\frac{B(y_{y,0} + 1)(y_{y,0}^3 - y_{y,0}(3 + \frac{6}{B}) + 2)}{y_{y,0}(y_{y,0} - 1)(By_{y,0}^2 - B - 2)}\right] + \mathcal{O}(\delta^2). \tag{A.44}$$

We see that the leading order term on the right-hand side vanishes due to (A.41a), so that: $y_T - y_{y,0} \sim \mathcal{O}(\delta^2)$. A similar exercise shows that $U_0 + \delta U_1 = u_{p,0}(y) + \mathcal{O}(\delta^2)$, i.e. the velocity field is given to $\mathcal{O}(\delta^2)$ by the Poiseuille solution of the droplet free flow. To summarise, insertion of an $\mathcal{O}(\delta)$ droplet within the plug region causes only an $\mathcal{O}(\delta^2)$ perturbation in both the yield surface position and the velocity field. However, the stress perturbation is of $\mathcal{O}(\delta)$, as is the pressure gradient perturbation. Additionally, the stress field within the unyielded plug region remains indeterminate. To explore this

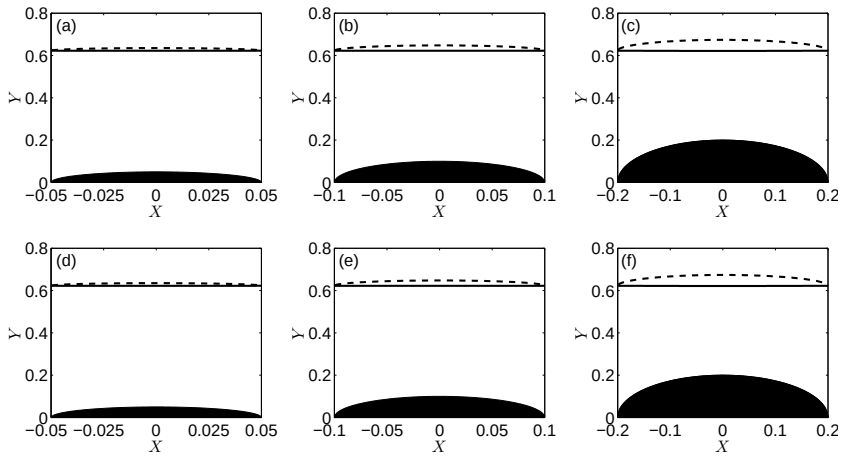

Figure A.3: Position of the yield surfaces $y_T(X)$ (solid line) and $y_y(X)$ (dashed line) for a range of different (elliptical) droplets at $B = 10$. Top row $L = 0.5$, bottom row $L = 0.75$ and columns left to right $H = 0.05$, 0.1 and 0.2. Note that $y_{y,0}$ is equal to the values of $y_y(X)$ at two ends. Due to the adopted scaling, all elliptic droplets are mapped to a circle with radius of H.

surprising feature, Fig. A.3 plots $y_T(X)$ and $y_y(X)$ for a range of different (elliptical) droplets at $B = 5$. As we see, the corrected yield surface position is nearly constant and coincides with $y_{y,0}$ (equal to the end values of $y_y(X)$).

Considering now the question of inertial effects, we see that for an $\mathcal{O}(\delta)$ encapsulated droplet as considered, the uniform Poiseuille flow gives an $\mathcal{O}(\delta^2)$ approximation to the velocity field in the region of the droplet (as well as away from the droplet). The yield surface perturbation is also of $\mathcal{O}(\delta^2)$. This suggest that the appropriate variation in the streamlines away from the uniform Poiseuille solution in the presence of an encapsulated droplet is in fact $\mathcal{O}(\delta^2)$ (instead of the $\mathcal{O}(\delta)$ used to derive and construct our perturbation approximation), and that consequently inertial effects may be legitimately neglected for $\delta^2 Re \ll 1$.

A.4 Order unity iso-dense droplets: $h(x) \sim \delta \sim 1$

We now turn to order unity droplets for which it is necessary to use computational solution. Motivated by the asymptotic results, we proceed under the assumption that the inertial terms may be small even for significant Re, i.e. that an encapsulated droplet held within the plug will not significantly perturb streamlines outside of the plug. This assumption we verify *a posteriori* from our numerical results. We also consider that the droplet and encapsulating fluid have the same density, i.e. $\chi = 0$. As we consider a Stokes flow problem, we impose symmetry conditions at $x = 0$, $x = -l/2$ and $y = 0$, and solve only for: $(x, y) \in [-l/2, 0] \times [0, 1]$. In the encapsulating fluid the Stokes equations are

$$0 = \frac{\partial u}{\partial x} + \frac{\partial v}{\partial y}, \tag{A.45a}$$

$$0 = -\frac{\partial p}{\partial x} + \frac{\partial \tau_{xx}}{\partial x} + \frac{\partial \tau_{xy}}{\partial y}, \tag{A.45b}$$

$$0 = -\frac{\partial p}{\partial y} + \frac{\partial \tau_{xy}}{\partial x} + \frac{\partial \tau_{yy}}{\partial y}. \tag{A.45c}$$

The constitutive laws are (A.5) & (A.6).

The droplet domain is $y \leq h(x)$ and within the droplet the fluid is assumed to move uniformly at the speed of the unyielded plug. Thus, we solve only in the encapsulating fluid domain. The boundary conditions are:

$$-p(0, y) + \tau_{xx}(0, y) = 0, \quad v(0, y) = 0, \quad y \in [H, 1] \tag{A.46a}$$

$$u(x, 1) = 0, \quad v(x, 1) = 0, \quad x \in [-l/2, 0] \tag{A.46b}$$

$$-p(-l/2, y) + \tau_{xx}(-l/2, y) = Gl/2, \quad v(-l/2, y) = 0, \quad y \in [0, 1] \tag{A.46c}$$

$$\tau_{xy}(x, 0) = 0, \quad v(x, 0) = 0, x \in [-l/2, -L] \tag{A.46d}$$

$$\tau_{nt}(x, h(x)) = 0, \quad -p(x, h(x)) + \tau_{nn}(x, h(x)) = 0, x \in [-L, 0] \tag{A.46e}$$

Note in (A.46b) that for simplicity we compute in a fixed frame of reference

instead of the moving frame, as translating by a constant $u_{p,0}$ can be imposed afterwards with no loss of generality. By imposing (A.46c) instead of the uniform Poiseuille flow we allow for the fact that the encapsulating fluid between droplets may not be fully developed. Indeed, below we study the required droplet spacing parameter l, needed for the droplets to be encapsulated. The parameter $Gl/2$ in (A.46c) is essentially the pressure drop along the computational domain. Each computation involves an iteration on G to ensure that the mean velocity is unity, i.e. we satisfy

$$\int_0^1 u(x, y)\ \mathrm{d}y = 1, \tag{A.47}$$

which has a unique solution due to the monotonicity of the flow rate with respect to the pressure drop.

A.4.1 Computational algorithm and benchmarking

The intrinsic difficulty in computing viscoplastic fluid flows comes from the yield stress, which implies an infinite effective viscosity in unyielded flow regions. Two families of methods are commonly used to resolve this difficulty. Regularization methods work by replacing the infinite viscosity with a very large finite value, adjusting (A.5). Two of the more popular choices of effective viscosity are those of [28] and [186]. A review of these methods is given by [101], in which the main drawbacks are explored. In particular regularization methods do not guarantee stress convergence and may fail to give the correct position of the yield surfaces. The potential errors are largest in flows with long-thin geometries; see e.g. [199]. For flows such as that here, where we investigate whether or not the droplet is fully encapsulated in unyielded fluid, regularization methods are unable to provide answers with certainty.

The alternative to regularization methods are algorithms such as the augmented Lagrangian method of [99, 111]. These work with the formulation of the Stokes flow as a minimization problem: wherein the functional to be minimized is non-differentiable due to the yield stress. The minimi-

sation problem (which has a unique solution) is relaxed into a saddle-point problem by introducing Lagrange multipliers. The Lagrangian functional is augmented with stabilization terms and typically solved iteratively using an Uzawa-type algorithm. A modern review of such methods is given by [112]. This is the type of algorithm that we adopt and it is implemented within the C++ Finite Element Method library *Rheolef*, written by P. Saramito and colleagues; see e.g. [214]. A particular feature of this implementation is the the mesh adaptivity, which focuses the mesh around the yield surfaces. Our implementation is slightly modified in order to accommodate the droplet geometry, boundary conditions and the iteration for G. Details of the implementation may be found in [199, 208]. Convergence bounds for the algorithm are given by [214]. In application we typically start with an initial mesh scale, say $d_0 \approx 0.02$, that defines the size of the initial (relatively uniform sized) unstructured triangular mesh. This is refined successively and typically 4 times for our computations. Fig. A.4 shows cycles of the adaptation for one specific case. After the 4th cycle the typical mesh sizes in the plug are ≈ 0.02; near the yield surface $\approx 0.001 \times 0.004$; near the wall: ≈ 0.002.

Starting with a smaller d_0 results in a progressively smaller mesh at each step of the adaptivity and hence a better converged solution. The effects of adaptivity on convergence are also significant for the first few cycles. This is illustrated in Fig. A.5 where we have compared the numerical results of the code for plane Poiseuille flow with the exact solution from §A.2.1. This shows that $||e_{\mathbf{u}}||$ and $||e_p||$, defined below, decays rapidly over the first few cycles of adaptation before leveling out, i.e. reducing the error after 4 cycles requires a smaller initial mesh d_0.

$$||e_{\mathbf{u}}|| = \frac{1}{N_{cells}} \sqrt{\sum_{N_{cells}} |\mathbf{u}_{comp} - \mathbf{u}_{exact}|^2} \tag{A.48a}$$

$$||e_p|| = \frac{1}{N_{cells}} \sqrt{\sum_{N_{cells}} (p_{comp} - p_{exact})^2} \tag{A.48b}$$

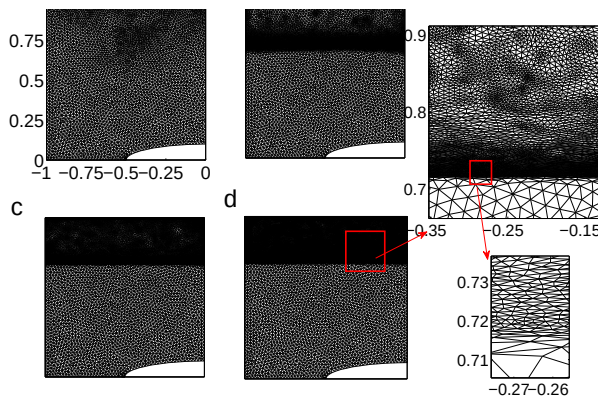

Figure A.4: Mesh adaptation cycles for the case of $B = 20$, $H = 0.1$ and $L = 0.5$, where we start with an initial mesh scale, $d_0 \approx 0.02$: a) cycle 1, 3165 elements; b) cycle 2, 12689 elements; c) cycle 3, 21425 elements; d) cycle 4, 37290 elements. After the 4th cycle the typical mesh sizes are: in the plug: 0.02; near the yield surface: 0.001×0.004; near the wall: 0.002.

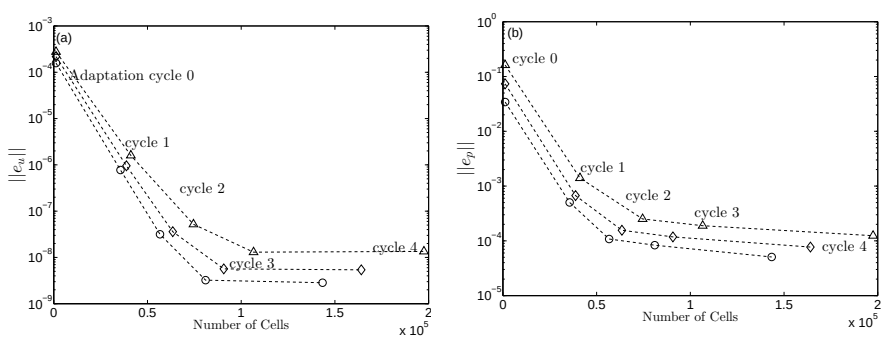

Figure A.5: Code Validation: Error of numerical results for channel Poiseuille flow compared to the exact solution; $\bigcirc$: $B = 10$, $\Diamond$: $B = 20$ and $\triangle$: $B = 50$. a) velocity and b) pressure

We are also able to compare our computed results against the asymptotic solutions over a range of small δ, e.g. fixed small H and varying L. This type of comparison verifies that the errors of leading order and corrected first order solutions are $\mathcal{O}(\delta)$ and $\mathcal{O}(\delta^2)$, respectively. The range of δ tested is however limited since for very small H the droplet becomes a *cut* in the encapsulating fluid, increasingly singular at the ends. On the other hand for larger L the encapsulating plug region breaks. As an aside, we mention that the plane Poiseuille flow velocity solution also gives an $\mathcal{O}(\delta^2)$ error when compared against the computed velocity, and interestingly a numerically smaller error than the corrected perturbation method.

A.4.2 Effects of droplet spacing

As we have already seen, the length of droplets has a significant effect on breaking of the encapsulating plug. With a restriction in L, if one is interested in the throughput of encapsulated droplets it is necessary to understand the effect of droplet spacing on the breaking process. Fig. A.6 shows an example sequence of computations for which the separation distance $l - 2L$ drops below a critical value and the plug regions start to yield. In this case, for $l = 1.625$ (Fig. A.6a) the plug has broken whereas for larger l an intact region exists. If the plug yields around the droplet the computed solution remains valid as solution to the Stokes flow, but in terms of an evolution problem the interface is free to deform and we would expect this deformation to induce a velocity field within the droplet.

Apart from the issue of plug breaking, a separate consideration is whether l is long enough for the flow to become fully developed between the droplets. The method we have chosen to study this compares the mean pressure gradient behind the drop with the analytical solution for plane Poiseuille flow:

$$\Delta p = \frac{p_l - p_L}{l/2 - L},$$

where p_l and p_L are the pressures at $x = -l/2$ and $x = -L$, respectively. For a range of droplet shapes we observe that at sufficiently large l the encapsulation of the droplet is intact and the Δp approaches the analytic

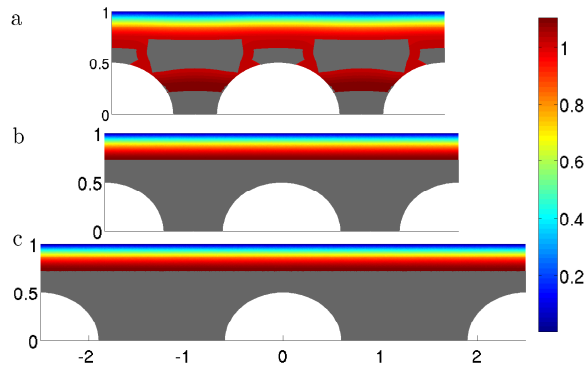

Figure A.6: Example of the effects of droplet spacing for $B = 20$, $H = 0.5$ and $L = 0.6$: a) $l = 1.625$; b) $l = 1.8$; c) $l = 2.5$. The colour map shows the range of speeds in the flow and grey areas show unyielded fluid.

value for a yield stress fluid (Fig. A.7). In fact Δp is always very slightly below the analytical value, due to a reduction very close to $x = -L$, where presumably the fluid senses the presence of the droplet. As a rule of thumb, if l is at least $2.5 \times \max\{2H, 2L\}$ we have found that the pressure drop values remains near constant.

A.4.3 Encapsulation and failure

We have computed approximately 400 encapsulation flows, as described. These cover the approximate ranges: $5 < B < 200$; $0.025 < H < 0.9$; $0.025 < L < 1.25$. Fig. A.8 illustrates some of the general trends observed. For each row of computations the Bingham number is held constant. The left-hand column has L constant and H varied; the right column has H fixed and variable L. The colourmap plots the speed of the fluid, with the grey area denoting the unyielded plug. We observe that there essentially are two different regimes of plug breaking:

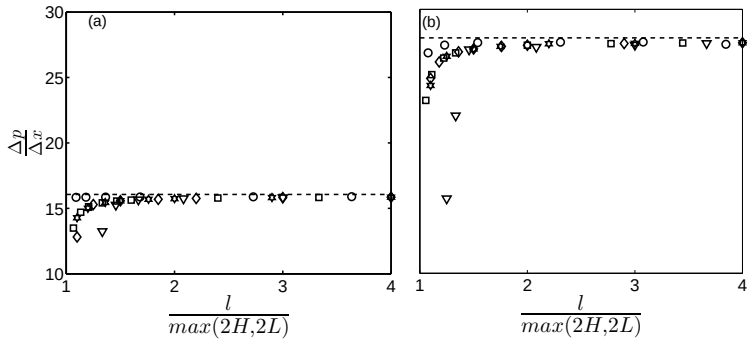

Figure A.7: Variation in the pressure drop upstream of the droplet plotted versus a scaled spacing between droplets. a) $B = 10$, $\triangledown$: $H = 0.45$, $L = 0.6$; $\bigcirc$: $H = 0.55$, $L = 0.15$; $\square$: $H = 0.05$, $L = 0.75$; $\star$: $H = 0.25$, $L = 0.25$ and $\Diamond$: $H = 0.375$, $L = 0.5$ b)$B = 20$, $\triangledown$: $H = 0.5$, $L = 0.6$; $\bigcirc$: $H = 0.65$, $L = 0.2$; $\square$: $H = 0.1$, $L = 0.9$; $\star$: $H = 0.25$, $L = 0.25$ and $\Diamond$: $H = 0.375$, $L = 0.5$. The broken lines show the pressure drop for Poiseuille flow.

Slender droplets : If the droplet aspect ratio $\delta = H/L$ is small (in other word the length of drop is much larger than its width) then the plug appears to yield initially close to the two tips of the droplet (left column of Fig. A.8).

Fat droplets : If the width of the droplet is similar or larger than the length, the plug appears to yield closer to $x = 0$, in the widest part of the droplet (right column of Fig. A.8).

This confirms that increasing either L or H will eventually yield the plug around the droplet, as was suggested by the rudimentary analysis in §A.2.3. The other remarkable observation is that the yield surface position is approximately constant for the simulations shown in Fig. A.8, up to and directly after the plug breaks (although of course with breaks after yielding). This implies that the stress distribution to the outside of the plug is not

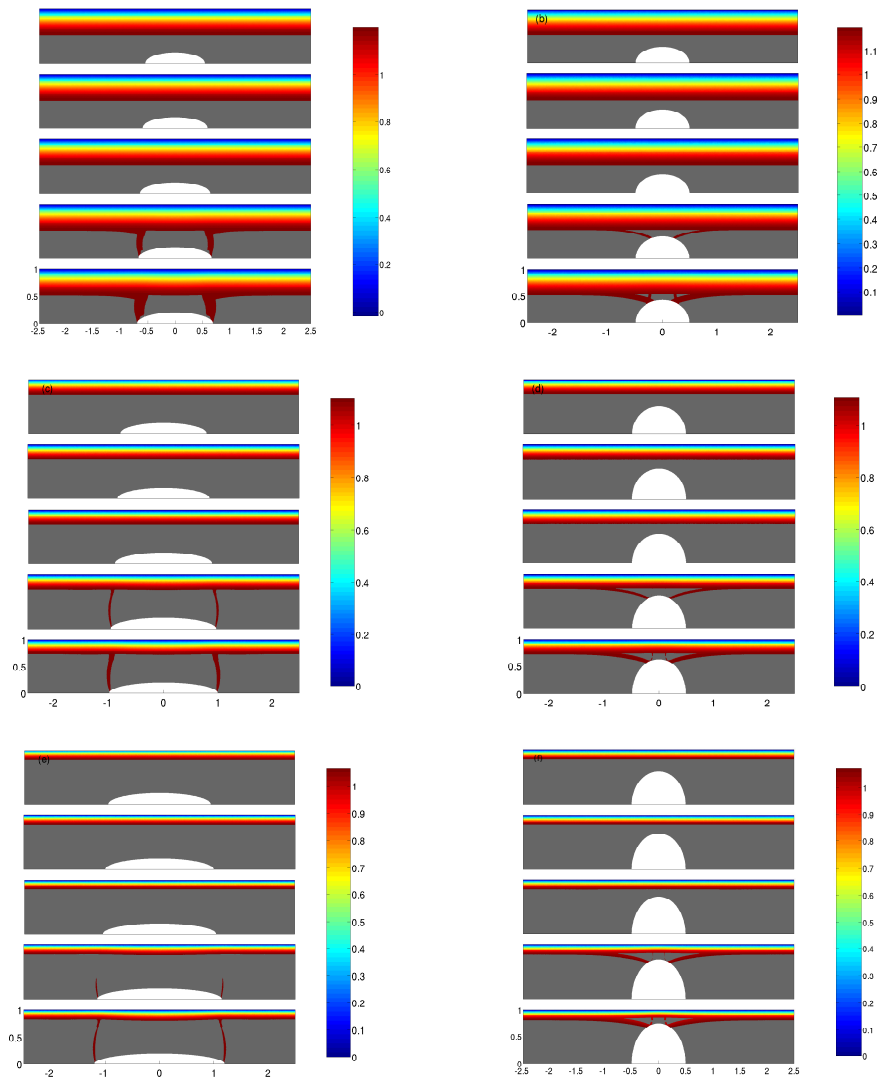

Figure A.8: Speed distribution (**u**) as the droplet gets larger. Rows represent constant Bingham number; $H = 0.2$ over left column (*slender drop*) and $L = 0.5$ over right column (*fat drop*). a) $B = 5$ and $L = 0.55$, 0.6, 0.65, 0.675 and 0.7; b)$B = 5$ and $H = 0.3$, 0.34, 0.375, 0.4 and 0.425; c)$B = 20$ and $L = 0.8$, 0.85, 0.9, 0.925 and 1;d) $B = 20$ and $H = .5$, 0.55, 0.575, 0.61 and 0.625; e)$B = 50$ and $L = 0.95$, 1, 1.05, 1.15, 1.2 f)$B = 50$ and $H = 0.6$, 0.65, 0.69, 0.725 and 0.75

greatly affected by plug breaking. Thus, the deduction from the asymptotic analysis of the past section: of a very small perturbation of the yield surface due to the droplet, appears to be valid for a broader range of aspect ratios $\delta = H/L$.

To examine the breaking mechanism, we have plotted the various stresses in Fig. A.9 for one sequence of slender drops ($B = 20$, $H = 0.2$ and increasing L. The first noticeable feature is that as L increases through the breaking transition the distribution of stresses remains qualitatively similar. Thus, the breaking itself does not affect the overall pattern of stresses which are dominated primarily by changes in droplet shape. Upstream and downstream of the droplet the stresses develop relatively quickly (within a channel width) and adopt distributions close to fully developed. The vertically oriented yielded regions (cracks?) coincide with a region within which the shear stress is focused: τ_{xy} becomes large and negative near the tips of the droplet. This is combined with significant extensional stresses $\tau_{xx} = -\tau_{yy}$. The basic mechanism appears to be that outlined in §A.2.3. In the absence of extensional stresses, the pressure must transition from its shear-layer values to zero at the droplet surface. This driving force is evidently larger at the tips of the droplet. One way of reducing the burden on the change in p is by taking up a part of the pressure within the extensional stresses. For example, on the interface where it is nearly flat the normal stress condition is $p = \tau_{yy}$ and we can observe that $|\tau_{yy}|$ becomes significant, changing sign towards the yield surface. In the centre of the droplets it appears that the distribution of τ_{xy} is shifted upwards by $h(x)$, but near to the ends of the droplet the stresses adapt to the far-field in a relatively narrow region.

The stress distributions in the case of fat droplets are illustrated in Fig. A.10. for $B = 20$, $L = 1.4$. Although the far-fields are similar to the slender droplet, the mechanism of breaking appears to be different. Again we have a transition as the droplet size is increased (now H). Considering the second example in §A.2.3 we might expect that

$$\frac{\partial \tau_{xy}}{\partial y} \sim \mathcal{O}(\frac{B}{y_y - H}),$$

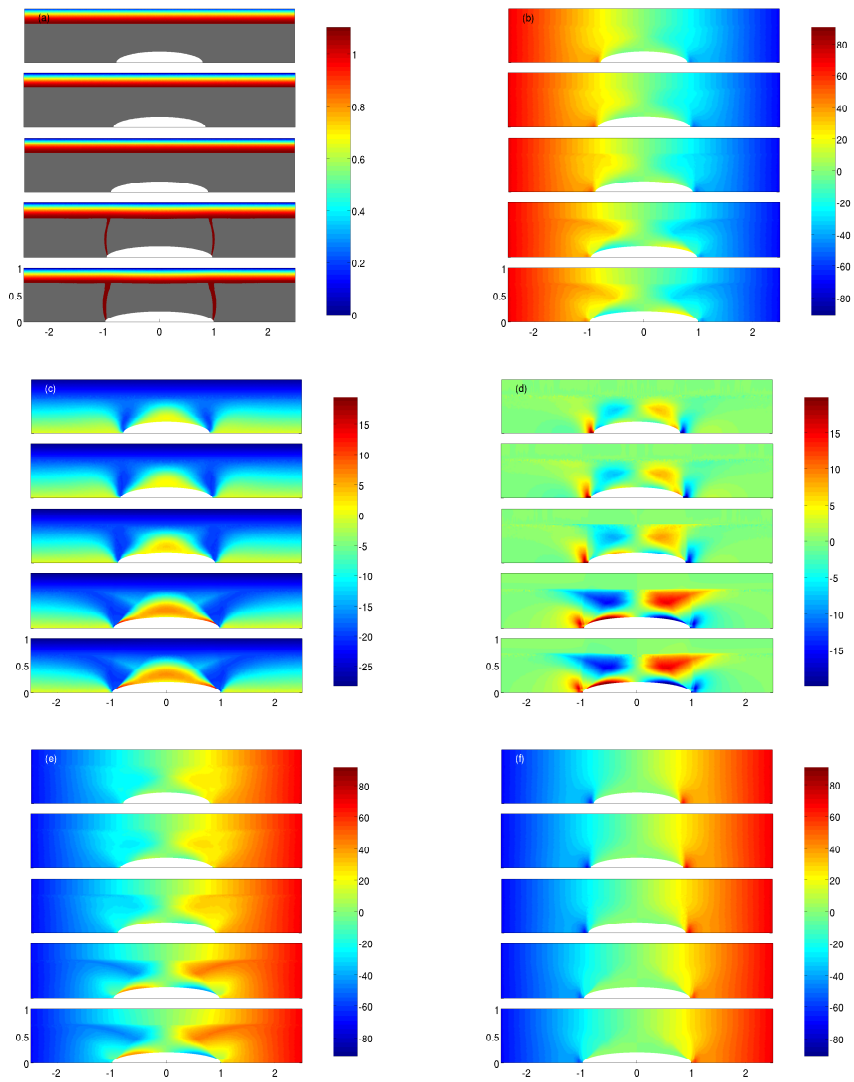

Figure A.9: Stress distribution as the droplet gets larger. $B = 20$, $H = 0.2$ and ;$L = 0.8$, 0.85, 0.9, 0.925 and 1. a) speed; b)pressure; c)τ_{xy}; d)τ_{xx}; e)$\sigma_{xx} = -p + \tau_{xx}$ and f)$\sigma_{yy} = -p + \tau_{yy}$

close to $x = 0$ (within a layer that is getting progressively short). If we suppose that the pressure gradient is partly constrained by the far-field plane Poiseuille flow pressure gradient, then we might expect that the y-derivative of τ_{xy} is balanced by x-derivatives in τ_{xx} which we observe in Fig. A.10. The yielding appears to occur at the ends of the central shear layer.

A.4.4 Perturbation of pressure

It is also insightful to quantify the perturbation of pressure as a result of insertion of the droplet inside the plug region. Figs. A.9 & A.10 indicate the distribution of the pressure perturbation is localised around the droplet positions. To quantify this we define:

$$\phi_p = \frac{|\Delta p_{\{H,L\}}(-X, X) - \Delta p_{\{0,0\}}(-X, X)|}{\Delta p_{\{0,0\}}(-1, 1)} \tag{A.49}$$

where $\Delta p_{\{H,L\}}(-X, X)$ is the pressure drop over the length $[-X, X]$ computed with an elliptic droplet of size H & L. Here X is selected as our computational length (which is chosen to ensure the flow is fully developed between droplets; see the discussion in §A.4.2). Thus, $\Delta p_{\{0,0\}}(-X, X)$ represents the pressure drop over the same length in an unperturbed Poiseuille flow. This difference is normalized by the pressure drop $\Delta p_{\{0,0\}}(-1, 1)$, representing the pressure drop in Poiseuille flow over a length equivalent to the channel width.

Fig. A.11 shows variation of ϕ_p with respect to the size of drop as well as the yield stress (B). Note that in each of the subplots the largest value of L or H that is illustrated corresponds to a case for which the plug yields. Figure A.11a is associated to *slender* drops where we see the pressure perturbation is less than 1% of pressure scale ($\Delta p_{\{0,0\}}(-1, 1)$). However, the effect of droplet size is more significant in the case of *fat* droplets; see Fig. A.11b. This is probably linked to the different failure mechanisms observed already for slender and fat droplets. For droplets that don't break the plug ϕ_p remains rather small. It is of course intuitive in both cases that larger

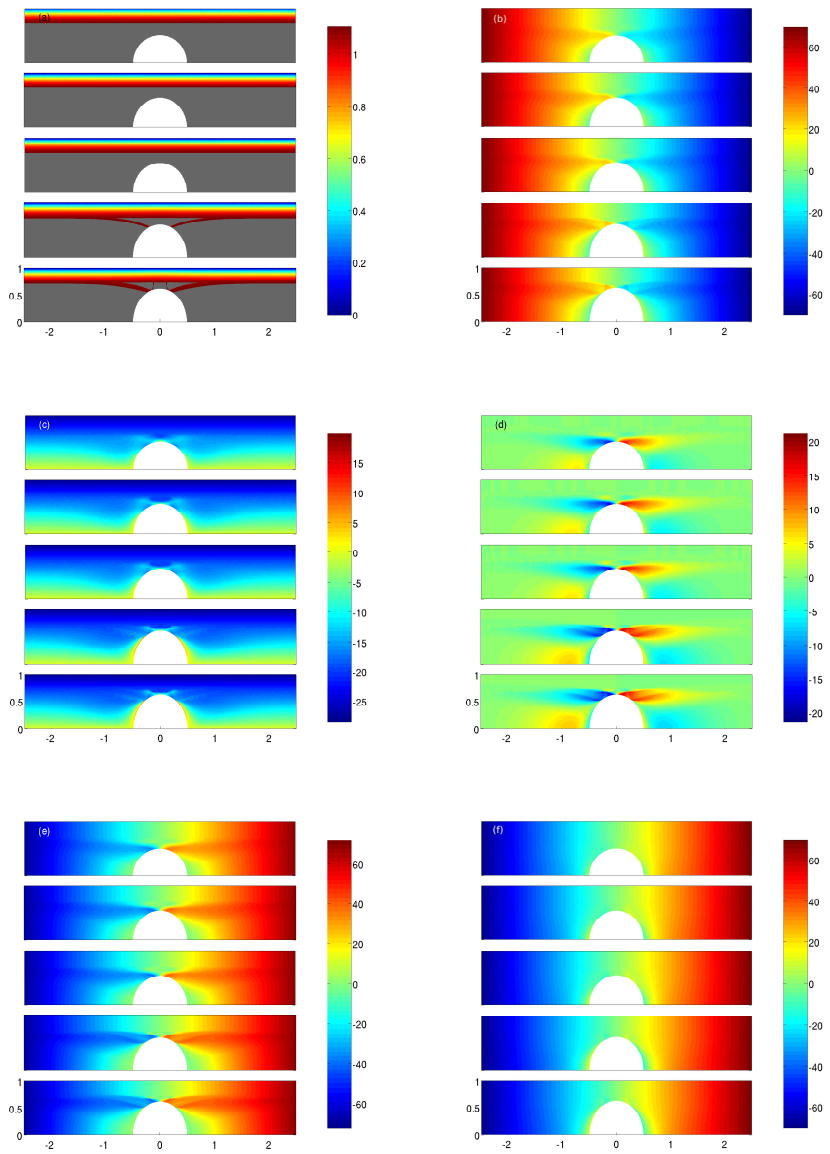

Figure A.10: Stress distribution as the droplet gets larger. $B = 20$, $L = 0.7$ and $H = 0.5$, 0.55, 0.575, 0.61 and 0.625. a) speed; b)pressure; c)τ_{xy}; d)τ_{xx}; e)σ_{xx} and f)σ_{yy}

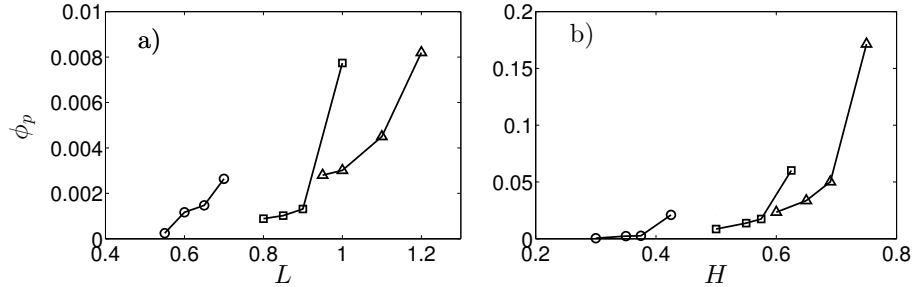

Figure A.11: Variation of pressure perturbation parameter ϕ_p with size of the droplet for different Bingham numbers ($\circ$: $B = 5$, $\square$: $B = 20$ and $\triangle$: $B = 50$); a) drops with varying length and constant height ($H = 0.2$) and b) drops with varying height and constant length ($L = 0.5$). In each subplot the largest value of L or H corresponds to a case with a yielded plug.

droplets lead to larger pressure perturbations. Equally, as remarked earlier, although increasing B increases the ability of the plug to resist yielding it also increases the frictional pressure drop, and hence the stress variation that must be accommodated within the plug.

A.4.5 Maximum size of encapsulated droplets

By successively iterating with respect to H and L we are able to approximately determine the limiting size of droplet that can remain encapsulated within the plug region. Fig. A.12 shows the critical values in the (L, H)-plane for five different values of Bingham number, B. This plot is the conclusion of approximately 400 different simulations. For a given Bingham number, any drop lying below the associated curve does not break the plug region. We see that for any Bingham number (no matter how large) we have a maximum values for the length and height of the droplet. The maximum height is mostly limited by the plug width. Although there is no similar simple physical limit for the maximum length, we still see that the growth of stresses for long droplets yields the plug. In fact the shape of the curves at small H indicates that for slender droplets the encapsulation becomes

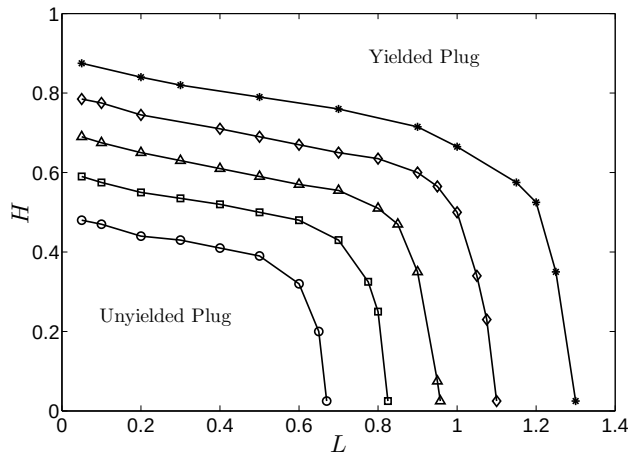

Figure A.12: Maximum size of encapsulated droplets, computed for five different B. ◯: $B = 5$; □: $B = 10$; △: $B = 20$, ◊: $B = 50$ and ⋆: $B = 200$

very sensitive to changes in the length, i.e. small increases in the length can break the plug (see also Fig.A.9a, c & e).

A last observation here is that the increase in size of droplet with B is much less than linear. Therefore, just increasing the yield stress of the encapsulating fluid does not allow correspondingly large droplets. The underlying reasons why seem to be captured in the simple analysis of §A.2.3. Long droplets break near the ends. Breaking arises from the need to bridge the discrepancy between non-zero (frictional) pressures in the yielded fluid layers and zero normal stress on the droplet surface. This discrepancy increases with L but also with B, i.e. the frictional pressure scales like $xB/y_{y,0}$. It is unclear what the asymptotic behaviour might be as $B \to \infty$. If we assume that the pressure discrepancy provides the main stress scale for τ, we'd expect the limiting lengths to satisfy $L \sim \mathcal{O}(y_{y,0}) \sim \mathcal{O}(1 - \frac{\sqrt{2}}{B^{1/2}})$ as $B \to \infty$, i.e. a finite limit would be attained. This analysis may be too simplistic.

A.5 Encapsulation with fluids of different densities

We now explore the effect of allowing a density difference between the fluids. Assuming the encapsulated fluid remains in steady rigid motion, the pressure field within the droplet is: $p = \chi x +$ constant, where we recall that $\chi = (\hat{\rho}_d - \hat{\rho})\hat{g}\hat{R}^2/(\hat{\mu}\hat{U}_0)$ represents the competition between buoyant and viscous stresses. Considering the preceding discussion and the simple analysis in §A.2.3, an intuitive notion is that by selecting $\chi = -B/y_{y,0}$ the pressure gradient in the droplet would match that in the yielded fluid layers. This would eliminate the need for normal stress gradients across the plug, and hence presumably reduce τ.

We test the above notion computationally. The code described earlier is adapted by discretizing both the droplet and carrier fluid domains. The additional body force term χ can be added to the droplet x-momentum equation, (or instead $-\chi$ added to the carrier fluid equations). Different fluid properties are assigned in each domain (e.g. $B = 0$ is inside the droplet) and the Stokes flow solution is computed on both domains simultaneously using the augmented Lagrangian algorithm described earlier.

Firstly, we address the question of whether the density difference might significantly affect breaking of the plug region. Fig. A.13a shows the maximum height H before the plug yields, for two droplets with different L at $B = 20$. We observe that the shorter droplet ($L = 0.4$) is relatively insensitive to χ, whereas the longer droplet ($L = 1.75$) shows remarkable sensitivity. Sensitivity to L *per se* is to be expected as the effect of χ naturally amplifies with x (or L), due to the channel orientation. We see that if the droplet is heavier than the carrier fluid ($\chi > 0$), encapsulation fails at a smaller sizes for the drop. On the other hand, for lighter droplet ($\chi < 0$) buoyancy tends to stabilize the encapsulation, allowing larger drops to be successfully encapsulated. For the case shown in Fig. A.13a, in which $B = 20$, we see that maximum size of the drop happens at $\chi \approx -27$ to -28. This approximately coincides with the frictional pressure gradient of the plane Poiseuille flow, (for $B = 20$ we find $\frac{\partial p}{\partial x} = -\frac{B}{y_{y,0}} \approx -27.8$). Thus, the

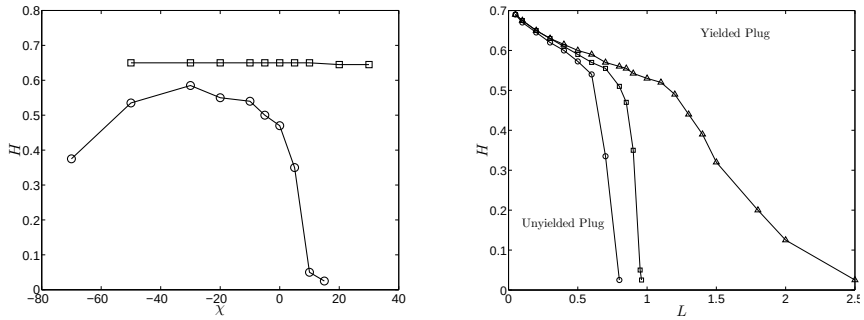

Figure A.13: $B = 20$ (a) Variation of maximum height (maximum H which does not break the plug) for two different length of drop □: $L = 0.4$ and ◯: $L = 1.75$ with density difference (χ). (b) Maximum size of drop for for three different χ. ◯: $\chi = 20$; □: $\chi = 0$ and △: $\chi = -20$.

notion that selecting $\chi \approx -B/y_{y,0}$ may provide an optimal size of encapsulated droplet appears reasonable. Essentially buoyancy acts to balance the frictional pressure losses for $\chi > -B/y_{y,0}$, but on decreasing χ still further strong buoyancy forces act to exert stress on the plug.

Note that although the normal stress discrepancy may be reduced for $\chi \approx -B/y_{y,0}$, the tangential stresses in the plug are still perturbed by the presence of the droplet. Thus, the droplet may still break the plug. Fig. A.13b shows the critical values of H and L for $B = 20$, above which the plug yields for three different $\chi = -20$, 0 and 20. Again we see favourable density difference (lighter droplets) allows the encapsulation of longer drops, whereas unfavourable density difference (heavier droplets) weakens the encapsulation capabilities.

Fig. A.14 explores variations in the stress fields as the density of the droplet is varied. The plug close to the central part of the droplet is largely unaffected by χ, but on increasing $|x|$ we observe generation of extensional stresses towards the ends of the droplet within the plug (Fig. A.14d). Increasing χ amplifies the size of extensional stresses and of the pressure in these regions, (Figs. A.14b & d). The stresses combine so that σ_{yy} shows

little variation in y (Fig. A.14f), which implies that the pressure variation in y is negatively amplified in τ_{xx}. The net effect is that the front of the droplet is stretched and the rear is compressed (in the x-direction); see Fig. A.14e. These normal stress gradient results in significant shear stresses (Fig. A.14c). The underlying pattern is not changed by $\chi > 0$, but simply amplified.

A.6 Droplet encapsulation in a pipe

For the purposes of practical application we now consider the analogous flow to that described in §A.2, but within a vertical pipe of radius $\hat{R}$. We describe the problem in a cylindrical coordinate system, assuming that the flow is axisymmetric with droplets traveling along the pipe axis. As in §A.2 a moving coordinate system is adopted. Lengths and velocities are scaled with $\hat{R}$ and $\hat{W}_0$ respectively where $\hat{W}_0$ is the mean velocity along the pipe, i.e. the flow rate is $\pi\hat{R}^2\hat{W}_0$. Denoting by $\hat{W}_p$ the fully developed plug velocity of the Hagen-Poiseuille flow (with no droplets), the variables are as follows:

$$(r, z, \theta) = \left(\frac{\hat{r}}{\hat{R}}, \frac{\hat{z} - \hat{W}_p\hat{t}}{\hat{R}}, \theta\right); \qquad (u, w) = \left(\frac{\hat{u}_r}{\hat{W}_0}, \frac{\hat{u}_z - \hat{W}_p}{\hat{W}_0}\right), \tag{A.50}$$

and $t = \hat{W}_p\hat{t}/\hat{R}$. The deviatoric stresses are scaled with $\hat{\mu}\hat{W}_0/\hat{R}$ as is the modified pressure (on subtracting the static pressure of the carrier fluid).

$$\hat{p} = \hat{p}_0 + \hat{\rho}\hat{g}\hat{z} + \frac{\hat{\mu}\hat{W}_0}{\hat{R}}p \tag{A.51}$$

Exploiting axisymmetry of the geometry, dimensionless form of continuity and momentum equations governing carrier fluid are

$$\frac{1}{r}\frac{\partial}{\partial r}(ru) + \frac{\partial w}{\partial z} = 0 \tag{A.52a}$$

$$Re\left(u\frac{\partial w}{\partial r} + w\frac{\partial w}{\partial z}\right) = -\frac{\partial p}{\partial z} + \frac{1}{r}\frac{\partial}{\partial r}(r\tau_{rz}) + \frac{\partial \tau_{zz}}{\partial z} \tag{A.52b}$$

$$Re\left(u\frac{\partial u}{\partial r} + w\frac{\partial u}{\partial z}\right) = -\frac{\partial p}{\partial r} + \frac{1}{r}\frac{\partial}{\partial r}(r\tau_{rr}) + \frac{\partial \tau_{rz}}{\partial z} - \frac{\tau_{\theta\theta}}{r} \tag{A.52c}$$

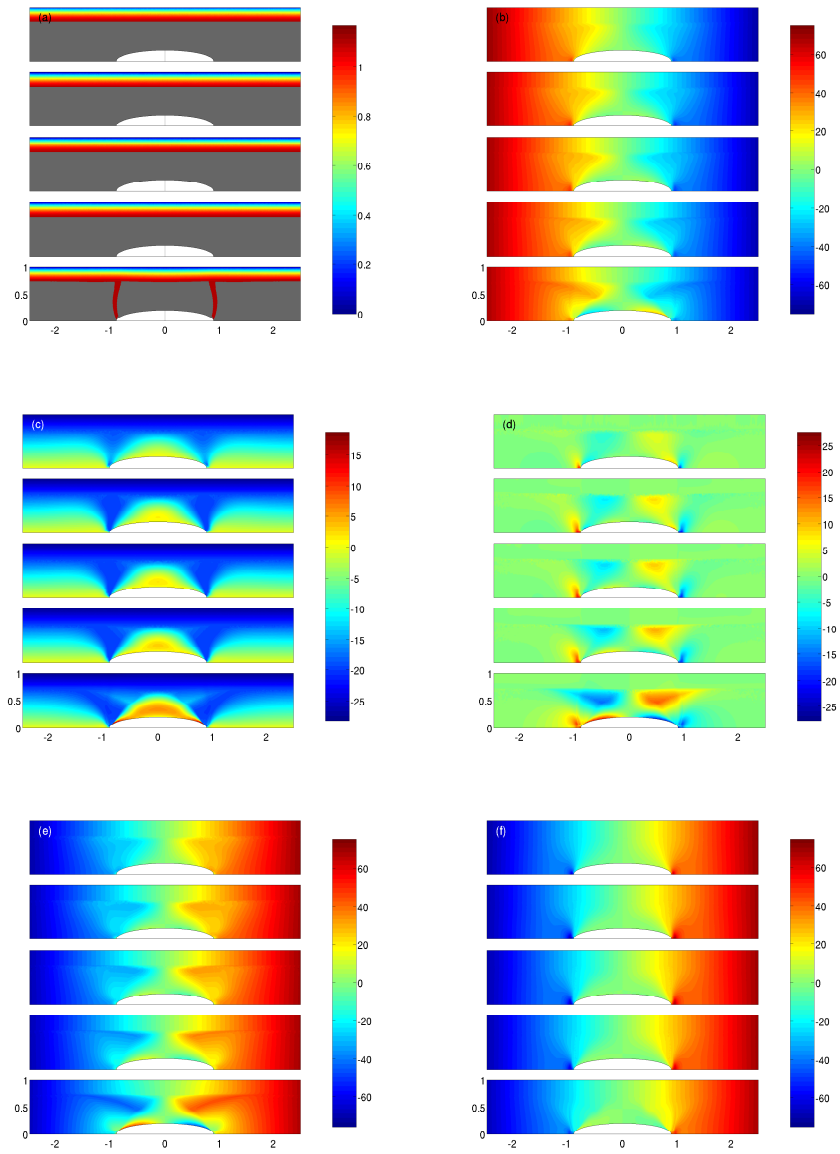

Figure A.14: Stress distribution as the droplet becomes heavier: $B = 20$, $L = 0.9$ and $H = 0.2$. From top to bottom in each panel: $\chi = -10$, -1, 0, 1 and 10. a) speed; b) pressure; c) τ_{xy}; d) τ_{xx}; e) σ_{xx} and f) σ_{yy}.

The constitutive relations are similar to (A.5), but now $\dot{\gamma} = \sqrt{\dot{\gamma}_{rr}^2 + \dot{\gamma}_{zz}^2 + \dot{\gamma}_{\theta\theta}^2 + 2\dot{\gamma}_{rz}^2}$ is the rate of strain, and $\tau = \sqrt{\tau_{rr}^2 + \tau_{zz}^2 + \tau_{\theta\theta}^2 + 2\tau_{rz}^2}$ is the deviatoric stress. The components are given by:

$$\dot{\gamma}_{rr} = 2\frac{\partial u}{\partial r}; \quad \dot{\gamma}_{\theta\theta} = 2\frac{w}{r}; \quad \dot{\gamma}_{zz} = 2\frac{\partial w}{\partial z}; \quad \dot{\gamma}_{rz} = \dot{\gamma}_{zr} = \frac{\partial w}{\partial r} + \frac{\partial u}{\partial z}. \tag{A.53}$$

Reynolds number and Bingham number are defined as $Re = \hat{\rho}\hat{W}_0\hat{R}/\hat{\mu}$ and $B = \hat{\tau}_Y\hat{R}/(\hat{\mu}\hat{W}_0)$.

As before, we consider a single droplet from our periodic train of droplets. The scaled droplet length is L and the maximal radius is H. The droplet surface is steady within the moving fame of reference and is denoted $r = h(z)$. Within the droplet we must satisfy:

$$\frac{1}{r}\frac{\partial}{\partial r}(ru) + \frac{\partial w}{\partial z} = 0 \tag{A.54a}$$

$$\phi Re\Big(u\frac{\partial w}{\partial r} + w\frac{\partial w}{\partial z}\Big) = -\frac{\partial p}{\partial z} + m\frac{1}{r}\frac{\partial}{\partial r}(r\frac{\partial w}{\partial r}) + m\frac{\partial^2 w}{\partial z^2} + \chi \tag{A.54b}$$

$$\phi Re\Big(u\frac{\partial u}{\partial r} + w\frac{\partial u}{\partial z}\Big) = -\frac{\partial p}{\partial r} + m\frac{1}{r}\frac{\partial}{\partial r}(r\frac{\partial u}{\partial r}) + m\frac{\partial^2 u}{\partial z^2} - m\frac{u}{r^2} \tag{A.54c}$$

where $\chi = \frac{(\hat{\rho}_d - \hat{\rho})\hat{g}\hat{R}^2}{\hat{W}_0\hat{\mu}}$. Similar boundary and interfacial conditions are satisfied as for the plane channel problem earlier. As before, it is assumed that the droplet translates uniformly within the moving plug.

A.6.1 Poiseuille flow solution

In a fixed frame of reference the Hagen-Poiseuille solution is easily found:

$$W_p(r) = \begin{cases} w_{p,0} & \text{if} \quad r \le r_{y,0}, \\ w_{p,0}\left[1 - \left(\frac{r - r_{y,0}}{1 - r_{y,0}}\right))^2\right] & \text{if} \quad r \ge r_{y,0}, \end{cases} \tag{A.55}$$

where $w_{p,0} = \frac{B}{2r_{y,0}}(1 - r_{y,0})^2$. On imposing the flow rate constraint we find that the yield surface position satisfies the following Buckingham equation:

$$r_{y,0}^4 - 4r_{y,0}(1 + \frac{3}{B}) + 3 = 0, \tag{A.56}$$

which has a unique zero in the interval $(0, 1)$.

A.6.2 Slender drop

For practical reasons it is advantageous to know if encapsulated droplets within a pipe flow also result in vanishing small perturbations of the flow streamlines. Thus, similar to §A.3 we re-scale the problem assuming a small slender droplet:

$$r = R, \quad \theta = \Theta, \quad z\delta = Z, \quad u = \delta U, \quad w = W, \quad p\delta = P. \tag{A.57}$$

Upon rescaling and neglecting the inertial terms, the governing equations are:

$$\frac{1}{R}\frac{\partial}{\partial R}(RU) + \frac{\partial W}{\partial Z} = 0 \tag{A.58a}$$

$$0 = -\frac{\partial P}{\partial Z} + \frac{1}{R}\frac{\partial}{\partial R}(R\tau_{RZ}) + \delta^2\frac{\partial \tau_{ZZ}}{\partial Z} \tag{A.58b}$$

$$0 = -\frac{\partial P}{\partial R} + \delta^2\frac{1}{R}\frac{\partial}{\partial R}(R\tau_{RR}) + \delta^2\frac{\partial \tau_{RZ}}{\partial Z} - \delta^2\frac{\tau_{\Theta\Theta}}{R} \tag{A.58c}$$

where $\tau_{rz} = \tau_{RZ}$, $\tau_{rr} = \delta\tau_{RR}$, $\tau_{\theta\theta} = \delta\tau_{\Theta\Theta}$ and $\tau_{zz} = \delta\tau_{ZZ}$. The constitutive relations are similar to (A.5), except that now:

$$\tau = \sqrt{\tau_{RZ}^2 + \delta^2\tau_{RR}^2 + \delta^2\tau_{\Theta\Theta}^2 + \delta^2\tau_{ZZ}^2} \tag{A.59a}$$

$$\dot{\gamma} = \sqrt{\dot{\gamma}_{RZ}^2 + \delta^2\dot{\gamma}_{RR}^2 + \delta^2\dot{\gamma}_{\Theta\Theta}^2 + \delta^2\dot{\gamma}_{ZZ}^2} \tag{A.59b}$$

and

$$\dot{\gamma}_{RZ} = \frac{\partial W}{\partial R} + \delta^2\frac{\partial U}{\partial Z} \tag{A.60a}$$

$$\dot{\gamma}_{RR} = 2\frac{\partial U}{\partial R} \tag{A.60b}$$

$$\dot{\gamma}_{\Theta\Theta} = 2\frac{W}{R} \tag{A.60c}$$

$$\dot{\gamma}_{ZZ} = 2\frac{\partial W}{\partial Z} \tag{A.60d}$$

We adopt a regular perturbation expansion in δ: $(P, W, U) = (P_0, W_0, U_0) + \delta(P_1, W_1, U_1) + \cdots$, substitute into the equations and derive the following leading order problem:

$$\frac{1}{R}\frac{\partial}{\partial R}(RU) + \frac{\partial W}{\partial Z} = 0 \tag{A.61a}$$

$$0 = -\frac{\partial P}{\partial Z} + \frac{1}{R}\frac{\partial}{\partial R}(R\tau_{RZ}) \tag{A.61b}$$

$$0 = -\frac{\partial P}{\partial R} \tag{A.61c}$$

Integrating the axial momentum equation from $R = h$ yields

$$\tau_{RZ} = \frac{\partial W_0}{\partial R} + B\mathrm{sgn}\left(\frac{\partial W_0}{\partial R}\right) = \frac{\partial W_0}{\partial R} - B = \frac{1}{2}\frac{\partial P}{\partial Z}.\left(R - \frac{h^2}{R}\right) \tag{A.62}$$

and defining the yield surface $R = R_y$ as where $\tau_{RZ} = -B$ we find:

$$\frac{\partial W_0}{\partial R} = \frac{1}{2}\frac{\partial P}{\partial Z}\left(R - R_y - \frac{h^2}{R} + \frac{h^2}{R_y}\right): \qquad \frac{\partial P}{\partial Z} = -\frac{2BR_y}{R_y^2 - h^2} \tag{A.63}$$

We can reconstruct the velocity in the fixed frame, using the no-slip condition at $R = 1$:

$$W_0(r) + w_{p,0} = \begin{cases} w_p & \text{if} \quad 0 \le R \le R_y \\ w_p\left[1 - \left(\frac{0.5(R-R_y)^2 + h^2(R-R_y)/R_y + h^2\ln(R_y/R)}{0.5(1-R_y)^2 + h^2(1-R_y)/R_y + h^2\ln R_y}\right)\right] & \text{if} \quad R_y \le R \le 1 \end{cases} \tag{A.64}$$

where the plug velocity is given by

$$w_p = B\frac{R_y}{R_y^2 - h^2}\left(\frac{(1-R_y)^2}{2} + \frac{h^2}{R_y}(1-R_y) + h^2\ln R_y\right) \tag{A.65}$$

Finally we use the unit flow rate condition to find the pressure gradient (equivalently R_y). This leads to the following Buckingham equation:

$$R_y^4 - 4(1 + 3/B)R_y + 3 + \frac{2h^2}{R_y}\left[(1-R_y)^2(2+R_y) + \frac{6}{B}\right] = 0, \tag{A.66}$$

which may be solved numerically for R_y.

Comparing the solution above with that in §A.6.1, we note that the leading order plug velocity, velocity profile and the Buckingham equation are all $\mathcal{O}(h^2)$ perturbations from the unperturbed Poiseuille flow solution, *c.f.* (A.64) & (A.66), (A.55) & (A.56), ...

The implications of this are two-fold. Firstly, in terms of the perturbation procedure there is no need to seek a correction to the solution at first order in δ. In practical terms, this means that for any small slender drop of aspect ratio δ the streamlines in the yielded layer will be perturbed by $\mathcal{O}(\delta^2)$, suggesting that inertial effects on the flow are of $\mathcal{O}(\delta^2 Re)$ as for the channel flow. Secondly, this suggests that a perturbation approximation of the above form would only require a first order correction when $h \sim \delta^{1/2}$. As $\delta = H/L$ is the droplet aspect ratio, this suggests $L \sim \delta^{-1/2}$. This hints that longer and wider droplets may be accommodated in the pipe geometry.

A.6.3 Examples of encapsulation and failure

We now present computed solutions of droplets as either L or H are increased until breaking point. Fig. A.15 shows yielding of the "slender" droplet and Fig. A.16 shows the "fat" droplet. Superficially, the yielding mechanism are similar to the channel flow in where the plugs break (ends or near the centre). However, as suggested by the previous section, the plugs generally break at larger values of H and L.

The main reason is in the normal stresses. The pressure distributions found are qualitatively similar between pipe and channel geometries. At the yield surface in the channel $-\sigma_{yy}$ is continuous and approximately equal to the pressure. The normal stress must then vanish at the droplet surface which transfers some of the pressure into τ_{yy}. Since $\tau_{xx} + \tau_{yy} = 0$ we experience extensional stresses along the plug, i.e. $\tau_{xx} \neq 0$, and particularly near the ends of the droplet. These normal stress gradients promote shear stresses τ_{xy}, but additional shear stresses result directly in the widest part of the droplet where the stress gradients must increase.

The pipe differs firstly in that although normal stresses are generated at the yield surface, τ_{rr} can now be balanced by the hoop stress $\tau_{\theta\theta}$ as well as

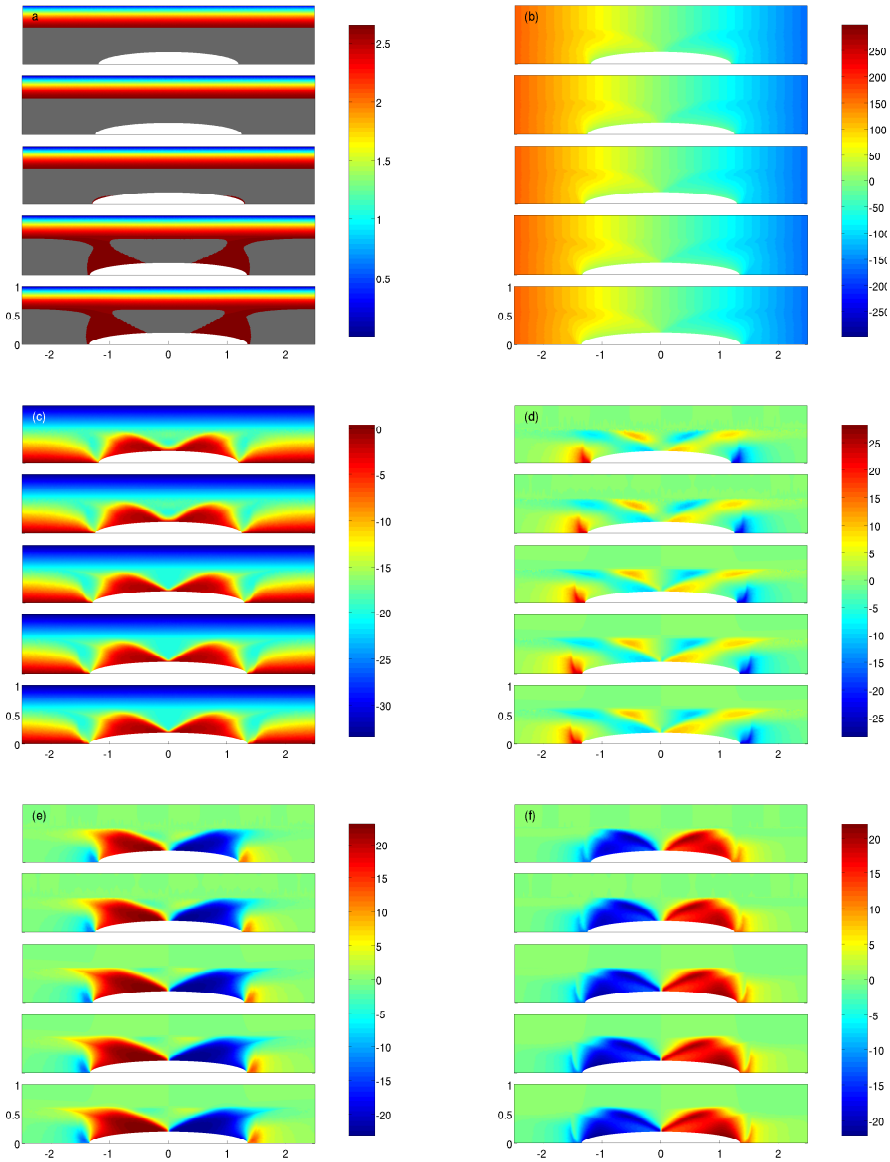

Figure A.15: Stress distribution in the axisymmetric geometry as the droplet gets longer: $B = 20$, $H = 0.4$ and $L = 1.2$, 1.25, 1.3, 1.34 and 1.45. a) velocity; b) pressure; c) τ_{rz}; d) τ_{zz}; e) τ_{rr} and f) $\tau_{\theta\theta}$.

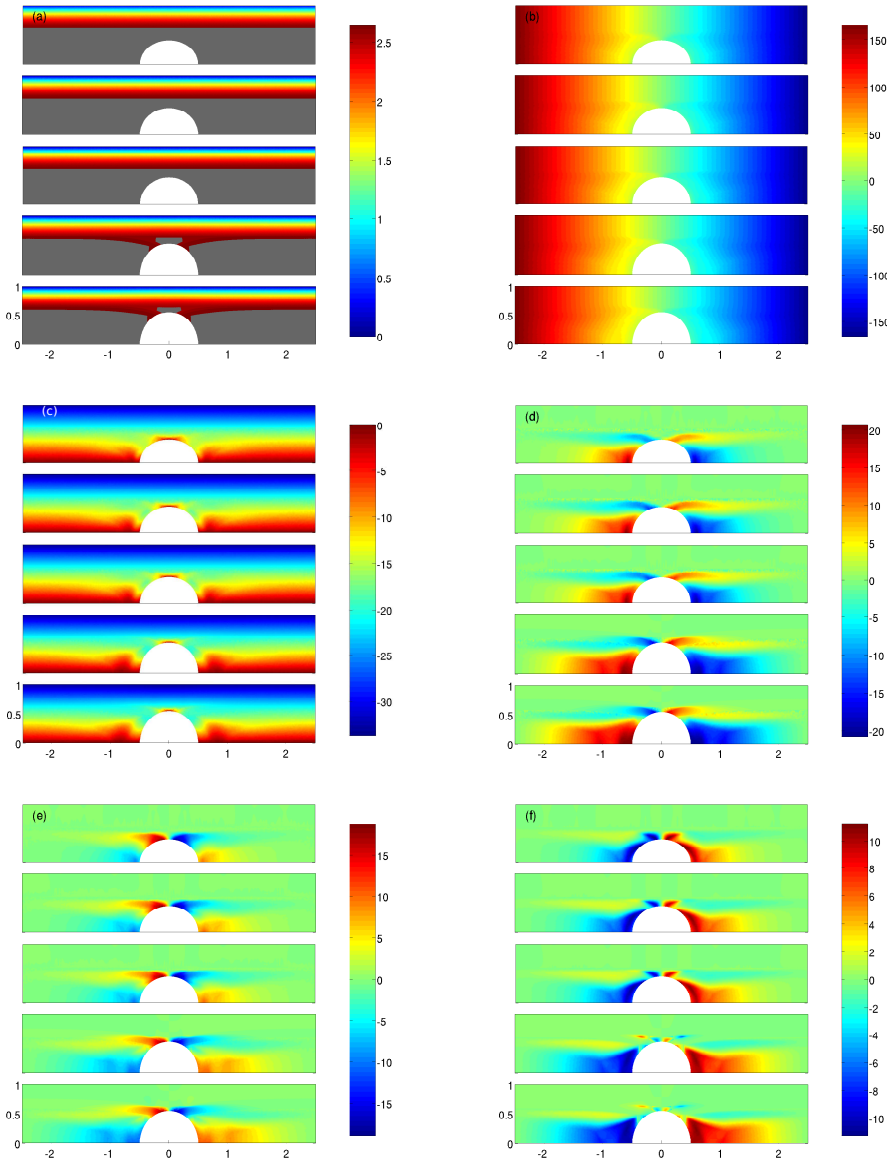

Figure A.16: Stress distribution in the axisymmetric geometry as the droplet height is increased: $B = 20$, $L = 0.5$ and ;$H = 0.4$, 0.45, 0.5, 0.525 and 0.55. a) velocity; b) pressure; c) τ_{rz}; d) τ_{zz}; e) τ_{rr} and f) $\tau_{\theta\theta}$.

by τ_{zz}. Indeed, comparing Figs. A.15e & f, we see that τ_{rr} and $\tau_{\theta\theta}$ largely cancel out over much of the plug, leaving only small bands where τ_{zz} is significant (Fig. A.15d). As a result, the shear stresses in much of the plug appear drastically reduced; see Fig. A.15c, occurring mostly close to $z = 0$.

Maximum size of encapsulated droplets

Following approximately 300 computations we have been able to quantify the maximal size of encapsulated droplets at four different Bingham numbers; see Fig. A.17. In order to have a better comparison between channel and pipe geometries, we include the channel data for $B = 10$. We see that in the range of slender droplets encapsulation is much easier in pipe geometry than in the channel although for short droplets the channel allows larger H. The computed results for the slender droplets are suggestive of $L \to \infty$ as $H \to 0$. Although consistent with the notion that $H \sim \delta^{1/2}$ and $L \sim \delta^{-1/2}$ (see §A.6.2), the slender geometries are not ideal for computations.

A.7 Discussion and summary

In visco-plastically lubricated flows, multi-layer flows are kept stable through the yield stress of the lubricating fluid, which prevents the interface from deforming; see e.g. [100, 126, 127, 130, 171]. In [123] this concept has been extended to multi-layer flows in which the interface is shaped, e.g. wavy, but again the yield stress prevents interfacial deformation. In this chapter we have extended the concept in a different direction. Steady Poiseuille flows of yield stress fluids along uniform ducts are characterized by unyielded central plug regions, traveling at constant speed along the duct. Here we have investigated whether we may encapsulate droplets of a second fluid within the plug region of the yield stress fluid, with again the shape held constant by the yield stress of the fluid.

We have shown that the above method is indeed feasible as a transport method. Using both asymptotic methods for slender droplets and computational solution otherwise, we have shown that these flows exist in both plane channel and pipe geometries. Introducing a droplet moving at the steady

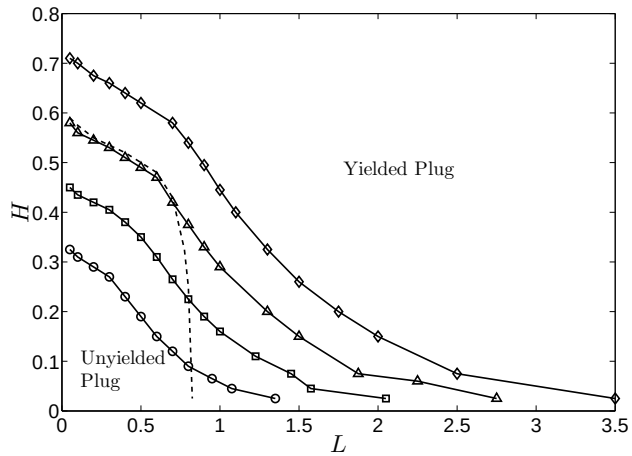

Figure A.17: Maximum size of encapsulated droplets for four different Bingham numbers. ◯: $B = 5$; □: $B = 10$; △: $B = 20$, ◊: $B = 50$ Included for comparison is a single curve showing the maximum size of droplet in the channel geometry for $B = 10$ (broken line).

speed of the plug does not deform the interface but does induce stresses within the carrier fluid. It is the latter that may lead to breaking of the plug. In both geometries we have found that the yield surface of the plug region containing the droplet is not significantly perturbed, apparently remaining near-planar as the droplet size is increased up until the point at which the plug breaks. From the asymptotic solution it appears that the deformation is of $\mathcal{O}(\delta^2)$ for slender droplets, where $\delta = H/L \ll 1$ represents the droplet aspect ratio. The significance of this result is that we can expect that inertial effects in the yielded part of the flow will scale like εRe, where ε is the aspect ratio of the streamlines, (i.e. $\varepsilon = \delta^2$ for slender droplets). Thus, we expect that the solutions and results we have computed here will retain their validity as approximations to the solution for significant Re, even though they are computed under Stokes flow assumptions. More clearly, the Stokes flow assumption produces an approximation that is

self consistent provided that $\varepsilon Re \ll 1$.

Note that it is the inertial terms that are responsible for flow instability. Our results suggest that the velocity perturbation due to the droplet is small. Thus, there is the possibility that these flows may be observable up to high Re. On the other hand note that the effect of the stress field perturbations in the yielded part of the flow are unpredictable in terms of stability. In the perturbation solution we have seen that the first order pressure gradient essentially compensates for the leading order (see Fig. A.2), resulting in a slightly reduced pressure drop over the length of the droplet, and the same effect is present in the computed results e.g. see Figs. A.9b, A.10b and similar. The reduction in pressure drop appears relatively small for as long as the unyielded plug remains intact. Fig. A.11 has presented examples of the pressure drop perturbation variation with H, L and B. The perturbation is insignificant for slender droplets, but for fat droplets may become significant compared to a typical pressure drop (over a length equal to the channel width), e.g. approaching 10% around yielding, for large B. Note that although this may be significant over the droplet length, it is less significant over the length between droplets. As we have shown, a minimal spacing of around 3 droplet lengths is required in order to allow the flow to become fully developed between droplets. Thus, for large l the net reduction in pressure drop is negligible.

In our results we have focused mainly on establishing feasibility of these flows, studying the stress distributions up until failure of the plug, and determining the limiting size of droplets. Two failure modes have been uncovered: droplets that become increasing slender tend to break the plug at the ends of the droplet, whereas those that become increasingly slender tend to break near the centre of the droplet. Loosely speaking, the end mode of breakage appears to be driven by normal stress development whereas the central mode is driven by tangential stress gradients. For elliptic (ellipsoidal) droplets we have computed the critical H & L at which breaking occurs for both channel and pipe geometries. Increasing the yield stress (via B) does increase the limiting droplet size, but not as much as might be expected. This is because the yield stress also increases the size of stresses found in

the flow, i.e. considered at constant flow rate.

The limiting values of H & L are different for channel and pipe, as might be expected. At the same B the channel may allow slightly larger H for the same L. Here the limiting factor is anyway the yield surface position, which is similar as a function of B. The limitation in terms of length shows a more significant difference, with the pipe able to encapsulate much longer droplets than the channel. The pipe geometry uses the hoop stress to reduce normal stress effects. A different way in which droplet size may be increased is via introduction of a density difference between fluids. When pumping in the direction of gravity, lighter droplets increase encapsulation volume (heavier if pumping against gravity). This increase in encapsulation volume is not unbounded, but appears to reach a maximum approximately when the frictional pressure gradient of the base flow matches the buoyancy, i.e.

$$\frac{\partial p_0}{\partial x} = -\frac{B}{y_{y,0}} = \chi \qquad \Rightarrow \qquad \frac{\hat{\tau}_Y}{\hat{g}\hat{R}y_{y,0}} = \hat{\rho} - \hat{\rho}_d. \tag{A.67}$$

On decreasing the buoyancy beyond this limit, buoyancy stresses contribute to breaking of the plug. Simplistically, the main mechanism of buoyancy at the limit (A.67) is to compensate within the droplet for pressure variations in the yielded layer. This then reduces the need for normal stress gradients between the droplet interface and yield surface.

Note that m plays no role in our analysis, as there is no flow within the droplet. For as long as the droplet is held in the plug, the droplet motion has no driving force. Thus, motions relative to the plug translation should decay viscously: essentially m comes into play influencing the speed of this decay.

The key advantage of the encapsulation methodology proposed in this chapter is that the yield stress holds the interface rigid, instead of relying on capillary forces as is common in many droplet encapsulation studies. Thus, we have not considered surface tension effects in the analysis. Depending on the chosen droplet fluid there may anyway be no surface tension. We note that in using miscible fluids in many practical situations Péclet numbers (based on molecular diffusion) are very large and with no relative droplet

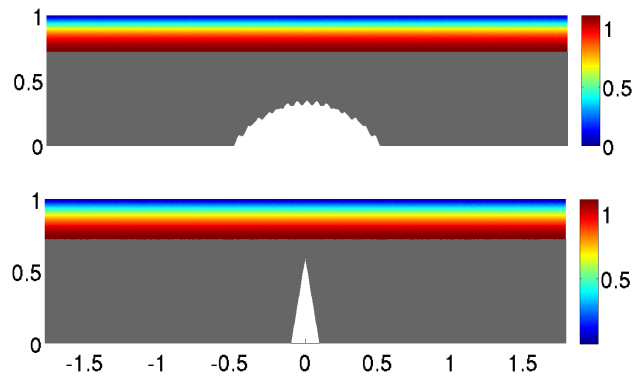

Figure A.18: Encapsulation of drops with exotic shapes.

motion dispersion is nullified. If the droplet is immiscible the validity of this neglect rests on the relevant stresses, and we expect our results to retain validity provided that

$$\hat{\tau}_Y \gg \frac{\hat{\sigma}_T}{\hat{\kappa}}, \tag{A.68}$$

where $\hat{\sigma}_T$ and $\hat{\kappa}$ are the surface tension coefficient and (a representative) radius of curvature of the droplet. Surface tension values between yield stress fluids and other fluids are not well known and reliable measurement techniques are still being developed, e.g. [39]. Nevertheless, for values typical of water and light oils, with yield stresses of $\sim$ 10Pa capillary effects are insignificant on lengthscales $\gtrsim$ 2 mm, which represents many industrial scale pumping operations. This is not to say that interesting flow effects might not be produced by encapsulating immiscible fluid droplets. Indeed, these may have some advantages in the forming part of such a flow where it is likely that the plug is unyielded as a droplet is introduced to the main flow. Study of such flows is for the future.

Methodologically, we have used asymptotic and computational methods. Asymptotic methods have proven successful but show limitations. Firstly,

they predict only the velocity and stress distributions outside the plug, but not the stress distribution inside the plug. Although we attempted to derive predictions of the (indeterminate) stress fields inside the plug, in order to predict breaking, we were unsuccessful. The computational solutions reveal rather complex stress distributions inside the plug, not easily inferred from the asymptotic analysis. Secondly, predicting other flow features such as spacing between successive droplets also was not possible asymptotically. Thirdly, as we assume *a priori* that the droplet translates rigidly in the plug, there is no way to include the density difference, i.e. we solve a 1 fluid problem with a perturbed droplet boundary.

Our focus has been on computational and analytical methods and our results certainly need experimental verification, which is intended in the future. Using idealized models such as the Bingham model have both advantages and disadvantages. The advantage is in being able to establish the key dynamical features in an unambiguous way. The disadvantage is that the assumption of rigid sub-yield behaviour is an acknowledged idealization. In practice the sub-yield (or low shear) rheological behaviour depends on the specific material, with viscous, elastic, thixotropic and viscoelastic descriptions being advanced accordingly. This has been a topical area of research for many years; see e.g. [21, 23, 65, 67, 167]. It is clear that in any experimental study of the encapsulation process introduced here, we will encounter sub-yield values of the stress field, meaning that the real material behaviour of the experiment may affect the results. This additional complexity does not however mean that the yield stress features of the idealized models will not be observed experimentally. For example, small bubbles and particles are commonly observed to remain trapped in yield stress fluids (such as Carbopol) over timescales of weeks/months, in accordance with the idealized notion of a yield stress. However, Stokes flow settling experiments reveal low Re flow fore-aft asymmetries in conflict with inelastic generalized Newtonian models; see e.g. [200]. As another example, theoretical and computational features of the VPL flows that motivated our study have been verified experimentally by [125, 130]. Thus, we believe that experimental study is certainly feasible and have reasonable confidence that model pre-

dictions can be realised.

Although we have not found any direct experimental study of the flows described, it is worth noting that solid particles are frequently transported by yield stress fluids. Drilled cuttings are removed from wellbores in this way, using drilling muds. Coal water suspensions have long been a way of transporting fuel over long distances and mined tailings are often transported to/from thickeners and tailings dams via pipelining. Many of these applications have significant density differences and pipelines oriented (approximately) horizontally. As well as a significant industrial literature there are some more targeted studies. Merkak and co-workers [159, 160] have studied the behaviour of neutrally buoyant spheres in horizontal pipe flows of Carbopol. At relatively low concentrations of particles of 1/8th the pipe diameter they show that the translational velocity of the particles approaches that of the plug as the Bingham number increases. For smaller diameter particles convergence to the plug velocity with B is faster. In these experiments the particles are distributed throughout the flow, rather than centrally positioned, and of course the interface conditions are different for droplet and rigid particle. Thus, direct comparison is not possible. The results of [159, 160] do however suggest that non-local effects of the particles on the stress field may be felt within the plug region even for dilute suspensions.

Other future areas for exploration include more realistic models for the yield stress fluids, e.g. shear-thinning and other effects. We do not expect qualitative differences in the ability to encapsulate in steady flows, but rheological effects such as visco-elasticity may aid in the establishment of these flows. Lastly, although we have computed elliptical shaped droplets in this chapter, in principle a yield stress allows any shape to be encapsulated. Fig. A.18 shows some exotic droplet shapes that do not yield the plug.

Appendix B

Some notes on computations

Throughout the thesis we have use the augmented Lagrangian method and have computed a wide range of flows. Each chapter outlines the computational algorithm and implementation details related to the computations carried out. However, there are a few additional aspects of the computations that we review here for completeness.

B.1 Convergence and mesh adaptation

We have used anisotropic mesh adaptation for all of our steady computations (chapters 2-5). BAMG [117] is the underlying mesh generator. It is constructive to explain the primary concepts of mesh adaptation here. First the solution is computed on an initial mesh $\mathcal{T}_0$. The user provides a metric M over the domain and the mesh generator tries to construct a new mesh in which the error of linear interpolation for M is equally distributed over all elements of the new mesh. The interpolation error in direction $\mathbf{d}$ over (triangular) element K is:

$$e_{K,\mathbf{d}} = h^2_{K,\mathbf{d}} \| \frac{\partial^2 M}{\partial \mathbf{d}^2} \|, \tag{B.1}$$

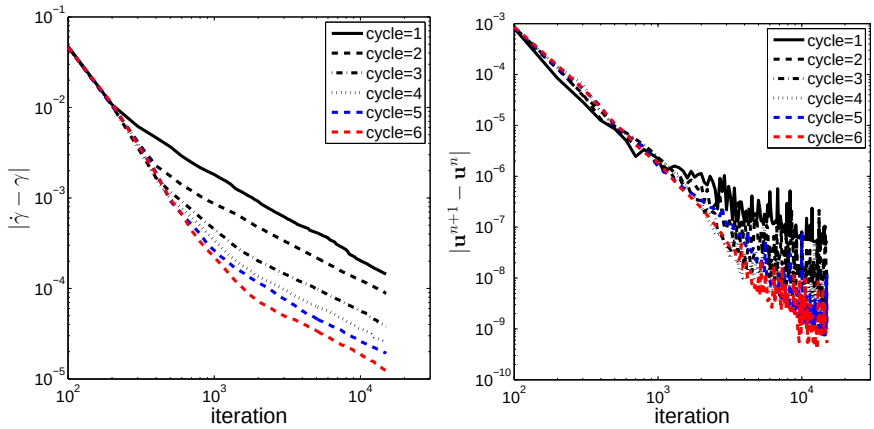

Figure B.1: Variation of residuals of strain rate multiplier (left) and velocity field (right) with mesh adaptation.

where $h_{K,\mathbf{d}}$ is the length of K in direction $\mathbf{d}$ and the second derivative along $\mathbf{d}$ is:

$$\frac{\partial^2 M}{\partial \mathbf{d}^2} = \mathbf{d}^T H_{0,h} \mathbf{d}. \tag{B.2}$$

Here $H_{0,h}$ is the discrete linear Hessian of the metric M:

$$H(M) = \begin{bmatrix} \dfrac{\partial^2 M}{\partial x^2} & \dfrac{\partial^2 M}{\partial x \partial y} \\ \dfrac{\partial^2 M}{\partial x \partial y} & \dfrac{\partial^2 M}{\partial y^2} \end{bmatrix}. \tag{B.3}$$

Let (λ_1, λ_2) be eigenvalues of the Hessian matrix and $(\mathbf{d}_1, \mathbf{d}_2)$ the respective eigenvectors. It follows that

$$\frac{\partial^2 M}{\partial \mathbf{d}_1^2} = \lambda_1, \quad \frac{\partial^2 M}{\partial \mathbf{d}_2^2} = \lambda_2. \tag{B.4}$$

The error $e_{K,\mathbf{d}}$ would be independent of $\mathbf{d}$ when $e_{K,\mathbf{d}_1} = e_{K,\mathbf{d}_2}$. This would mean

$$h_{K,\mathbf{d}_1}^2 |\lambda_1| = h_{K,\mathbf{d}_2}^2 |\lambda_2| = E_0, \tag{B.5}$$

where E_0 is the error requested by the user. With this analysis it can

be observed that the triangle K should be scaled by a factor $\sqrt{E_0/\lambda_i}$ in direction i.

We can see the effect of adaptation in Figure B.1 which shows the residuals of velocity and strain rate multiplier versus iteration number for a wavy channel computation, (with parameters $H = 2,\ L = 10,\ B = 100$). We observe that both velocity and strain rate fields converge faster with each adaption, for any given number of iterations. However, the impact of the adaption on the strain rate convergence is much more noticeable. This is a typical behaviour of the augmented Lagrangian algorithm, in which the multipliers converge slower than the velocity. Adaptation mainly helps to improve the accuracy of the multiplier convergence. This can be also verified in Figure B.2, in which we show the mesh and unyielded regions for first, second and sixth adaptation of the above computation. It appears that the shape of the unyielded regions improves significantly with successive adaptations.

B.2 Defining yield surfaces

In theory, the augmented Lagrangian algorithm converges to the exact yield stress flow solution. However in practice, (and quite apart from mesh convergence) any iterative algorithm is stopped at some point when the residual is less than some small tolerance value ϵ. This tolerance might affect the shape of the yield surfaces which are defined for the exact Bingham fluid flow as the level set where $\tau = B$ (Bingham number). Therefore, the shape of the yield surfaces could depend on the tolerance ϵ. Of course this problem exists in regularization methods as well because there is also an iteration in the solution variables, i.e. for the nonlinear viscosity. Therefore, in regularization methods 2 parameters cause error: the regularization parameter (sometimes called m), and ϵ while only the second one ϵ is present in augmented Lagrangian methods. Secondly, we can rationally expect to get good estimate of the true yield surfaces by using the contours of $\tau = B + \delta$, with δ chosen to be some small value, depending how much the augmented Lagrangian iteration convergence (ϵ). This same point is also mentioned in

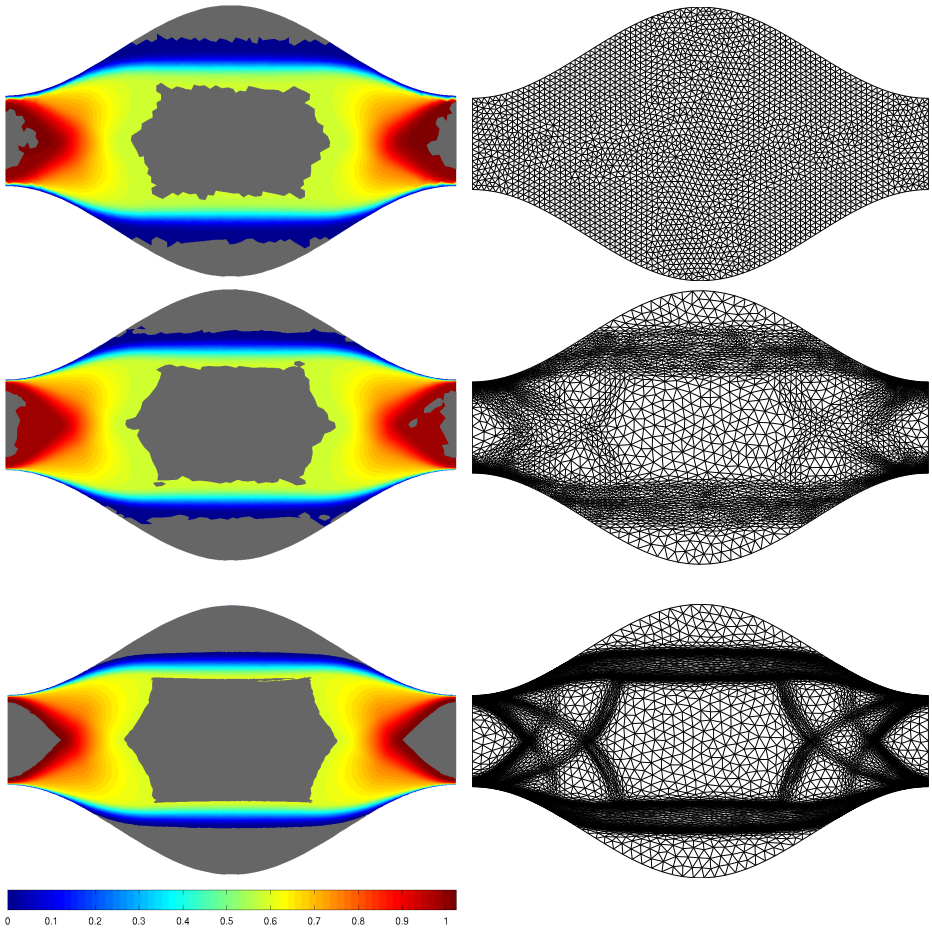

Figure B.2: The speed colormap with unyielded regions and the corresponding mesh for different adaptation cycles.

[256].

Our underlying intuition is that we know that the augmented Lagrangian iterations are converging to the correct solution in a triple of mathematical function spaces (velocity, strain rate and stresses), and in particular that the stress should converge in the space of admissible stresses, as discussed in Section 1.3. Then, the stress maximization principle means that the exact solution has a smaller deviatoric stress compared to the current iteration of

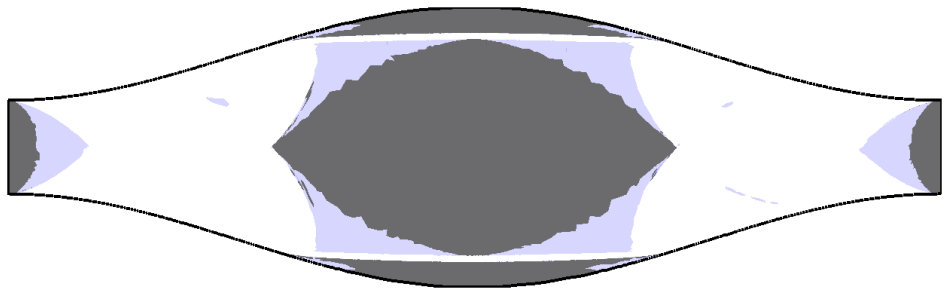

Figure B.3: The variation of contours for stress. The solid gray is $\tau = \tau_y$ and the lighter shows $\tau = \tau_y + .083$. Parameters are $H = 2,\ L = 20,\ B = 10000$.

the augmented Lagrangian algorithm. Therefore, the contour $\tau = B + \epsilon$ should include the unyielded plug regions. The value of ϵ to select would definitely depend on how much the iterations are converged. Generally, for higher Bingham number problems ϵ should be larger, as these cases are harder to converge for the prescribed maximum number of iterations. We have found that using $\epsilon = \mathcal{O}(|\dot{\boldsymbol{\gamma}}(\mathbf{u}) - \boldsymbol{\gamma}|)$ to be a good choice. Note that

$$\tau \leq B + \epsilon \Leftrightarrow \dot{\gamma}(\mathbf{u}) \leq \epsilon. \tag{B.6}$$

This means the regions where the the deviatoric stress is slightly above the yield stress are equivalent to those regions which have a slightly non-zero strain rate. Finally, we remark here that for many of the computed flows using exactly $\tau = B$ gives good results. Only for high Bingham number flows do we need to consider this way of estimating the true yield surface.

B.3 Ribbons of unyielded region

In Chapter 3 we saw that for some of the asymmetrical channels flows, e.g. Figure 3.4, a very thin *ribbon* of unyielded fluid forms. Apart from its thin geometry, a more interesting observation was that the pressure shows a sudden change (almost a jump) cross the two sides of this ribbon. To explore that this jump behaviour makes physical sense we plot the traction vector

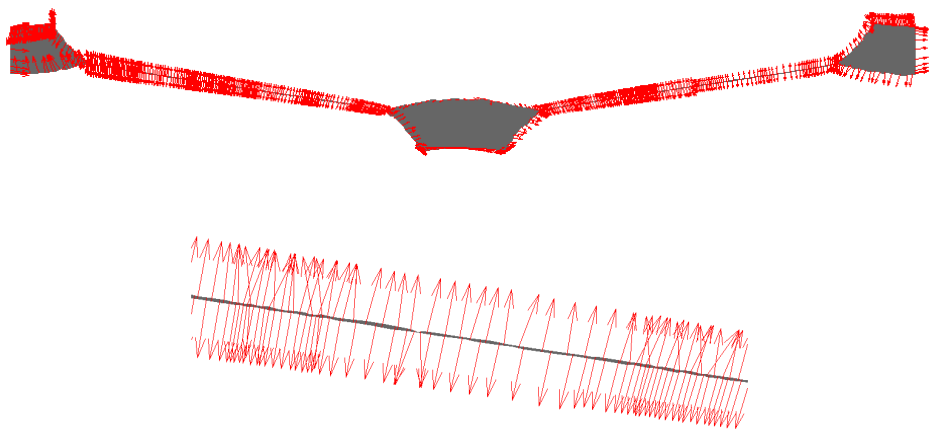

Figure B.4: The traction vector on the boundary of the unyielded regions for $B = 2$, $H = 3$, $L = 10$, $\psi = 0.5$ (top row in Figure 3.4). The bottom figure show a zoom on part of ribbon unyielded fluid which shows continuous traction along it.

on the sides of one such unyielded ribbon, in Figure B.4. It is evident that the traction vector is continuous along the thin ribbon of unyielded fluid.